Tailored Corotational Formulations for the Nonlinear Static and Dynamic Analysis of Bistable Structures

PUC-Rio - Certificação Digital Nº 1512807/CA

Thesis presented by Murillo Vinícius Bento Santana
with a view to obtaining the PhD Degree in Engineering Sciences (ULB - "Docteur en Sciences de l'Ingénieur") and in Civil Engineering (PUC–Rio - "Doutor em Engenharia Civil")
Année académique 2018-2019

Advisors : Prof. Dr. Paulo Batista Gonçalves (PUC–Rio)
Department of Civil and Environmental Engineering
and Prof. Dr. Péter Zoltán Berke (ULB)
Building, Architecture & Town Planning (BATir) Department

Thesis jury :

Paulo Batista Gonçalves (PUC–Rio, Advisor)
Péter Zoltán Berke (ULB, Supervisor)
Thierry Jacques Massart (ULB, Chair)
Mohammed Hjiaj (INSA Rennes, Secretary)
Vincent Denoël (University of Liège)
Ney Augusto Dumont (PUC–Rio)
Ricardo Azoubel da Mota Silveira (UFOP)

CNPq
Conselho Nacional de Desenvolvimento
Científico e Tecnológico

Murillo Vinícius Bento Santana

Tailored Corotational Formulations for the Nonlinear Static and Dynamic Analysis of Bistable Structures

Doctoral Thesis

Thesis presented to the *Programa de Pós–graduação em Engenharia Civil* of PUC–Rio and *Building, Architecture and Town Planning Department* of ULB in partial fulfillment of the requirements for the joint degree of *Doutor em Engenharia Civil* (PUC) and *Docteur en Sciences de l'Ingénieur* (ULB).

Advisor (PUC)   : Prof. Dr. Paulo Batista Gonçalves
Supervisor (ULB):   Prof. Dr. Péter Zoltán Berke

Rio de Janeiro
June 2019

Murillo Vinícius Bento Santana

Tailored Corotational Formulations for the Nonlinear Static and Dynamic Analysis of Bistable Structures

Thesis presented to the *Programa de Pós–graduação em Engenharia Civil* of PUC–Rio and *Building, Architecture and Town Planning Department* of ULB in partial fulfillment of the requirements for the joint degree of *Doutor em Engenharia Civil* (PUC) and *Docteur en Sciences de l'Ingénieur* (ULB). Approved by the undersigned Examination Committee.

Prof. Dr. Paulo Batista Gonçalves
Advisor (PUC)
Departamento de Engenharia Civil e Ambiental – PUC–Rio

Prof. Dr. Péter Zoltán Berke
Supervisor (ULB)
Building, Architecture & Town Planning Department – ULB

Prof. Dr. Thierry Jacques Massart
Building, Architecture & Town Planning Department – ULB

Prof. Dr. Ney Augusto Dumont
Departmento de Engenharia Civil e Ambiental – PUC – Rio

Prof. Dr. Ricardo Azoubel da Mota Silveira
Departmento de Engenharia Civil – UFOP

Prof. Dr. Mohammed Hjiaj
Institut National de Sciences Appliquées – INSA Rennes

Prof. Dr. Vincent Denoël
Université de Liège – ULiège

Rio de Janeiro, June the 11th, 2019

Murillo Vinícius Bento Santana

Graduated in *Civil Engineering* at the Federal University of Ouro Preto (MG, Brazil) in 2013. Obtained a master degree in *Civil Engineering Sciences* from the same institution in 2015.

To my family and friends, for all the support and care.

Acknowledgments

First, I would like to express my sincere gratitude to my advisors Profs. Paulo Gonçalves and Péter Berke, for their continous support and valuable advices. A special thanks to Prof. Ricardo Silveira, whose assitance, care and friendship made this journey considerably better, if not possible. I also would like to thank Prof. Deane Roehl for her extraordinary sensibillity, support, oportunities provided and trust.

I would like to thank my family, my mother Neusa, my sister Ludmilla and my grandma Minervina, for the long distance support. Their care, love, happiness, humor and optimism are priceless. A special thanks to the brothers that life gave to me: João Hélio and Lucas.

My life in Rio would never have been the same without the good times shared with my colleagues at the Tecgraf Institute. Especially, thanks to Jeferson, Augustinho, Erwan, Axelle and Luiz Fernando for their motivating words, support in my research, friendship and fun moments. I would also like to thanks "A galera do basquete da Lagoa" for the memorable moments together, friendship and fun. A special thanks to Thomas for the support, care and NBA games.

I would like to thank my colleagues at the BATir department for the support, friendship, kicker games, caipirinhas and fun times. A special thanks to Péter and Fernanda for all the support, care, barbecues and good conversations. I would also like to thank my friends from the ULB basketball, specially Ibrahim, Chris, Joséphine and Mike for the lunchs, talks, support and good times. I had a wonderful experience in Brussels due to you guys.

Abstract

Santana, Murillo Vinícius Bento; Gonçalves, Paulo Batista (Advisor - PUC); Berke, Péter Zoltán (Supervisor - ULB). **Tailored Corotational Formulations for the Nonlinear Static and Dynamic Analysis of Bistable Structures**. Rio de Janeiro, 2019. 178p. Tese de doutorado – Departamento de Engenharia Civil e Ambiental, Pontifícia Universidade Católica do Rio de Janeiro.

Large span reticulated structures are applied in a variety of engineering applications. Many of these structures present a nonlinear behavior involving both geometric and material nonlinearities with multistable configurations. Particularly, bistable structures are often subjected to instability phenomena, such as snap-through and bifurcations of the whole structure, individual units or single bars. The present work, focuses on two classes of bistable structural systems: pyramidal trusses (undesired instability) and deployable scissor structures (desired design instability). Theoretical and computational tools are developed to investigate the influence of the strain measure, elasto-plastic deformations and instability phenomena on the nonlinear static and dynamic response of bistable pyramidal trusses. A compliant corrotational spatial joint finite element formulation with finite size is developed and applied to study bistable deployable scissor modules. The analysis of bistable large span structures formed by the assembly of modules is also carried out. It's shown that the presence and interaction of the studied buckling sources have deep influence on the systems behavior and can ultimately determine their viability in practical applications.

Keywords

Resumo

Santana, Murillo Vinícius Bento; Gonçalves, Paulo Batista; Berke, Péter Zoltán. **Formulações Corrotacionais para a Análise Não Linear Estática e Dinâmica de Estruturas Biestáveis**. Rio de Janeiro, 2019. 178p. Tese de Doutorado – Departamento de Engenharia Civil e Ambiental, Pontifícia Universidade Católica do Rio de Janeiro.

Estruturas reticuladas espaciais com grandes vãos são encontradas em uma variedade de aplicações em engenharia. Muitas dessas estruturas apresentam um comportamento eminentemente não linear, envolvendo tanto não linearidades físicas quanto geométricas, o que leva em muitos casos a múltiplas configurações de equilíbrio. Em particular, estruturas biestáveis estão usualmente sujeitas a instabilidades por ponto limite (snap-through), bifurcações simétrica instável ao longo do caminho não linear de equilíbrio, instabilidade elástica de elementos individuais, devido à plastificação destes elementos ou a interação destes fenômenos. O presente trabalho tem como objetivo a análise detalhada de duas classes de estruturas biestáveis: treliças piramidais (instabilidade indesejada) e estruturas ajustáveis com elementos de tesoura (instabilidade desejada). Ferramentas teóricas e computacionais são desenvolvidas para a investigação da influência das medidas de deformação quadrática e logarítmica, deformações elasto-plásticas e instabilidades na resposta estática e dinâmica não linear de um módulo de treliça piramidal. Uma formulação corrotacional em elementos finitos é proposta para descrever a ligação espacial flexível encontrada nas estruturas ajustáveis biestáveis aqui estudadas. A análise de estruturas com grandes vãos formadas pela junção de módulos de treliças piramidais ou módulos ajustáveis é apresentada. Os resultados obtidos mostram que a presença e interação das diversas fontes de instabilidade têm uma grande influência no comportamento destas estruturas e pode determinar ou não a sua viabilidade em aplicações práticas.

Palavras-chave

Instabilidade, sistemas biestáveis, estruturas ajustáveis, oscilações não lineares, formulações corrotacionais

Table of contents

List of figures

List of tables

List of symbols

L	:	Bar/beam initial length
l	:	Bar/beam current length
H	:	Pyramidal truss initial height
z	:	Pyramidal truss current height
n	:	Pyramidal truss number of bars
B	:	Pyramidal truss initial base radius
b	:	Pyramidal truss current base radius
p_z	:	Pyramidal truss vertical reference load
p_r	:	Pyramidal truss horizontal reference load
m	:	Pyramidal truss apex node equivalent mass
x, y	:	Pyramidal truss apex node horizontal position (Cartesian)
r, θ	:	Pyramidal truss apex node horizontal position (Cylindrical)
ω_0, ω_h	:	Pyramidal truss initial natural frequency
ρ	:	Material specific mass
E	:	Material elastic modulus
K	:	Material plastic modulus
σ_y	:	Material initial yield stress
ε_y	:	Material initial yield strain
A	:	Cross section area
d	:	Cross section diameter
t	:	Cross section thickness
I_y, I_z	:	Cross section bending inertia
I_x	:	Cross section torsional inertia
r_g	:	Cross section radius of gyration

The scientific man does not aim at an immediate result. He does not expect that his ideas will be readily taken up. His work is like that of a planter, for the future. His duty is to lay foundation of those who are to come and point the way.

Nikola Tesla

1
Introduction

1.1
Reticulated bistable structures in engineering

Large span reticulated structures are present in several civil, mechanical, off-shore and aero-spatial engineering applications. Many of these structures present an initial curvature to increase their stiffness and load carrying capacity. However this may lead to multistable configurations and static and dynamic buckling may become an important design issue. Particularly, bistable structures are mechanical systems with two stable load-free configurations and are often composed from an assembly of linear structural elements, such as trusses and beams, using complex joints. The present work, focuses on two classes of bistable structural systems: pyramidal trusses and deployable scissor structures.

Pyramidal trusses possess an immediate practical interest since they are currently used in many present-day engineering structures (Figs. 1.1, 1.2 and 1.3), either as a main structural component or as constitutive units of more complex structures, from carbon nanostructures [7] to large geodesic domes [8] or double layer reticulated trusses or shells [9]. Lattice structures composed of pyramidal units can also be considered as a promising alternative in sandwich lightweight structures ([10], [11] and [12]).

These structures exhibit usually a highly nonlinear structural behavior involving both geometrical and material nonlinearities and are often subjected to instability phenomena, such as snap-through and bifurcations of the whole structure, individual units or single bars, being liable to catastrophic buckling. Because of their highly complex structural behavior, the development and use of appropriate numerical models are necessary to guide their realistic design and lead to an understanding on their complex structural static and dynamic behavior.

Ligarò and Valvo [9] studied the static elastic stability and load capacity of pyramidal space trusses considering moderate elastic deformations, making use of derived analytical expressions. However, the effect of local buckling and plasticity and the interaction between different buckling phenomena were not

Figure 1.1: London Stansted airport pyramidal truss system [1].
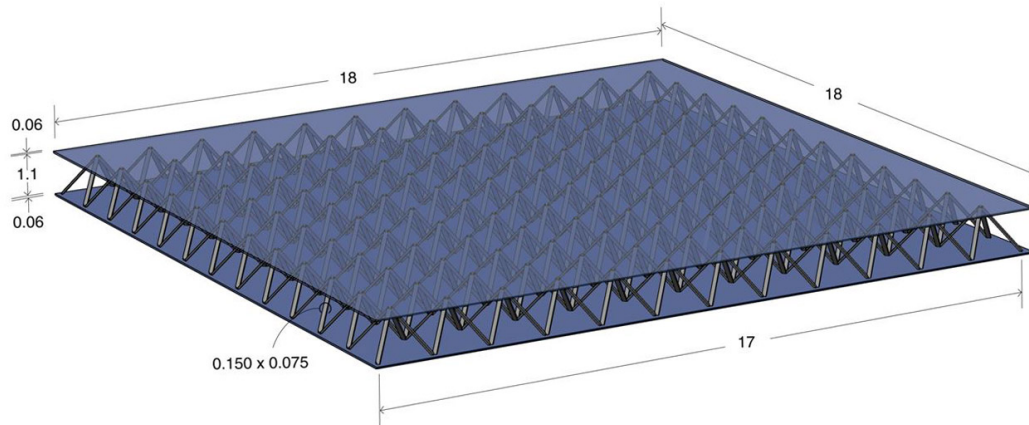
Figure 1.2: Lattice structure with pyramidal truss components [2] (dimensions in meters).

(a) [13]　　　　　　　　　　　(b) [14]

Figure 1.3: Geodesic dome with pyramidal truss components.

considered. Castro [15] and Orlando et al. [16] studied the complex dynamics of shallow elastic pyramidal trusses, while Orlando et al. [17] studied the influence

of transient escape and added load noise on the dynamic integrity of multistable systems (an extensive literature review on pyramidal truss systems is presented in Chapters 2 and 3).

In summary, to the author's best knowledge, pyramidal truss systems have been modeled considering moderate strains with a material linear elastic behavior, disregarding local instabilities (Euler buckling) and with a fixed (rigid) base. As the height/base ratio become sufficiently high, these assumptions are no longer valid and the effect of the base flexibility and the coupling of the plastic and local buckling modes on the system stability and load capacity have to be considered. This work proposes an extension of pyramidal truss modeling in this direction.

Among reticulated structures, deployable structures have recently received deserved attention in the literature due to their possible application in emergency shelters [18], exhibitions and recreational structures, temporary buildings, maintenance facilities [19] and spatial antennas [20], among others. Deployable structures are mechanical systems that can transform from a folded compact configuration to a deployed form, in which they can support external loads (Figs. 1.4, 1.5 and 1.6). The deployable scissor structures considered in this work are space frames consisting of straight elastic beams that are connected by complex joints. Their major advantages are the small volume they occupy during storage and transportation, the ease and speed of erection, and their re-usability. Due to these advantages, they offer possible alternatives for a wide range of civil, mechanical and aero-spatial engineering applications.

Figure 1.4: Hoberman dome transformation [3].

This work focuses particularly on bistable deployable structures, in which intended geometric incompatibilities between the members are introduced as a design strategy to instantaneously achieve structural stability when deployed. The intentionally incorporated geometric incompatibilities lead to axial and bending stresses of structural members during transformation, generating a
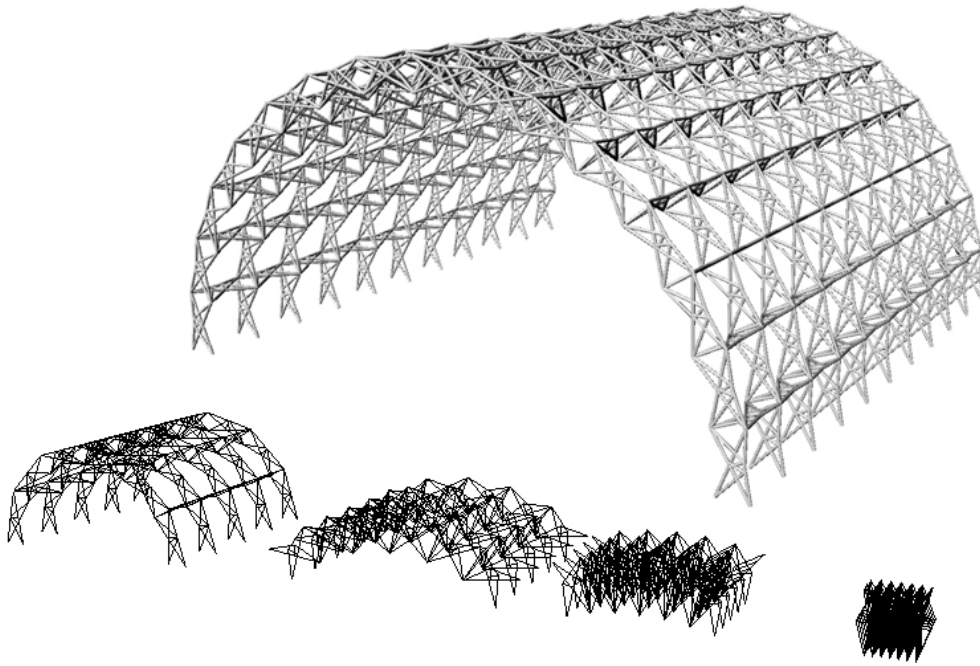
Figure 1.5: Multiple configurations of a deployable structure [4].
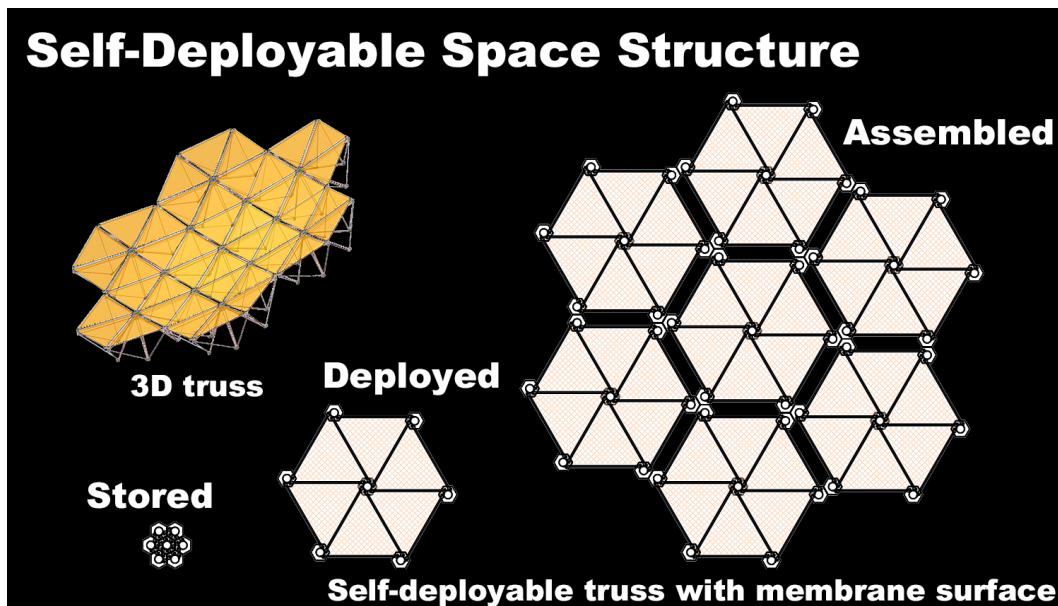
Figure 1.6: Self-deployable space structure [5].

controlled and desired snap-through behavior. In spite of the advantages of bistable scissor structures, few have successfully been built because of the complexity of their behavior and of their design process [21].

The bistable deployable structures studied in the present work were first proposed and investigated by Gantes [22] (a literature review dedicated

to bistable deployable structures is presented in Chapter 4). The structural response of the investigated deployable structures, as well as their behavior in the deployed configuration is exclusively obtained in previous works (e. g. [21]) using commercial finite element packages. In commercial finite element codes the behavior of an element is usually limited to pre-coded features that may not correspond to the complete set of required numerical ingredients.

A comprehensive analysis of the transformation of 3D bistable deployable structures must include several nonlinear effects and their appropriate treatment in a computational solution procedure (geometric nonlinearity, friction and snap-through). Additionally, for realistic designs hub sizes, beam spacing, friction and the finite stiffness of joints should also be incorporated. In this work the convoluted effect of the above ingredients is studied as novelty, through the development and application of a new corotational joint finite element, tailored for the analyses of bistable deployable structures.

As the investigated pyramidal trusses and deployable structures have a bistable behavior, they present two unloaded stable configurations, passing from one to another through external applied forces. For the pyramidal trusses, this phenomenon usually represents the (partial or complete) collapse of the structural system and, in order to be avoided, an accurate analysis of the pre-bucking and post-buckling behavior must be performed. For deployable structures, this phenomenon represents the transformation of the system between a folded and deployed configuration, and so, the determination of the key characteristics (such as the required force) can only be obtained through an advanced analysis of the system.

1.2
Problem statement and objectives

Many materials, in particular metallic materials, exhibit an elasto-plastic behavior, it is thus expected that metallic structures undergoing snap-through buckling may exhibit permanent deformations, due to the large stresses developed during this nonlinear process. Nevertheless, little is known on the influence of the elasto-plastic deformations on the stability of structures liable to snap-through or bifurcation buckling.

Additionally, compressive stresses in individual members may surpass the Euler buckling load. Euler buckling together with the unavoidable manufacturing geometric imperfections lead to bending of the structural members and, as the displacement increases, possibly to elasto-plastic behavior. Thus interaction between different geometrical and material nonlinear phenomena may occur, leading to a significant decrease in the load carrying capacity of

the structure [23].

To the author's best knowledge, previous works on pyramidal trusses are restricted to the elastic nonlinear behavior of the perfect idealized truss model considering only limit-point instability (snap-through buckling) or unstable symmetric bifurcation along the nonlinear equilibrium path with moderate strains (Ligarò and Valvo [9], Castro [15]). However, in real structures, structural instability may display a multifold nature depending on the geometrical and material parameters and imperfections.

There is thus a need for a deeper understanding of the complex bistable behavior of reticulated structures (particularly focusing here on pyramidal trusses) under different sources of nonlinear phenomena. In addition to snap-through and bifurcation buckling, the effect of the material elasto-plastic constitutive laws, the individual bars Euler buckling, the flexibility of the base, and their interaction are critical to structural safety. In particular, interactive buckling has a considerable effect on the imperfection sensitivity and load capacity of reticulated structures. A main objective of this work is the study of instability phenomena involving large displacements, rotations and high strains with proper numerical tools and benchmark analytical formulations.

Pyramidal trusses can be subject to dynamic loads (wind, earthquakes, machinery, moving loads) and structural instabilities also include dynamic jumps, therefore their elasto-plastic nonlinear dynamic behavior is of concern for a safe design. Accidents due to snow and wind of structural systems composed by pyramidal trusses leading to an inverted configuration (collapse) have been investigated in the literature [24, 25, 26]. Having in mind that large strains may occur, the analysis of the influence of different strain measures on the system stability and load capacity, as well as on its nonlinear oscillations and dynamic instabilities are of interest and are not covered systematically in the dedicated literature. Another main objective and original contribution of the present work is to quantify computationally the influence of large elastic and elasto-plastic strains on the pyramidal truss dynamic response.

To capture the true nonlinear structural behavior of bistable deployable structures a proper representation of the joint behavior (finite stiffness and friction) and kinematics (finite size and beam inter-distance) have to be incorporated in the numerical model. To the author's best knowledge this was not attempted earlier using a dedicated joint finite element, leaving a gap in the literature. The third main objective of this work is the study of the convoluted effect of the geometrical and material effects above through the application of a tailor-made joint finite element developed specifically for deployable structures.

The global aim of the present work is thus the development of theoretical and computational tools for the analysis of spatial reticulated structures, with focus on systems formed by a combination of bistable pyramidal trusses or an assembly of deployable modules. As bistable structures are subjected to the coupling of different nonlinear phenomena, the numerical tools are specifically designed to deal with the most relevant of them. The common feature of the developed numerical tools is that they all employ a corotational kinematics.

1.3
Originalities

One of the main interest of the proposed work for pyramidal truss structural behavior is the characterization of the static stability and load capacity considering large elasto-plastic deformations, the local Euler's buckling of the bars and the coupling of these effects. A new detailed theoretical and computational (corotational formulation) analysis of the truss considering not only limit-point instability and unstable symmetric bifurcation in the elastic regime, but also Eulerian buckling, plastic buckling, geometric imperfections, base flexibility and the interaction among these bifurcation phenomena is conducted.

The other main interest is the study of elastic and elasto-plastic nonlinear oscillations and dynamic instabilities under a vertical harmonic excitation force. The quadratic and logarithmic strain measures are used in nonlinear dynamics and their influence on the static and dynamic non-linear behavior is duly investigated together with the influence of plastic deformations.

For bistable deployable scissor structures, the current work aims at combining a set of ad hoc numerical ingredients in the modeling effort of the transformation, giving a contribution to the state of the art both from a computational development as well as an application point of view. The finite joint size and the beam thickness, the nonlinear elastic finite stiffness of the joints as well as friction are incorporated in the structural model and their influence and interactions are investigated. The finite elements that constitute the structural models (elastic beams and flexible frictional joints) are described in a corotational framework to properly capture the large rigid rotations during transformation.

Specific original contributions of the present work can be listed as:

- Assessment of the influence of different strain measures and large elastic and elasto-plastic strains on the static and dynamic structural response of pyramidal trusses;

- Proposal of closed form solutions for the nonlinear elastic and elasto-plastic equilibrium paths of pyramidal truss modules obtained in terms

of nondimensional geometrical and material parameters for moderate and large strains;

- Novel closed form expressions for the critical load of pyramidal trusses derived for different instability phenomenon;

- Computational assessment of the load capacity reduction of imperfect pyramidal trusses due to the interaction between snap-through, bifurcation buckling, Euler buckling and material yielding;

- Computational quantification of the influence of the base flexibility, the imperfection magnitude and shallowness/slenderness ratios for pyramidal trusses in statics;

- Computational static simulation of a large-span structure composed of pyramidal units considering different types of buckling interactions;

- Computational study of the influence of the elasto-plastic constitutive model and induced plastic energy dissipation on the nonlinear oscillations, dynamic instabilities and resonance curves of pyramidal trusses;

- Identification of chaotic attractors considering different nonlinear phenomena and design parameters (shallow and deep systems, plasticity, preload, initial conditions);

- Proposal of a novel joint finite element considering its finite stiffness, friction and finite size and its application in a bistable deployable scissor module (quantifying their influence on the structural behavior);

- Analysis of the deployment of large-span flat structures composed of bistable deployable modules considering the convolution of the effects above.

All computational simulations presented here are performed in a FE software developed by the author and written in the C++ programming language. The software is object oriented and includes FE formulations and solvers for both static and dynamic nonlinear analyses. The truss (App. B) and beam (App. C) FE formulations make use of a corotational reference frame to deal with large rigid body motions. The truss formulation takes into account moderate (quadratic) or large (logarithmic) strain measures and the material elastic or elasto-plastic behavior, while the beam formulation takes into account the progressive plastification of the cross section via the plastic zone method. The static nonlinear solver together with the used continuation methods and the dynamic nonlinear solvers are presented in (App. D).

1.4
Outline of the thesis

This manuscript is organized as follows. In Chapter 2 the static stability and load capacity of pyramidal truss structures are investigated in the elastic and elasto-plastic regime. The nonlinear oscillations and dynamic instabilities of pyramidal trusses subjected to an external vertical harmonic force are investigated through bifurcation diagrams of the Poincaré map and phase-space projections of the relevant attractors in Chapter 3. Bistable deployable structures are computationally investigated in Chapter 4. The nonlinear transformation between the two stable configurations (folded and deployed) is studied incorporating the effects of hub size, joints friction, flexibility and finite beam spacing. Finally, in Chapter 5 the main results obtained through the proposed computational and closed form developments and their application are listed and discussed, and the conclusions of this work are drawn. Suggestions for future work are also presented.

This manuscript contains several Appendices in which computational developments that were implemented for the numerical studies presented in the main body are thoroughly explained. Although these developments contain elements of novelty (systematically highlighted in the Appendices), they are not part of the core of the manuscript in order to keep the focus on the genuinely original findings.

2
Static analysis of bistable truss structures

2.1
Outline

The present chapter investigates the static nonlinear behavior and stability of pyramidal truss structures. An original analytical model of a truss module considering a general strain measure is derived together with closed form solutions for the nonlinear equilibrium paths, natural frequencies and critical parameters (limit, bifurcation and buckling points). Different types of nonlinear phenomena (snap-through, lateral bifurcation, elasto-plastic buckling, Euler buckling) are considered computationally and their influence on the load capacity and structural stability are investigated using quadratic and logarithmic strain measures. The numerical results are successfully compared with the derived closed form solutions, validating them. The coupling of Euler buckling and elasto-plastic deformations of the structural members is also numerically investigated. Finally, the response of a large span curved structure, formed by an assembly of pyramidal truss units, is investigated and the effect of initial curvature, number of modules, modules height, load symmetry and plastic deformations is also assessed. [1]

2.2
State of the art on static modeling of pyramidal trusses

The pyramidal truss considered in this work is shown in Fig. 2.1. It consist of $n \geq 3$ pinned bars connected at the apex node and equally separated at the base Γ so that the base nodes form a regular polygon of n sides. The pyramid has a height H, a base radius B and each bar's initial length is $L = \sqrt{B^2 + H^2}$.

The possible buckling of these truss systems is of importance in structural analysis and design and has been studied by many researchers in recent years. The von Mises truss (Fig. 2.2) is the plane counterpart of the pyramidal truss. It is a typical bistable structure which can buckle, depending on the height to span ratio, at a limit point or through an unstable symmetric bifurcation along the nonlinear fundamental equilibrium path [27]. Due to its complex nonlinear

---

[1]The contents of Chapters 2 and 3 are a convolution of two manuscripts submitted for publication to *International Journal of Solids and Structures* and *Nonlinear Dynamics*.

(a) Initial configuration (b) Deformed configuration
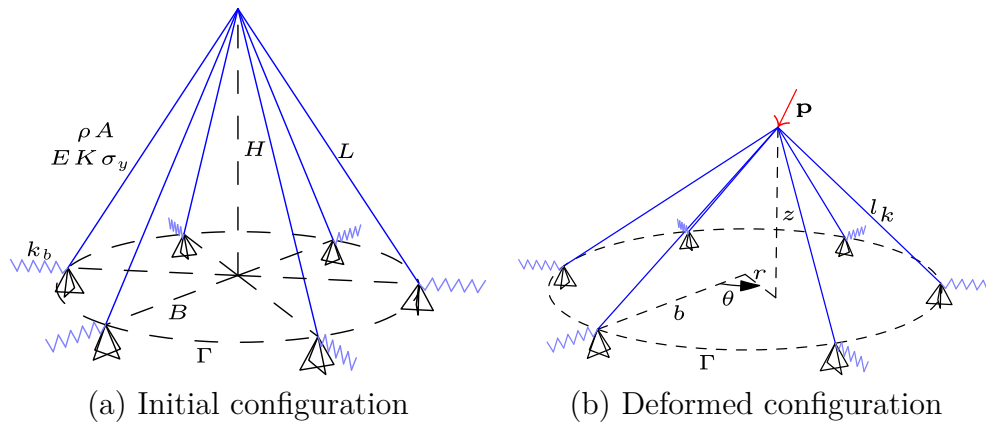
Figure 2.1: Geometry, coordinate systems and initial and deformed configurations of the pyramidal truss.

response, the von Mises truss has been customarily used as a benchmark in the numerical analysis of bistable structures [28]. Kala and Kalina [29] and Kwasniewski [27] investigated the static snap-through and equilibrium paths of the classical von Mises truss while Psotný and Ravinger [30] and Kalina [31] considered the effect of imperfections in its computational analysis. Recently, Halpernand and Adriaenssens [32] studied the in-plane buckling of shallow truss arches, while Plaut [33] investigated the snap-through of shallow domes under unilateral displacement control.
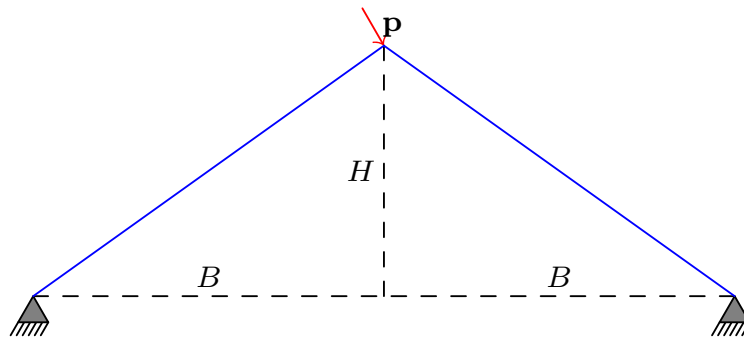
Figure 2.2: Geometry and initial configuration of the von Mises truss.

However, the majority of studies in the literature does not consider some important aspects in terms of column and spatial truss design such as the critical interaction between Euler buckling and material yielding. Bazzucchi et al. [34] studied the interaction between Eulerian buckling and snap-through of the imperfect 2D von Mises truss in terms of the slenderness and shallowness ratios, while Bazzucchi et al. [35] investigated the effect of shallowness and slenderness parameters, restraining conditions and imperfection patterns on the load carrying capacity of a von Mises arch-like structure. They indicated the importance of interactive buckling (i.e. coupling of different nonlinear

sources of buckling) on the imperfection sensitivity and load carrying capacity of shallow arch-like structures.

During exceptional loading, relevant to consider for a safe design, the axial force in the bars can reach the material elastic limit, and elasto-plastic deformation occurs. Fan et al. [36] and Zhi et al. [37] studied the elasto-plastic static and dynamic stability of single-layered reticulated shell truss structures. Unfortunately, studies in this field are very scarce, especially when coupled instability between different buckling modes are considered [38].

Several spatial truss configurations exhibit a bistable behavior, including shallow pyramidal trusses. These structures have received considerable attention lately due to their applications ranging from large space structures, deployable and morphing structures to nano or micro structures and meta-materials. The nonlinear behavior of arch-like bistable structures is a classical problem in the theory of structural stability [39]. Current research areas where bistable or multistable behaviors are of importance include deployable and morphing structures [40, 21], meta-materials [41, 42], energy harvesting structures [43], energy absorption structures [44], mechanical and electro-mechanical devices that switch between a discrete number of states [45, 46, 47], micro and nanostructures [48, 49, 50, 51] and aeronautical structures [52], among others. Recently, Brinkmeyer et al. [53, 54] studied pre-stressed morphing bistable domes and composite panels, Pontecorvo et al. [55] studied bistable arches in morphing applications and Cui and Santer [56] studied bistable composite shell surfaces. The effect of symmetric imperfections on bistable struts was studied by Cai et al. [57]. In the field of lattice structures Feng et al. [58] studied the mechanical behavior of hourglass truss lattice structures, Yungwirth et al. [59] tested experimentally the ballistic response of composite pyramidal lattice trusses, Danso and Karpov [60] investigated the bistability criterion for geometrically nonlinear structures and Wang et al. [61] studied the performance of truss panels with Kagomé cores. All of the works above are limited to structural systems with elastic moderate strains.

Ligarò and Valvo [9] derived an analytical expression of the internal energy for the static elastic behavior of pyramidal spatial trusses, considering moderate deformations using a quadratic strain measure and, from the *stationary condition* for the *potential energy*, the static nonlinear equilibrium equations were obtained, as well as the expressions for the stiffness matrix and stability parameters. The equilibrium paths were obtained for vertical and horizontal loading considering different geometrical parameters. Such closed form solutions for the structural behavior are very useful for design since they require a significantly smaller computational effort and complexity when com-

pared with numerical models, providing more general, often non-dimensional results. However the effect of local buckling and plasticity and the interaction between different buckling phenomena is usually not incorporated and is one of the main originalities developed in this Chapter.

In [9, 16, 62] an extension of analytical models of pyramidal trusses to finite strains is proposed using the Green quadratic strain measure, leading to neat analytical closed form solutions. However, in finite strain elasto-plasticity a more appropriate strain measure is the logarithmic strain, also called true strain or Hencky strain, which is a function of the stretch ratio (see, for example, Perić et al. [63], Naghdabadi et al. [64], Neff et al. [65]). In this chapter logarithmic strains are included in the analyses.

There is thus a gap in the literature when considering the general scope of pyramidal trusses nonlinear structural behavior subject to large strains, Euler buckling and material elasto-plastic deformations. The originality of this work is the incorporation of all the above phenomena. The current chapter presents an effort to better understand the influence of these effects on the system response.

A general closed form solution describing the equations of motion considering truss elements with geometrical and material nonlinear behavior is developed in Sec. 2.3. The static analysis of a single pyramidal truss module subject to horizontal and vertical loads is performed in Sec. 2.4. Both closed form and computational approaches are used in convolution all along this Chapter, showing a satisfying match. A large span curved structure formed by an assembly of pyramidal truss modules is analyzed in Sec. 2.5. Finally, in Sec. 2.6 the main conclusions of this chapter are drawn.

2.3
Derivation of a closed form solution

In the initial configuration (Fig. 2.1a), the apex and k^{th} base node coordinates are $\begin{bmatrix} 0 & 0 & H \end{bmatrix}^T$ and $\begin{bmatrix} B\cos(\theta_k) & B\sin(\theta_k) & 0 \end{bmatrix}^T$, respectively, with $\theta_k = 2\pi k/n$. The apex node is free to move and it's position in the deformed configuration is given in Cartesian coordinates by $\mathbf{x} = \begin{bmatrix} x & y & z \end{bmatrix}^T$, or in a cylindrical coordinate system by $\mathbf{x} = \begin{bmatrix} r & \theta & z \end{bmatrix}^T$. The base nodes can either be fixed or connected to flexible supports with a stiffness k_b and sliders allowing for their displacement *in the radial direction only*, representing the compliance of the foundation or the interaction with other modules. With a compliant base the assumption is made that the kth base node in the deformed configuration can move to the position $\begin{bmatrix} b\cos(\theta_k) & b\sin(\theta_k) & 0 \end{bmatrix}$. The structure is subjected to an arbitrary conservative (i.e. with a fixed direction) concentrated load

applied at the apex node $\mathbf{p} = \lambda \begin{bmatrix} p_r \cos(\theta_p) & p_r \sin(\theta_p) & p_z \end{bmatrix}^T$, where λ is the load multiplier factor of the reference load vector. Here, it is assumed that all joints in the truss behave as ideal frictionless hinges, and no moments are generated by nodal loads. Also, in order to avoid local buckling of the bars, the compressive force in each bar $\overline{f}$ must not exceed the critical load of a simply-supported column $F_{cr} = \pi^2 E A r_g^2 / L^2$ [34] where r_g is the minimum radius of gyration of the cross sectional area.

As the base nodes are initially fixed, considering the bar kinematics, the equivalent nodal mass concentrated in the apex node corresponds to a third of the pyramidal truss total mass. The system's kinetic energy $T(\dot{\mathbf{x}}, \dot{b})$ and the potential energy of the applied forces $V(\mathbf{x}, \lambda)$ are given respectively by:

$$T(\dot{\mathbf{x}}, \dot{b}) = \frac{m}{2} \left(\dot{\mathbf{x}}^T \cdot \dot{\mathbf{x}} + \dot{b}^2 \right) \tag{2-1}$$

$$V(\mathbf{x}, \lambda) = -\lambda \left[p_r r \cos\left(\theta - \theta_p\right) + p_z \left(z - H\right) \right] \tag{2-2}$$

with $(\dot{\ }) = d(\ )/dt$ being the time derivative and $m = n\rho AL/3$.

From the nodal positions in the deformed configuration, the length of the bar connecting the apex node and the kth base node l_k is given by:

$$l_k(r, \theta, z, b) = \sqrt{z^2 + r^2 + b^2 - 2rb\cos(\theta - \theta_k)} \tag{2-3}$$

From Eq. (2-3), the following polar symmetry relation can be obtained:

$$l_{i+k}\left(r, \varphi_i + \phi, z, b\right) = l_{i-k+1}\left(r, \varphi_i - \phi, z, b\right) \tag{2-4}$$

where $\varphi_i = (2i+1)\pi/n$ and $\phi \in (-\pi/n, \pi/n]$.

Considering an elastic material behavior, the system's strain energy $U(r, \theta, z, b)$ is written as:

$$U(r, \theta, z, b) = \frac{EAL}{2} \sum_{k=1}^{n} \varepsilon_k^2 + \frac{nk_b}{2} (b - B)^2 \tag{2-5}$$

As the kth bar's strain ε_k is a function of the axial stretch $\lambda_k = l_k/l_0$, from Eq. (2-4) the following symmetry relations can be obtained for the system's strain energy:

$$U(r, \varphi_i, z, b) = U(r, \varphi_j, z, b) \tag{2-6}$$

$$U(r, \varphi_i, z, b) = U(-r, \varphi_i, z, b) \qquad \text{for } n \text{ even} \tag{2-7}$$

$$U(r, \varphi_i, z, b) = U(-r, \varphi_i + \pi/n, z, b) \qquad \text{for } n \text{ odd} \tag{2-8}$$

$$U(r, \varphi_i + \phi, z, b) = U(r, \varphi_i - \phi, z, b) \tag{2-9}$$

As any angle θ can be decomposed in a unique manner as $\theta = \varphi_i + \phi$, for some par ($i \in \mathbb{Z}, \phi \in (-\pi/n, \pi/n]$), the above relations show that the system's strain energy U can be fully described with $\theta \in [0, \pi/n]$. This means that for an increasing number of bars n, the dependency on the angle θ becomes incrementally smaller as the interval $[0, \pi/n]$ converges asymptotically to a point. Also Eq. (2-7) implies that, for n even, U is symmetric with respect to r, while Eq. (2-8) shows that, for n odd, this symmetry is out of phase by π/n. Considering the popular quadratic strain measure for the sake of simplicity $\varepsilon_q = (l_k^2 - L^2)/(2L^2)$ (Eq. B-17), the strain energy U_q can be expressed as:

$$U_q(\mathbf{x}, b) = \frac{nEA}{8L^3}\left[\left(r^2 + z^2 - H^2\right)^2 + 2b^2 r^2\right] + \frac{nk_b}{2}(b - B)^2 \qquad (2\text{-}10)$$

The bar's strain energy U_q is completely independent of the angle θ and has a linear dependency on the number of bars n. The system's Lagrangian [66] is given by $\mathcal{L}(\mathbf{d}, \dot{\mathbf{d}}, \lambda) = T(\dot{\mathbf{d}}) - U(\mathbf{d}) - V(\mathbf{x}, \lambda)$. Applying Hamilton's principle, the nonlinear equations of motion are obtained as:

$$\frac{d}{dt}\left(\frac{\partial \mathcal{L}}{\partial \dot{\mathbf{d}}}\right) - \frac{\partial \mathcal{L}}{\partial \mathbf{d}} = \mathbf{0} \qquad (2\text{-}11)$$

$$m\ddot{\mathbf{x}} + \sum_{k=1}^{n} \overline{f}_k \mathbf{t}_k = \mathbf{p} \qquad (2\text{-}12)$$

$$m\ddot{b} + k_b(b - B) + \sum_{k=1}^{n} \overline{f}_k c_k = 0 \qquad (2\text{-}13)$$

where $\mathbf{d}^T = \begin{bmatrix} r & \theta & z & b \end{bmatrix}$ is the vector comprising the system's degrees of freedom and $c_k = [b - r\cos(\theta - \theta_k)]/l_k$.

Considering an elasto-plastic material behavior, the same nonlinear equations of motion can be obtained from equilibrium considerations. However, the bars axial force $\overline{f}_k$ must be computed accounting for the plastic behavior (details are given in Eqs. B-10 and B-19).

As previous works on the elastic response of pyramidal trusses [9, 15, 16, 17] make use of the quadratic strain measure (QSM), the elastic-plastic material straining is first treated here with the QSM. Note that, for metallic materials the elasto-plastic constitute relations are usually expressed in terms of the logarithmic strain measure (LSM) and the Cauchy (real) stress in the context of an hypo-elastic model. In the present work, a hyper-elastic constitutive law is used and the LSM is related to the Kirchhoff stress for the elasto-plastic deformations [67]. This assumption is justified as the structural member's volumetric change is small, and so the Cauchy and Kirchhoff stress measures approach one another. As common in metallic materials, the elasto-

plastic behavior is assumed to be symmetric, i.e. assuming equal response in tension and compression.

In the analytical expressions developed, the material initial yield strain $\varepsilon_y = \sigma_y/E$ is used to make them more compact and a monotonic vertical motion of the apex node is assumed. A classical return mapping algorithm is applied in the numerical simulations based on the stress.

The linearization of the equations of motion in the deformed equilibrium configuration allows the calculation of the system's natural frequencies ω_n [67]. In the initial (undeformed) configuration, and the base fixed, the vertical ω_0 and horizontal ω_h frequencies are the same for all of the strain measures since there is no initial structural deformation (i.e. load-free configuration), and are given by:

$$\omega_0^2 = \frac{3EH^2}{\rho l_0^4} \tag{2-14}$$

$$\omega_h^2 = \frac{3EB^2}{2\rho l_0^4} \tag{2-15}$$

In this case, due to the symmetry of the structure, there are two equal natural frequencies.

The nonlinear equations of motion (Eqs. 2-12 and 2-13) are:

$$\mathbf{M} \cdot \ddot{\mathbf{x}} + \mathbf{F}_i(\mathbf{x}) - \mathbf{F}_e(\lambda) = \mathbf{0} \tag{2-16}$$

where for the QSM the system's internal $\mathbf{F}_i(\mathbf{x})$ and external $\mathbf{F}_e(\lambda)$ force vectors and the mass matrix $\mathbf{M}$ are given by:

$$\mathbf{M} = m\mathbf{I} \tag{2-17}$$

$$\mathbf{F}_i(\mathbf{x}) = \frac{nEA}{2L^3} \begin{bmatrix} x\mu_1^2 & y\mu_1^2 & z\mu_2^2 \end{bmatrix}^T \tag{2-18}$$

$$\mathbf{F}_e(\lambda) = \lambda \begin{bmatrix} p_r \cos(\theta_p) & p_r \sin(\theta_p) & p_z \end{bmatrix}^T \tag{2-19}$$

with $\mu_1^2 = r^2 + z^2 + B^2 - H^2$ and $\mu_2^2 = r^2 + z^2 - H^2$. The system stiffness matrix is obtained by taking the variation of the internal force vector with respect to the apex node position $\mathbf{x}$ in Eq. (2-18), leading to:

$$\mathbf{K}(\mathbf{x}) = \frac{nEA}{2L^3} \begin{bmatrix} 2x^2 + \mu_1^2 & 2xy & 2xz \\ 2xy & 2y^2 + \mu_1^2 & 2yz \\ 2xz & 2yz & 2z^2 + \mu_2^2 \end{bmatrix} \tag{2-20}$$

Taking the linearization of the nonlinear equations of motion (Eqs. 2-12 and 2-13) in an equilibrium position, the natural frequencies ω_i and vibration

modes $\boldsymbol{\phi}_i$ for the loaded structure are obtained as:

$$\omega_{1,3}^2 = \frac{3E(\kappa_2^2 \mp \kappa_3^2)}{4\rho L^4} \quad \omega_2^2 = \frac{3E\mu_1^2}{2\rho L^4} \tag{2-21}$$

$$\boldsymbol{\phi}_{1,3} = \begin{bmatrix} +\cos(\theta) \\ +\sin(\theta) \\ 4z_s r_s/(\kappa_1^2 \mp \kappa_3^2) \end{bmatrix} \quad \boldsymbol{\phi}_2 = \begin{bmatrix} -\sin(\theta) \\ +\cos(\theta) \\ 0 \end{bmatrix} \tag{2-22}$$

where:

$$\kappa_1^2 = B^2 + 2\left(r^2 - z^2\right) \tag{2-23}$$

$$\kappa_2^2 = 4\left(r^2 + z^2\right) + B^2 - 2H^2 \tag{2-24}$$

$$\kappa_3^2 = \sqrt{B^4 + 4B^2\left(r^2 - z^2\right) + 4\left(r^2 + z^2\right)^2} \tag{2-25}$$

An equilibrium position is called stable if the stiffness matrix is positive definite or, equivalently, if all natural frequencies are real, and called unstable otherwise. A decision on structural stability thus requires assessing the structure's natural frequencies in the considered static analysis. The neutral equilibrium surfaces are geometric spaces with at least one null frequency component and represent the boundary between stable and unstable domains of the structural response (sets of equilibrium points where the stiffness matrix is positive definite). Setting $\omega_i = 0$, they are obtained as [9]:

$$z_1 = \pm\sqrt{\frac{2H^2}{3} - \frac{B^2}{2} - r^2 + \Delta z} \tag{2-26}$$

$$z_2 = \pm\sqrt{H^2 - B^2 - r^2} \tag{2-27}$$

$$z_3 = \pm\sqrt{\frac{2H^2}{3} - \frac{B^2}{2} - r^2 - \Delta z} \tag{2-28}$$

with:

$$\Delta z = \sqrt{\left(\frac{H^2}{3} - \frac{B^2}{2}\right)^2 + \frac{2}{3}B^2 r^2} \tag{2-29}$$

The determination of the static equilibrium points stability is important since only stable equilibrium points correspond to real configurations of structural systems. In reality, the computed unstable equilibrium configurations are perturbed by different sources of imperfections and are subject to instability phenomena, such as dynamic jumps to stable equilibrium configurations (these are incorporated in chapter 3).

Although the logarithmic strain measure better represents the constitute

elastic and elasto-plastic behavior of metallic materials in the finite strain domain, it yields complex expressions in a closed formulation formulation. Usually computational simulations are required to capture the structural behavior. The quadratic strain measure is used here as a direct extension of the literature [9, 15, 16] and because it allows the formulation of simple closed form expressions.

2.4
Single pyramidal truss module behavior

In this section, the stability and load capacity of a single pyramidal truss module are studied. The effects of four types of nonlinear behavior are considered for the vertical and horizontal loads: saddle-node bifurcation (snap-through), pitchfork bifurcation (lateral instabilities), bars Euler buckling and plasticity of the structural elements. A comparison between analytical and computational models (corotational finite element code developed in the Appendices) based on equilibrium paths (load vs. displacements curves) is presented as well.

The common model parameters are summarized in Tab. 2.1. Depending on the investigated nonlinear effect, an appropriate height, H, is selected. In the numerical simulations, the truss is discretized using only one finite element per bar while five finite elements are used for each beam. This choice guarantees convergence of the results when compared with finer discretizations. The minimal norm method (Sec. D.1.1) is used as a continuation strategy in the static nonlinear solver. As suggested by Ligarò and Valvo [9], the reference loads in the vertical and horizontal directions, when considered, are taken as $p_z = p_r = -(H/L)^3 (nEA/2)$. In addition, to extend the validity of the results, the following non-dimensional parameters are used in the analysis $\overline{z} = z/H$, $\overline{r} = r/H$, $\alpha = B/H$, $\beta = L/H = \sqrt{1+\alpha^2}$ and $\overline{\omega}_i = \omega_i/\omega_0$.

The non-dimensional parameters α and β are related to the base/height ratio and control the depth of the truss. For the same load level λ shallow and deep systems may have considerable different structural responses characterized by the non-dimensional apex node motion $\overline{r}$ and $\overline{z}$ and system natural frequencies $\overline{\omega_i}$.

2.4.1
Potential energy maps through analytical solution

The global nonlinear behavior of the pyramidal truss is governed by the topology of the total potential energy. The total potential energy of the

Parameter		Value
n	number of bars	6
B	pyramid base radius	7 m
d	cross section diameter	508 mm
t	cross section thickness	12.7 mm
E	material elastic modulus	200 GPa
σ_y	material yield stress	400 MPa
ρ	material mass density	7850 kg/m^3

Table 2.1: Numerical parameters used in the FE analysis of a single pyramidal truss module with a hollow circular cross section.

structure is given in non-dimensional form as $\overline{\overline{\Pi}} = (U + V)/(p_z H)$, and is evaluated here based on the closed form expressions of Sec. 2.3.

The *static unloaded equipotential curves* $(p_r = p_z = 0)$ and equilibrium configurations with a quadratic strain measure for three selected values of α are shown in Figs. 2.3 and 2.4, respectively. For $\alpha = 0.80 < 1.00$ (deep truss), Fig. 2.3(a), the potential energy displays five equilibrium positions, the origin, a local maximum (unstable), two additional equilibrium positions along the $\overline{z}$ axis at $\overline{z} = \pm 1.00$, corresponding to two local minima (stable – unloaded and stress-free configurations), and two additional equilibrium positions along the $\overline{r}$ axis at $\overline{r} = \pm\sqrt{1 - \alpha^2}$, corresponding to two symmetric saddles (unstable).

At $\alpha = 1.00$, Fig. 2.3(b), the two saddles coalesce with the maximum, leading to a degenerated saddle, with the only eigenvector in the direction of the $\overline{r}$ axis, reducing the number of equilibrium positions to three. For $\alpha = 1.20 > 1.00$ (shallow truss), Fig. 2.3(c), there are only three equilibrium positions, a saddle (unstable) at the origin and two symmetric minima (stable) along the $\overline{z}$ axis. So, $\alpha = 1.00$ corresponds to a critical value separating two types of global behavior.

The static unloaded equipotential curves with a logarithmic strain measure (LSM, $\varepsilon_k = \ln(l_k/L)$) for the same values of α are shown in Fig. 2.5. As for the QSM, there are three equilibrium points along the $\overline{z}$ axis: two minima corresponding to the undeformed initial and inverted equilibrium positions and a saddle corresponding to a flat stressed equilibrium configuration. Also, the two symmetric saddles along the the $\overline{r}$ axis are identified. However, when the LSM is considered, as the length of a compressed bar tends to zero, $\overline{\overline{\Pi}} \to \infty$ at $\overline{r} = \pm\alpha$ and $\overline{z} = 0$.

The equipotential curves in Fig. 2.3 and Fig. 2.5 correspond to the possible solutions (orbits) of the conservative Hamiltonian system $(\overline{\overline{\Pi}})$ in the configuration space $(\overline{r} \times \overline{z})$. The comparison of these two figures, shows clearly that the adopted strain measure has a strong influence on the free undamped
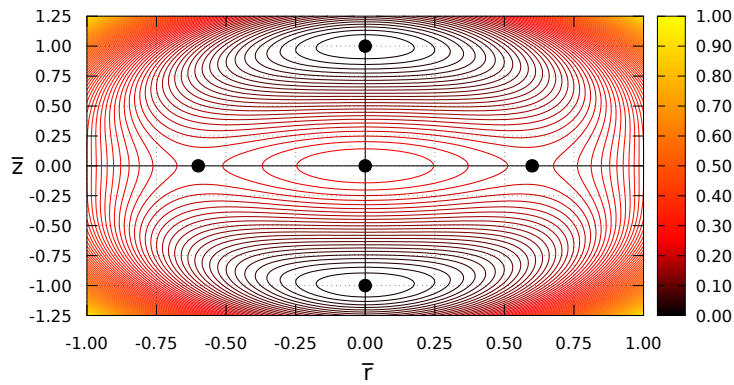
(a) $\alpha = 0.80$
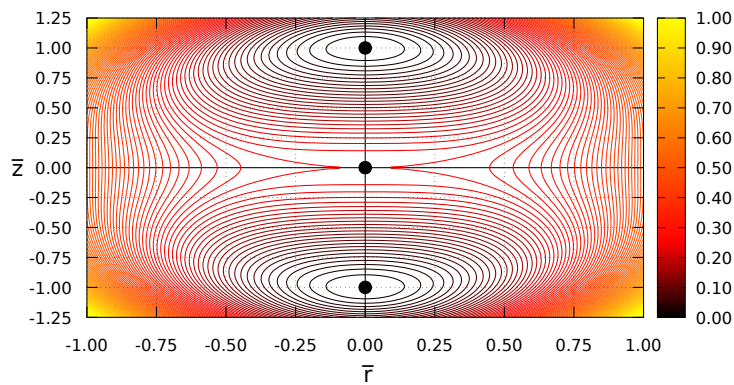
(b) $\alpha = 1.00$
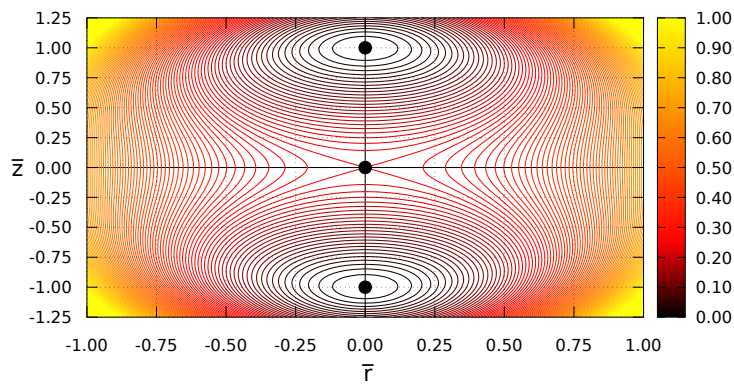
(c) $\alpha = 1.20$

Figure 2.3: Equipotential energy curves of the *unloaded structure* for selected values of α.

vibrations and that the results become clearly different as the deformation of the bars increases, thus leading to different global behaviors.

The equipotential curves of the *statically loaded truss* using the QSM for three load combinations with $\alpha = 0.80$ are shown in Fig. 2.6. The presence of vertical and/or horizontal load changes the topology of the total potential

| | (a) $\alpha = 0.80$ | (b) $\alpha = 1.00$ | (c) $\alpha = 1.20$ |
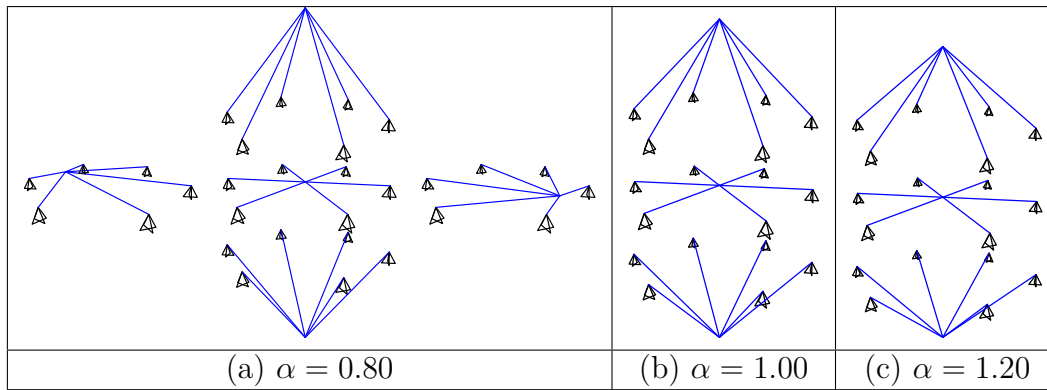
Figure 2.4: Equilibrium configurations of the *unloaded structure* for selected values of α considering a QSM.

energy, modifying the number of solutions (satisfying equilibrium), the position of the equilibrium points on the $(\bar{r}, \bar{z})$ plane and their stability (Fig. 2.7). In Fig. 2.6(a), the vertical load breaks the symmetry of the potential energy with respect to the $\bar{r}$ axis, shifting the equilibrium points away from it. Analogously, Fig. 2.6(b) shows how the horizontal load breaks the symmetry with respect to the $\bar{z}$ axis, changing the number of solutions and the position of the equilibrium points. In Fig. 2.6(c) the combination of the vertical and horizontal loads breaks completely the symmetries of the potential energy function, reducing the number of equilibrium configurations to one.

Figures 2.3 and 2.6 are in fact the cross sections of the four dimensional phase-space $(\bar{r}, \bar{z}, \alpha, \lambda)$ of the conservative system. The unstable manifolds of the saddles (unstable domains containing the saddle points) separate the initial conditions that lead to bounded solutions surrounding the stable equilibrium positions of the structure. The knowledge of these frontiers helps the designer to separate the phase space into safe and unsafe domains and evaluate the degree of safety of the system [16]. The results show that the geometric parameter α and the load direction have a significant influence on the energy landscape, thus controlling the behavior of the structure. In the following, a parametric analysis of the truss under vertical and horizontal loads with different structural depths is thus presented.

2.4.2
Structural response under horizontal load

The response of the pyramidal truss module under horizontal load $(p_z = 0, p_r \neq 0)$ is considered in this section. In Sections 2.4.2.1 and 2.4.2.2 the primary and secondary elastic equilibrium paths determined by Ligarò and Valvo [9] are reviewed and novel closed form expressions for the natural frequencies are proposed and validated numerically, clearly separating the
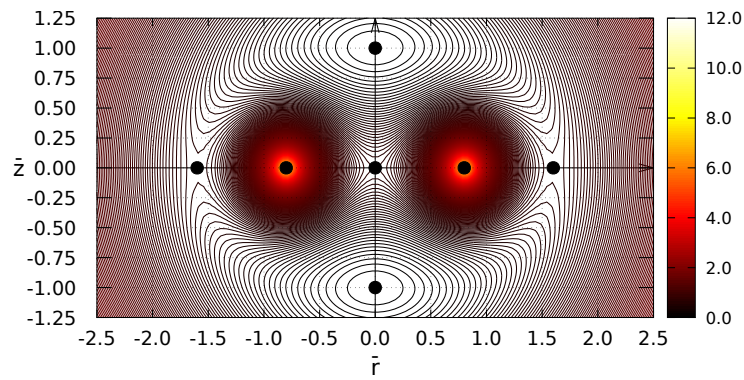
(a) $\alpha = 0.80$
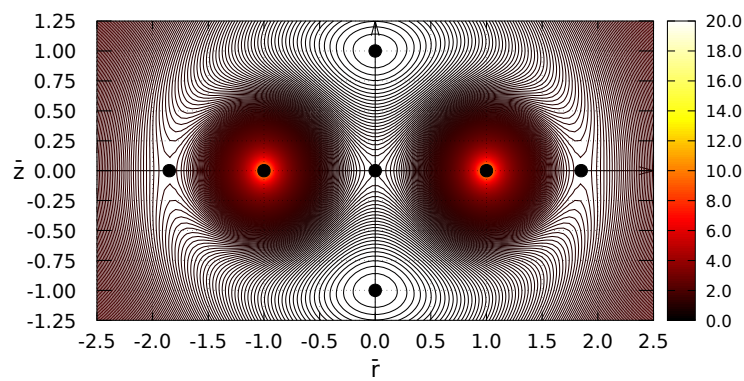
(b) $\alpha = 1.00$
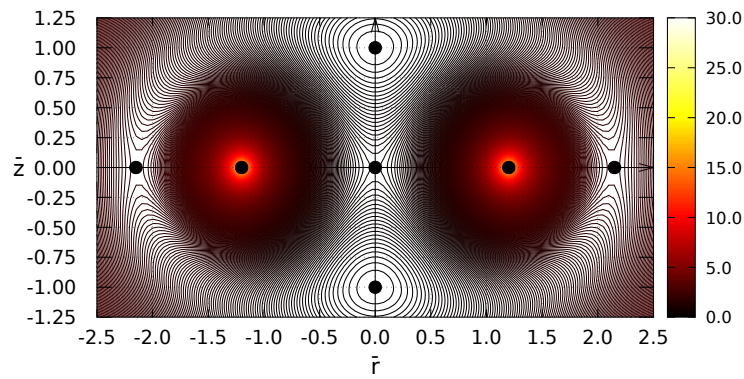
(c) $\alpha = 1.20$

Figure 2.5: Equipotential energy curves of the *unloaded structure* for selected values of α considering the LSM.

stable and unstable domains of the response. Although the focus of the current chapter is the static behavior of pyramidal trusses this is interesting because the fundamental frequency-load relation can be employed for the estimation of buckling loads using non-destructive experiments [68] and in the identification of structural parameters [69].
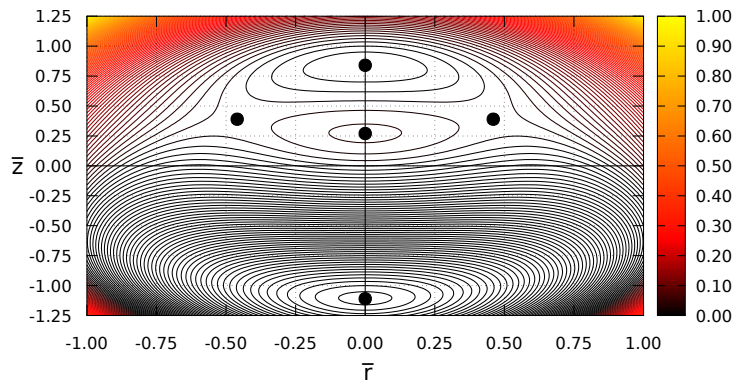
(a) $\lambda_v = 0.25, \lambda_h = 0.00$
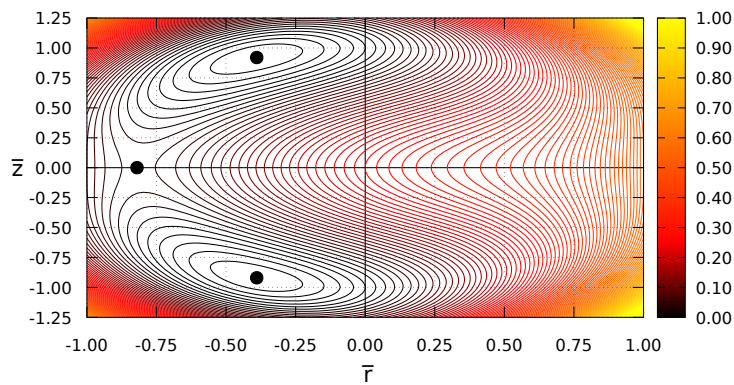
(b) $\lambda_v = 0.00, \lambda_h = 0.25$
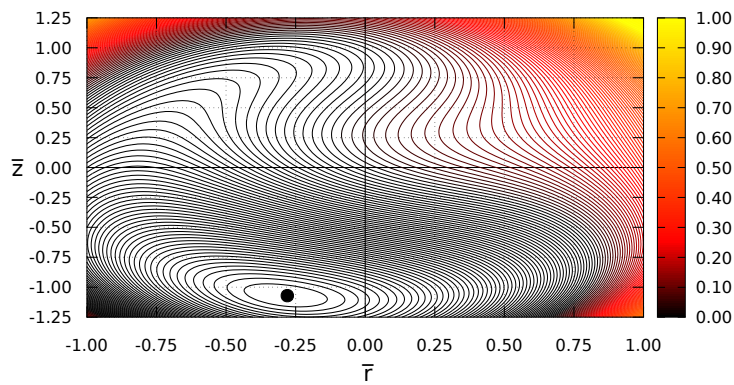
(c) $\lambda_v = 0.25, \lambda_h = 0.25$

Figure 2.6: Equipotential energy curves of the *loaded structure* with $\alpha = 0.80$.

Along the stable and unstable parts of the equilibrium paths, the bars are subjected to compressive axial forces, which can become greater than the Euler's buckling load [34, 35] or the stresses may reach the material yield limit [70], leading to an elasto-plastic nonlinear response. In such cases, the local instability of the bars and the plastic behavior of the material may influence the load carrying capacity of the structure. A novel study of

| (a) $\lambda_v = 0.25$ | (b) $\lambda_h = 0.25$ | (c) $\lambda_v = \lambda_h = 0.25$ |
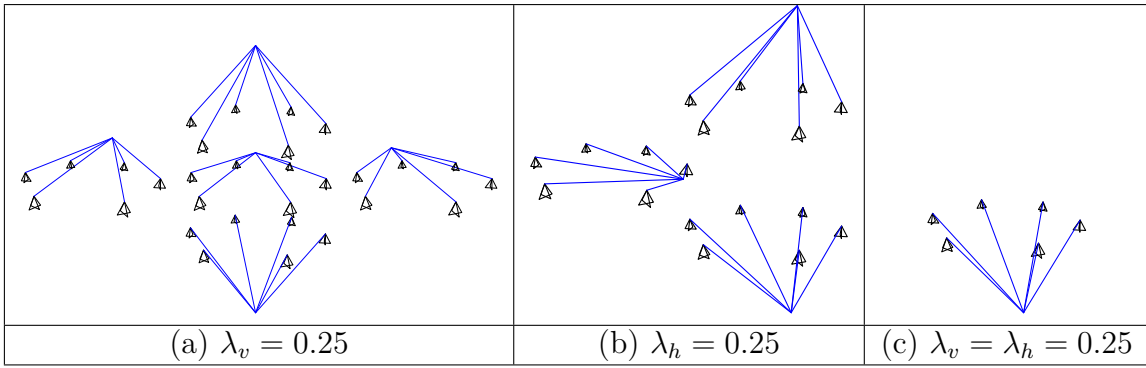
Figure 2.7: Equilibrium configurations of the *loaded structure* with $\alpha = 0.8$ and considering a QSM.

the influence of the bars Euler and elasto-plastic buckling on the structural response is presented in Sections 2.4.2.3 and 2.4.2.4, respectively, proposing novel closed form expressions for the limit load points (validated numerically). The numerical tools used in each analyses are summarized in Tab. 2.2.

Section	FE formulation	Strain measure	Material behavior
2.4.2.1	Bar	QSM	elastic
2.4.2.2	Bar	QSM	elastic
2.4.2.3	Beam	QSM	elastic
2.4.2.4	Bar	QSM	elasto-plastic

Table 2.2: Numerical tools used in the static analysis of a single pyramidal truss module under horizontal load.

2.4.2.1
Elastic primary path

The elastic response of the horizontally loaded pyramidal truss with the apex node inside the base circle Γ (Fig. 2.8) is considered here. Initially all bars are in compression and the system behavior is unstable since the truss would snap vertically to either the original or inverted configurations. However, this case is of interest since this equilibrium path may appear in computational simulations of the pyramidal truss under horizontal load.

As proven in [9], considering $z = 0$ and combining the x and y components of the Eqs. (2-18) - (2-19), the relation $\theta = \theta_p + \pi$ is satisfied and:

$$\lambda = \bar{r}\left(1 - \bar{r}^2 - \alpha^2\right) \tag{2-30}$$

Differentiation of this equation leads to the following limit point (local
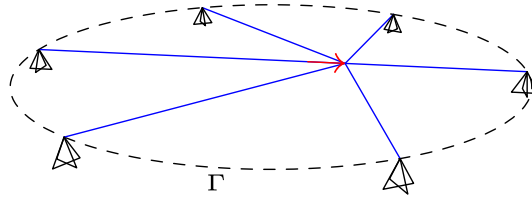
Figure 2.8: Equilibrium configuration of the truss elastic primary path under horizontal load ($\alpha = 1.2$).

extreme load) coordinates ($\bar{r}_l^h, \lambda_l^h$):

$$\bar{r}_l^h = \sqrt{3\left(1 - \alpha^2\right)}/3 \quad \lambda_l^h = 2\sqrt{3\left(1 - \alpha^2\right)^3}/9 \tag{2-31}$$

Thus for $\alpha > 1$ there is no limit point. From Eq. (2-21) the natural frequencies are given by:

$$\bar{\omega}_1^2 = \left(\bar{r}^2 - 1\right)/2 \tag{2-32}$$

$$\bar{\omega}_2^2 = \left(\bar{r}_s^2 + \alpha^2 - 1\right)/2 \tag{2-33}$$

$$\bar{\omega}_3^2 = \left(3\bar{r}_s^2 + \alpha^2 - 1\right)/2 \tag{2-34}$$

Therefore, the response is stable if $\bar{r} > 1$. The equilibrium paths obtained numerically and analytically are plotted in Fig. 2.9 and the variation of the natural frequencies with the applied load is illustrated in Fig. 2.10 for $\alpha = 1.20$ ($H = 5.83$ m), showing matching curves for the closed form and finite element solutions. The usual convention adopted in this work is that, solid and dashed lines correspond to stable and unstable configurations, respectively.
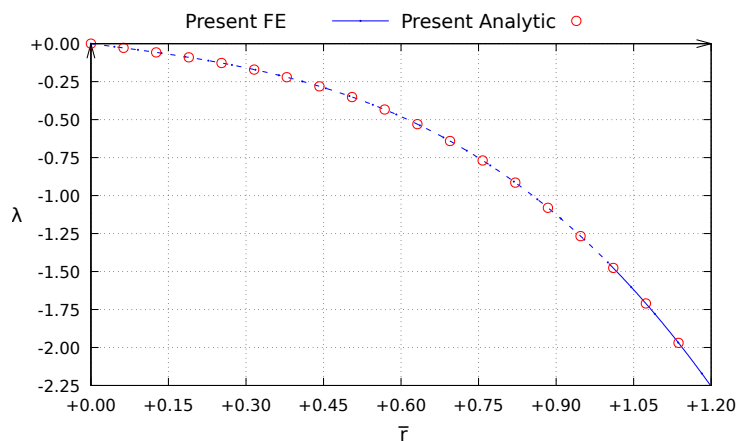
Figure 2.9: Fundamental equilibrium path for a shallow truss under horizontal load ($\alpha = 1.20$).
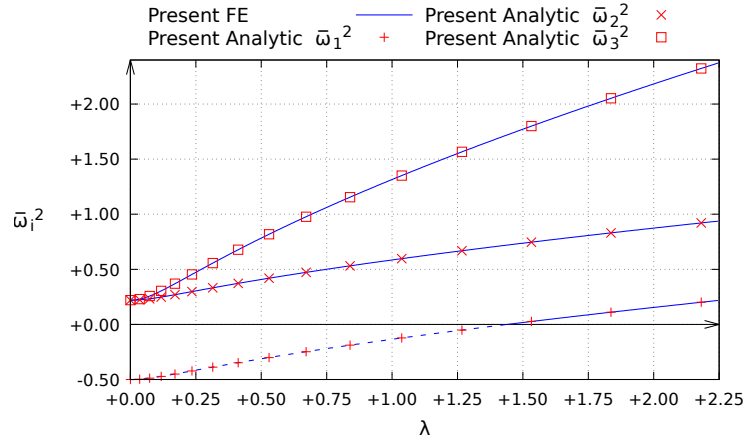
Figure 2.10: Variation of the natural frequencies with the horizontal load ($\alpha = 1.20$).

2.4.2.2
Elastic bifurcation

The elastic secondary equilibrium path is now studied, considering $z \neq 0$. From Eqs. (2-18) to (2-19) and taking $\theta = \theta_p$ and $z = \pm\sqrt{H^2 - r^2}$, the bifurcated path is obtained as:

$$\lambda = \alpha^2 \bar{r} = \alpha^2 \sqrt{1 - \bar{z}^2} \tag{2-35}$$

Differentiation of this equation leads to the following load limit point coordinates $(\bar{r}_b^h, \lambda_b^h)$:

$$\bar{r}_b^h = 1 \quad \lambda_l^h = \alpha^2 \tag{2-36}$$

From Eq. (2-21), the associated natural frequencies are given by:

$$\bar{\omega}_1^2 = \left[\alpha^2 + 2 - \sqrt{(\alpha^2 - 2)^2 + 8\alpha^2 \bar{r}_s^2} \right]/4 \tag{2-37}$$

$$\bar{\omega}_2^2 = \alpha^2/2 \tag{2-38}$$

$$\bar{\omega}_3^2 = \left[\alpha^2 + 2 + \sqrt{(\alpha^2 - 2)^2 + 8\alpha^2 \bar{r}_s^2} \right]/4 \tag{2-39}$$

Thus, the response is stable if $\bar{r} < 1$. The projections of the secondary path onto the the $\bar{z} \times \bar{r}$ and $\lambda \times \bar{z}$ planes computed numerically and analytically are shown in Fig. 2.11(a) and Fig. 2.11(b), respectively, and the variation of the natural frequencies with the applied load is illustrated in Fig. 2.12 for $\alpha = 0.70$ ($H = 10.0$ m), showing matching curves for the closed form and finite element solutions. The secondary path is stable as corroborated by the positive values of the square of the natural frequencies.
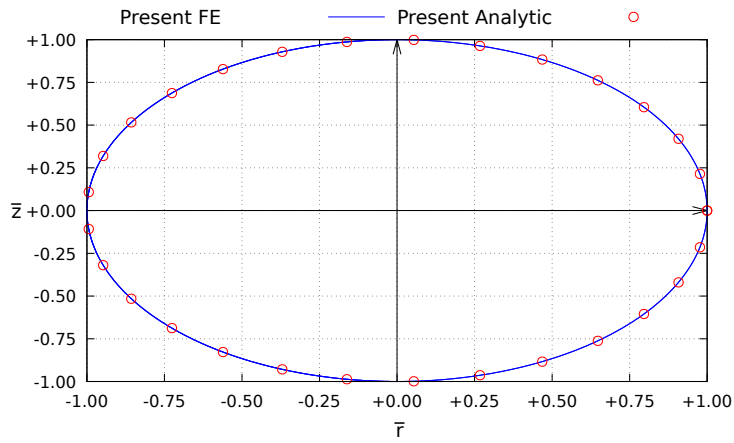
(a) $\overline{z} \times \overline{r}$
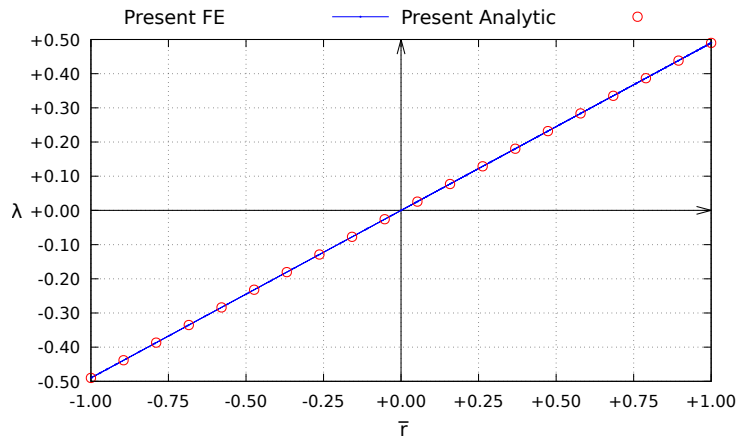
(b) $\lambda \times \overline{r}$

Figure 2.11: Secondary equilibrium path of a deep truss under horizontal load ($\alpha = 0.70$).
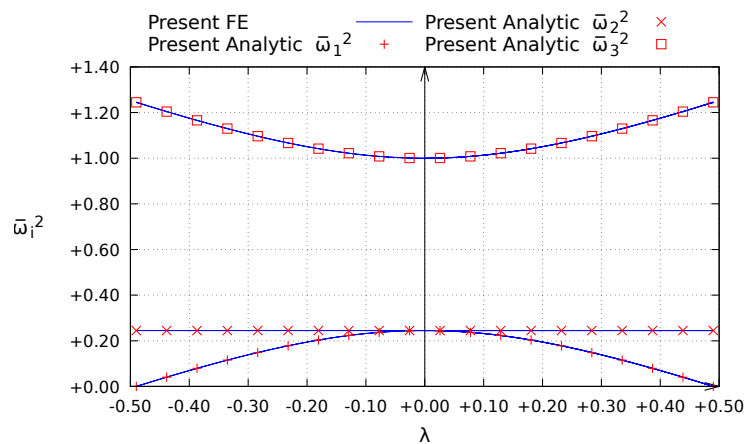
Figure 2.12: Variation of the natural frequencies with the horizontal load ($\alpha = 0.70$).

2.4.2.3
Euler buckling using a beam FE model

When the pyramidal truss is subjected to a horizontal load ($\theta = \theta_p$, $z^2 + r^2 = H^2$), some bars are in traction while others are in compression. From

Eq. (2-3) the most compressed bar has a length $l_k = \sqrt{z^2 + (B-r)^2}$. Thus its axial force, considering an elastic behavior, is given by $\overline{f}_k = -EABr/L^2$. The buckling point $(\overline{r}_f^h, \lambda_f^h)$ is then obtained analytically by comparing the axial force with the Euler buckling load $P_b = \pi^2 EI/L^2$, leading to:

$$\overline{r}_f^h = \pi^2 \overline{r}_g^2/\alpha \quad \lambda_f^h = \alpha \pi^2 \overline{r}_g^2 \tag{2-40}$$

Figure 2.13 shows the results of the finite element simulations, illustrating the influence of the truss height on the nonlinear response and load capacity considering beam buckling. The initial stiffness is progressively reduced as the bars under compression buckle. The closed form expression of the buckling point is favorably compared with the start of the stiffness reduction in the numerical simulations. Later, as the apex node reaches the base, the bars under traction oppose to the applied load and the system recovers its stiffness and load capacity.
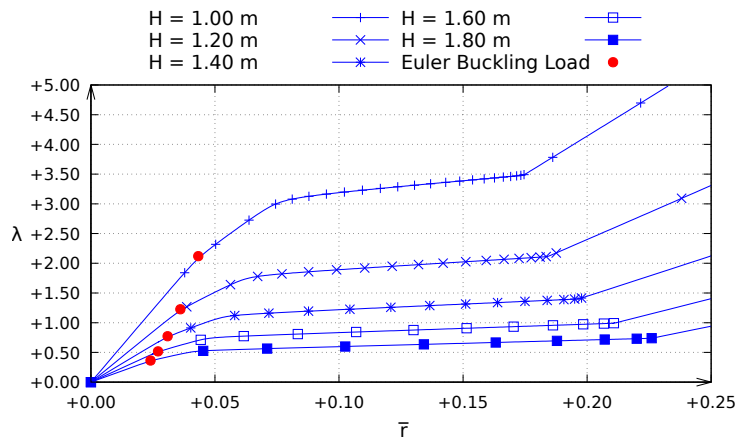
Figure 2.13: Influence of the height on the Euler buckling and nonlinear response of the horizontally loaded truss.

2.4.2.4
Plastic buckling response

Considering now the system subjected to a horizontal load *in the direction of one of the bars*, the yield point $\left(\overline{r}_y^h, \lambda_y^h\right)$ may be obtained analytically by equating the maximum axial force $\overline{f} = EArB/L^2$ and the yield axial force $P_y = A\sigma_y$, resulting in:

$$\overline{r}_y^h = \beta^2 \varepsilon_y/\alpha \quad \lambda_y^h = \beta^2 \alpha \varepsilon_y \tag{2-41}$$

Figure 2.14 shows the results of the finite element simulations, illustrating the influence of the truss height on the load capacity considering elasto-plastic

material behavior with zero hardening. The closed form expression of the yield point is favorably compared with the start of the stiffness reduction in the numerical simulations. The initial stiffness reduces suddenly when the two bars in the load direction (one in compression and one in tension) yield. As the other four bars yield subsequently in compression and tension, the truss stiffness decreases and finally becomes null (perfect plasticity).
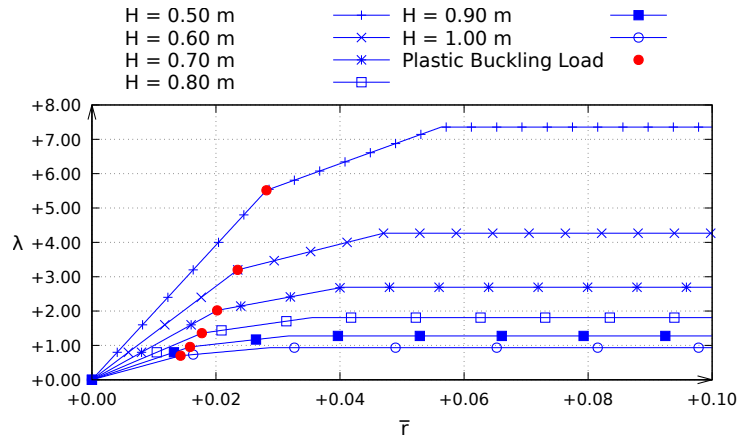
Figure 2.14: Influence of the truss height on the elasto-plastic response of the horizontally loaded system.

In all cases analyzed here the present FE results agree well with the analytical results, thus validating the developed closed form expressions. Based on Eqs. (2-31), (2-36), (2-40) and (2-41) the designer can identify the regions where different nonlinear phenomena may occur for the horizontal load without performing finite element simulations.

2.4.3
Structural response under vertical load

The response of the pyramidal truss module under vertical load ($p_r = 0, p_z \neq 0$) is considered here. In Sections 2.4.3.1 and 2.4.3.2 the primary and secondary elastic equilibrium paths determined by Ligarò and Valvo [9] are reviewed and novel closed form expressions for the natural frequencies are proposed and validated numerically, clearly separating the stable and unstable domains of the response. The influence of the strain measure on the elastic primary and secondary equilibrium paths is also investigated. A novel study of the influence of the bars Euler and inelastic buckling on the pyramidal truss structural response is presented in Sections 2.4.3.3 and 2.4.3.4, respectively, where closed form expressions for the limit load points are proposed and validated numerically. The complete closed form elasto-plastic equilibrium path is determined considering moderate and large strains both analytically

and through finite element simulations using the in-house developed code (Appendices). The numerical tools used in each analyses are summarized in Tab. 2.3.

Section	FE formulation	Strain measure	Material behavior
2.4.3.1	Bar	QSM and LSM	elastic
2.4.3.2	Bar	QSM and LSM	elastic
2.4.3.3	Beam	QSM	elastic
2.4.3.4	Bar	QSM and LSM	elasto-plastic

Table 2.3: Numerical tools used in the static analysis of a single pyramidal truss module under vertical load.

2.4.3.1
Elastic primary path

Initially the elastic symmetric response of the system (nonlinear primary equilibrium path) subjected to a vertical load at the apex node is considered ($r = 0$). From Eq. (2-12), considering the QSM $\varepsilon_k = (l_k^2 - L^2)/(2L^2)$ and LSM $\varepsilon_l = \ln(l_k/L)$, the respective nonlinear equilibrium paths are given by:

$$\lambda_q = \overline{z}\left(1 - \overline{z}^2\right) \tag{2-42}$$

$$\lambda_l = \beta^4 \frac{\overline{z}}{\overline{z}^2 + \alpha^2} \ln\left(\frac{1 + \alpha^2}{\overline{z}^2 + \alpha^2}\right) \tag{2-43}$$

In terms of the adopted non-dimensional variables, the equilibrium path using the QSM is independent of the values of the geometric parameters α and β that governs the truss depth (Fig. 2.1) [9], while the equilibrium path obtained using the LSM is a nonlinear function of these geometric parameters as would be expected from systems with a high geometrical nonlinear behavior. The equilibrium path obtained with the finite element formulation is favorably compared with the developed analytical solution in Fig. 2.15(a). For low values of $\alpha = B/H$ (deep truss), the pyramidal truss is subjected to large strains as it moves from the initial configuration to the inverted one, and the difference between the strain measures appears clearly. The fundamental equilibrium path with logarithmic strains approaches asymptotically to the one for QSM as α increases, and for a shallow truss ($H \ll B$) the response is practically independent of the strain measure.

The system load limit points can be determined through the following equations:

$$\frac{\partial \lambda_q}{\partial \overline{z}} = 1 - 3\overline{z}^2 = 0 \tag{2-44}$$
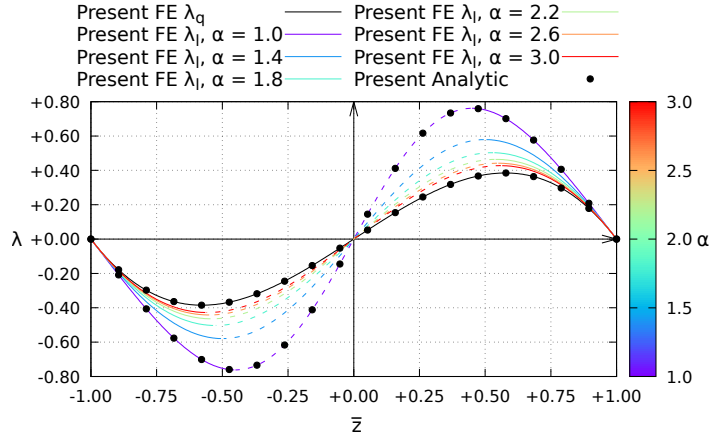
(a) Equilibrium path
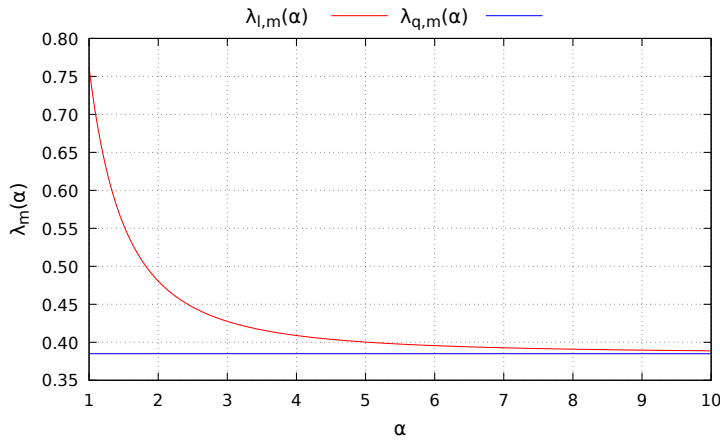
(b) Limit point

Figure 2.15: Influence of the strain measures and geometric parameter α on the fundamental nonlinear equilibrium path and limit point for vertical load and elastic material behavior.

$$\frac{\partial \lambda_l}{\partial \bar{z}} = \hbar^2 \left[\left(\alpha^2 - \bar{z}^2 \right) \ln(\hbar) - 2\bar{z}^2 \right] = 0 \tag{2-45}$$

where $\hbar = (1 + \alpha^2)/(\bar{z}^2 + \alpha^2)$.

Using this condition, the coordinates of the two limit-points $\left(\bar{z}_{q,m}^v, \lambda_{q,m}^v \right)$ for the QSM are obtained as:

$$\bar{z}_{q,m}^v = \pm\sqrt{3}/3 \quad \lambda_{q,m}^v = \pm 2\sqrt{3}/9 \tag{2-46}$$

For the logarithmic equilibrium path there are also two limit points $(\pm\bar{z}_{l,m}^v, \pm\lambda_{l,m}^v)$, but they have an implicit nonlinear dependency on α, as illustrated in Fig. 2.15(b), where the two limit point loads are plotted as a function of α. In both cases, the limit points correspond to the snap-through jump between the initial to the inverted configurations. As the difference between the two strain measures reduces for small deformations, the limit

point using the LSM approaches asymptotically from above $\lambda_{q,m} = 2\sqrt{3}/9$ as α increases.

From Eq. (2-21), the QSM natural frequencies of the loaded structure are:

$$\overline{\omega}_1^2 = \left(4\overline{z}_s^2 + \alpha^2 - 2 - |\alpha^2 - 2\overline{z}_s^2|\right)/4 \tag{2-47}$$

$$\overline{\omega}_2^2 = \left(\overline{z}_s^2 + \alpha^2 - 1\right)/2 \tag{2-48}$$

$$\overline{\omega}_3^2 = \left(4\overline{z}_s^2 + \alpha^2 - 2 + |\alpha^2 - 2\overline{z}_s^2|\right)/4 \tag{2-49}$$

If $|\overline{z}| > \sqrt{2}/2\alpha$, $\omega_1 = \omega_2$, otherwise $\omega_2 = \omega_3$. This is due to the inherent symmetries of the structural system and may lead to internal resonances, as the different vibration modes can transfer energy from one to another.

The equilibrium path and limit points for $\alpha = 1.20$ (shallow structure) are shown in Fig. 2.15 and the variation of the square of the natural frequencies with the applied load considering the QSM is plotted in Fig. 2.16. The stability of the nonlinear equilibrium paths is evaluated here from the Hessian matrix and the eigenvalues are proportional to the square of the natural frequency. The square of the lowest natural frequency becomes zero at the two limit points and negative between these points (unstable equilibrium path), while the two other frequencies are always positive. Thus, for shallow trusses ($\alpha > 1$), the fundamental nonlinear equilibrium path is unstable for $|\overline{z}| < \sqrt{3}/3$ and the structure jumps to an inverted position at the limit points (snap-through buckling).
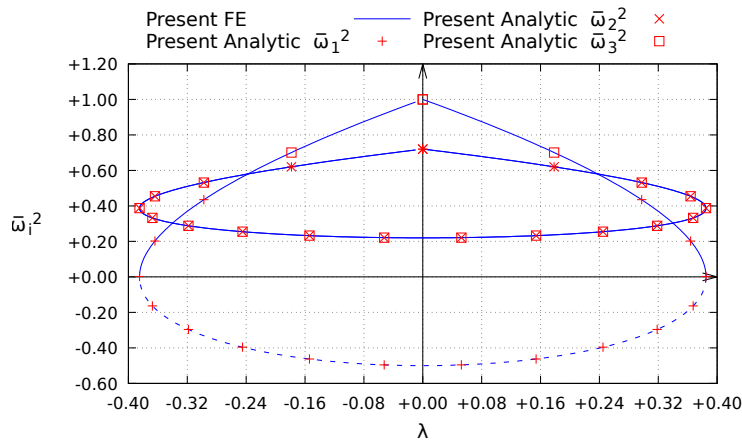
Figure 2.16: Variation of the natural frequencies with the vertical load magnitude ($\alpha = 1.20$).

2.4.3.2
Elastic bifurcation

The existence of additional bifurcation points (that appear due to lateral instabilities) along the nonlinear equilibrium path is investigated here. As α increases (i.e. structural depth decreases) the truss under vertical load may also lose stability through an unstable symmetric bifurcation along the nonlinear equilibrium path, breaking the system symmetry ($r \neq 0$). The bifurcation points appear in pairs.

Considering the QSM and combining the x and y components in Eqs. (2-18)-(2-19) leads to:

$$\lambda = \alpha^2 \overline{z} \tag{2-50}$$

The coordinates of the bifurcation points along the fundamental path, $(\overline{z}_{q,b}, \lambda_{q,b})$, are the intersections of the equilibrium paths given by Eqs. (2-42) and (2-50), and are:

$$\overline{z}_{q,b}^v = \pm\sqrt{1-\alpha^2} \quad \lambda_{q,b}^v = \pm\alpha^2\sqrt{1-\alpha^2} \tag{2-51}$$

Therefore, bifurcation occurs only if $\alpha \leq 1$.

For the LSM, after some algebraic manipulation, the linearization of Eq. 2-12 provides the following relation for the critical configuration:

$$\alpha = \sqrt{\frac{\lambda_1^2 \ln(\lambda_1^2)}{(1-\lambda_1^2)\ln(\lambda_1^2) - 1}} \tag{2-52}$$

Although Eq. (2-52) can't be solved analytically for λ_1, the term inside the square root is only non-negative for $\lambda_1 \in [0,1]$. This result is expected, since the pyramidal truss can only suffer bifurcation when the bars are subjected to compression. Also, the right hand side of Eq. (2-52) has a horizontal tangent at $\lambda_1 = \pm\exp\left(\frac{1}{4} - \frac{\sqrt{5}}{4}\right)$, corresponding to a maximum value of $\alpha_m = 0.5092$. This means that the bifurcation in the system can only occur if $\alpha \leq \alpha_m$, which is approximately half of the value obtained with the QSM. This large difference is justified by the fact that bifurcation due to lateral instabilities only occurs in deep trusses, and so at the bifurcation point the strains in the members are large (the results from the two strain measures thus differ considerably).

Figure 2.17 shows the computational results, illustrating the equilibrium path and apex node trajectory of the truss for both strain measures and $\alpha = 0.5$. For the elastic vertically loaded structure a horizontal geometric imperfection of $0.01\% H$ in the x direction of the apex node position is

considered in the FE numerical analysis in order to capture the bifurcation computationally. The magnitude of the imperfection has only a small influence on the system load capacity. Its major influence is to allow the identification of the bifurcation point and to shift from the pre-buckling to the post-buckling path using the continuation algorithm. As the eigenvalues of the system stiffness are monitored along the complete equilibrium path, all bifurcations are determined.

The unstable post-buckling path (dashed lines) connects the two bifurcation points. There is an increase in the bifurcation load from the quadratic to logarithmic case. However, there is also a sharp increase in the initial declivity of post-buckling path which, according to Koiter post-buckling theory, leads to an increase in the imperfection sensitivity [71]. As the post-buckling path approaches the flat configuration, the equilibrium path of the logarithmic case approaches asymptotically that of the quadratic case, where the two paths intersect.
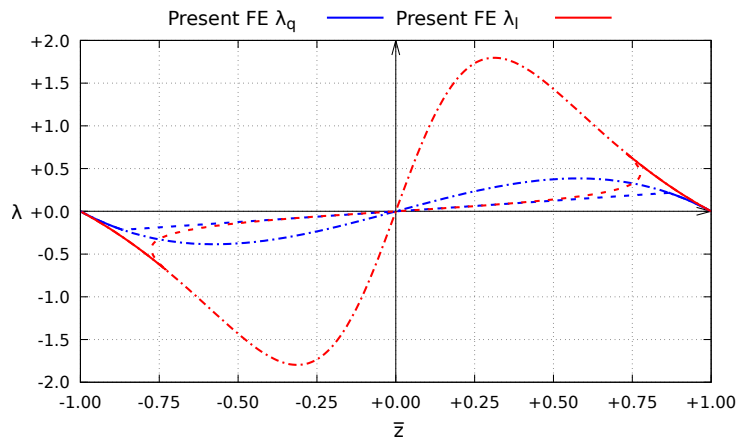
(a) $\lambda \times \overline{z}$
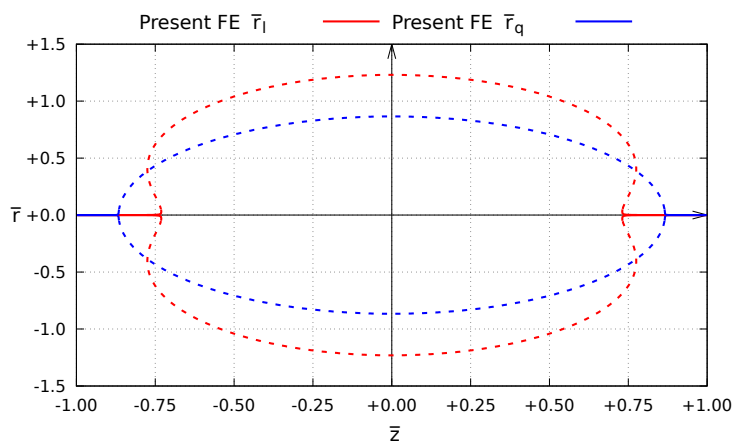
(b) $\overline{r} \times \overline{z}$

Figure 2.17: Projections of the nonlinear equilibrium paths under vertical load ($\alpha = 0.5$).

In addition, for the QSM, from Eqs. (2-46) and (2-51), the limit point $(\overline{z}_{q,m}^v, \lambda_{q,m}^v)$ and bifurcation point $(\overline{z}_{q,b}^v, \lambda_{q,b}^v)$ under vertical load coincide for $\alpha = \sqrt{6}/3$. For $\alpha > \sqrt{6}/3$, the bifurcation point appears along the unstable part of the nonlinear equilibrium path, without influencing the load carrying capacity of the truss. The bifurcation point disappears for $\alpha > 1$. Along the secondary branch, the natural frequencies are given by:

$$\overline{\omega}_1^2 = \left[2 - 3\alpha^2 - \sqrt{(\alpha^2 - 2)^2 - 8\alpha^2\overline{z}_s^2}\right]/4 \tag{2-53}$$

$$\overline{\omega}_2^2 = 0 \tag{2-54}$$

$$\overline{\omega}_3^2 = \left[2 - 3\alpha^2 + \sqrt{(\alpha^2 - 2)^2 - 8\alpha^2\overline{z}_s^2}\right]/4 \tag{2-55}$$

The variation of the square of the natural frequencies with the applied load is illustrated in Fig. 2.18 for $\alpha = 0.7$ ($H = 10.0$m). The elliptical post-buckling path is unstable ($\omega_2 = 0$ and $\omega_1^2 < 0$). At the bifurcation point the truss jumps to an inverted stable equilibrium position.
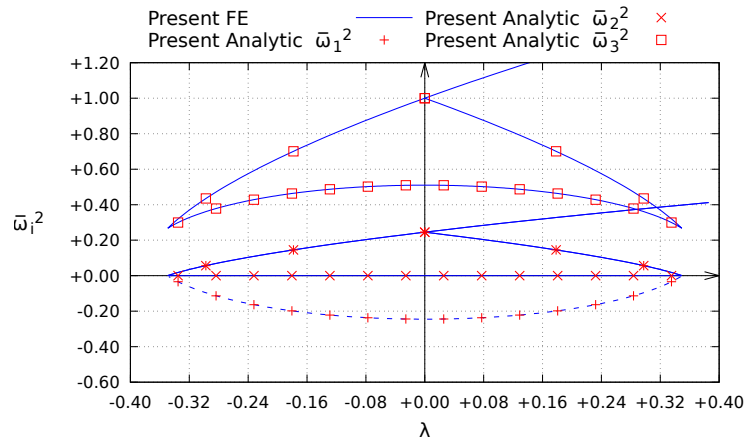
Figure 2.18: Variation of the natural frequencies with vertical load ($\alpha = 0.70$).

2.4.3.3
Euler buckling using a beam FE model

The system stability and load capacity considering the elastic buckling of the bars (saddle-node bifurcation for the imperfect system) are investigated here. For the buckling analysis of the pin-ended bars, the spatial beam formulation presented in Appendix C is used in the FE analysis. A small initial imperfection along the beams of the form $10^{-3}L\sin(\pi x/L)$ is assumed in order to numerically capture in the FE analysis the instability.

Considering an initial symmetric response ($r = 0$) using the QSM, Eq. (2-3) provides the axial force in the bars as $\overline{f} = EA(z^2 - H^2)/(2L^2)$. The beam buckling load [72] is $P_b = \pi^2 EI/L^2$ and equating $\overline{f}$ and P_b, the buckling points

$(\overline{z}_{q,f}^v, \lambda_{q,f}^v)$ can be obtained analytically as:

$$\overline{z}_{q,f}^v = \pm\sqrt{1 - 2\pi^2\overline{r}_g^2} \quad \lambda_{q,f}^v = \pm 2\pi^2\overline{r}_g^2\sqrt{1 - 2\pi^2\overline{r}_g^2} \tag{2-56}$$

where, $\overline{r}_g = r_g/H$ and $r_g^2 = I/A$ is the cross section radius of gyration.

Elastic buckling occurs if $H > H_f = \sqrt{2}\pi r_g$. For the chosen numerical parameters the minimum height at which this occurs is $H_f = 0.78$ m. Figure 2.19 shows the numerical results of the simulations, illustrating the influence of the truss height on the load capacity considering buckling. As the truss height increases, the axial compressive force increases in the elements, causing them to buckle earlier, greatly reducing the system load capacity. In terms of the present non-dimensional parameters the slenderness parameter of each bar is given by $L/r_g = \beta/\overline{r}_g$.
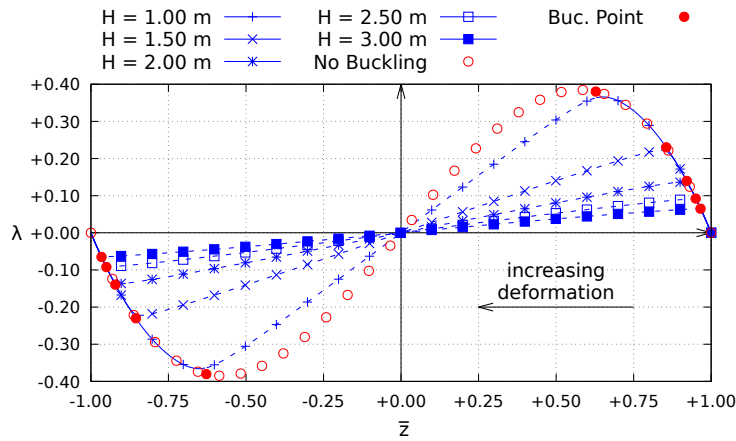
Figure 2.19: Influence of the system height on the buckling response of deep trusses under vertical load.

The effect of an initial symmetric (umbrella and inverted umbrella) and antisymmetric (alternate) small geometric imperfection was also tested. In all cases the system follows practically the same equilibrium path with a small sensitivity to the type of imperfection. Thompson and Hunt [39] have shown that, among all of the bifurcation types, the saddle-node bifurcation exhibits the lowest imperfection sensitivity, further confirming the result obtained in the present work. The effect of an random imperfection magnitude varying in each structural element was not investigated.

2.4.3.4
Plastic buckling response

The truss stability and load capacity considering the elasto-plastic behavior of the material in now examined. For monotonic loading, plasticity occurs when the strain in a bar ε becomes equal to the elastic yield strain $\varepsilon_y = \sigma_y/E$.

The yield points (determined using this criterion) for the QSM and LSM can be obtained analytically as:

$$\overline{z}_{q,y}^{v} \pm \sqrt{1 \pm 2\beta^2 \varepsilon_y} \qquad\qquad \lambda_{q,y}^{v} = \pm 2\beta^2 \varepsilon_y \sqrt{1 \pm 2\beta^2 \varepsilon_y} \qquad (2\text{-}57)$$

$$\overline{z}_{l,y}^{v} = \pm\sqrt{\dfrac{1+\alpha^2}{\exp(\pm 2\varepsilon_y)} - \alpha^2} \qquad \lambda_{l,y}^{v} = \pm 2\varepsilon_y \exp(\pm 2\varepsilon_y)\beta^2 \overline{z}_{l,y}^{v} \qquad (2\text{-}58)$$

From the equations above, the snap-through process in compression only occurs in the elastic regime if:

$$\alpha_q \geq \sqrt{\dfrac{1 - 2\varepsilon_y}{2\varepsilon_y}} \qquad\qquad\qquad\qquad\qquad\qquad (2\text{-}59)$$

$$\alpha_l \geq [\exp(2\varepsilon_y) - 1]^{-\frac{1}{2}} \qquad\qquad\qquad\qquad\qquad (2\text{-}60)$$

which corresponds for most metal structures to rather shallow systems.

Figure 2.20 shows the variation of $\overline{z}_{l,y}$ for the pyramidal truss under vertical load generating tension and compression as a function of α for a nominal yield strain of $\varepsilon_y = 0.2\%$. In this case the snap-through occurs entirely in the elastic range only if $\alpha \geq 15.8$.
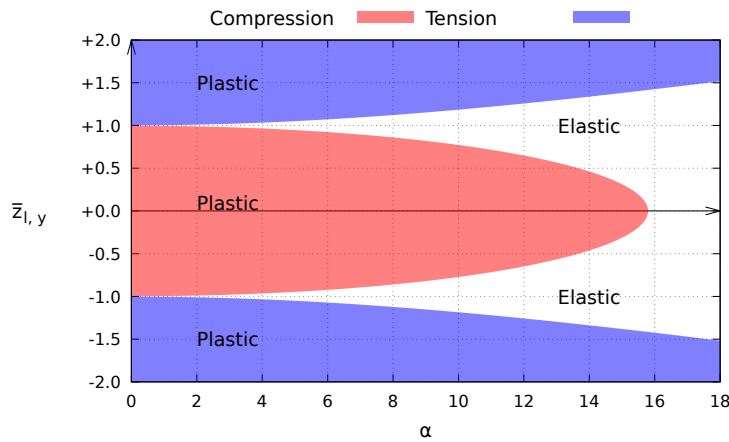
Figure 2.20: Pyramidal truss elasto-plastic response as a function of α (LSM).

Thus, it is expected that most metal trusses will exhibit plastic deformation before they reach the limit point and plastic snap-through occurs.

Note that, this limit value of α will decrease as the support stiffness k_b decreases (representing a more flexible base), and elastic buckling can occur for increasingly smaller values of α (this topic is treated in Sec. 2.4.5).

For deep trusses an unstable symmetric bifurcation, leading to an asymmetric buckling mode may occur at a lower load level then the ones predicted in Eqs. (2-57) and (2-58) along the fundamental equilibrium path. This hap-

pens when the fundamental path becomes unstable and the truss jumps to an inverted position.

Figure 2.21 shows the results of the numerical simulations, illustrating the influence of the truss height on its load capacity considering an elasto-plastic material behavior. The closed form expression of the yield point is favorably compared with the plastic buckling using finite element models with perfect plasticity. Similar to the observations in Sec. 2.4.3.3, as the truss height increases, the bars axial compressive force increases in a nonlinear manner, triggering plastic deformations at lower load levels, greatly reducing the system load capacity.
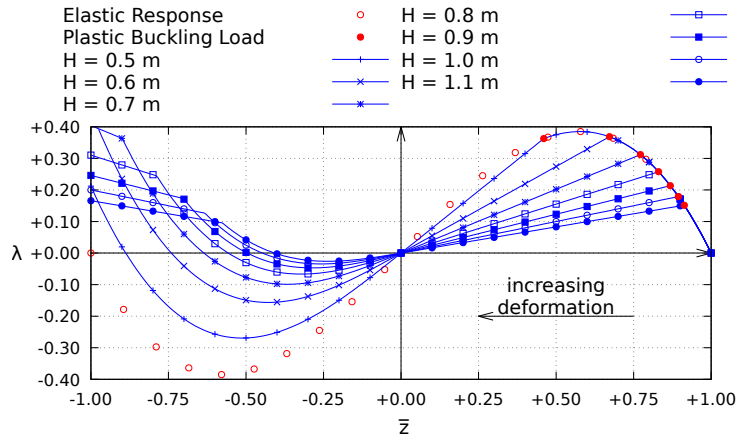
Figure 2.21: Influence of the height on the truss elasto-plastic behavior under vertical load.

After the elasto-plastic buckling permanent structural deformations are present. In the initial stress free configuration ($\lambda = 0$) there is an equilibrium configuration at $z = 0$ (base plane), however, due to the permanent deformations the element lengths are shortened, moving the buckled stress free configurations to a value of $|\bar{z}_p| < 1$. As the height and, consequently, plastic deformations increases the value of $|\bar{z}_p|$ decreases.

When the system response reaches the yield point, the stress in all elements becomes equal to the yield stress σ_y. Considering an elasto-plastic material with hardening, the ensuing unstable equilibrium path is given by:

$$\lambda_q = 2\beta^2[(1-\eta)\varepsilon_y - \eta\varepsilon]\bar{z} \tag{2-61}$$

$$\lambda_l = \beta^4\left[2\left(1-\eta\right)\varepsilon_y + \eta\ln\left(\frac{1+\alpha^2}{\bar{z}^2+\alpha^2}\right)\right]\frac{\bar{z}}{\bar{z}^2+\alpha^2} \tag{2-62}$$

where $\eta = K/(E+K) \in [0,1]$.

The maximum compressive strain occurs when the apex node reaches the base plane ($z = 0$) and is given by $\varepsilon_m = -\alpha^2/(2\beta^2)$ for the QSM and

$\varepsilon_m = \ln(\alpha/\beta)$ for the LSM. After this, the compressive strain decreases along the unstable path and, considering an elasto-plastic material behavior with hardening, the system response becomes eventually elastic in tension with a residual plastic deformation ε_r:

$$\varepsilon_r = (1 - \eta)(\varepsilon_m + \varepsilon_y) \tag{2-63}$$

The stress in the elements becomes $\sigma = E(\varepsilon - \varepsilon_r)$ and the resulting equilibrium path can be written as:

$$\lambda_q = \beta^2 \left[2\varepsilon_r + \frac{1 - \bar{z}^2}{1 + \alpha^2} \right] \bar{z} \tag{2-64}$$

$$\lambda_l = \beta^4 \left[2\varepsilon_r + \ln\left(\frac{1 + \alpha^2}{\bar{z}^2 + \alpha^2} \right) \right] \frac{\bar{z}}{\bar{z}^2 + \alpha^2} \tag{2-65}$$

The new stress free configuration is characterized by $\varepsilon = \varepsilon_r$, leading to:

$$\bar{z}_{q,p} = \sqrt{1 + 2\beta^2 \varepsilon_r} \tag{2-66}$$

$$\bar{z}_{l,p} = \sqrt{(1 + \alpha^2)\exp(2\varepsilon_r) - \alpha^2} \tag{2-67}$$

As the load further increases, the material begins to yield in traction. This point is characterized by the tension limit strain $\varepsilon_t = (1 - 2\eta)\,\varepsilon_m + 2\,(1 - \eta)\,\varepsilon_y$. The resulting tension yield point is then:

$$\bar{z}_{q,t} = \sqrt{1 + 2\beta^2 \varepsilon_t} \tag{2-68}$$

$$\bar{z}_{l,t} = \sqrt{(1 + \alpha^2)\exp(2\varepsilon_t) - \alpha^2} \tag{2-69}$$

After the stress reaches the yield value in tension, the ensuing stable equilibrium path is given by:

$$\lambda_q = \beta^2 \left[2\,(1 - \eta)\,\varepsilon_h + \eta\left(\frac{1 - \bar{z}^2}{1 + \alpha^2} \right) \right] \bar{z} \tag{2-70}$$

$$\lambda_l = \beta^4 \left[2\,(1 - \eta)\,\varepsilon_h + \eta \ln\left(\frac{1 + \alpha^2}{\bar{z}^2 + \alpha^2} \right) \right] \frac{\bar{z}}{\bar{z}^2 + \alpha^2} \tag{2-71}$$

where $\varepsilon_h = 2\eta\varepsilon_m - (1 - 2\eta)\varepsilon_y$.

Figure 2.22 shows the equilibrium path for $\alpha = 8.0$ and $\alpha = 1.2$ obtained by the FE formulation together with the analytical expression for each segment of the nonlinear elasto-plastic equilibrium path for $\eta = 0$ and $\eta = 0.15$ (i.e. different hardening behaviors), showing an excellent match. As shown in Figure 2.21(b), for $\alpha = 1.2$ plastic deformations are observed for very low load levels leading to a strong decrease in the load carrying capacity with

$\eta = 0$. For $\eta \neq 0$ a limit point appears along the elasto-plastic fundamental path, which increases with η, increasing the load carrying capacity of the truss. As η approaches one (the plastic tangent approaches the value of the Young modulus E) the curve converges to the elastic response obtained previously, as expected.
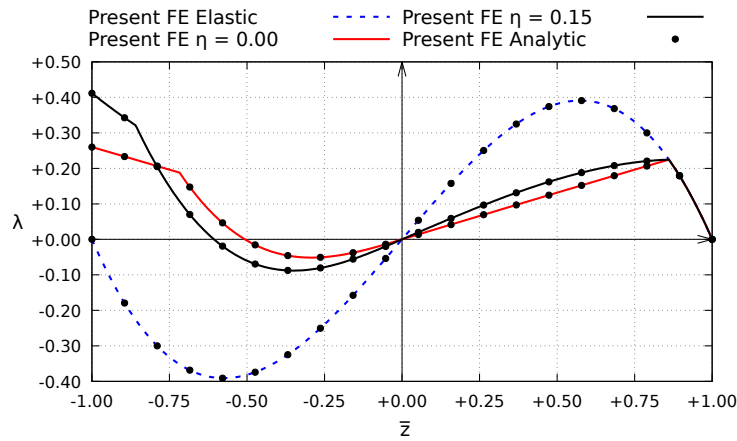
(a) $\alpha = 8.0$
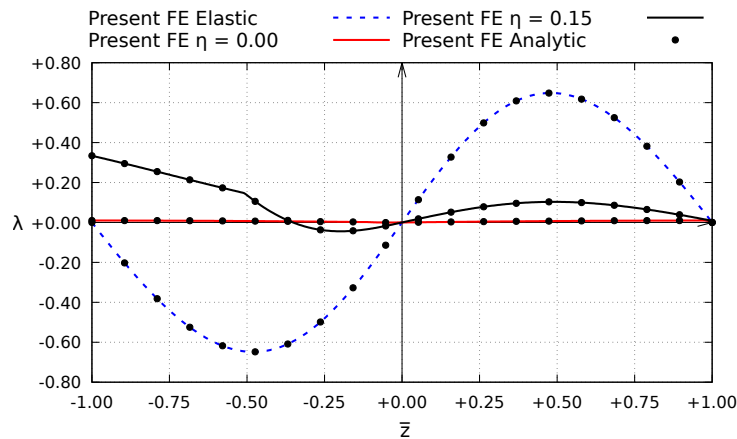
(b) $\alpha = 1.2$

Figure 2.22: Elasto-plastic equilibrium paths of the truss under vertical load (LSM).

2.4.3.5
Variation of the critical load with truss height

The goal of this section is the analytical calculation of how the critical load parameter λ_{cr} varies as a function of the geometric parameter α (i.e. the truss depth), for different instability phenomena and considering the QSM (for the sake of simplicity), using Eqs. (2-46), (2-51), (2-56) and (2-57). Figure (2.23) shows the limit point load parameter of the elastic truss, with a constant value of $2\sqrt{3}/9$ which corresponds to an upper bound of the critical loads.

For $\alpha \leq 1$, an unstable symmetric bifurcation occurs along the nonlinear equilibrium path, breaking the system symmetry. For $\alpha \leq \sqrt{2}B/(2\pi r_g)$ the compressive axial force in the elements cause them to buckle. With the chosen numerical parameters buckle will happen if $\alpha \leq 8.99$. Finally, for $\alpha \leq \sqrt{(1 - 2\varepsilon_y)/(2\varepsilon_y)}$, elasto-plastic deformation occurs. As α decreases, each instability phenomenon initially occurs along the unstable fundamental path until the critical value coincides with the limit point load, at which point the two phenomena occur simultaneously. For lower values of α the instability occurs for load values lower than $2\sqrt{3}/9$, thus reducing the load carrying capacity of the structure.

Which phenomenon first occurs depends on the geometric and material characteristics of the truss. In the vicinity of the crossing and tangent points between two curves, interactive buckling may occur, thus leading to a further decrease in the load capacity. For example, with $\alpha = 0.5$ the truss elements buckle, soon latter are subject to plastic deformations and then the system bifurcates through lateral instabilities. For $\alpha = 4$ the truss elements are first subject to plastic deformations and then buckle. For $\alpha = 16$ (very shallow truss) the system is subject only to snap-through.
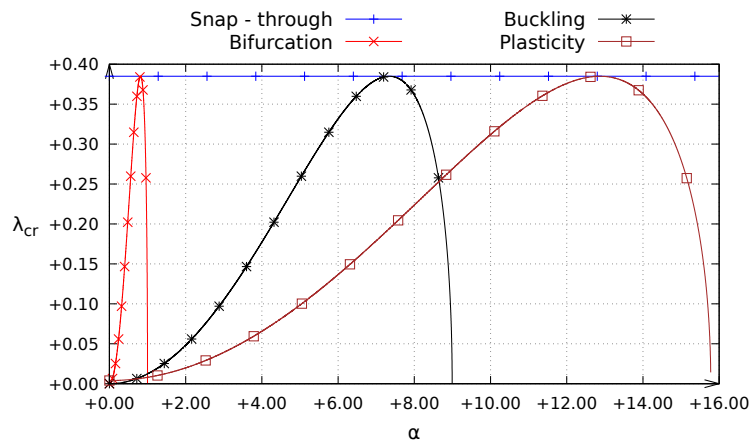
Figure 2.23: Variation of the critical load with the design parameter α (QSM).

2.4.4
Interactive buckling

In the previous sections elastic snap-through and bifurcation buckling, Euler buckling and material yielding were *considered individually*. However, in terms of the truss design, the decrease of load capacity due to the complex interaction between these phenomena is important [73, 74] in a broad range of the geometric parameter α, as observed in Fig. 2.23. Most of the studies on interactive buckling are in the field of elastic deformations [34]. However most

steel structures are designed in such a way that their strength limit lies in the elasto-plastic range. Thus, it is important to quantify the effects of plastic deformations in the case of interactive buckling [38].

Here the system stability and load capacity considering elasto-plastic buckling is investigated in a purely computational approach, being an original contribution to the state of the art, using a corotational fiber beam finite element (Appendix C). A small initial geometric imperfection on the beam straightness given by $e \sin(\pi x/L)$ (see Fig. 2.24a) is assumed in the simulations. The cross-section is discretized into 150 fibers, as illustrated in Fig. 2.24b, considering 30 and 5 angular and radial divisions, respectively. As the shallow trusses are studied in this Section the QSM is adopted in the analyses.

(a) Truss initial imperfection   (b) 30×5 mesh
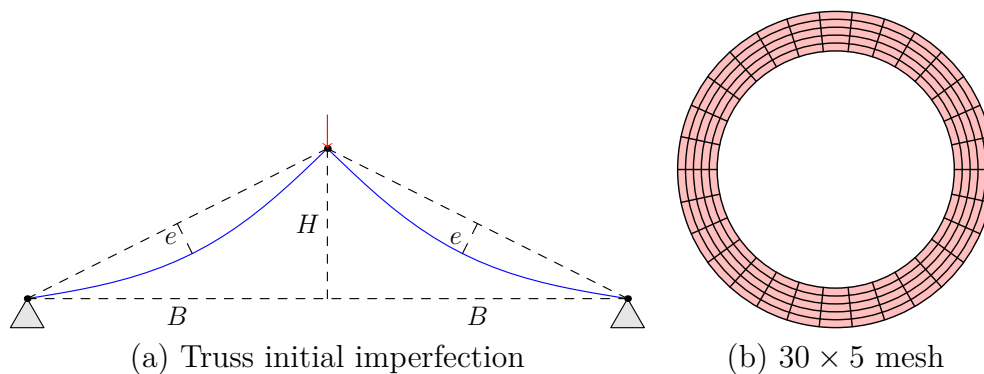
Figure 2.24: Initial geometric imperfections on the pyramidal truss and cross-section discretization.

From Eqs. (2-56) and (2-57), it is observed that at $\alpha = 8.65$ the Euler buckling load and the plastic buckling load are equal (Fig. 2.23). So, in the vicinity of this value the interaction between Euler buckling and material yielding is expected to be stronger. Figure 2.25 shows for $\alpha = 8.65$ the nonlinear equilibrium paths considering a range of values for the geometric imperfection e expected in real structures.

Geometric imperfections on the beam straightness of tolerable magnitude (i.e. acceptable manufacturing imperfections) introduce bending from the onset of loading. The imperfection magnitude is usually limited by design specifications and is normally given as a fraction of the length of the member. The decrease of load capacity intensifies with the initial imperfection magnitude, as also observed in the literature for pinned bars [75]. On the other hand, as the imperfection magnitude tends to zero (e.g. $e = L/10000$), the response converges asymptotically to the analytical elasto-plastic solution illustrated in Fig. 2.22.

Figure 2.26 shows the imperfection sensitivity curve for this geometry, where the limit point load of the imperfect structure is divided by the limit
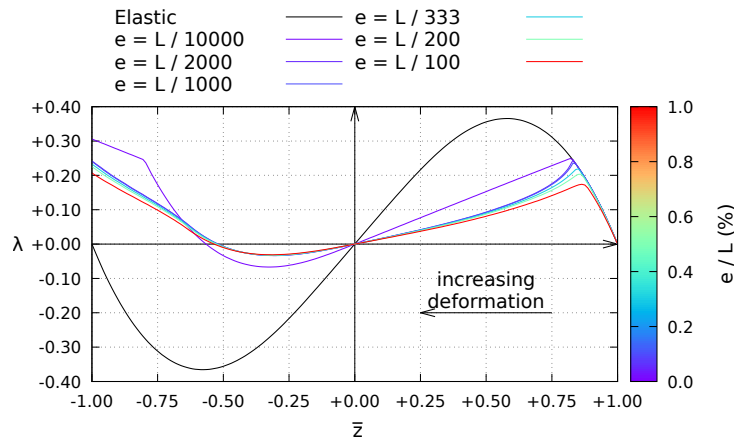
Figure 2.25: Influence of the initial geometric imperfection magnitude on the elasto-plastic response ($\alpha = 8.65$).

plastic load (Eq. 2-57). The load capacity is greatly reduced, even for small imperfections. The decrease of the limit point load is around 20% when the imperfection magnitude is 0.5% of the bar length L. In all cases the unloaded inverted configuration exhibits large permanent plastic deformations.
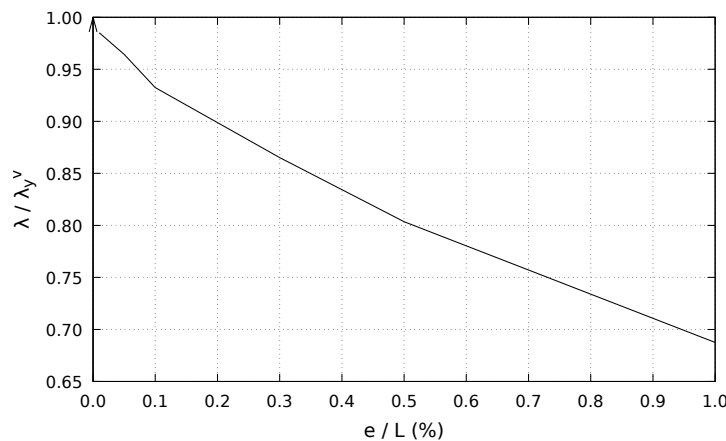
Figure 2.26: Influence of initial imperfection on the elasto-plastic limit load ($\alpha = 8.65$).

Figure 2.27 shows the influence of the geometric parameter α on the nonlinear response of the imperfect truss with $e = L/500$, which is the usual straightness tolerance for tubular members (p. 42 of [74]). For small α (deep truss) the interaction between the Euler and plastic buckling happens for low load levels, as expected. The buckling load increases with α until the limit load in the fundamental path is reached and the interactive buckling starts to happen after the snap-through.

Figure 2.28 shows the variation of the limit point load of the imperfect structure divided by the limit point load of the perfect elastic truss (Eq. 2-46) with $\alpha \in [6, 16]$ (see Fig. 2.23). In this interval, for $\alpha = 7.34$ the snap-
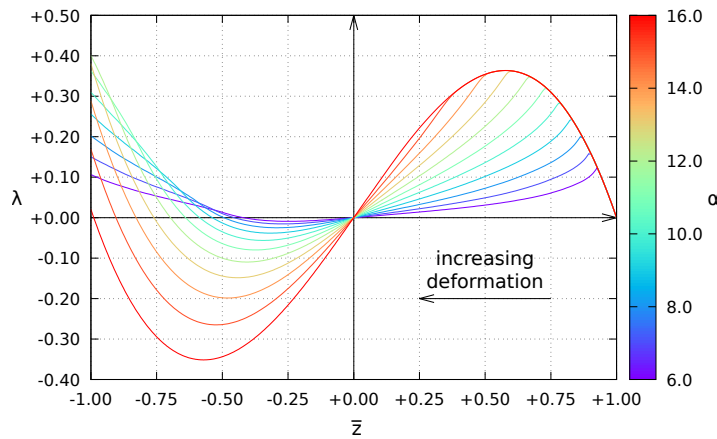
Figure 2.27: Influence of α on the elasto-plastic response ($e = L/500$).

through and Euler buckling load are equal, for $\alpha = 8.65$ the Euler and inelastic buckling occur simultaneously, while for $\alpha = 12.87$, the snap-through and inelastic buckling loads coincide. Thus in this interval the interaction among these three nonlinear phenomena is active.
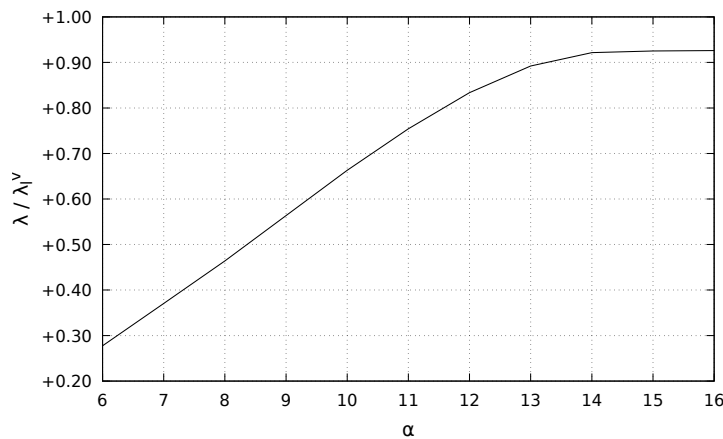
Figure 2.28: Influence of the geometric parameter α on the elasto-plastic limit load ($e = L/500$).

As α increases (the truss height and the length of the bars decrease) the limit point load increases and approaches asymptotically the limit point load of the imperfect elastic truss, which is 7% less than that of the perfect truss (for $\alpha = 16$ the buckling process occurs in the elastic regime). Again the interaction of Euler buckling and material yielding is quite significant. The critical load of the imperfect structure for $\alpha = 16$ is about 30% lower than the elastic limit point load of the perfect structure, $\lambda_l^v = 2\sqrt{3}/9$.

As α decreases, the beam length increases and for small values of α a pitchfork (symmetric) bifurcation occurs. As shown in Fig. 2.23, in this region, for imperfect trusses interaction between the pitchfork bifurcation, Eulerian buckling and material yielding may occur.

Figure 2.29 shows the nonlinear response of the truss for $\alpha = 0.90$ and $e = L/500$. This leads to a huge decrease in the load carrying capacity and increase in the declivity of the post-critical path (see inset figure) when compared with the elastic case (see Fig. 2.19). This indicates, according to the stability theory, high imperfection sensitivity [39].
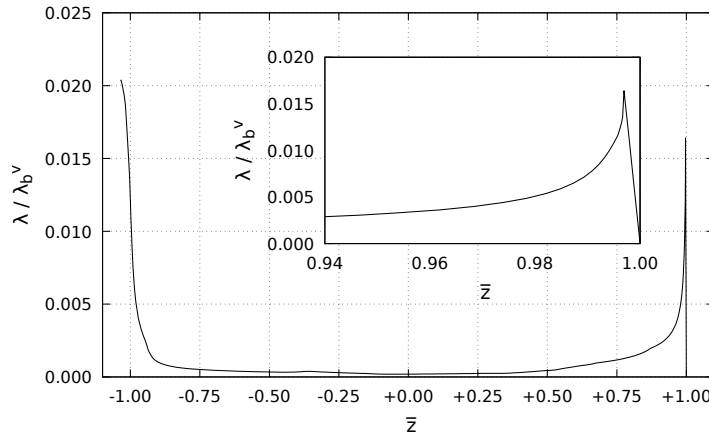
Figure 2.29: Interaction of the pitchfork bifurcation, Euler buckling and material yielding ($\alpha = 0.90, e = L/500$).

2.4.5
Incorporating flexible supports

In structures composed of pyramidal truss modules, the base nodes of each module are not rigidly fixed which affects the flexibility of the whole structure. The interaction between the modules is mainly governed by the forces transmitted through their bases. The influence of the base flexibility on the symmetric structural response is therefore important for the understanding of the behavior of large structural systems and a simplified model is set up here (uniform radial base displacement assumption).

In the numerical simulations, the base nodes are constrained to move in the radial direction by static condensation of the appropriate degrees of freedom. The more general case, with complex kinematics, could be treated through other numerical methods, such as Lagrange multipliers and penalization. The base nodes are considered to move by the same amount b for the sake of simplicity.

Figure (2.30) shows the fundamental equilibrium paths obtained for a selected range of values of the parameterized base stiffness $\overline{k}_b$. The pyramidal truss becomes a mechanism when $\overline{k}_b = 0$, representing a lack of the lateral constraint by the supports. As the base stiffness increases, the load capacity increases, approaching the fixed base solution as $\overline{k}_b$ tends to infinity.
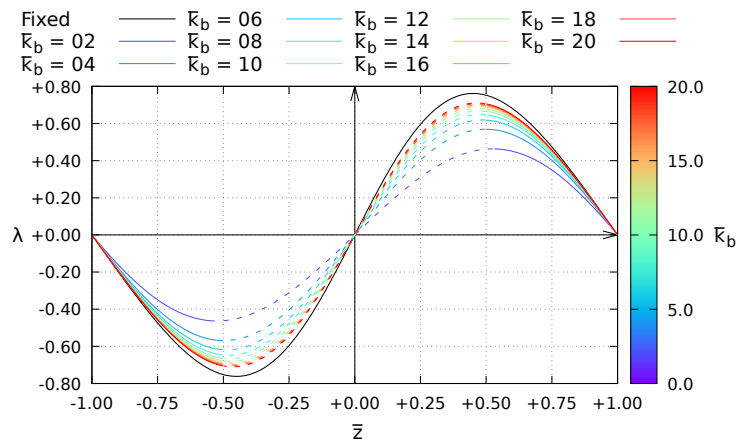
Figure 2.30: Influence of the base flexibility on the structural response ($\alpha = 1$).

The consideration of the flexibility of the supports, or equivalently the interaction with other modules through their base nodes, thus has a considerable influence on the truss load capacity and should be included in the design process.

2.5
Pyramidal curved truss

In this Section, to illustrate the nonlinear behavior of more complex structures, a large span structure composed of n pyramidal trusses in both directions (Fig. 2.31) is analyzed. The structure has a span of $L = 20.00$ m in both directions and an initial rise in the vertical direction, as observed in many practical applications, increasing its initial stiffness and load capacity. The rise is modeled as a parabola with a height h and the modules have a height H (both h and H are varied in a parametric study). The material of the elements is the same as adopted for the analysis of the pyramidal truss module (Tab. 2.1). The tubular cross section has a diameter $d = 35.6$ cm and a thickness $t = 2.5$ cm. The numerical parameters used in each analysis are summarized in Tab. 2.4. The truss is subjected to its self-weight, which is negligible compared to its load capacity. An additional vertical, uniformly distributed load q is applied on the top nodes. The nodes along the two straight sides are fixed. This example is for purely computational purposes, illustrating that the findings presented for individual modules appear on larger structures composed of the assembly of single pyramidal truss modules as well.
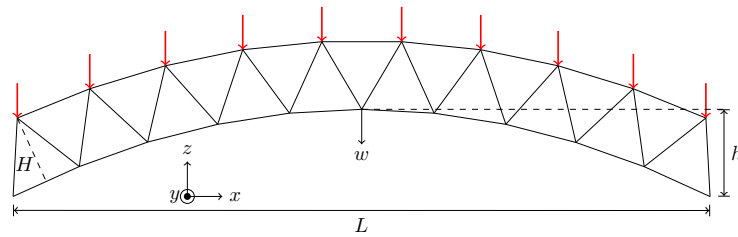
(a) Dimensions
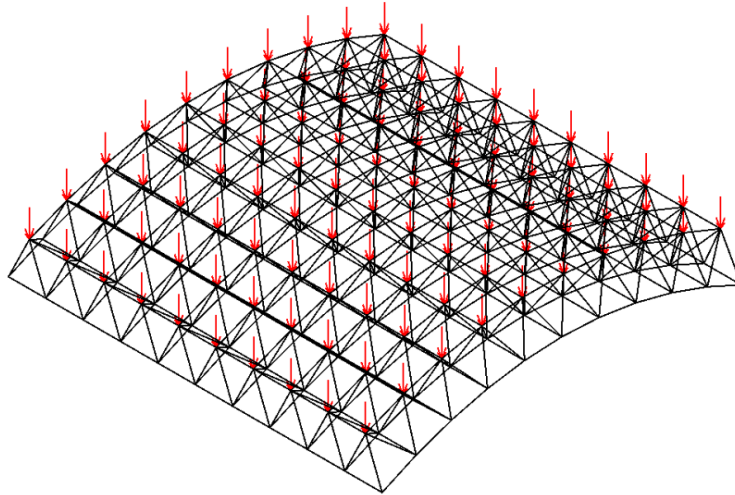
(b) Finite element model

Figure 2.31: Structure composed of pyramidal truss modules.

Section	Rise (h)	Units (n)	Height (H)	Load	Material behavior
2.5.1	vary	10	1.00 m	symmetric	elastic
2.5.2	1.25 m	vary	1.00 m	symmetric	elastic
2.5.3	1.25 m	10	vary	symmetric	elastic
2.5.4	1.90 m	10	1.00 m	asymmetric	elastic
2.5.5	1.25 m	10	1.00 m	symmetric	elasto-plastic

Table 2.4: Numerical parameters used in the FE analysis of the pyramidal curved truss.

2.5.1
Influence of the initial curvature

The effect of h, related to the initial curvature of the structure, is investigated taking $n = 10$ modules and $H = 1.00$ m. Figure 2.32 shows the results of the static nonlinear analysis considering a variable height h. For $h = 0.00$ m the initial stiffness and nonlinearity are small. The structure becomes stiffer as the rise h increases and the load capacity also increases. However, the nonlinearity of the structure is also more pronounced, and for $h \geq 0.50$ m a limit point appears. The load and displacement difference between the maximum and minimum limit points increases monotonously with h. Fig. 2.33 shows the deformed configuration after snap-through buckling. For

these geometries no Euler buckling is observed. The maximum compressive load increases with h and for $h = 1.25$ m it is equal to 152 MN while the corresponding Euler buckling load is equal to 165 MN.
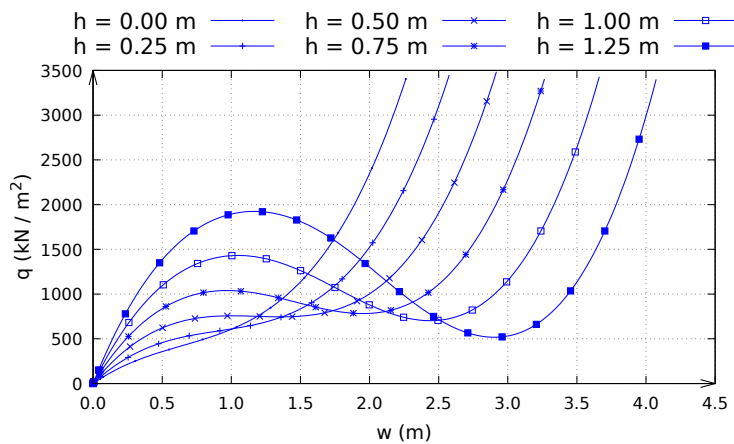
Figure 2.32: Influence of the initial curvature on the nonlinear structural response ($\alpha = 1.41$).
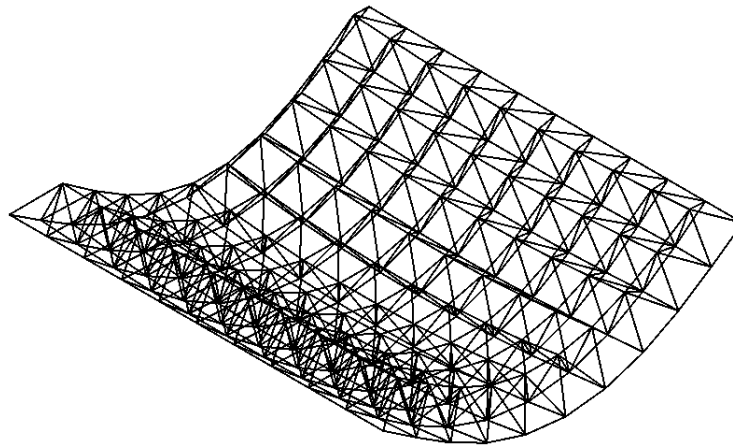
Figure 2.33: Structure final deformed configuration.

2.5.2
Influence of the number of modules

The effect of the number of pyramidal modules n is now studied considering a rise of $h = 1.25$ m and module height $H = 1.00$ m. Figure 2.34 shows the results of the static nonlinear analysis considering a variable number of units n. As the number of modules increases, the length of each individual bar is reduced, increasing the structure stiffness and load capacity, and better distributing the vertical load q on the apex nodes. The geometric parameter α of each unit also varies, altering their properties and consequently the system's structural behavior. Also, due to the length reduction, the Euler buckling load

of the bars increases and the system becomes less susceptible to this type of instability. For $n = 14$, the maximum compressive load is equal to 152 MN while the corresponding Euler buckling load is equal to 323 MN. For all values of n the truss displays a bistable behavior and the difference between the upper and lower limit loads increases with n.
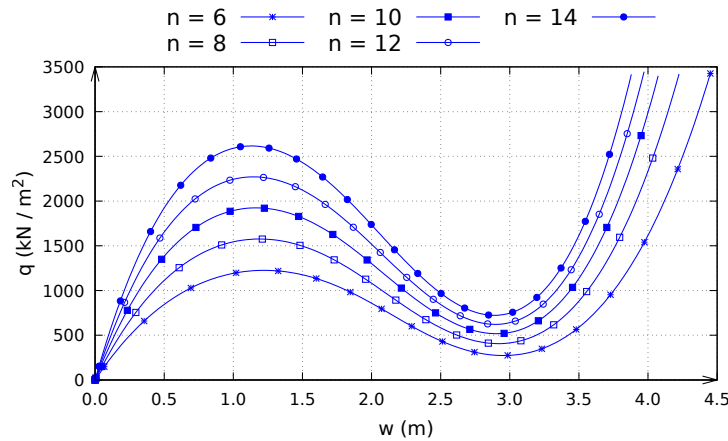
Figure 2.34: Influence of the number of modules on the structural response.

2.5.3
Influence of the modules height

The effect of the modules height H is now studied considering a rise $h = 1.25$ m and number of modules $n = 10$. Figure 2.35 shows the results of the static nonlinear analysis considering a variable modules height H. As the modules height increases, each individual module becomes stiffer, increasing the structural stiffness and load capacity. However, since the load is distributed among the same number of nodes, the bars axial force increases, while the Euler buckling load is reduced (due to longer elements) and the system becomes more susceptible to this local instability. For $H = 1.20$ m and $H = 1.40$ m Euler buckling occurs.

2.5.4
Influence of the load asymmetry

The effect of load asymmetry is now investigated by applying a symmetric and asymmetric distributed vertical load on the top nodes of the structure. The asymmetric load is modeled by increasing the symmetric one by 20 % on one half and decreasing it by the same amount on the other half of the structure, thus maintaining the total load constant. The structure has a rise $h = 1.90$ m, $n = 10$ modules in each direction with height $H = 1.00$ m. Figure 2.36 shows the results of the static nonlinear analysis. When subjected to the
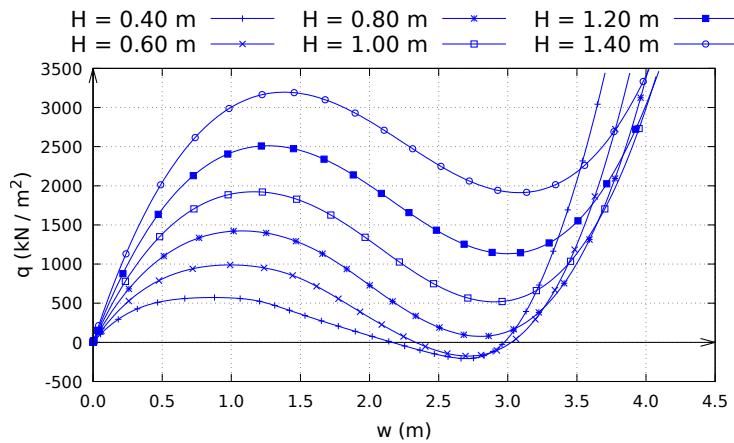
Figure 2.35: Influence of the modules height on the structural response.

symmetric load, the structure has a limit point load of $q = 4000\text{kN/m}^2$. For the asymmetric case, the maximum load is $q = 3570\text{kN/m}^2$, representing a reduction of 10.75 % of the system load capacity. The break of symmetry is illustrated by the system deformed configuration subject to symmetric and asymmetric loads (Fig. 2.37). Several load and displacement limit points are observed in the asymmetric case, showing a more complex response similar to the behavior observed in bistable shallow arches [32].
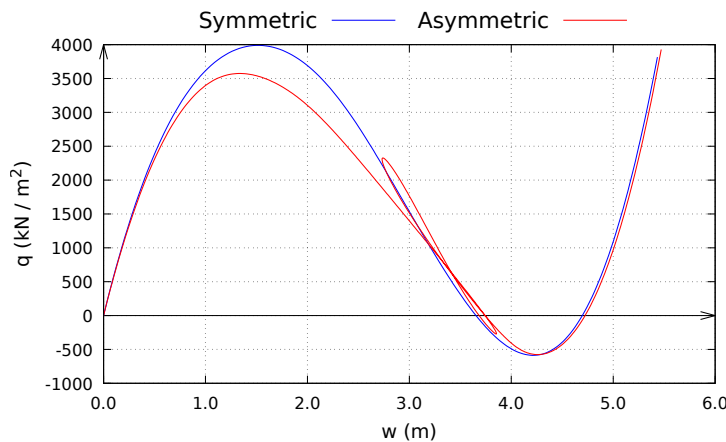
Figure 2.36: Influence of the load asymmetry on the structural response ($\alpha = 1.41$).

2.5.5
Influence of the material elasto-plastic behavior

The effect of the elasto-plastic behavior is now studied considering a rise of $h = 1.25$ m, $n = 10$ modules in each direction with a height of $H = 1.00$ m. The maximum yield stress of modern steels, depending on their composition, can approach 3000 MPa, while the elastic modulus remains practically constant ($E = 200\text{GPa}$). The first curve in Fig. 2.38 refers to a yield strength of 400MPa,

(a) Symmetric load
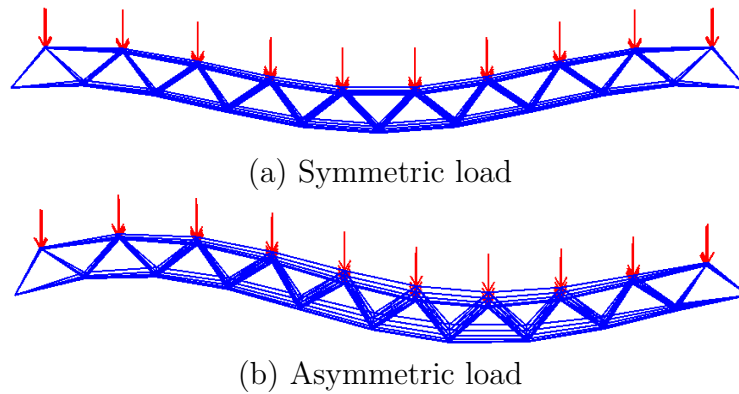
(b) Asymmetric load

Figure 2.37: Equilibrium configurations of the structure subject to symmetric and asymmetric loads ($\alpha = 1.41$).

while the second one to a yield strength of 2400MPa, which would correspond to an ultra-high-strength steel with yield strength between 1400 and 2400 MPa [76]. As expected, the plastic buckling load increases with the material yield strength, however at higher load levels the geometrical nonlinearity is more prominent, leading to a faster reduction of the post-yield system stiffness. As the deformation increases the two elasto-plastic curves approach one another. Even if a high yield strength (well above the maximum value used in most practical applications) is considered, a sharp reduction of the critical load is observed, converging to the structural response of conventional steel structures.
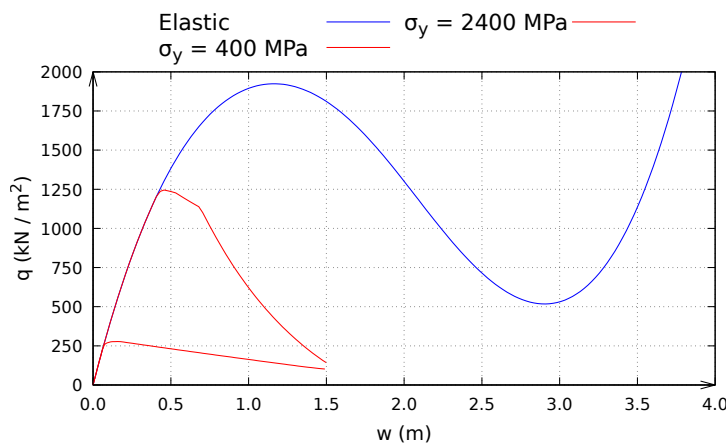
Figure 2.38: Influence of the material nonlinearity on the structural response ($\alpha = 1.41$).

2.6
Conclusions

In this chapter, nonlinear analyses of pyramidal trusses were carried out with emphasis on stability and load carrying capacity. In addition, novel analytical solutions were proposed and validated for the nonlinear equilibrium

paths, critical loads and natural frequencies of single modules considering both elastic and elasto-plastic behavior, Eulerian buckling and the flexibility of the base nodes. The FE results were favorably compared with the analytical results, validating the closed form approach.

For a truss under vertical or horizontal load, instability due to limit point and pitchfork bifurcations along the fundamental nonlinear equilibrium path as well as instability due to individual bar buckling and elasto-plastic behavior of the material was investigated. In each case, a parametric analysis was carried out to study the influence of the truss height to base ratio (shallowness parameter) on the structural behavior and load carrying capacity of the system.

For shallow structures, the instability was observed to be due to the existence of two limit points along the nonlinear equilibrium path, where an unstable path to an inverted position (snap-through buckling) occurred. For very shallow systems, this occurred in the elastic range. For deeper (non-shallow) structures, however, the fundamental equilibrium path was unstable before the structure reached the limit point and the truss lost stability through unstable symmetric bifurcation. The ensuing unstable secondary elliptical equilibrium path connects this critical point to its mirror inverted position. This bifurcation is associated to an asymmetric buckling mode. Again after reaching the bifurcation point the structure jumps to an inverted configuration.

Along both paths and along the unstable path the elements are subjected to high compressive axial forces, that can become greater than the Euler's buckling load of individual bars or the stresses may reach the material elastic limit, leading to an elasto-plastic nonlinear response. In such cases, the local instability of the bars and the plastic behavior of the material was observed to decrease substantially the load carrying capacity of the structure.

Analytical expressions in terms of the geometric and material parameters were obtained to define what type of buckling occurs.

The consideration of the flexibility of the base nodes led to a decreasing of the load capacity, as expected.

The influence of the interaction of snap-through instability, Eulerian buckling and plastic deformations on the imperfection sensitivity and load carrying capacity of the spatial truss was investigated using finite element simulations. The results showed that in a wide range of the shallowness parameter interactive buckling may occur, leading to further decrease of the load carrying capacity of the spatial truss.

A parametric analysis of a large span curved structure composed of several pyramidal truss modules was investigated. The structure exhibited a bistable behavior except for small rise values. The upper limit point load was

observed to increase with the initial curvature, number of modules and module height.

As it will be seen in Chapter 4, the mechanical properties of the joints connecting the beam elements (finite size, flexibility and friction) may have a considerable influence on the pyramidal truss load capacity and stability, inducing new buckling modes. In future works, an appropriate joint finite element should thus be included in the finite element simulations. The structural behavior of large span structural systems inspired from built design could be evaluated.

3
Dynamic analysis of bistable truss structures

3.1
Outline

In this chapter the nonlinear oscillations and dynamic instabilities of pyramidal truss modules under harmonic vertical load are investigated through bifurcation diagrams of the Poincaré map and phase-space projections of the relevant attractors. The effects of snap-through, lateral instabilities, material nonlinear behavior on the system dynamic response, as well as the influence of a static preload and initial conditions are investigated in the main resonance region. Detailed bifurcation analyses of structural systems are usually carried out using low order models (direct integration of equations of motion with a few degrees of freedom). Here, the proposed algorithm is part of the developed FE software (Appendices B and D) and permits to study the influence of the parameters investigated in the static buckling analysis on the nonlinear oscillations of the pyramidal truss under harmonic load.

The chapter is organized as follows: in Section 3.2 a review on the dynamic behavior of pyramidal trusses is presented, together with the main goals in this work. A novel closed form solution for the unloaded elastic symmetric orbits is proposed is Sec. 3.3. The computational procedure used in the numerical simulations is presented in Sec. 3.4. The dynamic nonlinear behavior of shallow trusses is investigated in Sec. 3.5. Section 3.6 considers the response of shallow trusses subject to a static preload. In Section 3.7 the lateral instabilities of deep trusses are investigated, and an elasto-plastic material response is incorporated in Sec. 3.8. The elastic and elasto-plastic bifurcation diagrams of the system (showing the variation of the vibration amplitude as a function of the excitation frequency) are traced in Sec. 3.9. The influence of the initial conditions on the dynamic response is investigated in Sec. 3.10. Finally, the main conclusions of this chapter are drawn in Sec. 3.11. [1]

[1]The contents of Chapters 2 and 3 are a convolution of two manuscripts submitted for publication to *International Journal of Solids and Structures* and *Nonlinear Dynamics*.

3.2
State of the art on dynamic modeling of pyramidal trusses

Pyramidal truss modules or large span structures formed by their assembly are often subject to dynamic external loads such as wind, earthquakes, machinery and/or moving loads (traffic). The resulting nonlinear oscillations may include dynamic instabilities and elasto-plastic deformations, being a concern for design safety.

The bistable nature of pyramidal trusses allows for multiple equilibrium configurations for a given static load level, as shown in Chapter 2. Similarly, multiple dynamic responses (coexisting solutions) may appear for the same dynamic load level as a result of different load sequences. The response may suffer a *period-multiplying cascade* (oscillate with a period that is a multiple of the excitation period) or present a *chaotic* (non-periodic) behavior. These phenomena can be considered undesirable, because they make the design process extremely complex and hinder obtaining a controlled motion of the system. The presence of coexisting solutions make the system response non deterministic and may turn the design process very complex or even nonviable with simple approaches.

The dynamic nonlinear behavior of pyramidal trusses has been studied in the literature restricted to an elastic material response and moderate strains (quadratic strain measure). Castro [15] and Orlando et al. [16] deduced the nonlinear equations of motion for this system under vertical harmonic excitation and studied through bifurcation diagrams, phase space projections, time responses and basins of attraction the complex dynamics of shallow elastic pyramidal trusses, while Orlando et al. [17] studied the influence of transient escape and added load noise on the dynamic integrity of multistable systems.

Previous predictions of the elastic pyramidal truss dynamic behavior show a predominant period-doubling cascade or chaotic behavior. Considering the elasto-plastic material behavior (a new contribution to the state of the art, developed in this chapter), a considerable portion of the energy introduced in the system by the external harmonic excitation may be dissipated in the oscillations due to plastic deformations, critically influencing the dynamic response.

The analysis of the nonlinear vibrations and dynamic bifurcations of elasto-plastic reticulated structures has not yet been investigated extensively in the dedicated literature. It is well known that nonlinear dynamic phenomena are strongly dependent on the characteristics of the oscillator restoring force (internal forces in the elements as a response to external excitations). However, as pointed out by Palmov [77], unjustifiably little attention is paid in the

vast literature on the free and forced vibrations of elasto-plastic bodies, in particular the nonlinear vibrations of structures involving material and geometrical nonlinearities. Among the earlier contributions in this field, Pratap et al. [78, 79, 80] studied the nonlinear free and forced oscillations of a bilinear hysteretic elasto-plastic oscillator with kinematic hardening. The forced response is particularly complex, as the motion undergoes numerous bifurcations, from periodic to quasi-periodic to chaotic motions. Later, Pratap and Holmes [81] studied the local and global dynamic behavior of a single degree of freedom parametrically excited elasto-plastic oscillator. Gerstmayr and Irschik [82] presented a numerical strategy for vibrations of elasto-plastic beams. Liu and Huang [83] investigated the steady state responses of a SDOF viscous elasto-plastic oscillator under sinusoidal loading. They also derived the maximum driving force amplitude to avoid oscillations in the plastic range. Challamel and Gilles [84] studied the stability and the dynamics of a harmonically excited elastic-perfectly plastic oscillator, with the hysteretic system described as a non-smooth forced autonomous system. Kalmár-Nagy and Shekhawat [85] analyzed the transient and steady-state response of an oscillator with hysteretic restoring force under sinusoidal excitation. The elasto-plastic nonlinear vibrations analysis of beams and columns was conducted by Karagiozov and Karagiozova [86], Savi and Pacheco [87], Ribeiro and van der Heijden [88], Ribeiro [89] and Grognec et al. [90]. In a related area, Lacarbonara and Vestroni [91] investigated the responses and codimension-one (1D subsets) bifurcations in Masing-type and Bouc–Wen hysteretic oscillators. Bifurcations, including jump phenomena, symmetry-breaking, complete period-doubling cascades, fold, and secondary Hopf were obtained.

To the author's best knowledge there is currently a lack of knowledge regarding the dynamic behavior of pyramidal trusses subject to large elasto-plastic deformations. In particular, no experimental results concerning pyramidal trusses subject to extreme loads were found. The goal of this work is thus investigate numerically the influence of the finite strain measure and geometrical and material parameters on the nonlinear elasto-plastic oscillations of pyramidal truss modules.

To better understand its fundamental dynamic characteristics, novel analytical expressions for the phase plane orbits of the unloaded elastic symmetric system are proposed and discussed in this work, allowing the identification of the boundaries between stable and unstable oscillations.

For deep trusses subject to moderate or large loads the quadratic and logarithmic strain measures differ considerably (as shown in chapter 2), in-

fluencing the characteristics of the dynamic response in terms of vibration amplitude, period, chaotic behavior and stability. Their comparison is done in the dynamic regime here using closed for expressions and numerical simulations. Subsequently, the influence of finite elastic and elasto-plastic strains on the snap-through and lateral instabilities are investigated computationally making use of the logarithmic strain measure (LSM).

Although the material stiffness decreases in the elasto-plastic regime, the energy dissipation may be a dominant factor, reducing the oscillations amplitude and eliminating the domains with chaotic behavior and period cascades. The influence of the material elasto-plastic behavior on the nonlinear forced vibrations constitutes a novel contribution of practical significance since most metal bistable structures may exhibit elasto-plastic behavior due to large amplitude resonant vibrations and escape from the pre-buckling potential well.

Dynamic loads in civil engineering applications, such as wind and earthquake, are usually not harmonic but exhibits broadband frequency spectrum and may act in different directions. In the present work, only a vertical harmonic nodal load is considered for the sake of simplicity.

3.3
Unloaded elastic symmetric phase planes through analytical solution

Some insight on the pyramidal truss module dynamic behavior can be obtained by tracing its *phase space*, which are geometric regions describing the evolution of state variables of the system with respect to time. In this section, the phase planes of the pyramidal truss considering the apex node nondimensional vertical velocity ($\dot{z}/\omega_0$) and position ($\overline{z}$) are traced for the unloaded elastic system assuming symmetric oscillations ($\overline{r} = 0$). To this end, a novel closed form expression describing the topology of the phase plane is developed.

With no horizontal movement assumed for the apex node, all bars have the same length ($l = \sqrt{z^2 + B^2}$) and are subject to equal elastic strains ε. As there are no external loads or damping considered, the system mechanical energy $T + U$ is conserved, hence:

$$T + U = T_0 + U_0 \tag{3-1}$$

$$\frac{n\rho AL}{6}\dot{z}^2 + \frac{nEAL}{2}\varepsilon^2 = \frac{n\rho AL}{6}\dot{z}_0^2 + \frac{nEAL}{2}\varepsilon_0^2 \tag{3-2}$$

Dividing the above equation by the factor $nEAL/2$ the following nondi-

mensional form is obtained:

$$\left(\frac{\dot{\bar{z}}}{\beta^2\omega_0}\right)^2 + \varepsilon^2 = \left(\frac{\dot{\bar{z}}_0}{\beta^2\omega_0}\right)^2 + \varepsilon_0^2 = A_0^2 \tag{3-3}$$

where A_0 is a nondimensional constant energy level, which is a function of the initial conditions $(\bar{z}_0, \dot{\bar{z}}_0)$ and the choice of the strain measure $\varepsilon_0 = \varepsilon(\bar{z}_0)$.

From Eq. (3-3) the *orbits* (curves on the phase plane) can be parameterized making use of a dummy variable ψ as:

$$\varepsilon = A_0 \cos(\psi) \tag{3-4}$$
$$\dot{\bar{z}} = \omega_0 \beta^2 A_0 \sin(\psi) \tag{3-5}$$

The nondimensional vertical position $\bar{z}$ can be obtained from the strain measure definition. The inverse of Eqs. B-17 and B-18 provides the following parametrization for the QSM and LSM, respectively:

$$\bar{z}_q = \pm\sqrt{1 + 2\beta^2 A_0 \cos(\psi)} \tag{3-6}$$
$$\bar{z}_l = \pm\sqrt{\beta^2 \exp\left[2A_0 \cos(\psi)\right] - \alpha^2} \tag{3-7}$$

The phase plane with orbits on different energy levels, A_0, are plotted in Fig. 3.1 with $\alpha = 1.0$ ($H = B$), where the black dots represent the stable ($\bar{z} = \pm 1$) and unstable ($\bar{z} = 0$) *fixed points* (static equilibrium positions). In a linear system, the phase plane would consist of concentric ellipses, with the center representing the single attractor. The bistable nature of the pyramidal truss considerably alter the topology of the orbits. For low energy levels, the pyramidal truss oscillates around either the original ($\bar{z} = +1$) or inverted ($\bar{z} = -1$) stable configurations. Points like this, to which the system oscillations approach or are bounded to, are named *attractors*. As the energy level increases, the orbits eventually cross the origin (unstable fixed point) and the system oscillates around the two stable configurations.

The region in which the system oscillations around the original stable attractor are bounded by the homoclinic orbit associated with the saddle (unstable configuration) is called *pre-buckling well*. The second region, associated with the inverted truss position, also bounded by a homoclinic orbit of the saddle is called *post-buckling well*. The boundary of this region (the homoclinic orbits) can be determined by selecting the orbit that passes by the saddle, and so the corresponding energy level is obtained form Eq. (3-3) as $A_p = -\varepsilon(0)$. The minus sign is chosen as the bars are subject to compression when the apex node is located in the base plane. For the QSM and LSM, the corresponding
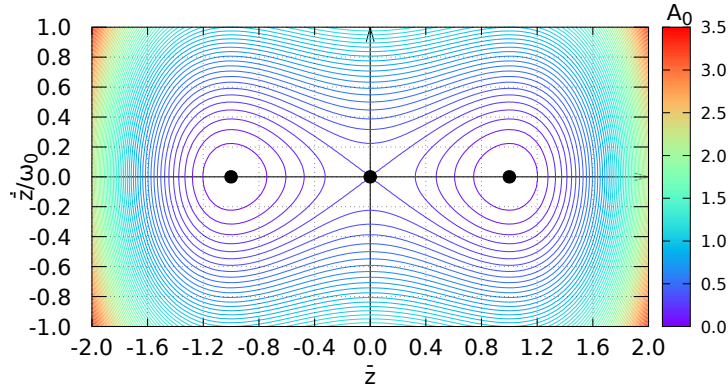
(a) QSM
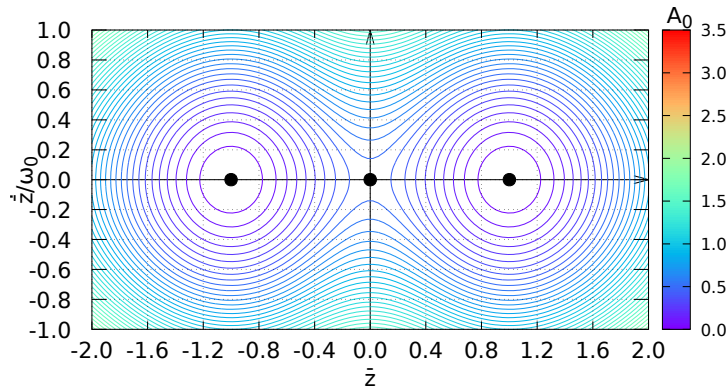
(b) LSM

Figure 3.1: Phase planes for different non-dimensional energy levels of the unloaded elastic pyramidal truss ($\alpha = 1.0$).

energy levels are given by, respectively:

$$A_{p,q} = \frac{1}{2\beta^2} \tag{3-8}$$

$$A_{p,l} = \ln\left(\frac{\beta}{\alpha}\right) \tag{3-9}$$

The pre-buckling well for both strain measures is illustrated in Fig. 3.2. As can be observed, with $\alpha = 1.0$ the truss is subject to large strains while oscillating and so the results with the two strain measures differ considerably. The LSM provides a larger domain, meaning that the QSM over-constrain the limit displacements and velocities that causes the system to pass by an unstable point and oscillate around the two attractors.

For elastic nonlinear dynamic problems, energy conserving integration methods are available in the literature. Although the conservation of energy is not considered in nonlinear solvers presented in App. D.2, the selection of an appropriate time step ensures the precision of the computational results.

Whenever possible, the obtained numerical results were compared favorably with derived closed form time solutions, validating them.
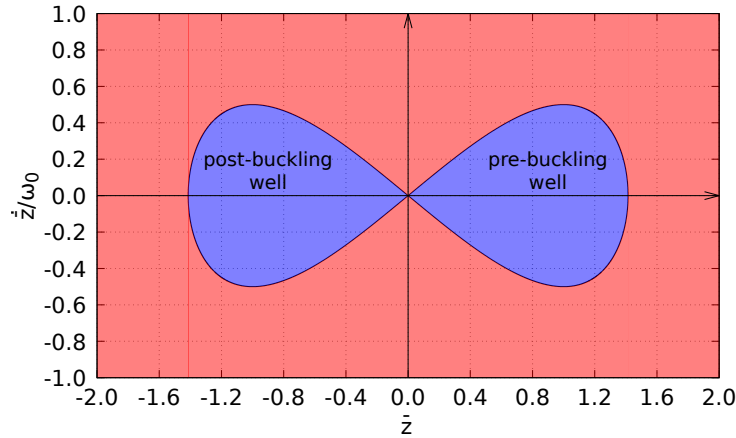
(a) QSM
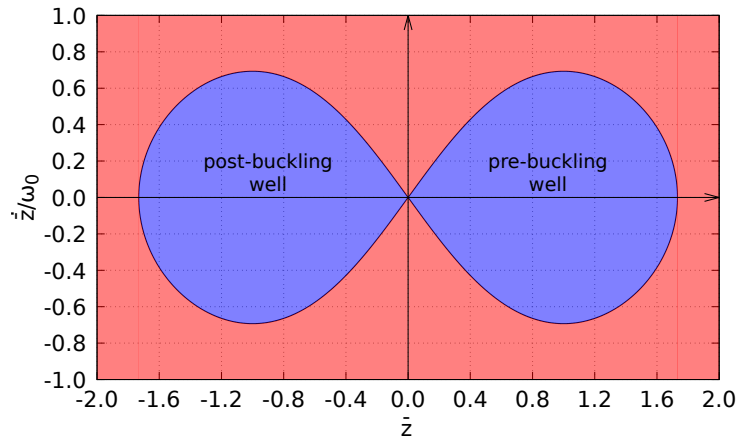
(b) LSM

Figure 3.2: Pre-buckling and post-buckling wells of the unloaded elastic pyramidal truss ($\alpha = 1.0$).

3.4
Computational FE model

The assumption is made that a single pyramidal truss module is subjected to a vertical external harmonic force given by $P\sin(\omega t)$, where P is the force magnitude and ω is the excitation frequency (Fig. 3.3). The same geometrical and material parameters of the pyramidal truss module from Sec. 2.4 are used here (Tab. 2.1). The bifurcation diagrams (variation of the vibration amplitude with respect to P or ω) are obtained by a brute force method. For each increment or decrement of the control parameters (P or ω), the stable fixed points coordinates of the Poincaré map (intersections of the periodic orbits with specific Poincaré sections taking fixed P and ω values) are computed using the finite element method [92] with one element per bar and taking the

base nodes fixed. The structural response is computed using a given set of initial conditions and values for the parameters P or ω.

The analysis is performed using the nonlinear finite element truss formulation developed in Appendix B, and either the Newmark (Sec. D.2.1) or the 4th order Runge-Kutta (Sec. D.2.2) solution methods are applied for the time integration of the equations of motion. In the algorithm, at each step, the bar strains are computed as a function of the nodal positions, and the stresses are updated through the material constitutive law using the last equilibrium configuration as reference (updated Lagragian formulation). A viscous damping equal to 4.0% of the critical value of the unloaded structure is considered in the analyses. Although this value is an overestimation for steel structures (usually 0.5%), it reduces considerably the computational cost involved in obtaining the bifurcation diagrams. Also, this value has been suggested for structures undergoing large elasto-plastic deformations [93]. Each time integration operation consists of $n_p = 40$ periods, of which $n_d = 10$ are discarded as transient response (Fig. 3.4a). For the remaining periods (steady state solution), the Poincaré map is recorded after every excitation period. In each excitation period $n_t = 500$ time integration points are used, summing up to a total of $n_s = n_p n_t = 2 \times 10^4$ time steps. In all simulations, one finite element per bar is used. As the use of the LSM requires the computation of the logarithmic function, the computational cost is much higher in the dynamic nonlinear simulations if compared with the QSM, which only requires the computation of polynomial functions. In the performed simulations, the computation time was in some cases five times larger.

To obtain a clear understanding of the bifurcation scenario and to identify coexisting solutions, the control parameter (load P or frequency ω) is separately incremented to a maximum value and subsequently decremented to its initial value in $n_m = 2000$ steps (Fig. 3.4b) yielding a good compromise between accuracy and computational cost. At each control parameter ramping the dynamic structural response for n_p periods of the harmonic excitation is computed. With fixed geometrical and material parameters of the pyramidal truss, one bifurcation map requires n_m dynamic nonlinear finite element simulations. The numerical tools used in each section are summarized in Tab. 3.1.

3.5
Dynamics of elastic shallow trusses

A pyramidal truss under a vertical harmonic force $P\sin(\omega t)$ with $\alpha = 1.20$ (shallow truss) and a fixed non-dimensional load frequency parameter
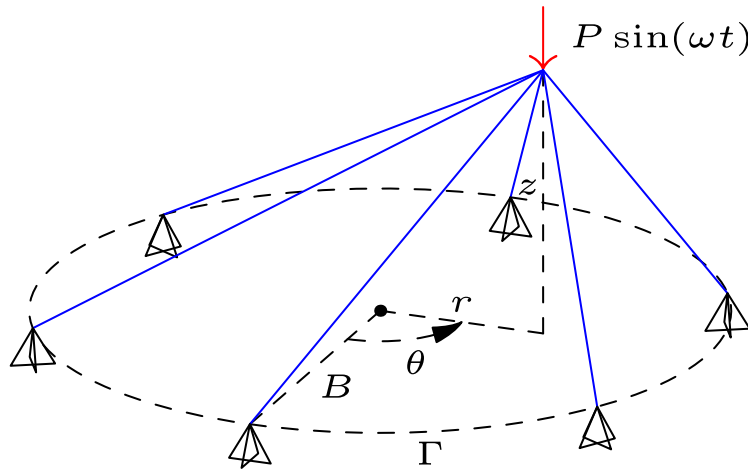
Figure 3.3: Pyramidal truss subject to a vertical harmonic load.
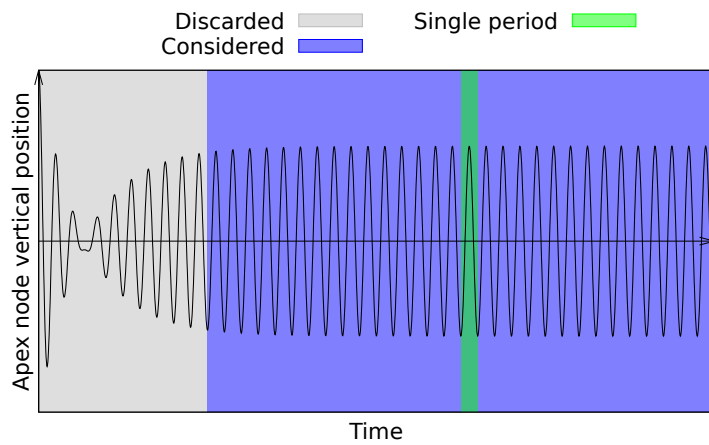
(a) Time response for a fixed value of the control parameter
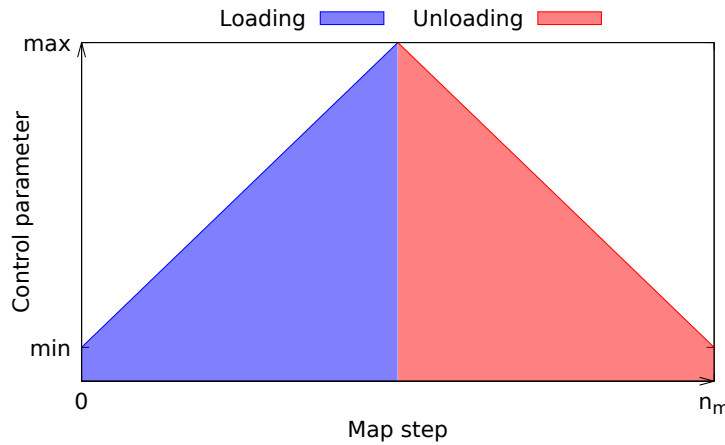
(b) Control parameter variation

Figure 3.4: Control parameter variation and time response on the brute force method.

$\overline{\omega} = \omega/\omega_0 = 1.00$ is considered first. This choice puts the simulations in the critical main resonance region, where the largest oscillation amplitudes are expected. The non-dimensional force magnitude parameter $\overline{p}_z = P/p_z$ is the

Section	Control Parameter	Strain measure	Material behavior
3.5	load (P)	QSM and LSM	elastic
3.6	load (P)	QSM and LSM	elastic
3.7	load (P)	LSM	elastic
3.8	load (P)	LSM	elasto-plastic
3.9	frequency (ω)	LSM	elasto-plastic

Table 3.1: Numerical tools used in the dynamic analysis of a single pyramidal truss module under vertical load.

control variable, and both strain measures ($\varepsilon_q = (l_k^2 - L^2)/(2L^2), \varepsilon_l = \ln(l_k/L)$) are considered and compared here with a purely elastic material behavior.

For the QSM (Fig. 3.5a), starting from the unloaded equilibrium position, $\overline{z} = 1.00$ (solution in blue), the shallow truss first exhibits a period one (i.e. has the same period as the excitation) small amplitude solution with increasing amplitude. Initially, the vibration of the system occurs in the pre-buckling well, i.e. around the initial configuration. At $\overline{p}_z = 0.32$ it undergoes a period doubling bifurcation (with a period two times that of the excitation) and at $\overline{p}_z = 0.36$ the response escapes from the pre-buckling well, and the truss exhibits large cross-well motions, passing by the initial and inverted configurations. In this region, chaotic and periodic motions with different periods are observed. At $\overline{p}_z = 0.68$ only a period one large amplitude response is observed up to $\overline{p}_z = 1.00$. This is the same response as obtained for the load magnitude decrease (unloading process, in red). This response remains up to $\overline{p}_z = 0.32$, where a *dynamic jump* (discontinuity on the bifurcation diagram) to the original period one small amplitude oscillation within the pre-buckling well is detected, as a consequence of a saddle-node bifurcation. The response converges to the initial truss position ($\overline{z} = 1.00$) as the load is ramped to zero. The system dynamic response with different load sequences varies considerably, showing the existence of multiple solutions.

For the LSM (Fig. 3.5b), the structure exhibits initially a period one solution with increasing amplitude up to $\overline{p}_z = 0.41$, where a period doubling bifurcation occurs, and at $\overline{p}_z = 0.44$ the response escapes from the pre-buckling well. Compared to the QSM, similar to the static case (Fig. 2.15), there is an increase of 28% in the period doubling bifurcation load and of 22% in the escape load (the force magnitude required to escape from the pre-buckling well). After escape, the bifurcation sequence associated with the two strain measures are completely different, as expected, since after escape the truss enters the large deformations domain. For the LSM three chaotic regions are observed preceded by different bifurcation sequences. As in the previous case, upon decreasing the load, the response converges to the initial truss configuration.

The dynamic response also varies with the loading sequence, as a result of coexisting solutions.
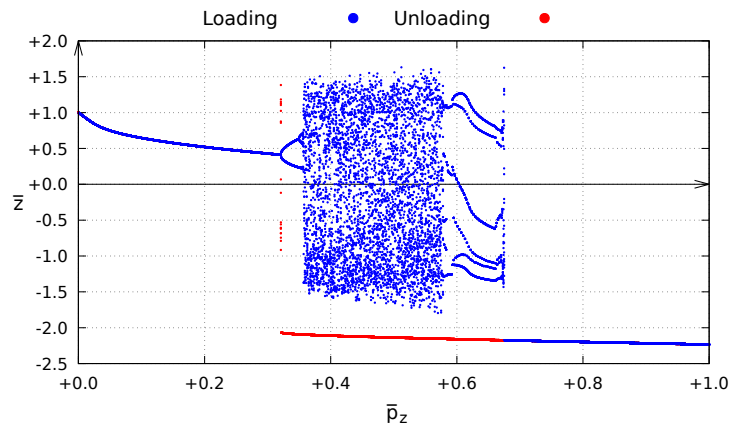
(a) QSM
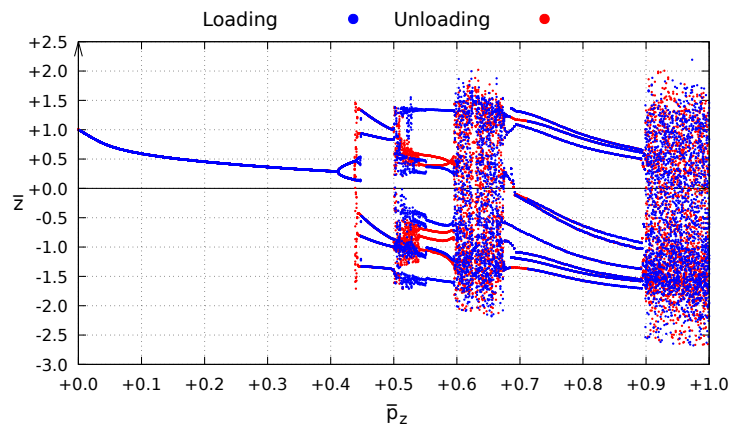
(b) LSM

Figure 3.5: Influence of the adopted strain measure on the bifurcation diagram of the Poincaré map for $\alpha = 1.2$.

To illustrate the influence of the strain measure on the elastic solution, Fig. 3.6 shows phase plane projections of some of the attractors for $\bar{p}_z = 0.1$ and $\bar{p}_z = 0.8$. The strain measure influences not only the magnitude but also the period of the steady state solution. For $\bar{p}_z = 0.1$ the maximum vibration amplitude and velocity using the LSM is higher than the same values obtained for the QSM and the inverse occurs for $\bar{p}_z = 0.8$. In this latter case, the QSM response has the same period as the excitation while the LSM response is subject to a period-doubling cascade.

When considering a *very shallow truss* ($\alpha = 8.0$) practically the same bifurcation sequence is observed for both strain measures (Fig. 3.7). This result is expected, since very shallow trusses are usually subjected to small strains, a regime in which all strain measures yield similar responses. The only difference occurs during unloading; after the jump at $\bar{p}_z = 0.32$ the QSM and

(a) $\overline{p}_z = 0.1$

(b) $\overline{p}_z = 0.8$
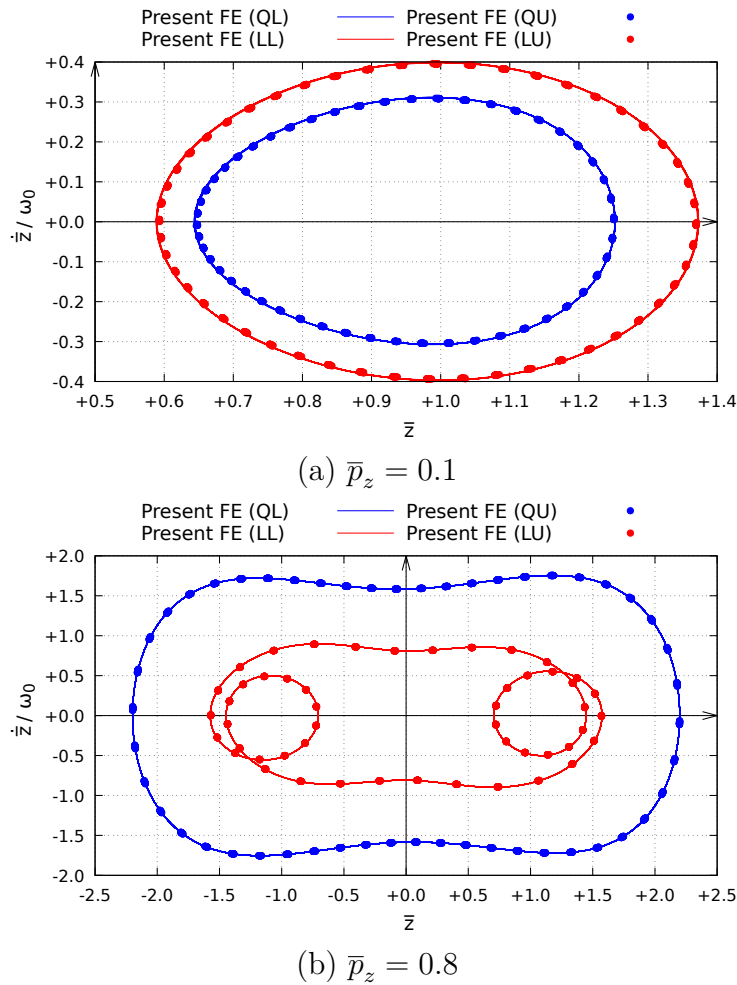
Figure 3.6: Influence of the adopted strain measure on the steady-state solution for $\alpha = 1.2$. QL: QSM, loading; QU: QSM, unloading; LL: LSM, loading; LU: LSM, unloading.

LSM solutions converge to different attractors. Note that due to the symmetry of the potential function of the unloaded system with respect to $\overline{z} = 0$ (see Fig. 2.3 and Fig. 2.5), a mirror image of this bifurcation diagram is obtained [16] starting at the inverted initial configuration $\overline{z} = -1.0$. Thus, for small values of $\overline{p}_z$ up to the escape load, these two branches of in-well solutions coexist, leading to mirror *basins of attraction* (region of influence of an attractor in the phase-space) [16].

3.6
Influence of static preload on the response of elastic shallow trusses

All civil engineering structures in a dynamic environment are subjected to a static preload (self-weight, loads from other structural components, among others). The magnitude of this preload varies from case between applications and may influence in the dynamic response (specially for high preloads). This
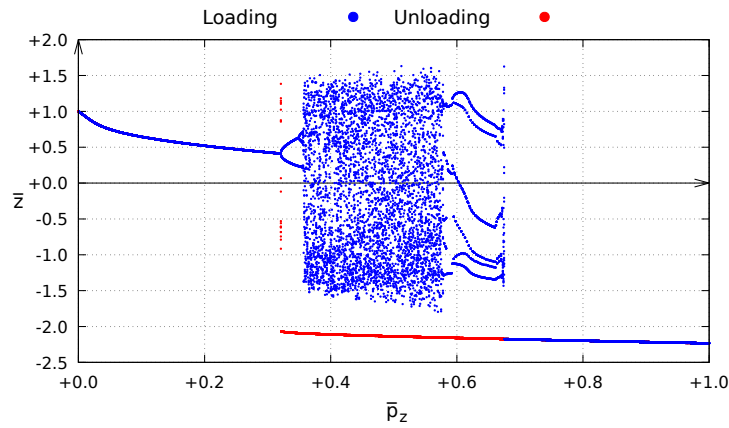
(a) QSM
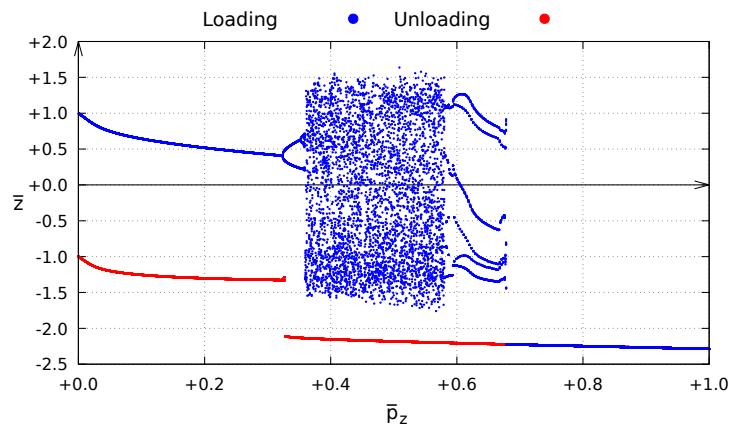
(b) LSM

Figure 3.7: Influence of the adopted strain measure on the bifurcation diagram of the Poincaré map for $\alpha = 8.0$.

effect is investigated in this section. Figure 3.8 shows the bifurcation diagram of the elastic truss of Sec. 3.5 ($\alpha = 1.20$) considering a static preload $\bar{p}_s = 0.6\lambda_{l,m}$ (Eq. 2-43), i.e. 60 % of the static snap-through limit load. This value is selected because a preload close to $\lambda_{l,m}$ would cause the system to jump directly to the inverted configuration, not allowing it to vibrate in the pre-buckling well. Additionally, considering such a high preload would not be realistic for civil engineering applications. All results in the following were obtained using the LSM only, as it is a more realistic strain measure and better represents the elastic and elasto-plastic material constitutive behavior (App. B).

Comparing these results to the structure without static preload (Fig. 3.5b), it can be observed that the chosen static preload has a large influence on the dynamic buckling load even though the same bifurcation sequence is observed to lead to the escape from the pre-buckling well. After escape a completely different bifurcation sequence is obtained: first the structure jumps to a small amplitude period one oscillation within the post-buckling well (the

post-buckling well is much deeper and broader than the pre-buckling one [16], resulting in a more prominent chaotic behavior), which undergoes a period doubling bifurcation at $\bar{p}_z = 0.51$ and is followed by a broad window of large amplitude chaotic cross-well motions. After unloading the structure converges to the inverted equilibrium position.

Thus the influence of static preload can be determinant in the truss dynamic behavior and increases with its magnitude. A special care should be thus taken in a through design process to verify whether its influence has to be incorporated.
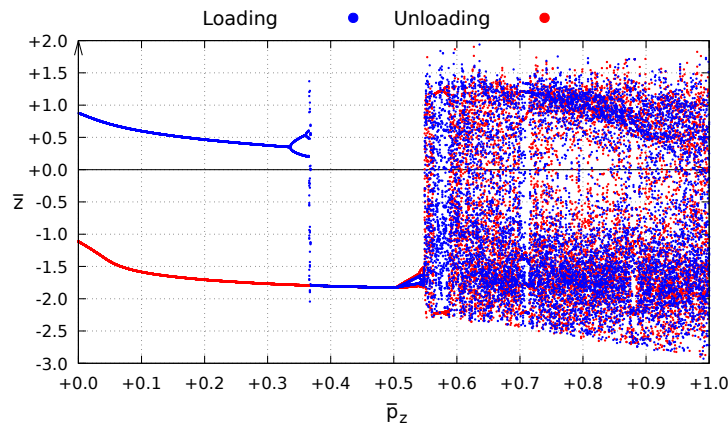
Figure 3.8: Bifurcation diagram of the statically pre-loaded system ($\alpha = 1.20$).

3.7
Dynamics of elastic deep trusses

The dynamic behavior of deep trusses can differ considerably from shallow ones since these structures can be subject to large strains, as observed in Chapter 2. Also, as the axial compressive force in the truss elements increase with the pyramid depth, lateral instabilities may appear and influence the dynamic response of the system. As show in Sec. 2.4.3.2, for a static vertical load, the elastic truss is subject to this type of buckling if $\alpha < 0.5092$ (with the LSM). The following analysis is carried out with $\alpha = 0.50$ to incorporate this effect. The results for the coordinates $\bar{z}$ and $\bar{r}$ of the fixed points of the Poincaré map are shown in Figs. 3.9(a) and Fig. 3.9(b), respectively.

Both in the loading and unloading cases only symmetric responses are obtained for $\bar{p}_z < 0.55$. At $\bar{p}_z = 0.55$ the dynamic response becomes asymmetric ($\bar{r} \neq 0$, i.e. a horizontal displacement component of the apex node appears) as the load increases due to a period doubling bifurcation, followed by a period-doubling cascade up to a chaotic region starting at $\bar{p}_z = 0.82$.

Upon unloading (in red) a rather different bifurcation sequence is observed, indicating the presence of coexisting solutions in a broad range of the load magnitude. Fig. 3.10 illustrates the symmetric responses detected previous to the period-doubling bifurcation. For $\bar{p}_z = 0.40$ only one attractor is observed during the loading and unloading sequences, with the truss vibrating around the initial configuration. However for $\bar{p}_z = 0.45$, this response coexists with a large amplitude period five cross-well complex response. Therefore, deep systems present a more complex dynamic response than shallow ones, with lateral instabilities and different chaotic regions and period cascades.

Figure 3.11 shows for $\bar{p}_z = 0.60$ and $\bar{p}_z = 0.80$ three projections of the four dimensional $(\bar{r}, \bar{z}, \dot{\bar{r}}, \dot{\bar{z}})$ periodic attractors. For both load levels the 4-dimensional attractor (in blue) coexists with the 2-dimensional attractor (in red), showing the multiplicity and complexity of the dynamic solutions. Since the system is elastic, due to the symmetries of the potential energy with respect to the $\bar{z}$ and $\bar{r}$ axes (see Fig. 2.5), the corresponding mirror attractors exist (although not shown here).
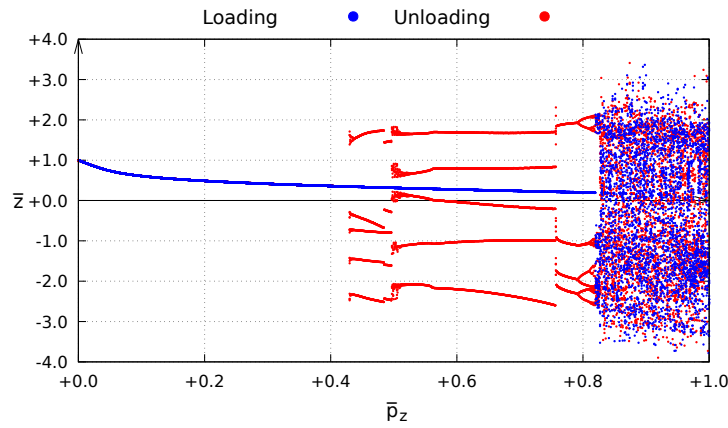
(a) $\bar{z} \times \bar{p}_z$
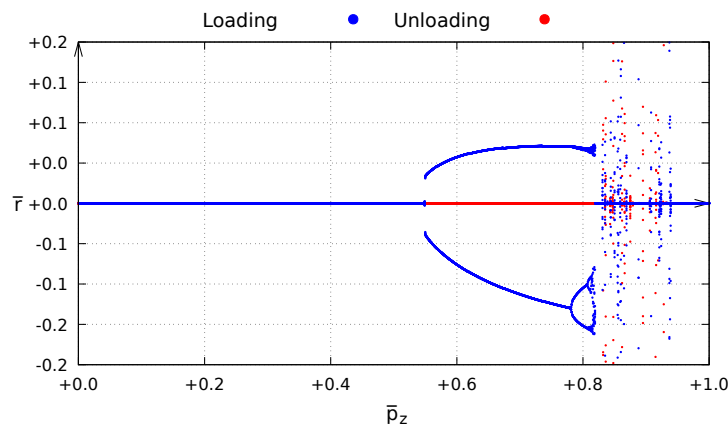
(b) $\bar{r} \times \bar{p}_z$

Figure 3.9: Deep truss bifurcation diagrams of the Poincaré map ($\alpha = 0.50$).

(a) $\overline{p}_z = 0.40$

(b) $\overline{p}_z = 0.45$
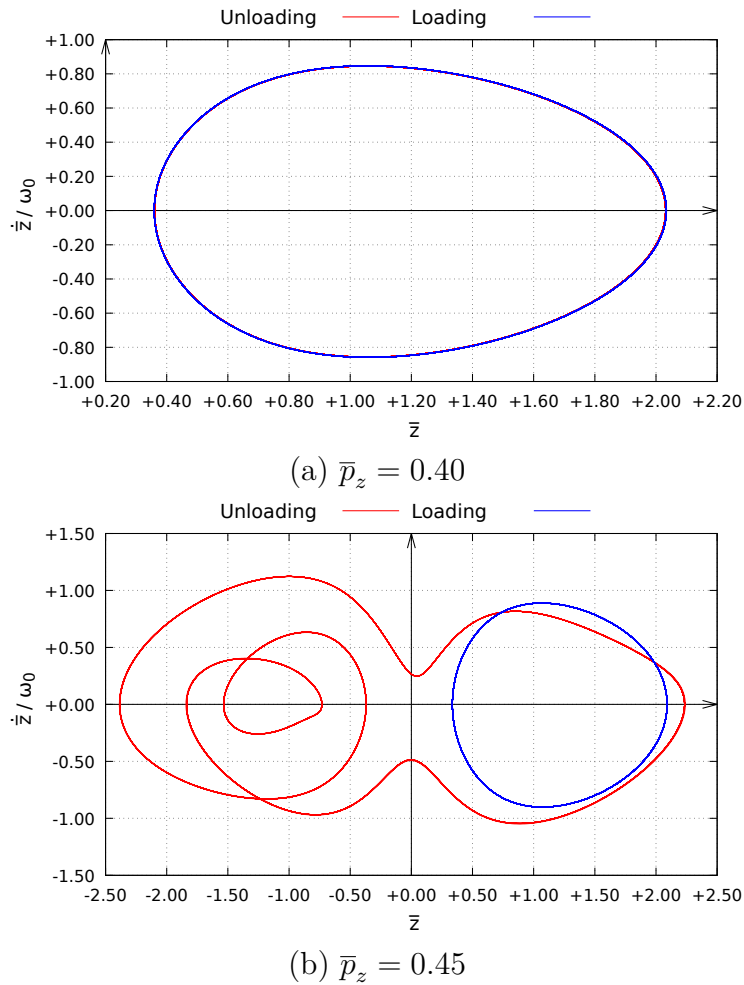
Figure 3.10: Deep truss phase planes ($\alpha = 0.50$).

Fig. 3.12 shows the projection of the Poincaré section considering $n_p = 5000$ excitation periods for $\overline{p}_z = 0.90$ obtained during the loading and unloading processes. After each integration period ($n_t = 500$ time integration points) the coordinates ($\overline{z}$, $\dot{\overline{z}}$) are marked in the phase plane. The fine fractal structure of the chaotic attractor, represented by the three almost self-similar geometric objects, can be observed in the two cases and is a clear indication of the high degree of nonlinearity presented by the system. A similar fractal structure was obtained by Orlando et al. [17] while investigating multistable systems. Due to the presence of coexisting bifurcation diagrams within the pre and post-buckling wells which can undergo different types of bifurcations as well as large cross-well solutions, the truss can exhibit several coexisting attractors in the main resonance region for a given load magnitude. Similar phenomena were shown by Orlando et al. [16, 17], where up to five coexisting solutions were detected in the bifurcation analysis.

In conclusion, depending on the load increment, during the unloading process different sequences of solutions can be followed by the numerical al-

(a) $\overline{p}_z = 0.60$

(b) $\overline{p}_z = 0.80$
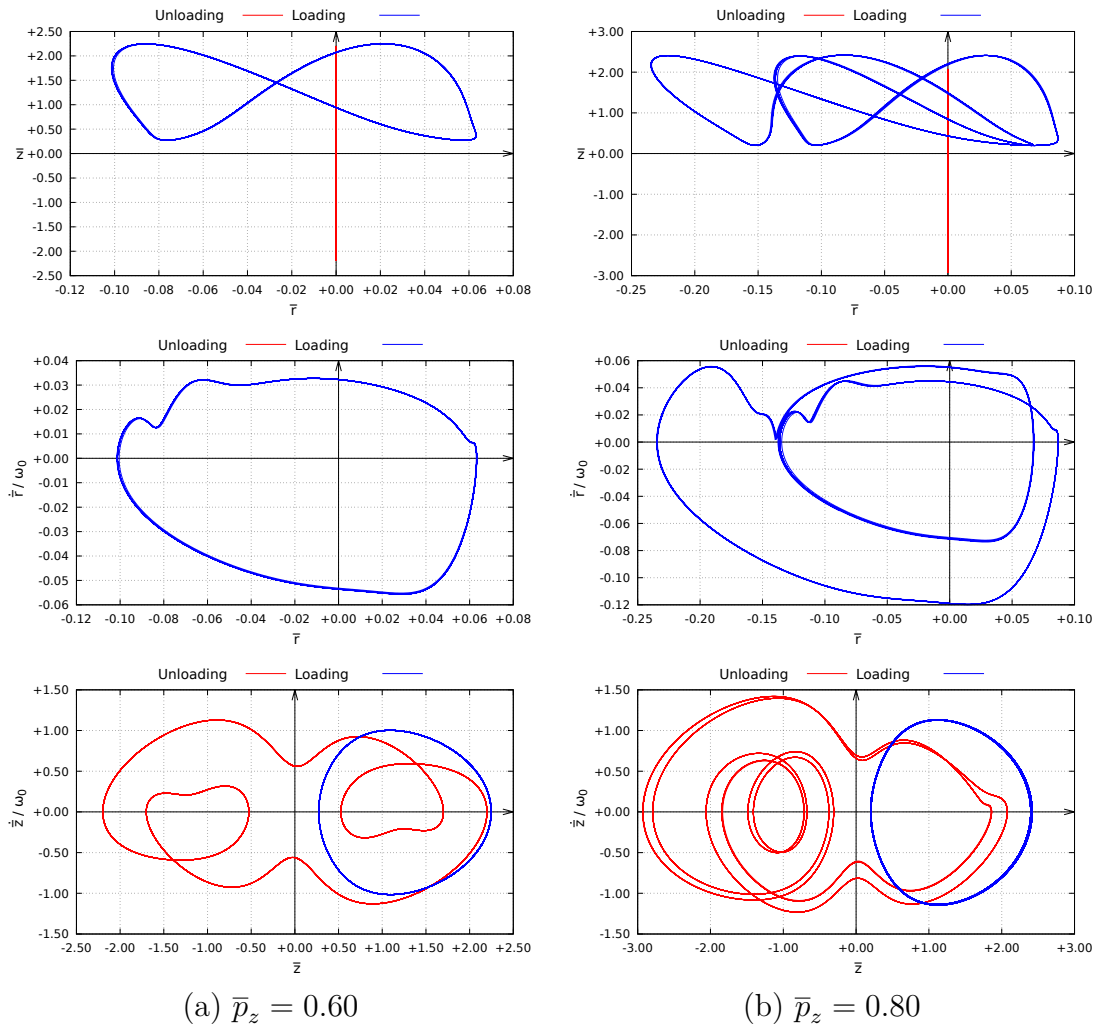
Figure 3.11: Deep truss phase planes ($\alpha = 0.50$).

gorithm. As an example, Fig. 3.13 shows two different bifurcation sequences obtained using respectively 50 (in red) and 500 (in black) integration periods. The considerable variation of the computed solutions under different bifurcation sequences and numerical parameters illustrates how the elastic truss complex dynamic response turns the controlled motion and design of the system challenging. When the system is subject to elasto-plastic deformations, part of the energy introduced by the harmonic excitation is dissipated and a more controlled motion is expected.

3.8
Incorporating elasto-plastic behavior

For most materials, dynamic jumps and escape from the pre-buckling well leads to large stresses and strains with possible elasto-plastic oscillations. Here the influence of the plastic behavior of the material on the dynamic nonlinear response is investigated without considering a static preload. Shallow and deep

(a) Loading
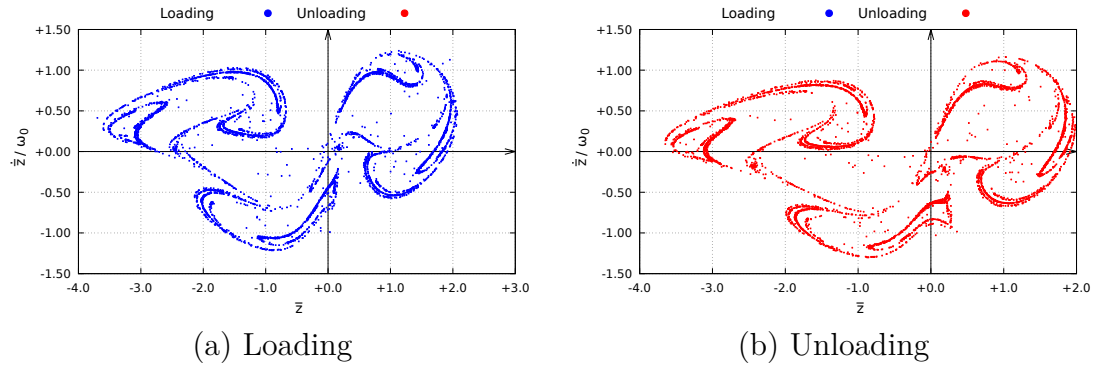
(b) Unloading

Figure 3.12: Projections of the Poincaré sections of the chaotic attractor onto the $\overline{z} \times \dot{\overline{z}}$ plane for $\overline{p}_z = 0.9$ and $\alpha = 0.5$.
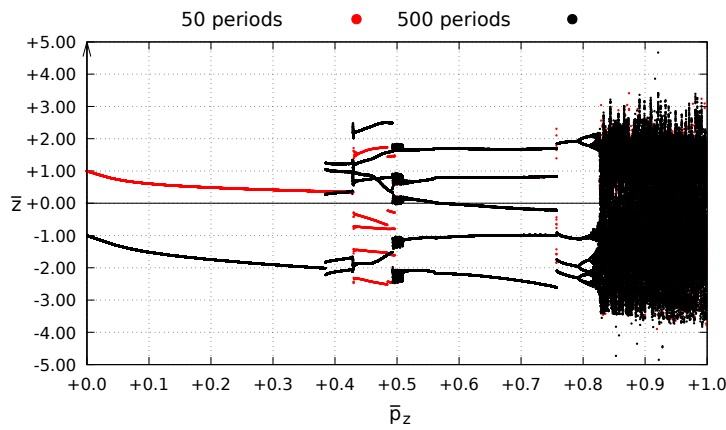
Figure 3.13: Different bifurcation sequences during the unloading process due to existence of various competing attractors.

truss behaviors are considered and compared.

Figure 3.14 shows the bifurcation diagram for a *shallow truss* with $\alpha = 8.00$ considering a nonlinear material response with different values of strain hardening parameter $\eta = K/(E + K)$. Initially the structural response is elastic but, as the vibration amplitudes increase in the main resonance region, plastic deformation appears (Eq. 2-58). Each value of the strain hardening nondimensional parameter η results in completely different bifurcation scenarios, demonstrating the complexity of the elasto-plastic dynamic response on the one hand and the large influence of plastic energy dissipation on the structural response on the other hand.

For $\eta = 0$, i.e. a perfectly plastic assumption, a smoother variation of the Poincaré coordinates $(\overline{p}_z, \overline{z})$ and smaller vibration amplitudes than those in the elastic case are observed (see Fig. 3.7) due to the dissipation of mechanical energy through the plastic deformations. As the load increases (blue branch) the period one solution becomes unstable at $\overline{p}_z = 0.23$ and the truss jumps to a period four solution which is followed by a period halving cascade and

return to period one at $\bar{p}_z = 0.65$. The blue and red branches converge at a flip bifurcation point at $\bar{p}_z = 0.88$. For higher load levels only one attractor is observed until $\bar{p}_z = 1.00$. Upon unloading, the truss follows the red branch of the pitchfork bifurcation and a period doubling bifurcation is detected at $\bar{p}_z = 0.65$. It is followed by a second period doubling cascade, and as the load decreases, more evolved solutions are observed until $\bar{p}_z = 0.08$. Here there is a discontinuous jump to a period one solution and the response converges to an unloaded inverted configuration with large residual deformations ($\bar{z} = -0.57$).

For higher values of the strain hardening nondimensional parameter $\eta \neq 0$ the elements capacity to store elastic energy increases with accumulated plastic deformations. The response follow the same initial period one solution branch up to $\bar{p}_z = 0.24$. At this point a jump to an inverted configuration occurs. After this, the solution is highly affected by the value of the strain hardening parameter with several jumps and discontinuities, revealing a complex bifurcation scenario. In all cases large residual deformations are observed. It is emphasized that since the elasto-plastic response depends on the load history, different bifurcations sequences may be obtained depending on the loading/unloading process. The results show that the solutions are highly dependent on the value of the strain hardening parameter η influencing the plastic energy dissipation.

Fig. 3.15 illustrates the phase-plane of the stable solutions detected during loading and unloading processes for selected values of $\bar{p}_z$ and perfect plasticity. Comparing with the previous examples, large cross-well motions are rare due to the dissipative effect of plasticity, reducing or eliminating the chaotic domains of the response. Therefore, the system nonlinear elastic and elasto-plastic, oscillations are considerably different and the consideration of the materials plastic behavior can be of importance in the dynamic design of pyramidal trusses.

The computational results show the existence of multiple dynamic solutions in the elasto-plastic domain. In Fig. 3.15(a), for $\bar{p}_z = 0.2$, the small amplitude period one solution within the pre-buckling well coexists with a complex solution within the post-buckling well (see Fig. 3.14(a)). In Figs. 3.15(b) and 3.15(c), for $\bar{p}_z = 0.40$ and $\bar{p}_z = 0.60$ respectively, two symmetric period two solutions are observed. Finally, in Fig. 3.15(d), for $\bar{p}_z = 0.80$, the two period one solutions preceding the flip bifurcation are shown.

The results for a *deep truss* with $\alpha = 1.20$ are shown on Figs. 3.16 and 3.17. As deep trusses are usually subject to large strains and consequently large stresses, the plastic deformation of the elements start for lower load magnitudes compared with shallow structures. As a consequence, the effects of plastic deformation increase with the truss height (similar to the observations

(a) $\eta = 0.00$

(b) $\eta = 0.05$

(c) $\eta = 0.15$

(d) $\eta = 0.30$
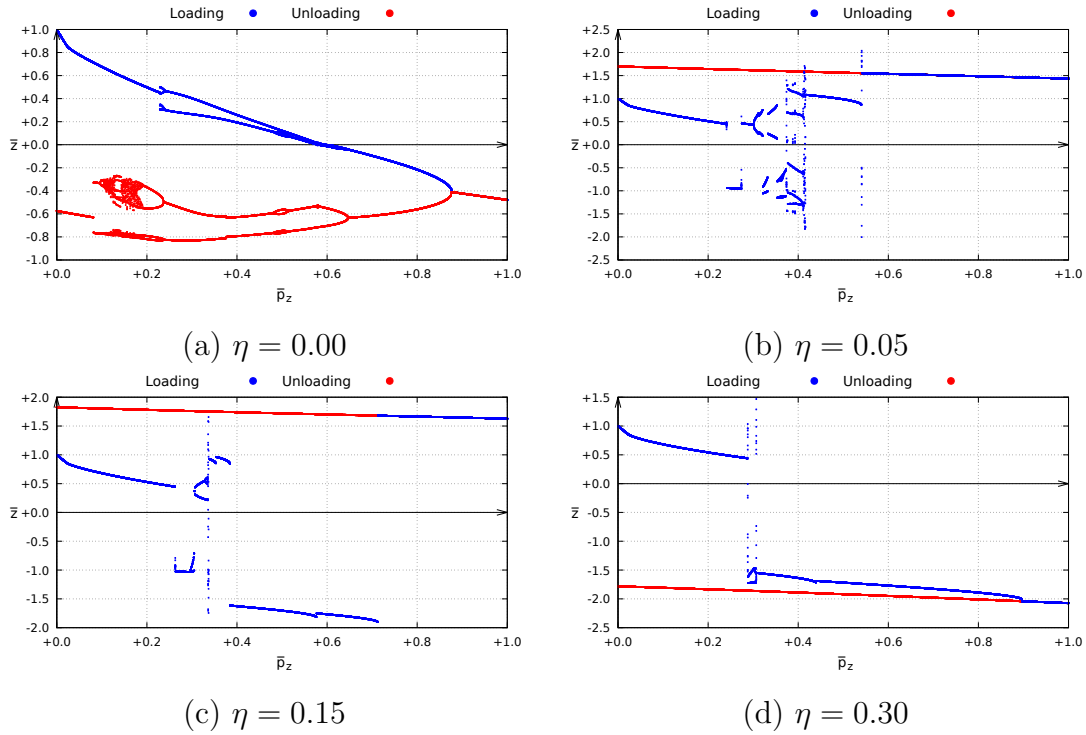
Figure 3.14: Bifurcation diagram considering the elasto-plastic material behavior ($\alpha = 8.0$).

(a) $\overline{p}_z = 0.2$

(b) $\overline{p}_z = 0.4$

(c) $\overline{p}_z = 0.6$

(d) $\overline{p}_z = 0.8$
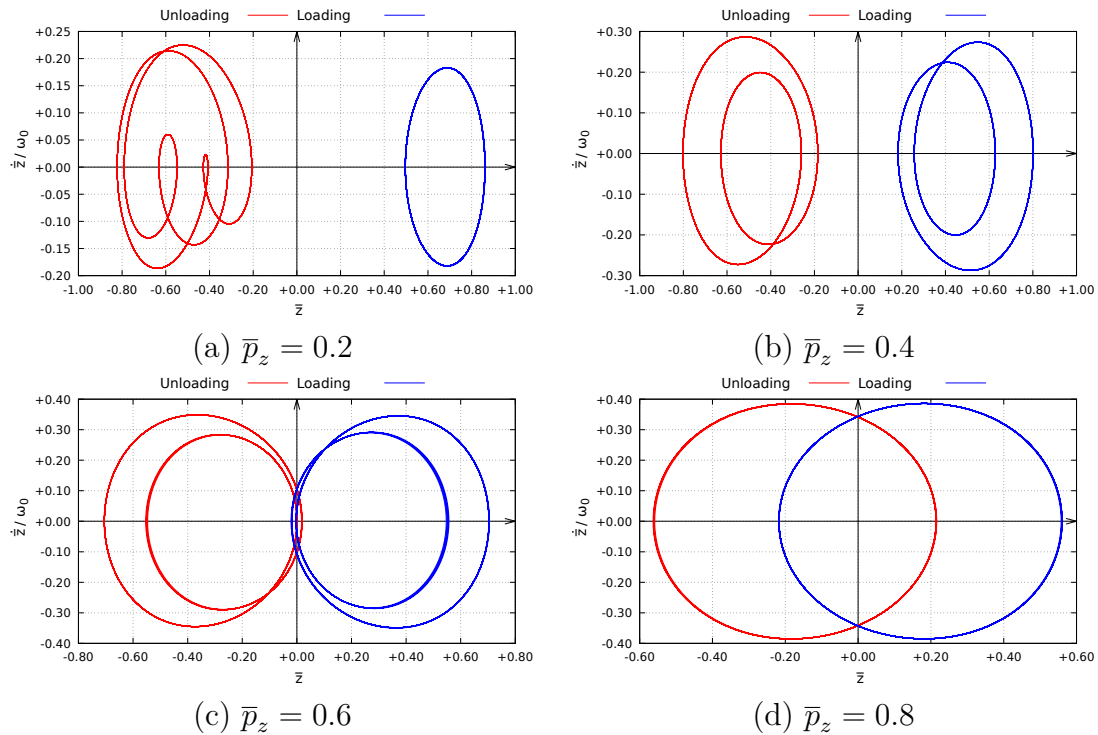
Figure 3.15: Phase plane considering the elasto-plastic material behavior ($\alpha = 8.0, \eta = 0.00$).

made in the static analysis of Chapter 2). For $\eta = 0.00$, the plastic bifurcation occurs for a very low load. For $\eta > 0$, the structure is capable of supporting

higher load levels and escape from the pre-buckling well is observed. Again, as the load continues to increase, several jumps and bifurcations are observed with periodic solutions of various orders, however chaotic motions are not detected up to $\overline{p}_z = 1.00$.

(a) $\eta = 0.00$

(b) $\eta = 0.05$

(c) $\eta = 0.15$

(d) $\eta = 0.30$
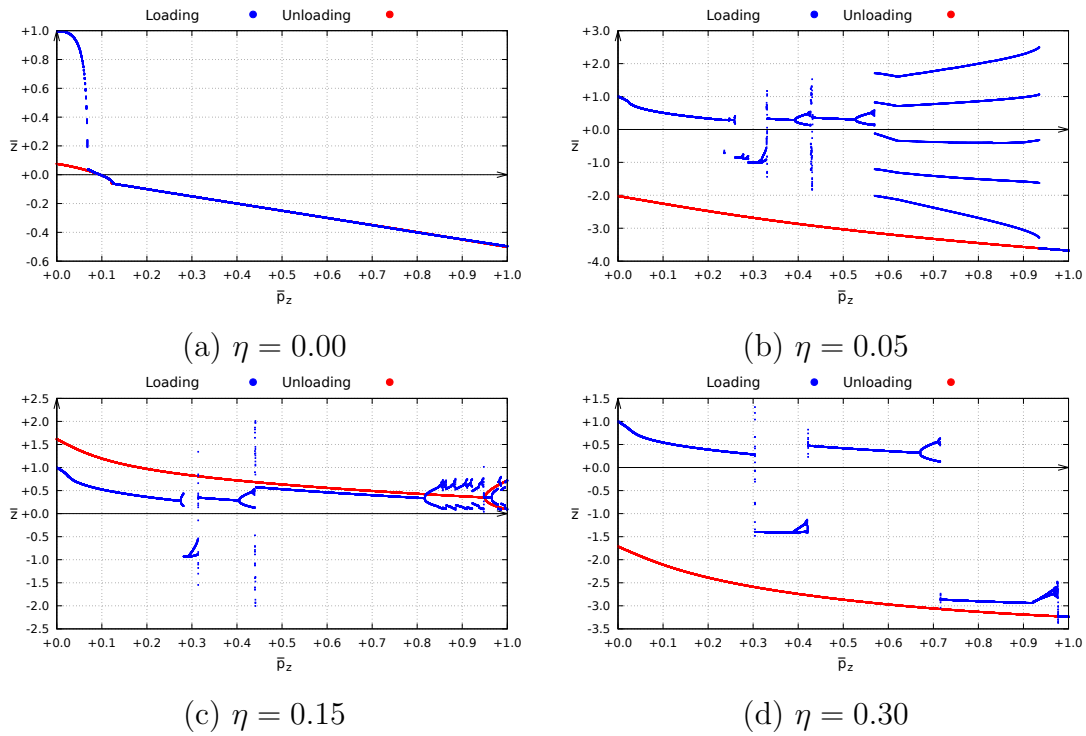
Figure 3.16: Bifurcation diagram considering the elasto-plastic material behavior ($\alpha = 1.2$).

(a) $\overline{p}_z = 0.10$

(b) $\overline{p}_z = 0.60$
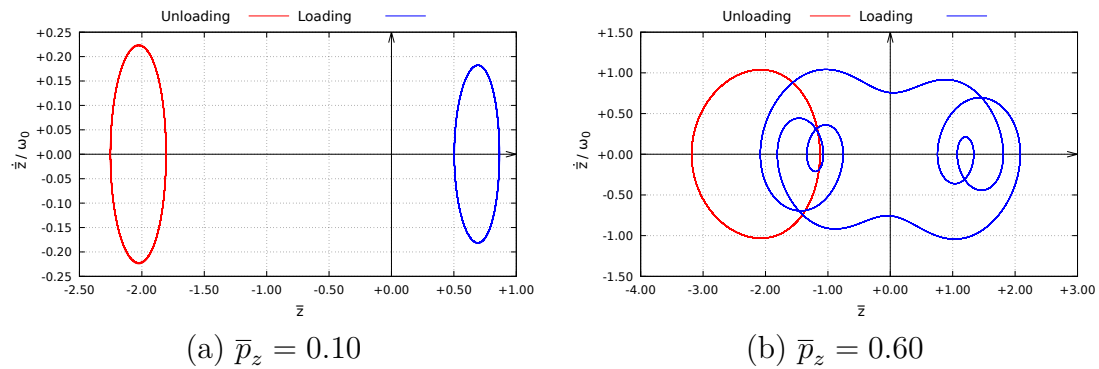
Figure 3.17: Phase plane considering the elasto-plastic material behavior ($\alpha = 1.2$, $\eta = 0.05$).

3.9
Influence of the excitation frequency

In this section the bifurcation diagrams are obtained considering the excitation frequency parameter $\overline{\omega} = \omega/\omega_0$ as control variable and maintaining

the *harmonic excitation force magnitude fixed* (without static preload). The elastic and elasto-plastic dynamic response of shallow and deep systems are compared.

Figure 3.18 shows the bifurcation diagrams of a *shallow truss* with $\alpha = 8.0$ for different fixed values of the load magnitude $\bar{p}_z$, considering an elastic material (and LSM). For $\bar{p}_z = 0.02$ the response is practically correspond to the one observed in a linear system, with a resonant peak at $\bar{\omega} = 1$. As the fixed load increases, the bifurcation diagram bends to the left due to the geometric nonlinearity softening effect. For $\bar{p}_z > 0.04$ two saddle-node bifurcations are detected leading to jumps (discontinuities on the bifurcation diagrams) from the non-resonant to the resonant branch as the frequency parameter increases (jumps from the resonant branch to the non-resonant branch also appears as the frequency parameter decreases). The maximum vibration amplitude increases with an increasing value of the fixed $\bar{p}_z$. At $\bar{p}_z = 0.02$ the structure jumps to the inverted position and cross-well motions are detected in the vicinity of the main resonance region. A secondary peak appears around $\bar{\omega} = 0.5$, also due to the geometrical nonlinearity. For higher values of the excitation frequency the truss vibrates again around the unloaded configuration.

Figure 3.19 shows the results for the same shallow truss ($\alpha = 8.0$), for different values of the fixed load magnitude $\bar{p}_z$, but considering an *elasto-plastic* material with strain hardening ($\eta = 0.30$). For $\bar{p}_z = 0.02$ the response is elastic and linear, with coincident loading and unloading paths, because the yield strength is not reached. At $\bar{p}_z = 0.04$, in the main resonance region around $\bar{\omega} = 1$, the vibration amplitudes however induce stresses high enough to generate plastic deformations. For high excitation frequencies the loading and unloading paths match. However, as the excitation frequency decreases, a new solution path appears just to the right of $\bar{\omega} = 1$ (in red) due to the accumulated plastic deformations.

The results in Fig. 3.20, showing the bifurcation diagrams for four selected values of η and $\bar{p}_z = 0.04$ are used to explain the influence of the elasto-plastic behavior and the strain hardening parameter for this shallow truss. Initially, in the low frequency range, the vibration amplitude increases slowly and the response remains elastic. For $\bar{\omega} > 0.8$ the vibration amplitude increases and becomes practically linear for low values of η. When $\bar{\omega}$ decreases (red), the effect of the accumulated plastic deformations increases (e.g for $\eta = 0.00$ rather large deformations are observed) and in the unloaded process the pyramidal truss oscillates around the new configuration with permanent deformations. As observed in Fig. 3.19 and 3.20 when compared to Fig. 3.18
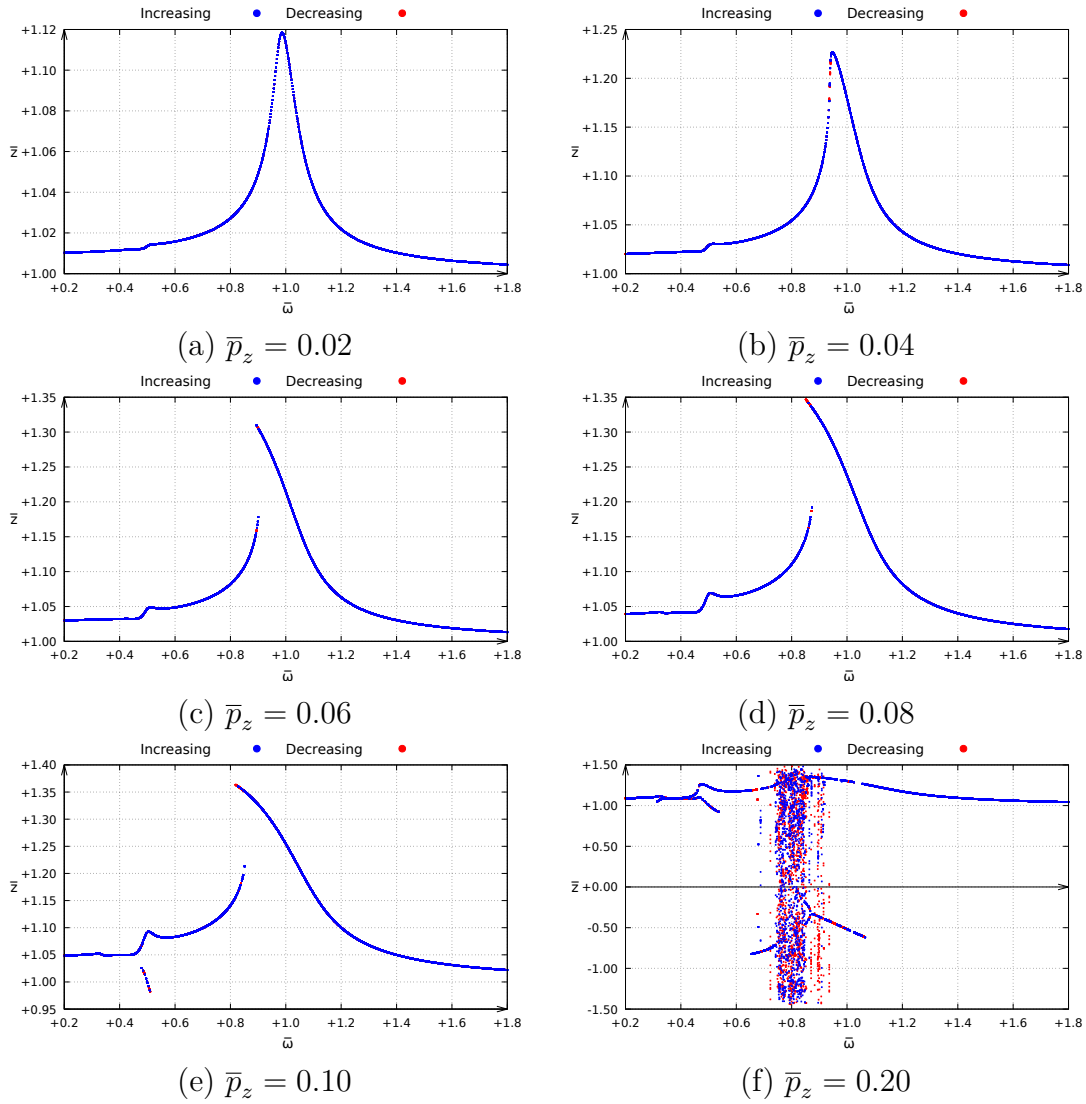
Figure 3.18: Bifurcation diagrams for a shallow truss with $\alpha = 8.0$ and increasing values of the load magnitude $\bar{p}_z$, considering an elastic material and the LSM.

the softening effect due to geometric nonlinearities and the resulting jumps practically disappear when the material nonlinearity is taken into account.

The results with $\eta = 0.00$ in a broader range of the frequency domains are shown in Fig. 3.21. In this particular case, as the material response presents no hardening, the system stiffness in the elasto-plastic domain is due to its geometrical part, leading to a different response in the unload process. The peak load is located at $\bar{\omega} = 3.43$ moving from the resonance region of the elastic system.

A similar behavior is observed for *deep trusses* when considering *elasto-plastic behavior* (Fig. 3.22 for $\alpha = 1.2$). However, as η tends to zero, the material nonlinearity has a more dominant influence on the structural response as expected.
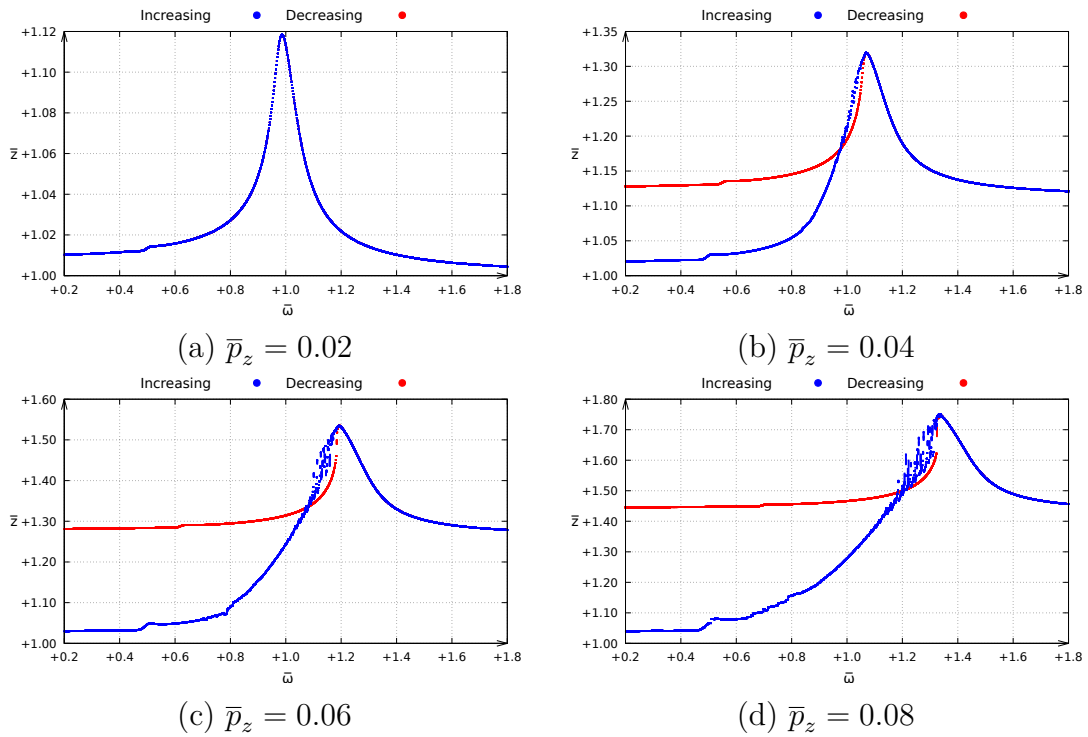
Figure 3.19: Bifurcation diagrams for a shallow truss with $\alpha = 8.0$ and increasing values of the load magnitude $\overline{p}_z$, considering an *elasto-plastic* material with $\eta = 0.30$.
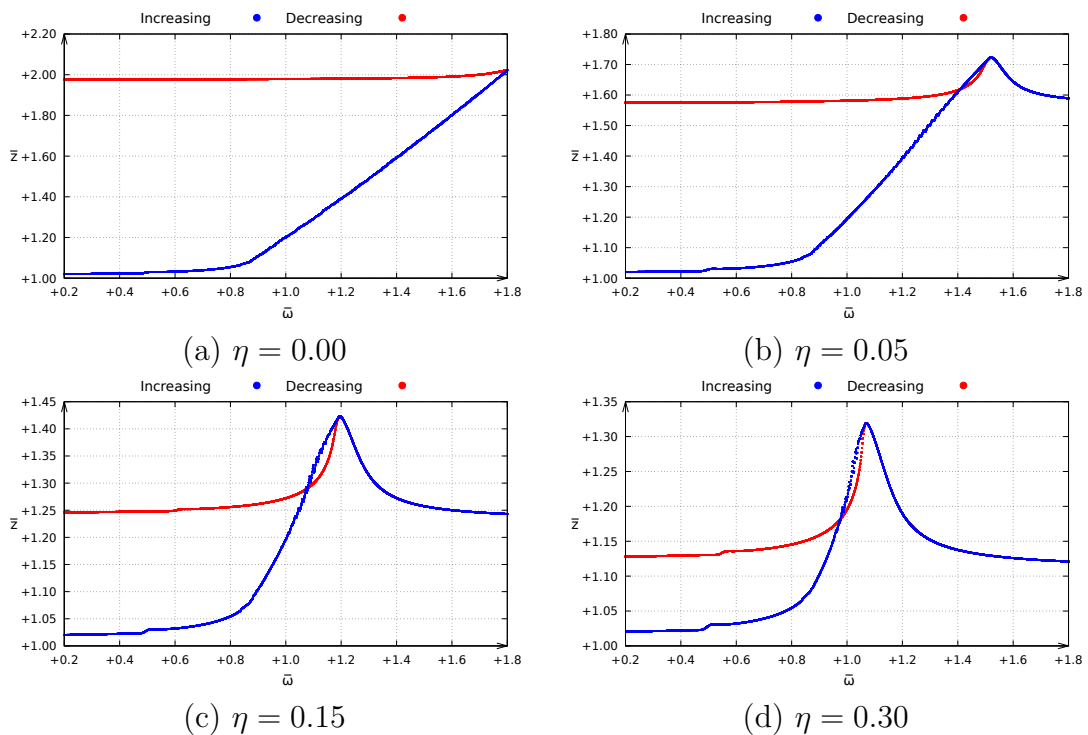
Figure 3.20: Bifurcation diagrams for a shallow truss with $\alpha = 8.0$, $\overline{p}_z = 0.04$ with elasto-plastic behavior and different values of the strain hardening parameter η.
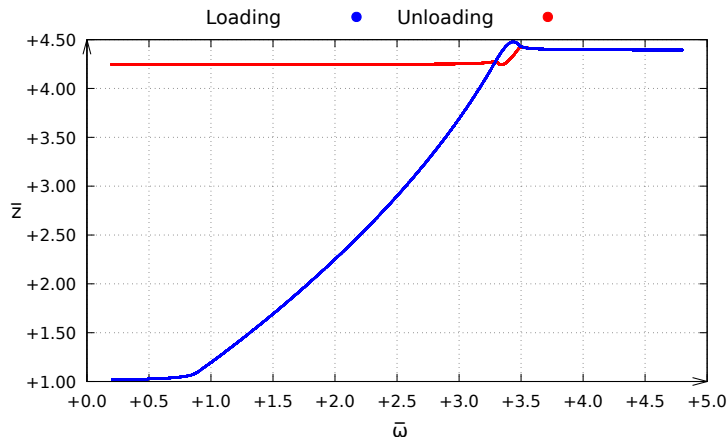
Figure 3.21: Bifurcation diagram for a shallow truss with $\alpha = 8.0$, $\overline{p}_z = 0.04$ and $\eta = 0.00$ in a broader range of the frequency domain.

(a) $\eta = 0.00$

(b) $\eta = 0.05$

(c) $\eta = 0.15$

(d) $\eta = 0.30$
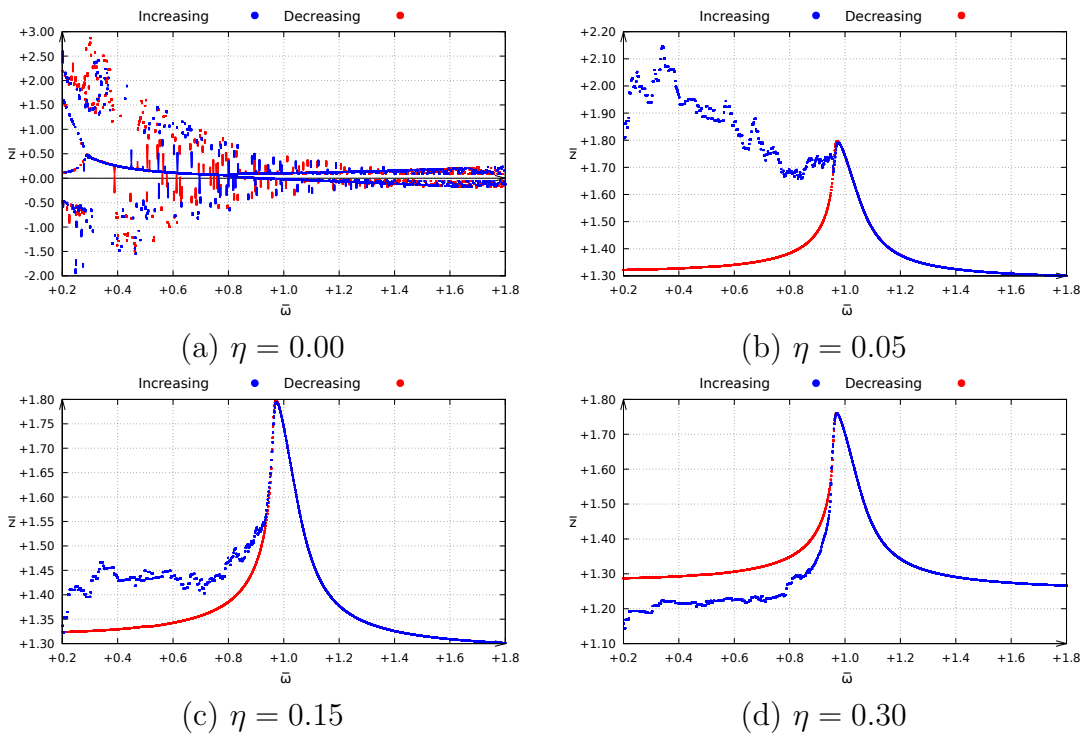
Figure 3.22: Bifurcation diagrams with $\alpha = 1.2$, $\overline{p}_z = 0.08$ and different values of η.

Figure 3.23 shows the elasto-plastic phase planes for the bifurcation diagrams displayed in Fig. 3.21 as the excitation frequency increases and decreases in the main resonance region for $\overline{\omega} = 0.8$ and four selected values of the strain hardening parameter η. These results illustrate the influence of the strain hardening parameter on the transient and steady state responses. For $\eta = 0$, the plastic attractor is continuously moving with the evolution of the accumulated plastic deformations. For $\eta = 0.05$, two separate attractors are observed and as η further increases start to approach one another.

(a) $\eta = 0.00$ (b) $\eta = 0.05$

(c) $\eta = 0.15$ (d) $\eta = 0.30$
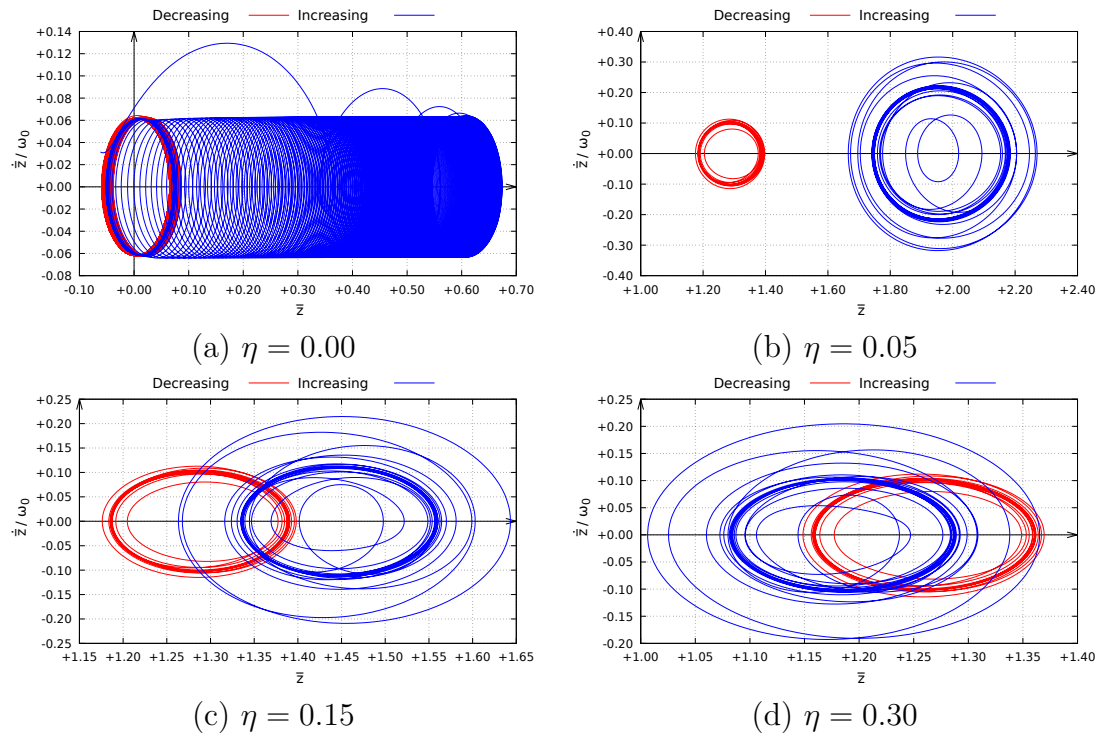
Figure 3.23: Elasto-plastic solutions for $\alpha = 1.2$, $\overline{p}_z = 0.08$ and $\overline{\omega} = 0.8$.

3.10
Influence of the choice of the initial conditions

The elasto-plastic attractors depend on the load time-history (as shown earlier) and initial conditions. The focus is shifted on the latter in this Section. To illustrate the influence of the initial conditions on the transient and steady state vibrations of the elasto-plastic shallow pyramidal truss module, the apex node displacement time histories for $\alpha = 8.0$, fixed $\overline{\omega} = 0.8$, fixed $\overline{p}_z = 0.04$ and $\eta = 0.00$ are investigated using *different initial values of the vertical displacement.*

Some of the obtained results are shown in Fig. 3.24. It is observed that, depending on the initial conditions, the truss vibrates around different equilibrium points. Due to the accumulated plastic deformations the attractor moves along the z axis, as already exemplified in the preceding bifurcation diagrams.

3.11
Conclusions

The dynamic nonlinear analyses of shallow and deep bistable pyramidal truss modules were carried out with emphasis on their nonlinear vibrations and instabilities, considering geometrical nonlinearities and elastic and elasto-plastic material behaviors. Two key questions were investigated: the influence

(a) $\overline{z}_0 = 1.9$ (b) $\overline{z}_0 = 1.7$ (c) $\overline{z}_0 = 0.9$

(d) $\overline{z}_0 = 0.6$ (e) $\overline{z}_0 = 0.3$ (f) $\overline{z}_0 = -0.2$

(g) $\overline{z}_0 = -0.6$ (h) $\overline{z}_0 = -0.8$ (i) $\overline{z}_0 = -1.3$
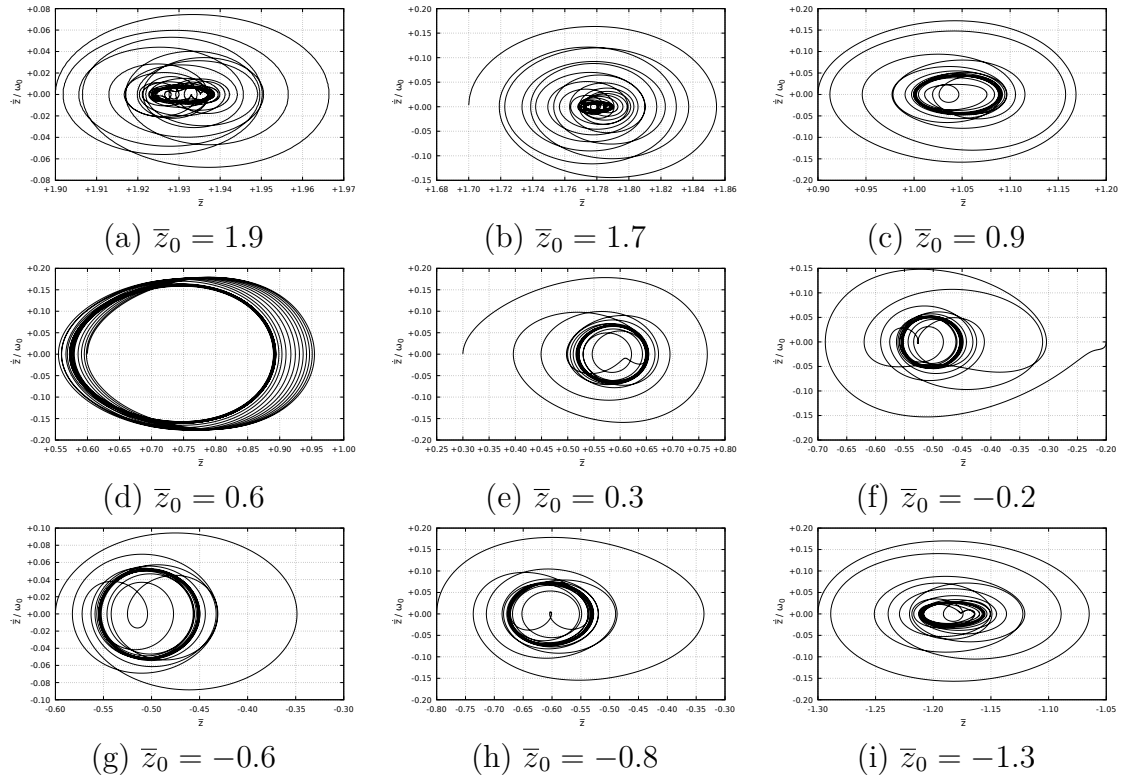
Figure 3.24: Influence of the initial conditions on the transient and steady state elasto-plastic nonlinear vibrations of the truss under harmonic load ($\alpha = 8.0$, $\overline{\omega} = 0.8$ and $\overline{p}_z = 0.04$).

of the adopted strain measures (QSM and LSM) and the influence of the material constitutive law on the nonlinear dynamic response of the pyramidal truss. The logarithmic strain measure was better suited to represent the structural behavior in the numerical simulations (as seen in chapter 2), specially when elasto-plastic deformations are considered and although more complex, should be used when possible.

An original closed form expression of the phase space for the unloaded elastic symmetric system was developed and investigated, the boundaries of the pre-buckling and post-buckling wells were determined. The non-dimensional minimum energy levels required to cross the boundaries and initiate the large cross-well motion of the system were determined.

Using the developed FE software, the nonlinear oscillations and dynamic instabilities of the pyramidal truss under vertical harmonic excitation were investigated through bifurcation diagrams of the Poincaré map and phase-space projections of the relevant attractors.

A parametric analysis was conducted to study the influence of the truss geometry and strain hardening parameter. The complex topology of the bistable truss potential energy was observed to result in coexisting solutions in the main resonance region, including in-well and cross-well periodic and

chaotic attractors. For deep pyramidal trusses with a high height/base ratio (α) the strain measure has a considerable influence on the dynamic response and leads to cross-well solutions for different dynamic load levels.

The influence of static preload was investigated and considerably different bifurcation sequences and chaotic behavior was observed. Its effect may have to be considered in the dynamic analyses of pyramidal trusses as a function of its magnitude.

The dissipation of energy in the plastic deformations was shown to dramatically influence the dynamic response of shallow and deep systems, eliminating the its chaotic behavior and leading to smaller oscillation amplitudes. When material hardening is considered the structural system exhibits a more complex response, including multiple period doubling and dynamic jumps. The elasto-plastic deformations of the material should be included in the analyses and may be necessary for an accurate dynamic design.

Energy dissipation through friction or use of complaint, energy absorbing elastic materials could attenuate the chaotic motions of the system, making the design more straightforward. In future works this effect could be investigated.

4
Computational modeling of bistable deployable structures

4.1
Outline

The 3D deployable frames studied in this work are structures composed of elastic beam elements connected by complex joints. During transformation a controlled, desired snap-through allows the instantaneous stabilization of the structure in an open and in a closed, compact configuration. To ensure that the transformation is reversible the beams deformations are restricted to the elastic domain. The mechanics of the transformation is highly nonlinear, since it relies on finite rotations of the structural elements. It is strongly influenced by geometrical features required for a manufacturing-ready design, such as the finite size of structural elements and sufficient spacing between the beams. These features are generally disregarded in the usual wireframe-based design, but they are taken into account in this work by applying a tailor-made corotational 3D joint finite element, developed to incorporate naturally finite joint size, finite nonlinear joint stiffness and friction effects. The formulation of the proposed joint FE is presented and the performance of the numerical implementation is verified using computational benchmarks. The joint FE is then applied to the numerical investigation of the transformation response of bistable deployable structures from a single module case to large, complex structures. Among other findings, it is shown that the incorporation of finite joint size and beam spacing in the numerical model leads to a different snap-through mechanism that significantly reduces the peak force required for transformation, which could be a basis for future design strategies. Additionally the performance of structures applying the bistable structural pattern on the whole structure or following an entirely modular design (interconnected single modules) is also compared, as a function of the structural size.

The Chapter is organized as follows: Following an introduction in Sec. 4.2, the 3D corotational joint finite element formulation is presented in Sec. 4.3. Computational developments are validated through benchmark examples in Sec. 4.4. The transformation behavior of a bistable deployable module is investigated in details in Sec. 4.5. The transformation load vs displacement

curves are analyzed and the effects of the joint friction, hub size, beam width and joint dimensions are assessed. Section 4.6 is dedicated to the analysis of more complex bistable deployable structures formed by the assembly of deployable modules. Finally, in Sec. 4.7, conclusions and suggestions for future work are given. [1]

4.2
State of the art

Deployable scissor structures are space frames consisting of straight elastic beams that are connected by complex joints, forming a compact bundle in the closed configuration that can be unfolded into a large, load bearing structure. Their major advantages are the small volume they occupy during storage and transportation, the ease and speed of erection, and their reusability. Due to these advantages, they offer possible alternatives for a wide range of civil engineering applications such as emergency shelters, exhibition and recreational structures.

Transformable scissor structures for aerospace applications have been studied in the literature [94, 95], considering for instance their dynamic behavior [96, 97, 98]. While the concept of transformation is similar, due to the difference in size, manufacturing tolerances and loading conditions, i.e. need of taking into account gravity in the deployed configuration [99], the findings from this field are not directly applicable to civil engineering structures. Without the intention of constituting an exhaustive list, several recent efforts for civil engineering applications of deployable structures can be referred to. Alegria Mira et al. [18] studied a deployable scissor arch as an emergency shelter and Van Mele et al. [100] investigated scissor-hinged retractable membrane structures. For an extensive review on deployable structures, the interested reader is referred to Fenci and Currie [101].

The focus of the present work is a specific type of deployable structures, in which intended geometric incompatibilities between the members are incorporated as a design strategy to instantaneously achieve structural stability, i.e. a ready-to-use service state. During transformation these geometric incompatibilities lead to compression and bending of the beams, resulting in a controlled structural snap-through. Such structures are referred to as bistable deployable structures, because of their two stable states: folded and deployed [102]. In spite of the advantages of bistable scissor structures, few have suc-

---

[1]The contents of Chapter 4 are a convolution of a manuscript submitted for publication to *Mechanical Systems and Signal Processing.*

cessfully been built because of the complexity of their behavior and of their design process that requires advanced computational modelling [21].

A comprehensive analysis of the transformation of 3D bistable deployable structures must include several nonlinear effects and their appropriate treatment in a computational solution procedure (geometric nonlinearity, friction and snap-through). In these structures, revolute joints define the connections between beams and their relative movement generates friction that can considerably increase the load required for transformation [22]. During the transformation, the beams and joints are subjected to large displacements and rotations and their motion is composed of a rigid body part and straining (since the elements bend and buckle) that has to be appropriately described in a numerical model. Structural joints are used in the beam-to-beam connections, as well as in the hubs at which more than two beams meet. For the sake of simplicity they are most often considered in numerical models as rigid links with zero compliance in the constrained directions [103]. They can however be attributed a finite stiffness to, which was shown to be beneficial to compensate for possible geometrical manufacturing tolerances [21]. The choice of the joint stiffness model obviously influences the structural deformation and the load distribution. Considering the complexity of these nonlinear effects and their interaction, computational modeling gives a useful contribution to the understanding and quantitative prediction of the transformation behavior of bistable deployable structures and is a basis for establishing rigorous design strategies.

The bistable deployable structures studied in this contribution were first proposed and investigated by Gantes et al. [102]. Recently Arnouts et al. [21] further investigated this class of deployable structures taking geometrical imperfections into account that naturally appear during manufacturing (uncertainty on the beams length, eccentricity of the pivot points, hinge stiffness and misalignment). In the works above the transformation and structural response in the deployed configuration were obtained using commercial finite element packages that are usually limited to pre-coded features that may not correspond to the complete set of required numerical ingredients. To the author's best knowledge there are no experimental works in the literature regarding this type of bistable deployable structures.

In the present work it is shown that the behavior of bistable scissor structures is also strongly influenced by geometrical features that need to be incorporated for a manufacturing-ready design, such as the finite size of structural elements and sufficient spacing between the beams. These features are generally disregarded in the usual wireframe-based design and numerical

investigation, except for the hub size [104, 21]. Here, a more complete set of ingredients is considered by applying a tailor-made corotational 3D joint finite element to the modelling of bistable deployable structures, developed to incorporate naturally finite joint size, finite nonlinear joint stiffness, beam spacing and friction effects. The development of such a 3D hinge finite element dedicated to deployable structures and the computational study considering all these effects are unprecedented and original to the author's best knowledge.

To ensure capturing a complex nonlinear structural behavior, several authors proposed numerical developments of interest for deployable structures. Crisfield [105], Pacoste and Erikkson [106] and Battini and Pacoste [6] developed 3D corotational beam formulations and applied them to investigate the instability of 3D frames. The computational modeling of joints has been treated in the literature in a number of different ways. Nikravesh and Chung [107] and Sugiyama et al. [108] used nonlinear constraints coupled with the equilibrium equations, to include the contribution of the joints. Jelenic and Crisfield [109] used nonlinear 'master-slave' relationships to represent the joint connecting the nodal degrees of freedom. Geradin and Cardona [66] considered both nonlinear constraints and small local deformations in the modeling of different types of joints. These approaches consider that the joints have an infinitesimal size (i.e. geometrically reduced to a single point) and are either rigid or have a linear stiffness, and so are not adapted to a comprehensive analysis of deployable scissor structures with finite stiffness.

The current work aims at combining a set of ad hoc numerical ingredients in the modeling effort of the transformation of bistable deployable structures, giving a contribution to the state of the art both from a computational development as well as an application point of view. The finite joint size and the beam thickness, the nonlinear elastic finite stiffness of the joints as well as friction are incorporated in the structural model and their influence and interactions are investigated. Different large bistable deployable structures are studied using the developed finite element, applying the bistable structural pattern on the whole structure (single built approach) or following an entirely modular design (interconnected single modules), their transformation performance as a function of their size is compared.

4.3
Corotational 3D joint finite element

Joints are mechanisms present in the connection of two beams that constrain their relative motion through their constitutive behavior and dimensions. Figure 4.1 shows a simple hinge joint, separating the beam midaxes by a dis-

tance s and allowing their relative rotation θ around a given axis perpendicular to the theoretical common plane of the beams.
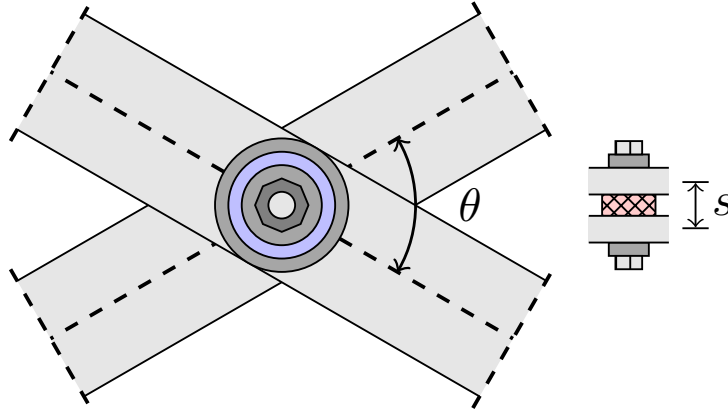
Figure 4.1: A finite size hinge joint connecting two beams ($s > 0$).

During transformation (folding and unfolding), the joints of bistable deployable scissor structures are subjected to large displacements and rotations. In deployable scissor structures, as the connected beams bend and buckle, the axis of each revolute joint changes direction considerably, which needs to be taken into account thoroughly in a numerical model. In the case of flexible joints, the relative motion of the connected nodes deforms the joint material and the rotation around the joint axis creates a friction resistance, influencing the load distribution in the connected beams and the overall behavior of the structure. The appropriate computational treatment of such joints must then include these geometric nonlinear effects and the corresponding constitutive behaviors.

Joints are usually treated as dependencies and/or nonlinear constraints that nodal displacements and rotations have to respect, together with the system of nonlinear equilibrium equations ([109], [107], [108]). In another approach, the joint can be treated as a finite element, combining relative displacements and rotations of the nodes with the joint constitutive relations, as contributions to the system internal force vector and stiffness matrix [66], leaving more flexibility in the possible constitutive relationships.

In the present work, a finite element formulation is introduced and used to represent the joints in the computational model of bistable deployable scissor structures. The formulation makes use of a corotational system and considers the joint complex constitutive behavior, including friction and finite dimensions which is of fundamental importance for an accurate analysis of bistable deployable scissor structures (Section 4.5). Local deformations in the beams, e.g. due to very low wall thickness, are not incorporated in the present model.

When dealing with large displacements and rotations in finite element formulations, it is beneficial to adopt a corotational methodology. This consists in defining a local coordinate system that follows the finite element rigid body motion, and hence, with respect to this system, only the part of the motion that generates deformations is measured. In this procedure, the movement is brought to the local system uncoupled from rigid body motion, and the strains, stresses, forces and stiffness are computed in this corotational frame. These local quantities are returned to the global structural coordinate system through a transformation, where the equilibrium of the structure is verified.

This split of the kinematics is particularly useful because it separates the geometric nonlinearity from the local nonlinear material behavior. This allows taking advantage of the high performance features of standard finite element formulations, such as the interpolation functions in the local frame, while considering the rigid body large displacements and rotations in the element. The present joint formulation is coupled to a corotational beam formulation that has been implemented but is not treated in this paper to keep focus on the novelties. The main equations of the beam formulation are given in Appendix C.

4.3.1
Corotational kinematics

The proposed joint finite element is composed of two nodes, separated by a distance s, corresponding to the beam midaxis interdistance of the beams it connects. The two joint nodes have initial coordinates $\mathbf{X}_a$ and $\mathbf{X}_b$ and the joint has an initial triad $\mathbf{s}_i$ associated to it. If the distance between the two nodes s is not null, then $\mathbf{s}_3$ is chosen in the direction of the line that connects the two nodes, otherwise this direction is provided as an additional input data. In both cases, $\mathbf{s}_1$ is arbitrarily selected in the plane normal to $\mathbf{s}_3$ and $\mathbf{s}_2 = \mathbf{s}_3 \times \mathbf{s}_1$. In the current configuration, the two connected nodes are subjected to the global translations $\mathbf{u}_a$ and $\mathbf{u}_b$ and rotation tensors $\mathbf{R}_a$ and $\mathbf{R}_b$, translating to the positions $\mathbf{x}_a$ and $\mathbf{x}_b$ and rotating the initial triad $\mathbf{s}_i$ to the nodal triads $\boldsymbol{\mu}_i$ and $\boldsymbol{\xi}_i$, respectively (Fig. 4.2). From Eq. (A-5):

$$\boldsymbol{\mu}_i = \mathbf{R}_a \cdot \mathbf{s}_i \tag{4-1}$$

$$\boldsymbol{\xi}_i = \mathbf{R}_b \cdot \mathbf{s}_i \tag{4-2}$$

Based on the 3D rotation description given in Appendix A, from Eq.

(A-9), the rotation tensors $\mathbf{R}_a$ and $\mathbf{R}_b$ may be written as:

$$\mathbf{R}_a = \boldsymbol{\mu}_i^T \cdot \mathbf{s}_i \tag{4-3}$$

$$\mathbf{R}_b = \boldsymbol{\xi}_i^T \cdot \mathbf{s}_i \tag{4-4}$$

Setting $\boldsymbol{\mu}_i$ as the local triad, the relative rotation tensor $\overline{\mathbf{R}}$ rotates the local system to the triad $\boldsymbol{\xi}_i$:

$$\overline{\mathbf{R}} = \mathbf{R}_b \cdot \mathbf{R}_a^T = \boldsymbol{\xi}_i \cdot \boldsymbol{\mu}_i^T \tag{4-5}$$

(a) corotational motion

$$\left\{ \begin{array}{c} u_{x,i} \\ u_{y,i} \\ u_{z,i} \\ \theta_{x,i} \\ \theta_{y,i} \\ \theta_{z,i} \end{array} \right\} \quad i \underset{\longleftarrow\; s\; \longrightarrow}{\rule{8cm}{0.4pt}} j \quad \left\{ \begin{array}{c} u_{x,j} \\ u_{y,j} \\ u_{z,j} \\ \theta_{x,j} \\ \theta_{y,j} \\ \theta_{z,j} \end{array} \right\}$$

(b) degrees of freedom
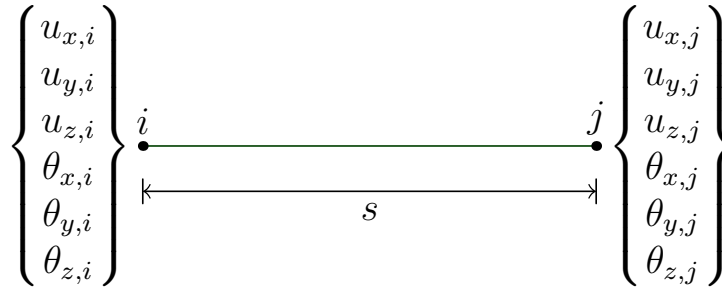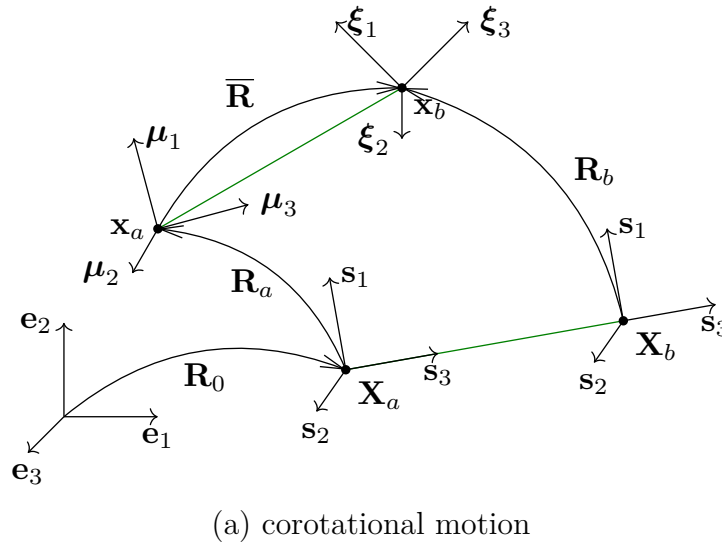
Figure 4.2: Corotational joint motion and degrees of freedom.

Setting $\mathbf{x}_a$ as the origin of the local system, the relative displacement (translation) components $\overline{u}_i$ are:

$$\overline{u}_i = \boldsymbol{\mu}_i^T \cdot (\mathbf{x}_b - \mathbf{x}_a) - \mathbf{s}_i^T \cdot (\mathbf{X}_b - \mathbf{X}_a) \tag{4-6}$$

With help of Eqs. (A-12), (A-13) and (A-14), the relative rotation direction $\overline{\mathbf{n}}_r$, the rotation angle $\overline{\theta}_r$ and the rotation components $\overline{\theta}_i$ are given

by:

$$\bar{\mathbf{n}}_r = \frac{\boldsymbol{\mu}_i \times \boldsymbol{\xi}_i}{2\sin(\bar{\theta}_r)} \tag{4-7}$$

$$\bar{\theta}_r = \arccos\left[\frac{1}{2}\left(\boldsymbol{\xi}_i^T \cdot \boldsymbol{\mu}_i - 1\right)\right] \tag{4-8}$$

$$\bar{\theta}_i = \frac{\bar{\theta}_r}{2\sin(\bar{\theta}_r)}\left(\boldsymbol{\xi}_j^T \cdot \boldsymbol{\mu}_k - \boldsymbol{\xi}_k^T \cdot \boldsymbol{\mu}_j\right) \tag{4-9}$$

4.3.2
Internal force computation

In this Section the chosen joint constitutive relationships are presented (4.3.2.1). The local internal forces are computed making use of them and transformed back to the global set of axes (4.3.2.2).

4.3.2.1
Constitutive relations

The studied joint is shown in Fig. 4.3 and the design parameters and mechanical components are illustrated in Fig. 4.4. The local forces $\bar{n}_i$ and moments $\bar{m}_i$ energetically conjugate through the virtual work variation δU to the relative displacement (translation) $\delta \bar{u}_i$ and rotation $\delta \bar{\theta}_i$ variations, respectively, are computed through the joint constitutive relations. The triad $\mathbf{s}_i$ is defined so that $\mathbf{s}_3$ corresponds to the hinge initial axis direction and $\mathbf{s}_1$ and $\mathbf{s}_2$ are in the plane normal to $\mathbf{s}_3$. The central pin has a radius r_h. A spacer, with width s_h, is located in the hinge center in order to avoid contact between the beams. There is a compliant nonlinear elastic cylindrical layer inside the case, with width w_h and thickness t_h, that is directly connected with the joint out-of-plane motion allowing reversible relative displacements and rotations.

Several deformation modes of this joint assembly can be identified, as described in the following. The relative translation in the axis current direction $\bar{u}_3$ generates a shearing deformation in the elastic layer and an associated resisting force $\bar{n}_3$ (Fig. 4.5). Assuming a small relative displacement $\bar{u}_3$ and hence an elastic linear behavior with stiffness $\bar{k}_3^n$, the hinge axial force can be obtained as:

$$\bar{n}_3 = \bar{k}_3^n \bar{u}_3 \tag{4-10}$$

The relative rotation in the axis direction $\bar{\theta}_3$ generates a friction resistant moment $\bar{m}_3$ in the axis current direction. The friction is considered here through an elastic-plastic model (Fig. 4.6). The relative rotation $\bar{\theta}_3$ is split
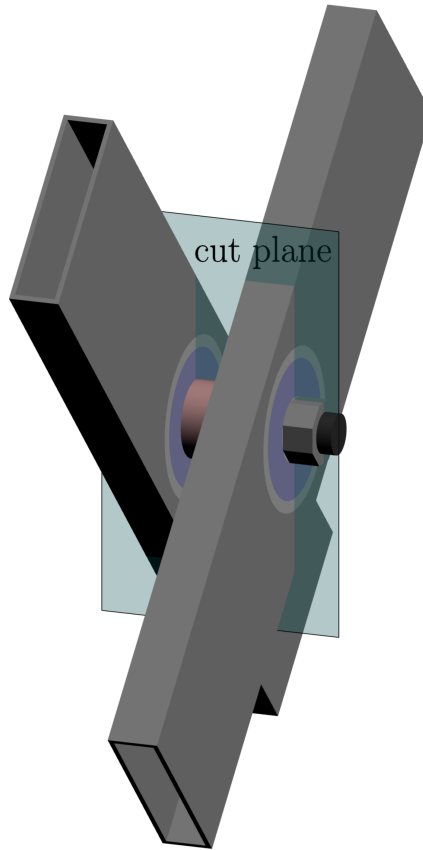
Figure 4.3: Hinge joint connecting two beams (3D representation).
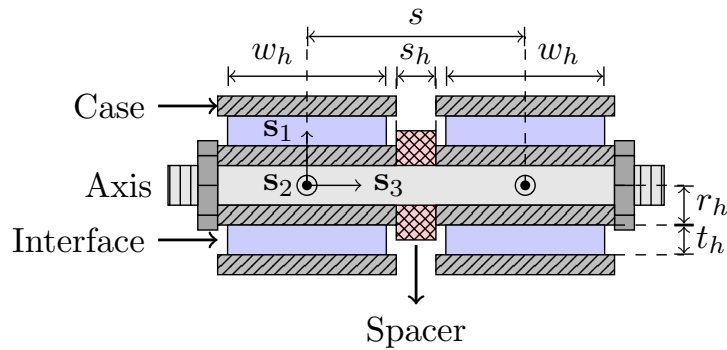
(a) cut view
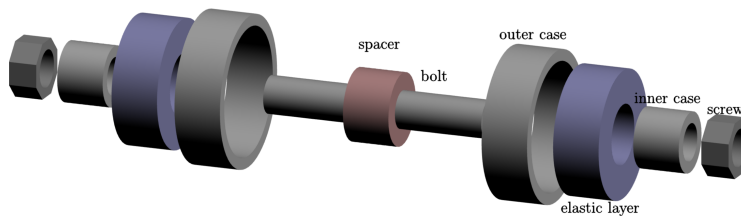
(b) components

Figure 4.4: Hinge detailed description.

into an elastic $\overline{\theta}_3^e$ and a plastic $\overline{\theta}_3^p$ part:

$$\overline{\theta}_3 = \overline{\theta}_3^e + \overline{\theta}_3^p \tag{4-11}$$
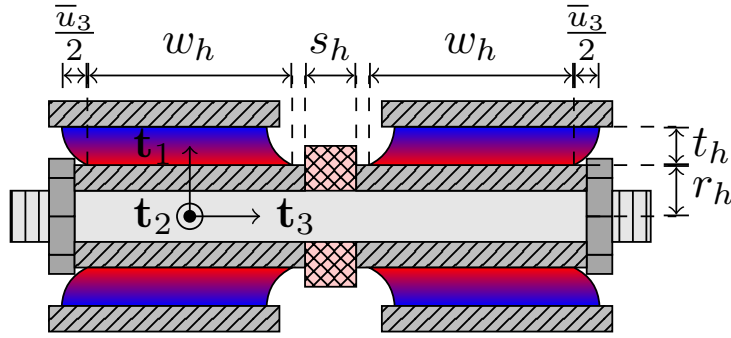
Figure 4.5: Hinge deformation due to the axial relative motion (cut view).
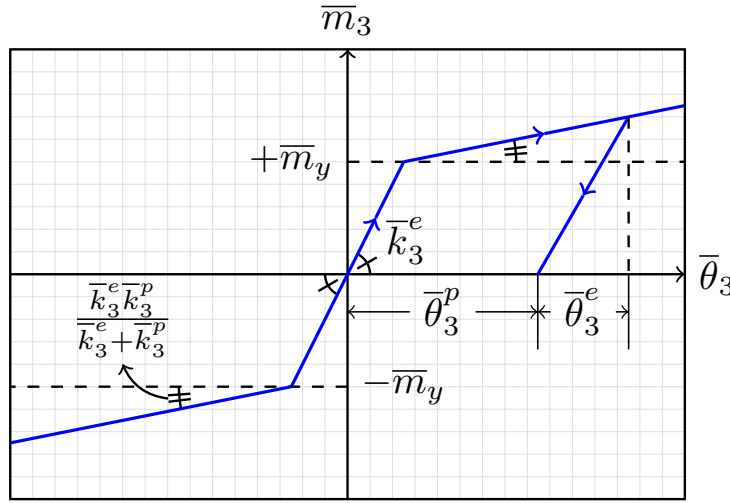
Figure 4.6: Hinge moment on the axis direction.

The axis moment $\overline{m}_3$ is related to the rotations through an elastic modulus $\overline{k}_3^e$ as:

$$\overline{m}_3 = \overline{k}_3^e \overline{\theta}_3^e = \overline{k}_3^e \left(\overline{\theta}_3 - \overline{\theta}_3^p \right) \tag{4-12}$$

This moment is also constrained to a yield curve f_p, which is a function of the initial yield moment $\overline{m}_y$, the plastic modulus $\overline{k}_3^p$ and the hardening parameter α_p according to:

$$f_p = |\overline{m}_3| - \left(\overline{m}_y + \overline{k}_3^p \alpha_p \right) \leq 0 \tag{4-13}$$

The plastic rotation $\overline{\theta}_3^p$ and the hardening parameter α_p are connected as:

$$\dot{\overline{\theta}}_3^p = \text{sign}(\overline{m}_3)\dot{\alpha}_p \tag{4-14}$$

In a solution step $n+1$, given $\overline{\theta}_{3,n+1}$, $\overline{\theta}_{3,n}^p$ and α_n, the new plastic state $\overline{\theta}_{3,n+1}^p$ and α_{n+1}, and the axis moment $\overline{m}_{3,n+1}$ and stiffness $\overline{k}_{33,n+1}^m$, can be

obtained following a standard return mapping routine [110]. The current plastic state $\overline{\theta}_{3,n}^p$ and α_n is stored in each joint as history variables. In this work the frictional behavior of the joints is restricted to a perfect plastic model, i.e. $\overline{m}_y = cte$ in the subsequent simulations.

The elastic layer acts in such a way that, in the beginning, when the triads $\mathbf{s}_i$, $\boldsymbol{\mu}_i$ and $\boldsymbol{\xi}_i$ are aligned, it offers an initial rotational stiffness $\overline{k}_0^m$ in the plane normal to the joint axis formed by $\mathbf{s}_1$ and $\mathbf{s}_2$. As a relative rotation perpendicular to the current axis ($\overline{\theta}_1$ and $\overline{\theta}_2$) takes place, the elastic nonlinear layer starts deforming (Fig. 4.7), increasing its stiffness. For a limit rotation $\overline{\theta}_l$, corresponding to the elastic layer material maximum deformation, the stiffness $\overline{k}_\alpha^m$ and resisting moment $\overline{m}_\alpha$ tend to infinity. This means that, the relative rotations in this plane are restricted to $|\overline{\theta}_\alpha| < \overline{\theta}_l$. The moments $\overline{m}_\alpha$ and rotational stiffness $\overline{k}_\alpha^m$ are described here by a cutoff model written as (see also Fig. 4.8):

$$\overline{m}_\alpha = \frac{1}{2}\overline{k}_0^m\overline{\theta}_l \ln\left(\frac{\overline{\theta}_l + \overline{\theta}_\alpha}{\overline{\theta}_l - \overline{\theta}_\alpha}\right) \tag{4-15}$$

$$\overline{k}_\alpha^m = \frac{\partial \overline{m}_\alpha}{\partial \overline{\theta}_\alpha} = \overline{k}_0^m\left(\frac{\overline{\theta}_l^2}{\overline{\theta}_l^2 - \overline{\theta}_\alpha^2}\right) \tag{4-16}$$
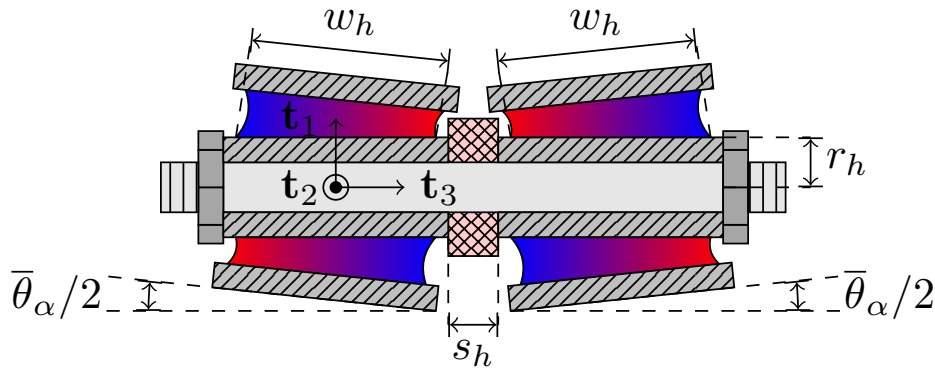
Figure 4.7: Hinge deformation due to relative rotation (cut view).

Analogously, the elastic layer can also deform due to the relative translations $\overline{u}_\alpha$ (Fig. 4.9) with an initial stiffness $\overline{k}_0^n$ in the original configuration. The translational resisting force $\overline{n}_\alpha$ and stiffness $\overline{k}_\alpha^n$ tends to infinity as the relative translation $\overline{u}_\alpha$ approaches the limit displacement $\overline{u}_l$, associated to an allowed maximum deformation. This constrains the relative translations to $|\overline{u}_\alpha| < \overline{u}_l$. The force $\overline{n}_\alpha$ and the translational stiffness $\overline{k}_\alpha^n$ are described by a cutoff model as:

$$\overline{n}_\alpha = \frac{1}{2}\overline{k}_0^n\overline{u}_l \ln\left(\frac{\overline{u}_l + \overline{u}_\alpha}{\overline{u}_l - \overline{u}_\alpha}\right) \tag{4-17}$$
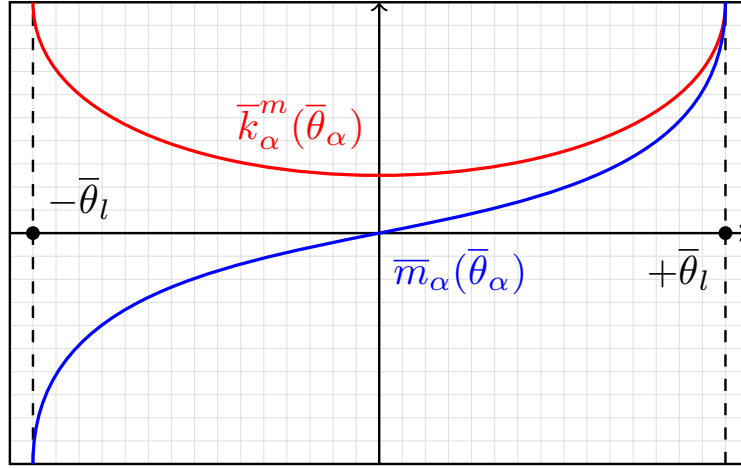
Figure 4.8: Hinge moment perpendicular to the axis.

$$\overline{k}_\alpha^n = \frac{\partial \overline{n}_\alpha}{\partial \overline{u}_\alpha} = \overline{k}_0^n \left(\frac{\overline{u}_l^2}{\overline{u}_l^2 - \overline{u}_\alpha^2} \right) \tag{4-18}$$
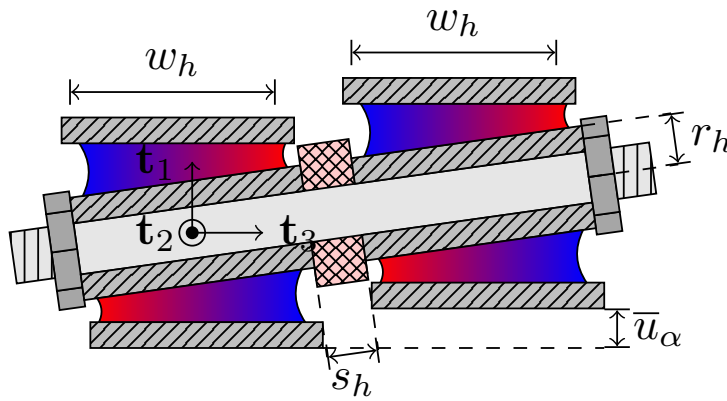
Figure 4.9: Hinge deformation due to relative motion (cut view).

4.3.2.2
Local to global internal forces

The joint local internal force is transformed to the global structural axes by equating the virtual work in both systems. From Eq. (4-6) and (4-9), the variation of the relative rotations $\delta\overline{\theta}_i$ and displacements $\delta\overline{u}_i$ components are given by:

$$\delta\overline{\theta}_i = \mathbf{q}_i^T \cdot (\delta\boldsymbol{\omega}_b - \delta\boldsymbol{\omega}_a) \tag{4-19}$$

$$\delta\overline{u}_i = \boldsymbol{\mu}_i^T \cdot (\delta\mathbf{x}_b - \delta\mathbf{x}_a) + \mathbf{w}_i^T \cdot \delta\boldsymbol{\omega}_a \tag{4-20}$$

Taking the increment of the displacement $\Delta\left(\delta\overline{u}_i\right)$ and rotation $\Delta\left(\delta\overline{\theta}_i\right)$

variation components results in:

$$\Delta\left(\delta\overline{u}_i\right) = \delta\boldsymbol{\omega}_a^T \cdot \widehat{\boldsymbol{\mu}}_i \cdot \left(\Delta\mathbf{x}_b - \Delta\mathbf{x}_a\right) - \ldots$$
$$- \left(\delta\mathbf{x}_b - \delta\mathbf{x}_a\right)^T \cdot \widehat{\boldsymbol{\mu}}_i \cdot \Delta\boldsymbol{\omega}_a + \ldots$$
$$+ \delta\boldsymbol{\omega}_a^T \cdot \left(\widehat{\mathbf{x}}_b - \widehat{\mathbf{x}}_a\right) \cdot \widehat{\boldsymbol{\mu}}_i \cdot \Delta\boldsymbol{\omega}_a \tag{4-21}$$

$$\Delta\left(\delta\overline{\theta}_i\right) = \left(\delta\boldsymbol{\omega}_a - \delta\boldsymbol{\omega}_b\right)^T \cdot \mathbf{Q}_i^a \cdot \Delta\boldsymbol{\omega}_a - \ldots$$
$$- \left(\delta\boldsymbol{\omega}_b - \delta\boldsymbol{\omega}_a\right)^T \cdot \mathbf{Q}_i^b \cdot \Delta\boldsymbol{\omega}_b \tag{4-22}$$

In the above equations, the rotation gradient $\mathbf{q}_i$ and translation gradient $\mathbf{w}_i$, and the rotation hessians $\mathbf{Q}_i^a$ and $\mathbf{Q}_i^b$, are given by:

$$\mathbf{w}_i = \boldsymbol{\mu}_i \times \left(\mathbf{x}_b - \mathbf{x}_a\right) \tag{4-23}$$

$$\mathbf{q}_i = \overline{g}_r\overline{\theta}_i\overline{\mathbf{n}}_r + \overline{f}_r\left(\boldsymbol{\xi}_j \times \boldsymbol{\mu}_k - \boldsymbol{\xi}_k \times \boldsymbol{\mu}_j\right) \tag{4-24}$$

$$\mathbf{Q}_i^a = \overline{g}_r\left(\overline{\mathbf{n}} \cdot \mathbf{q}_i^T + \mathbf{q}_i \cdot \overline{\mathbf{n}}_r^T - \overline{\theta}_i\mathbf{N}_a\right) + \ldots$$
$$+ \overline{h}_r\overline{\theta}_i\overline{\mathbf{n}}_r \cdot \overline{\mathbf{n}}_r^T + \overline{f}_r\left(\widehat{\boldsymbol{\xi}}_j \cdot \widehat{\boldsymbol{\mu}}_k - \widehat{\boldsymbol{\xi}}_k \cdot \widehat{\boldsymbol{\mu}}_j\right) \tag{4-25}$$

$$\mathbf{Q}_i^b = \overline{g}_r\left(\overline{\mathbf{n}} \cdot \mathbf{q}_i^T + \mathbf{q}_i \cdot \overline{\mathbf{n}}_r^T - \overline{\theta}_i\mathbf{N}_b\right) + \ldots$$
$$+ \overline{h}_r\overline{\theta}_i\overline{\mathbf{n}}_r \cdot \overline{\mathbf{n}}_r^T + \overline{f}_r\left(\widehat{\boldsymbol{\mu}}_k \cdot \widehat{\boldsymbol{\xi}}_j - \widehat{\boldsymbol{\mu}}_j \cdot \widehat{\boldsymbol{\xi}}_k\right) \tag{4-26}$$

Where the following variables are introduced:

$$\overline{f}_r = \frac{\overline{\theta}_r}{2\sin(\overline{\theta}_r)} \tag{4-27}$$

$$\overline{g}_r = \frac{1}{\overline{\theta}_r} - \cot(\overline{\theta}_r) \tag{4-28}$$

$$\overline{h}_r = 1 - \frac{2}{\overline{\theta}_r}\left(\frac{1}{\overline{\theta}_r} - \cot(\overline{\theta}_r)\right) \tag{4-29}$$

$$\mathbf{N}_a = \cot(\overline{\theta}_r)\overline{\mathbf{n}}_r \cdot \overline{\mathbf{n}}_r^T + \frac{\widehat{\boldsymbol{\xi}}_i \cdot \widehat{\boldsymbol{\mu}}_i}{2\sin(\overline{\theta}_r)} \tag{4-30}$$

$$\mathbf{N}_b = \cot(\overline{\theta}_r)\overline{\mathbf{n}}_r \cdot \overline{\mathbf{n}}_r^T + \frac{\widehat{\boldsymbol{\mu}}_i \cdot \widehat{\boldsymbol{\xi}}_i}{2\sin(\overline{\theta}_r)} \tag{4-31}$$

In the particular case where $\overline{\theta}_r \to 0$ the above expressions become indefinite, and so their limit is used in place:

$$\mathbf{q}_i = \left(\boldsymbol{\xi}_j \times \boldsymbol{\mu}_k - \boldsymbol{\xi}_k \times \boldsymbol{\mu}_j\right)/2 \tag{4-32}$$

$$\mathbf{Q}_i^a = \left(\widehat{\boldsymbol{\xi}}_j \cdot \widehat{\boldsymbol{\mu}}_k - \widehat{\boldsymbol{\xi}}_k \cdot \widehat{\boldsymbol{\mu}}_j\right)/2 \tag{4-33}$$

$$\mathbf{Q}_i^b = \left(\widehat{\boldsymbol{\mu}}_k \cdot \widehat{\boldsymbol{\xi}}_j - \widehat{\boldsymbol{\mu}}_j \cdot \widehat{\boldsymbol{\xi}}_k\right)/2 \tag{4-34}$$

The variation of the virtual work δU can now be expressed in terms of

the local and global systems:

$$\delta U = \overline{n}_i \delta \overline{u}_i + \overline{m}_i \delta \overline{\theta}_i \tag{4-35}$$

$$\delta U = \delta \mathbf{x}_a^T \cdot \mathbf{n}_a + \delta \boldsymbol{\omega}_a^T \cdot \mathbf{m}_a + \dots$$
$$+ \delta \mathbf{x}_b^T \cdot \mathbf{n}_b + \delta \boldsymbol{\omega}_b^T \cdot \mathbf{m}_b \tag{4-36}$$

Therefore, the internal force $\mathbf{f}$ may be obtained combining the equations above with Eqs. (4-19) - (4-20), as:

$$\mathbf{n}_a = -\overline{n}_i \boldsymbol{\mu}_i \tag{4-37}$$

$$\mathbf{n}_b = +\overline{n}_i \boldsymbol{\mu}_i \tag{4-38}$$

$$\mathbf{m}_b = +\overline{m}_i \mathbf{q}_i \tag{4-39}$$

$$\mathbf{m}_a = -\overline{m}_i \mathbf{q}_i + \overline{n}_i \mathbf{w}_i \tag{4-40}$$

Note that as the origin of the local system is set in $\mathbf{x}_a$ and a finite joint size is considered ($s = \|\mathbf{x}_b - \mathbf{x}_a\| > 0$), the eccentricity of the nodal force $\mathbf{n}_b$ acting on the opposing node generates an additional term in the moment $\mathbf{m}_a$ acting on the base node.

4.3.3
Derivation of the consistent tangent stiffness

The consistent tangent stiffness is required to ensure a quadratic convergence rate of the Newton-Raphson iterations of the solution procedure. The joint coherent tangent stiffness $\mathbf{K}$ can be obtained expressing the equality of the increment of the virtual work $\Delta(\delta U)$ in both the global and local systems:

$$\Delta(\delta U) = \delta \mathbf{d}^T \cdot \mathbf{K} \cdot \Delta \mathbf{d} \tag{4-41}$$

$$\Delta(\delta U) = \overline{k}_{ij}^n \delta \overline{u}_i \Delta \overline{u}_j + \overline{k}_{ij}^m \delta \overline{\theta}_i \Delta \overline{\theta}_j + \dots$$
$$+ \overline{n}_i \Delta(\delta \overline{u}_i) + \overline{m}_i \Delta(\delta \overline{\theta}_i) \tag{4-42}$$

With, $\overline{k}_{ij}^n = \partial \overline{n}_i / \partial \overline{u}_j$ and $\overline{k}_{ij}^m = \partial \overline{m}_i / \partial \overline{\theta}_j$. Combining the equations above with Eqs. (4-19) - (4-20) and (4-21) - (4-22), the joint stiffness $\mathbf{K}$ can be obtained as:

$$\mathbf{K} = \begin{bmatrix} \mathbf{K}_{11} & \mathbf{K}_{12} & \mathbf{K}_{13} & \mathbf{K}_{14} \\ \mathbf{K}_{21} & \mathbf{K}_{22} & \mathbf{K}_{23} & \mathbf{K}_{24} \\ \mathbf{K}_{31} & \mathbf{K}_{32} & \mathbf{K}_{33} & \mathbf{K}_{34} \\ \mathbf{K}_{41} & \mathbf{K}_{42} & \mathbf{K}_{43} & \mathbf{K}_{44} \end{bmatrix} \tag{4-43}$$

$$\mathbf{K}_{11} = \mathbf{K}_{33} = +\overline{k}_{ij}^n \boldsymbol{\mu}_i \cdot \boldsymbol{\mu}_j^T \tag{4-44}$$

$$\mathbf{K}_{13} = \mathbf{K}_{31} = -\overline{k}_{ij}^{n}\boldsymbol{\mu}_i \cdot \boldsymbol{\mu}_j^{T} \tag{4-45}$$

$$\mathbf{K}_{32} = +\overline{k}_{ij}^{n}\boldsymbol{\mu}_i \cdot \mathbf{w}_j^{T} - \overline{n}_i\widehat{\boldsymbol{\mu}}_i \tag{4-46}$$

$$\mathbf{K}_{23} = +\overline{k}_{ij}^{n}\mathbf{w}_i \cdot \boldsymbol{\mu}_j^{T} + \overline{n}_i\widehat{\boldsymbol{\mu}}_i \tag{4-47}$$

$$\mathbf{K}_{12} = -\overline{k}_{ij}^{n}\boldsymbol{\mu}_i \cdot \mathbf{w}_j^{T} + \overline{n}_i\widehat{\boldsymbol{\mu}}_i \tag{4-48}$$

$$\mathbf{K}_{21} = -\overline{k}_{ij}^{n}\mathbf{w}_i \cdot \boldsymbol{\mu}_j^{T} - \overline{n}_i\widehat{\boldsymbol{\mu}}_i \tag{4-49}$$

$$\mathbf{K}_{24} = -\overline{k}_{ij}^{m}\mathbf{q}_i \cdot \mathbf{q}_j^{T} - \overline{m}_i\mathbf{Q}_i^{b} \tag{4-50}$$

$$\mathbf{K}_{42} = -\overline{k}_{ij}^{m}\mathbf{q}_i \cdot \mathbf{q}_j^{T} - \overline{m}_i\mathbf{Q}_i^{a} \tag{4-51}$$

$$\mathbf{K}_{44} = +\overline{k}_{ij}^{m}\mathbf{q}_i \cdot \mathbf{q}_j^{T} + \overline{m}_i\mathbf{Q}_i^{b} \tag{4-52}$$

$$\mathbf{K}_{34} = \mathbf{K}_{14} = \mathbf{K}_{43} = \mathbf{K}_{41} = \mathbf{0} \tag{4-53}$$

$$\mathbf{K}_{22} = +\overline{k}_{ij}^{n}\mathbf{w}_i \cdot \mathbf{w}_j^{T} + \overline{k}_{ij}^{m}\mathbf{q}_i \cdot \mathbf{q}_j^{T} + \dots$$
$$+ \overline{n}_i\left(\widehat{\mathbf{x}}_b - \widehat{\mathbf{x}}_a\right) \cdot \widehat{\boldsymbol{\mu}}_i + \overline{m}_i\mathbf{Q}_i^{a} \tag{4-54}$$

In the above equations, the terms involving the local stiffness $\overline{k}_{ij}^{n}$ and $\overline{k}_{ij}^{m}$ represent the material stiffness, while the terms involving local forces $\overline{n}_i$ and moments $\overline{m}_i$ represent the geometric stiffness. As expected, the material part is related to the deformation of the joint and preserves the symmetry of the local stiffness $\overline{k}_{ij}^{n}$ and $\overline{k}_{ij}^{m}$. However, the geometric part is related to the rigid body motion of the joint and is not symmetric. This is associated to the lack of commutation property of 3D rotations.

4.4
Validation of the formulation

4.4.1
Incorporating friction

In order to validate the friction model and the large rotations implementation, the joint formulation (and the beam formulation as given in Appendix C) are applied to a single scissor-like element shown in Fig. 4.10. Considering the beams to be rigid with a length $2L$, having no separation of the midaxes ($s = 0$) and a perfect plastic frictional behavior of the hinge ($\overline{k}_3^e \approx \infty$ and $\overline{k}_3^p = 0$), with yield moment $\overline{m}_y$, the system response may be obtained from equilibrium considerations as:

$$P(\theta) = \frac{\overline{m}_y}{L}\sec\left(\frac{\theta}{2}\right) \tag{4-55}$$

In the numerical model, the beams have length $L = 1$ m, are made of steel with elastic modulus $E = 200$ GPa and Poisson's ratio $\nu = 0.30$, with a rectangular cross section with 4 cm height and 1 cm width. The joint yield
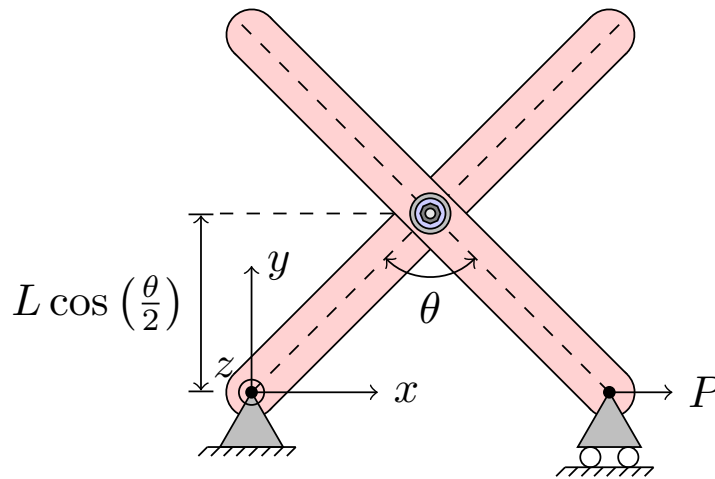
Figure 4.10: Scissor-like element opening with lateral force.

moment is $\overline{m}_y = 1$ Nm and the rotational stiffness are $\overline{k}_3^e = 100$ kNm/rad. A value of $\overline{k}_3^p$ slightly superior to zero was taken to ease the convergence of the computation.

Starting from a closed module ($\theta = 0$), the yield moment $\overline{m}_y$ generates a friction resistance and a force $P(0) = m_y/L$ has to be applied to initiate the motion. As the module opens, the vertical distance between the joint and the load application point decreases and a higher force $P(\theta)$ is required to equilibrate the friction moment $\overline{m}_y$. The numerical results, with one element per beam half length, are favorably compared with the analytical solution in Fig. 4.11.
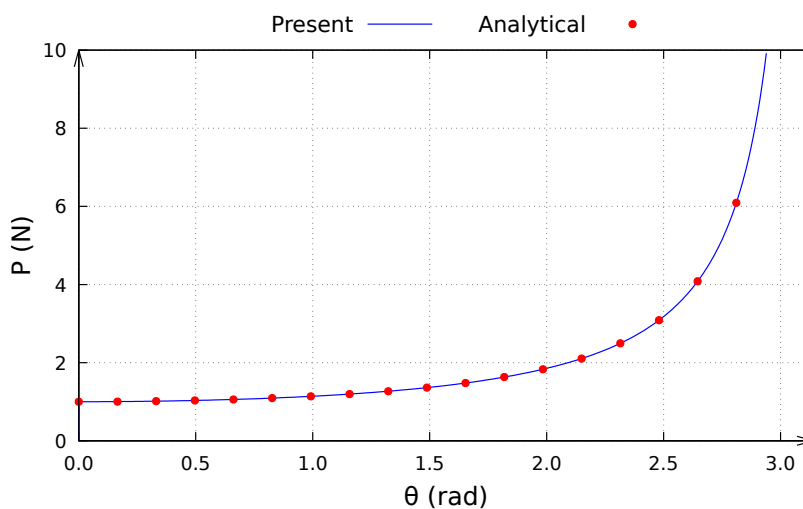
Figure 4.11: Scissor-like element equilibrium path.

4.4.2
Rotational flexibility

The rotational flexibility perpendicular to the joint axis and the elastic nonlinear behavior of the hinge layer are now validated applying the joint element to the two beams system shown in Fig. 4.12a. The beams are considered as rigid, meaning that the hinge nodes relative rotation θ is a direct consequence of the compliance of the elastic layer, when subjected to the torsion moment m. From equilibrium considerations, the system response may be stated as:

$$m = \frac{1}{2}\bar{k}_0^m \bar{\theta}_l \ln\left(\frac{\bar{\theta}_l + \theta}{\bar{\theta}_l - \theta}\right) \tag{4-56}$$

(a) torsion moment

(b) axial force
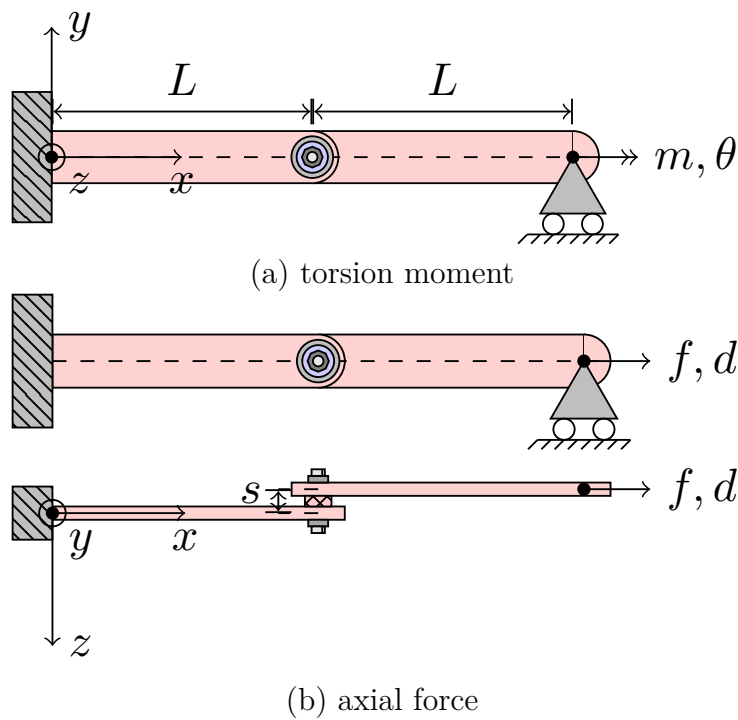
Figure 4.12: Two beam hinged system.

In the computation, the beams have a length $L = 1$ m and are made of the same material and cross section as before. The joint rotational initial stiffness is $\bar{k}_0^m = 1$ Nm/rad and the limit rotation is $\bar{\theta}_l = 10°$ ($\pi/18$ rad).

With the deformation of the elastic layer, the applied torque f increases, tending to infinite as the rotation d approaches the limit $\bar{\theta}_l$, as expected. The numerical results, with one element per beam half length, match the analytical solution in Fig. 4.13, where the dashed line represents the limit rotation $\bar{\theta}_l$.
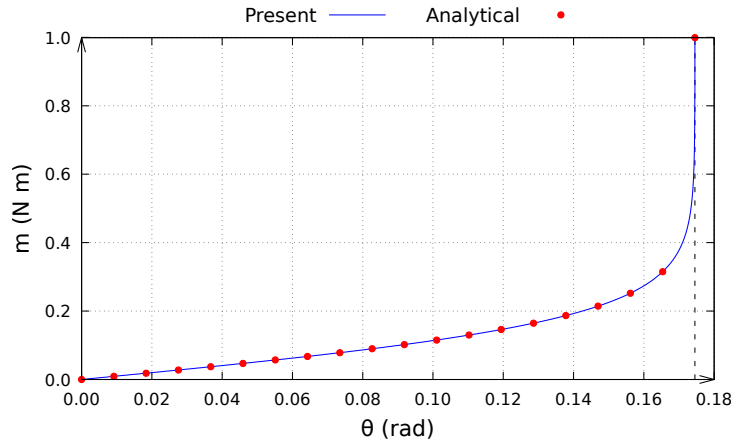
Figure 4.13: Equilibrium path of the two beam system subjected to a torsion moment.

4.4.3
Translational flexibility

The translational flexibility in the elastic nonlinear behavior of the hinge layer is now validated considering an axial force f and the generated displacement d in the two beam system (Fig. 4.12b). Again, the beams are considered rigid, meaning that the hinge nodes relative motion d is a direct consequence of the elastic layer flexibility. From equilibrium considerations, the system response may be stated as:

$$f = \frac{1}{2}\overline{k}_0^n \overline{u}_l \ln\left(\frac{\overline{u}_l + d}{\overline{u}_l - d}\right) \tag{4-57}$$

In the simulation, the beams have a length $L = 1$ m and are made of the same material and cross section as before. The joint's translational initial stiffness is $\overline{k}_0^n = 1$ N / m and the limit translation is $\overline{u}_l = 1$ cm. The distance between the beams midaxis are assumed to be $s_1 = 1$ cm and $s_2 = 2$ cm.

With the deformation of the elastic layer, the applied force f increases, tending to infinite as the displacement d approaches the limit $\overline{u}_l$, as expected. The numerical results, with one element per beam, match the closed form solution in Fig. 4.14, where the dashed line represents the limit displacement $\overline{u}_l$. The midaxis distance s creates an eccentricity of the force f and generates a bending moment $f \times s$ in the beam on the left, which is captured by the joint formulation in the numerical analysis.
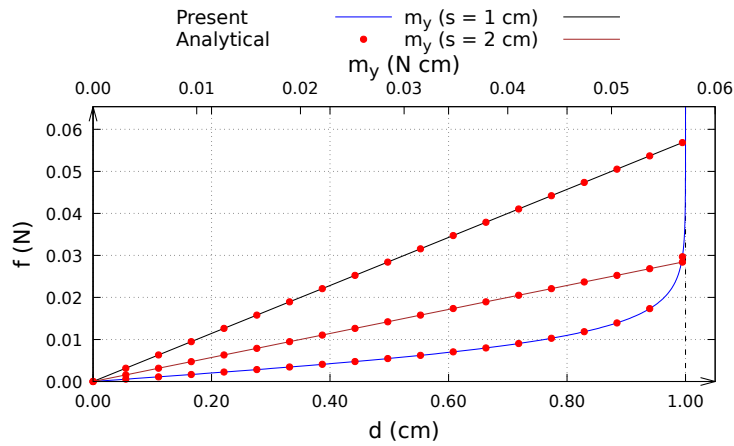
Figure 4.14: Equilibrium path of the two beam system subjected to an axial force.

4.5
Transformation of a single flat bistable module

In this Section, the proposed corotational joint formulation is used to analyse a square deployable module (Fig. 4.15). This module, has been studied in many research contributions ([21], [102], [22], [111], [104], [112], [113] and [103]) to investigate the behavior of bistable deployable scissor structures. The influence on the transformation response of the self weight, joint friction and stiffness, hub size, beam and spacer thickness (influencing *s*) are investigated here. In all simulations, the beams remain elastic, ensuring the reversibility of the transformation. The beams half-length are modeled with five finite elements, which is a converged mesh. The cylindrical arc-length method (Sec. D.1.1) is used as a continuation method in the static nonlinear solver.
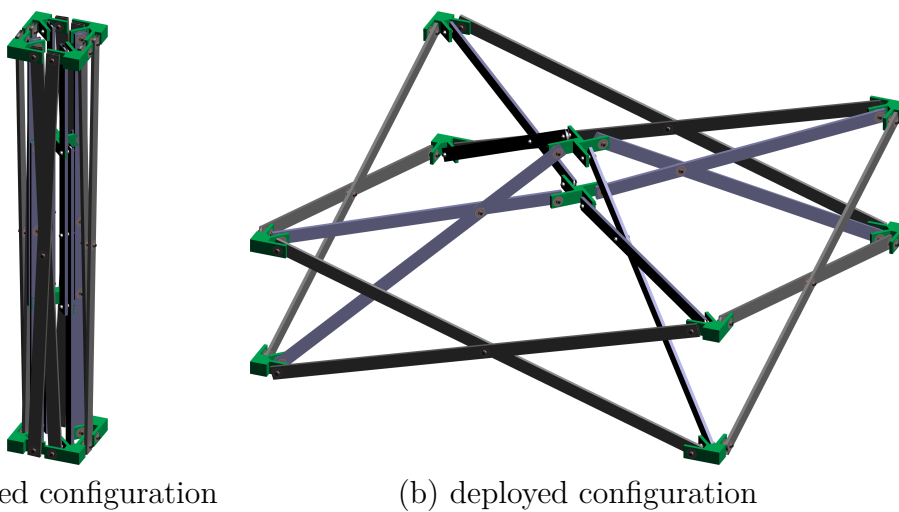
(a) folded configuration   (b) deployed configuration

Figure 4.15: Deployable module.

Material parameters that are different from the ones chosen in the

previous literature are selected, aiming for a civil engineering application. The inner and outer diagonal scissor-like elements are assumed to be made of aluminum, with elastic modulus 70 GPa, Poisson's ratio 0.35 and a specific mass of 2700 kg/m^3. All elements have a hollow rectangular cross-section, with width 1 cm, height 4 cm and thickness 1 mm. The central and outer hubs, connecting the beams, are modeled as a rigid grid of beam elements. Initially, the joints are considered frictionless ($\overline{m}_y = \overline{k}_3^p = 0$) and, a high rotational ($\overline{k}_0^m = 100$ kNm/rad) and translational ($\overline{k}_0^n = 100$ kN / m) stiffnesses are chosen to model rigid links.

4.5.1
Geometric design

The deployable module dimensions are shown in Fig. 4.16. The model is constructed using the geometric design principles proposed by [22], respecting the condition of zero deformation energy in the deployed and folded configurations. With the transformation, the volume occupied by the module in the folded configuration is dramatically reduced if compared with the deployed configuration. Here, the chosen basic dimensions are $L = 1.00$ m, $h_1 = 0.50$ m and $h_2 = 0.40$ m. A hub size of $r = 5$ cm is selected to allow the connection of all beam elements to the hub. As a new feature from the joint formulation, a spacing $s = 2$cm representing the beams and joints thickness is introduced.
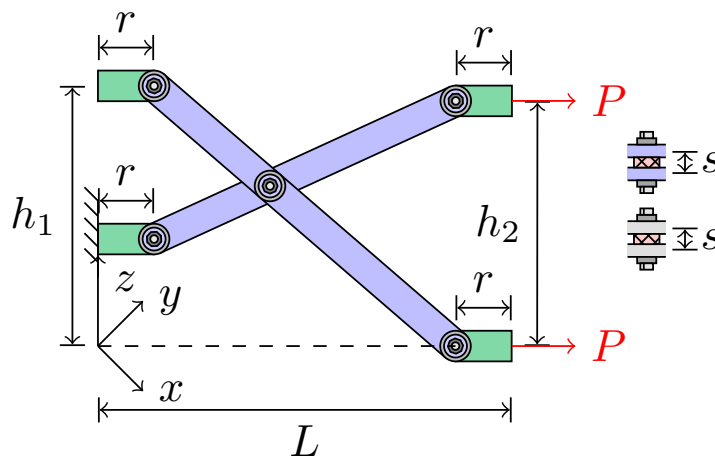
Figure 4.16: Diagonal scissor module dimensions and boundary conditions.

4.5.2
Transformation

The displacements and rotations in the middle node of the lower central hub are fixed. A horizontal force P is applied in the diagonal direction of each central node of the side hubs. The vertical translation of the central hub w

is used as a measure of the efficiency of the transformation, since it is related to the volume change between the configurations. In the numerical model, each beam is discretized in four finite elements, which was verified to be a converged mesh for the investigated problem. Initially, the hub size, as well as the joint and beam thickness are neglected ($r = s = 0$), as in [22] for the sake of simplicity and to define a reference case. However, in the present work the module self weight is taken into account, since it is always present in civil engineering applications.

Fig. 4.17 shows the equilibrium path during the deployment and folding operations. Initially, in the deployed configuration, the self weight deforms the module, generating a downward displacement of $w = -0.08$ cm. During folding, the gravitational loads act against the deployment, with a limit load $P = 441$ N at $w = 2.90$ cm. After the limit point, the system becomes unstable and the load starts decreasing, vanishing at $w = 14.8$ cm. The loads keeps decreasing, reaching a minimum load of $P = -31.0$ N at $w = 21.3$ cm further followed by an increase until the folded state is reached. The results obtained were compared with [21], yielding a good match.

For the sake of completeness, a simulation without gravity loads was also performed to assess the influence of self weight on the transformation. The curve neglecting gravity is close to the one taking self weight into account for this light structure (with a total mass of 5.5 kg). The area between the curves with and without gravity loads can be interpreted as the work done by those forces. As gravity loads are always present in civil engineering applications, all further results presented consider the self weight.

During the transformation (deployment or folding), the beams deform and buckle, defining the structural response. As expected in an elastic response, the deployment (D) and folding (F) processes follow the same equilibrium path. The dashed line in all figures represents the ideal, theoretical displacement corresponding to a fully folded configuration, determined using a rigid wireframe model [22] for which the module fully closes into a line. During the deployment, the inner and outer elements then buckle in-plane, i.e. in the common plane of the connected beams.

4.5.3
Joints friction effect

To assess the influence of friction on the module response, the joints friction moment limit $\overline{m}_y$ is chosen to vary from 1 Nm up to 5 Nm, corresponding to approximately 1% of the peak bending moment in the beams during the transformation (331 Nm), while still neglecting the hub size and
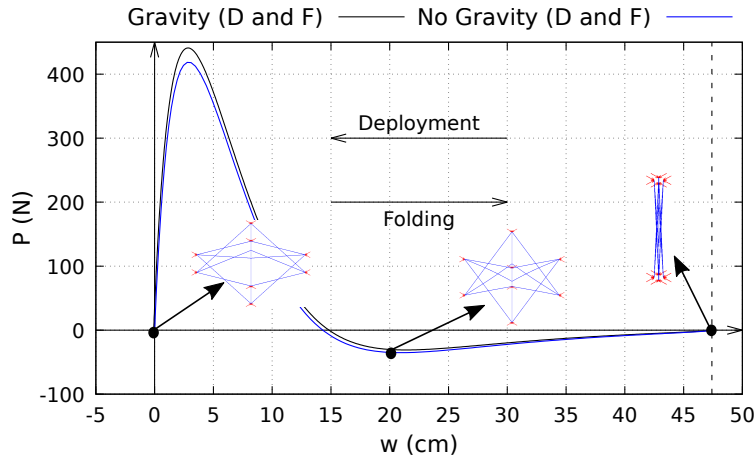
Figure 4.17: Deployable module transformation response in the reference case.

beams thickness ($r = s = 0$). The chosen frictional behavior is rigid perfectly plastic ($\overline{k}_3^e = 1$ kNm / rad and $\overline{k}_3^p = 1$ Nm/rad). Figure 4.18 shows the effect of the friction on the transformation response. As expected, while folding, the maximum load required for the deployment increases with the friction limit moment and all the curves with friction are above the frictionless result. Analogously, during the deployment, the maximum load required for the deployment increases in absolute value, as the friction moment acts against the motion of the module. The differential area between frictional and frictionless curves represents the work done by friction, dissipating energy during the transformation. The load negative part of the equilibrium path reduces with the presence of the friction moment during the folding process, and increases during the deployment.
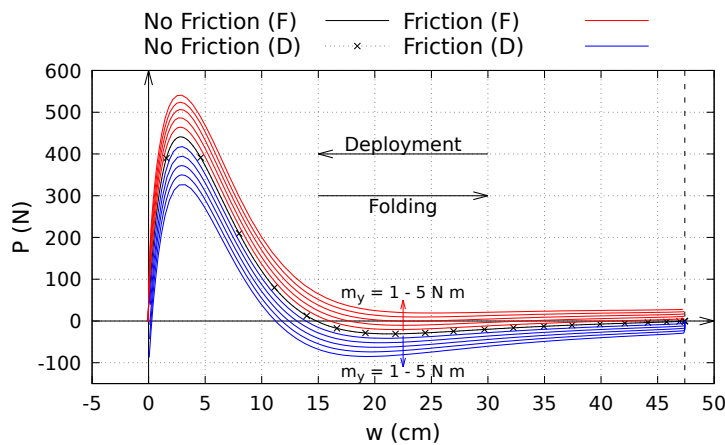
Figure 4.18: Friction effect on the deployable module transformation.

The module behavior during deployment (D) and folding (F) is shown in Fig. 4.19. As could be expected, without friction, the system response is elastic and the deployment and folding paths are equal. With friction ($\overline{m}_y = 5$Nm),

the hinge axis moment always opposes the motion, and changes its sign in the beginning of deployment, causing a load jump near the fully closed state (dashed line).
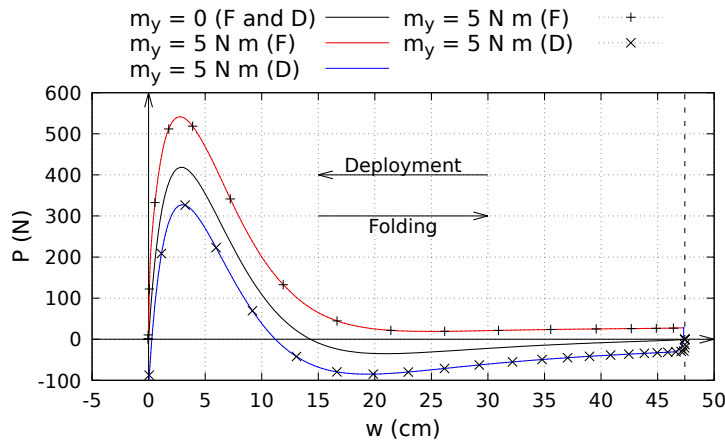
Figure 4.19: Deployable module loading and unloading with friction.

4.5.4
Hub size influence

The effect of the hub size (r) on the structural response is considered separately in Fig. 4.20. Considering $r \neq 0$ the geometric design is altered to respect the bistable condition, i.e. the structure is redesigned to the new geometric condition. The peak load is increased to 678 N at $w = 2.92$ cm for $r = 5$ cm, which represents an increment of 54% relative to the result with $r = 0$ cm. This is associated to the fact that, considering the hub size (r) with the other geometric parameters (L, h_1 and h_2) fixed, the length of the inner and outer beams is reduced, increasing their resistance to the in-plane buckling that controls the deployment. After the local maximum, the load starts decreasing, vanishing at $w = 16.9$cm. Then, the load continues decreasing until reaching a local minimum of $P = -26.7$ N at $w = 23.1$ cm. After, the load starts increasing, but passes by another local minimum of $P = -44.9$ N at $w = 39.2$ cm before vanishing as the module closes at $w = 39.6$cm.

It is interesting to note that the hub size also reduces the displacement w corresponding to the fully closed configuration, resulting in a less compact folded configuration. Again, the inner and outer beam elements buckle in-plane and, as could be expected, the deployment (D) and folding (F) processes follow the same path. As a finite hub size is always present, being a requirement for the assembly of the structural elements, all further results presented in this work consider $r = 5$ cm.
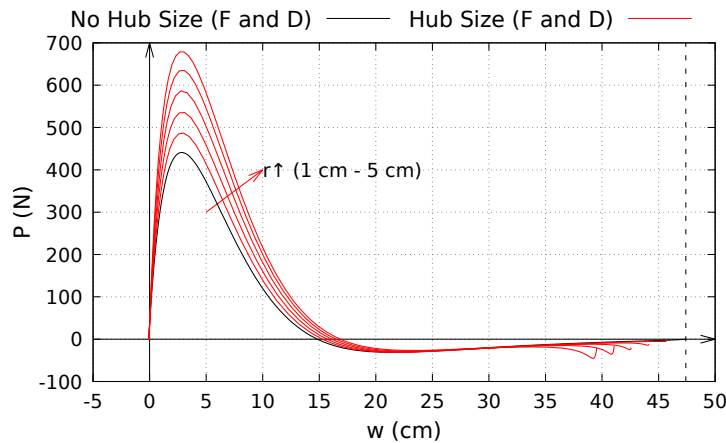
Figure 4.20: Hubs size effect on the module response.

4.5.5
Beam and joint thickness effect

As a new feature provided by the joint formulation, the effect of the beam and joint thickness on the structural response is shown in Fig. 4.21. Considering the beams thickness ($s = 1$ cm), the peak load is reduced to 245N at $w = 1.11$cm, only 36% of the one in Section 4.5.4. This significant load decrease is explained by the out of plane buckling of the inner and outer beam elements that generates a twist in the module. Bending moments appear, generated by the axial forces in the connected beams due to the midaxes separation s, changing the buckling mode from in-plane to out of plane buckling. In some real life models, this effect is also observed, as illustrated in Fig. 4.22. After the local maximum, the load starts decreasing, vanishing at $w = 17.1$cm. As before, the load continues decreasing until reaching a local minimum of $P = -20.1$N at $w = 25.5$cm. After, the load starts increasing, but passes by another local minimum of $P = -44.9$ N at $w = 39.2$ cm before vanishing as the module closes at $w = 39.6$cm. When considering the joint spacer ($s = 2$ cm) the beams midaxes are further separated and the generated eccentricity increases. The module is then more prone to the out of plane buckling and the peak load is slightly reduced to $P = 233$ N at $w = 1.60$ cm.

As observed in the curves with $s = 1$ cm and $s = 2$ cm in Fig. 4.21, the magnitude of the separation of the beams midaxis s have only a small influence on the peak load of the transformation. Numerical simulations with $s = 0.1$ cm provided a peak load of 257 N. This is due to the fact the a small separation is able to activate numerically the out-of-plane buckling of the beam elements, which is responsible for the harsh decrease on the peak load. This result is similar to the bifurcation of the pyramidal truss module studied in Sec. 2.4.3.2, where a small imperfection is added in the model in

order to numerically capture the instability.

The system buckles in the elastic regime, therefore the deployment (D) and folding (F) processes follows the same path. As the beams and joints thickness are always present, all further results presented in this work consider $s = 2$ cm, in addition to other effects. In some applications, the out of plane buckling can be a desired effect since the peak load required for the transformation decreases significantly and may eliminate the need of machine driven transformation. Hence, the spacer size could be considered as a design parameter.
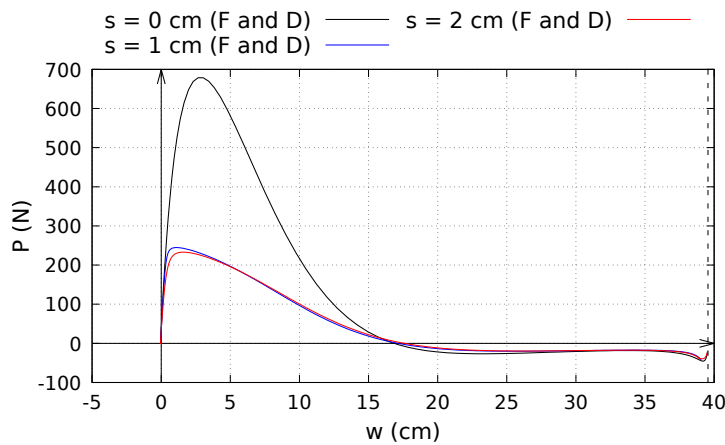
Figure 4.21: Beams and joints thickness effect on the module response.

4.5.6
Joints stiffness influence

The effect of the joints stiffness $(\overline{k}_0^m)$ on the structural response is shown in Fig. 4.23. With the out of plane buckling, the hinges are subjected to bending moments and the joints stiffness has a significant impact on the maximum load required for the transformation. A higher joint stiffness hinders while a low joint stiffness promotes the out of plane buckling of the inner scissor-like elements. For $\overline{k}_0^m = 2$ kNm, the peak load is reduced to 194N at $w = 1.79$cm, only 79% of the one observed in Section 4.5.5. After the peak load point, all curves approach the one with $\overline{k}_0^m = 100$ kNm as the module continues to transform and the twist generated by the out of plane buckling is reduced. This effect not only compensates for manufacturing imperfections, but is useful to reduce the peak load required for the transformation and hence could be a design parameter for future designs.
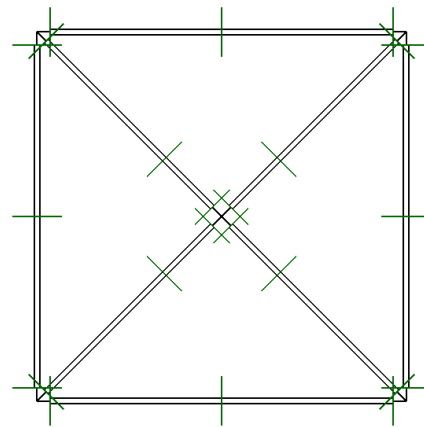
(a) deployed
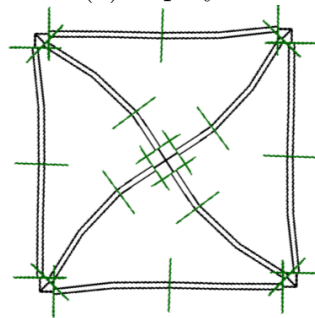
(b) intermediate
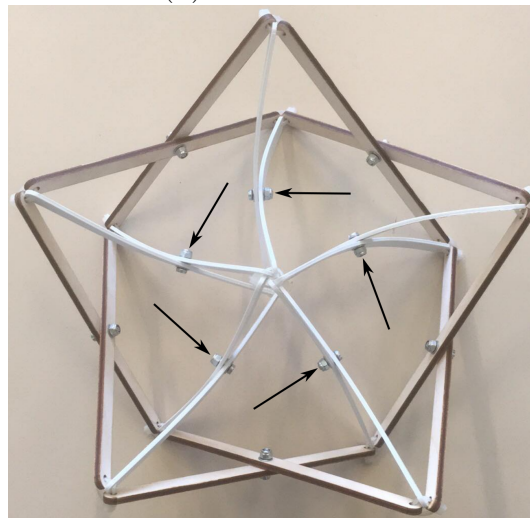
(c) real toy module during transformation

Figure 4.22: Deployable module configurations.

4.6
Transformation of flat bistable deployable structures

In this Section assemblies of the flat bistable deployable module analyzed in the previous section are investigated to illustrate the nonlinear behavior of more complex structures. The material, joints, cross section properties and geometric design of the modules are the same as in Section 4.5. Initially, the joints are considered frictionless. As verified in [21], the model choice of joints
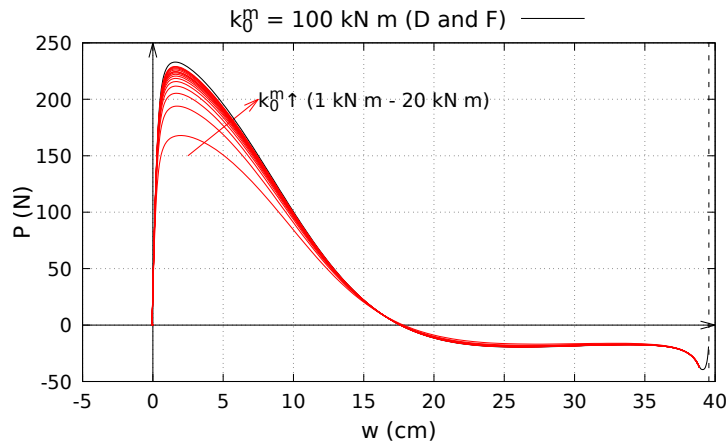
Figure 4.23: Joints stiffness effect on the module response.

as flexible elements partly accommodates the imperfections that the structural system may exhibit.

Two types of assembly alternatives are adopted. In the first one the modules are connected continuously one after the other, sharing edges (Fig. 4.24a). In the second one the modules are connected by plates (modeled here by a rigid network) leading to a fully module-based structure (Fig. 4.24b). In this case, the rectangular plates connecting the modules are considered to have a size of 5 cm.

The inner scissor-like elements can be connected to the hubs according to two configurations (Fig. 4.25). The first orientation $(+)$ causes the module beams and joints to be twisted in the positive z direction (Fig. 4.16) during the transformation, while the second orientation $(-)$ causes the twisting to be in the opposite direction. When forming structural systems composed of 1D or 2D arrays of the deployable modules, the twisted orientation can be chosen to be uniform or alternate along the structure (Fig. 4.26). During the numerical simulations it was verified that in both cases the maximum bending moments occurs in the inner diagonal elements of the modules. However, the alternate approach results in lower bending moments acting on the connecting plates (modular built) and hubs (single built), as the efforts on neighbor modules tend to equilibrate with one another. Therefore, in the following numerical simulations the alternate approach is used.

4.6.1
1D assembly

The simplest assembly of the deployable modules in terms of kinematics is the line structure shown in Fig. 4.27. It consists of a linear array of modules. The structure is supported on the bottom and on one side, while pushed (or
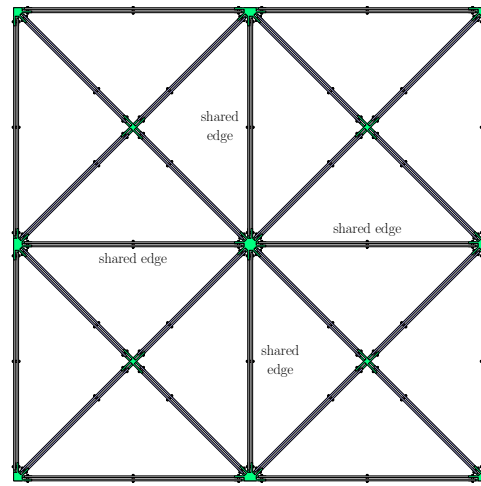
(a) Single built assembly
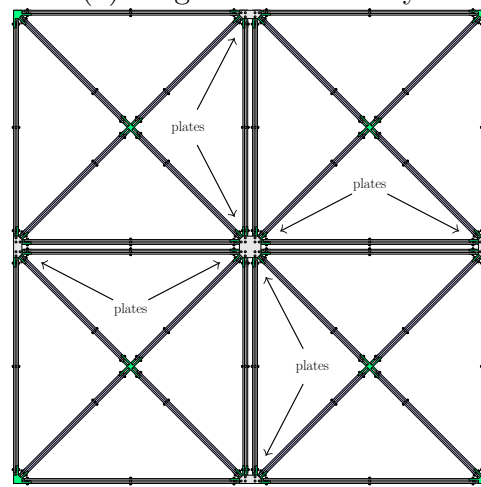
(b) Modular assembly

Figure 4.24: Assembly alternatives in a 2 x 2 grid.

$(+)$ $(-)$
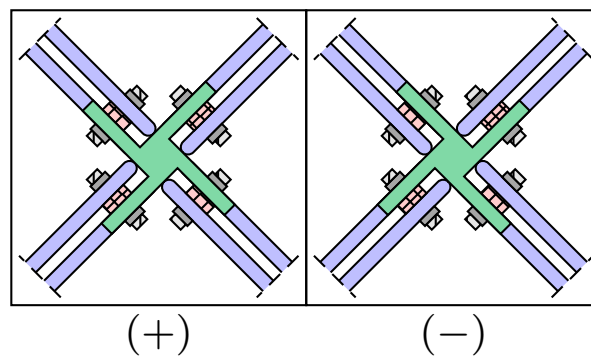
Figure 4.25: Modules twist direction.

pulled) on the other extremity during the folding (or deployment) process.

Figure 4.28 shows the effect of the number of modules on the structural response for both single built and modular approaches. The horizontal

(+)	(+)	(+)	(+)	(+)
(+)	(+)	(+)	(+)	(+)
(+)	(+)	(+)	(+)	(+)
(+)	(+)	(+)	(+)	(+)
(+)	(+)	(+)	(+)	(+)

(a) Uniform twist

(+)	(−)	(+)	(−)	(+)
(−)	(+)	(−)	(+)	(−)
(+)	(−)	(+)	(−)	(+)
(−)	(+)	(−)	(+)	(−)
(+)	(−)	(+)	(−)	(+)

(b) Alternate twist

Figure 4.26: Assembly twist alternatives in a 5 x 5 grid.

translation of the loaded hubs u is used as a measure of the efficiency of the transformation. As expected, the number of modules has a small influence on the peak load, as the line assembly transfers the efforts from one module to the next like a set of springs connected in series. For the single built assembly the peak load is 2.80 kN and for the modular assembly it is 3.28 kN (15% higher). In both cases, the system is subjected to a lateral instability when 5 modules are used, characterized by a small snap-back in the control displacement u and leading to a non uniform deployed state of the modules during some stages of the transformation. The first peak load (positive) occurs approximately for the same displacement in all cases, while the second peak load (negative) position varies as a function of the number of modules.

The single built approach results in lighter structural system, as there

(a) folded   (b) deployed
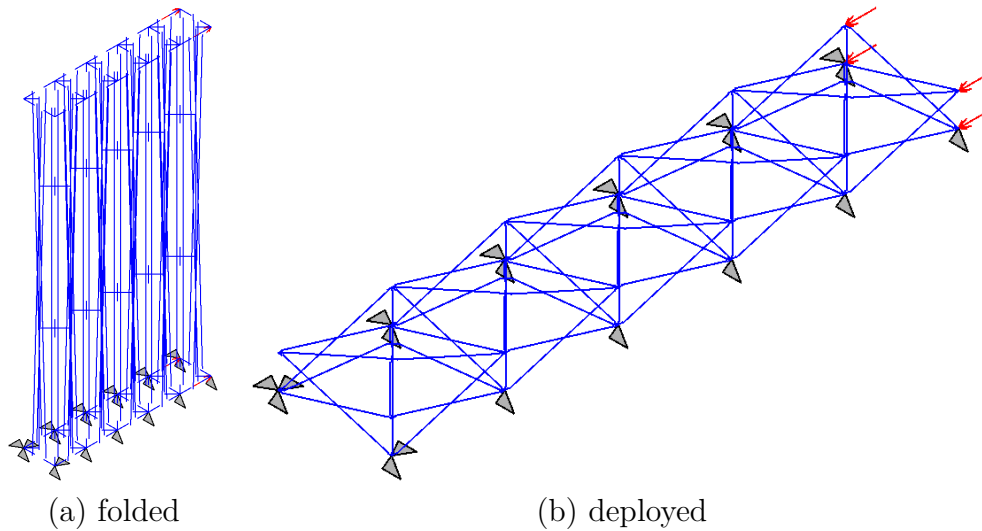
Figure 4.27: 1D assembly of the deployable modules.

(a) Continuous assembly

(b) Modular assembly
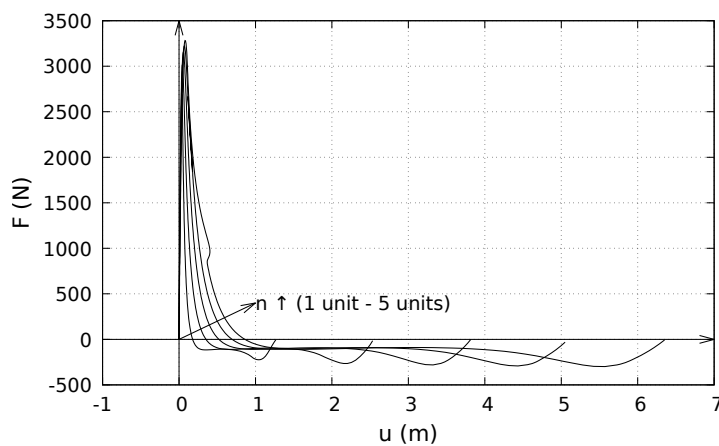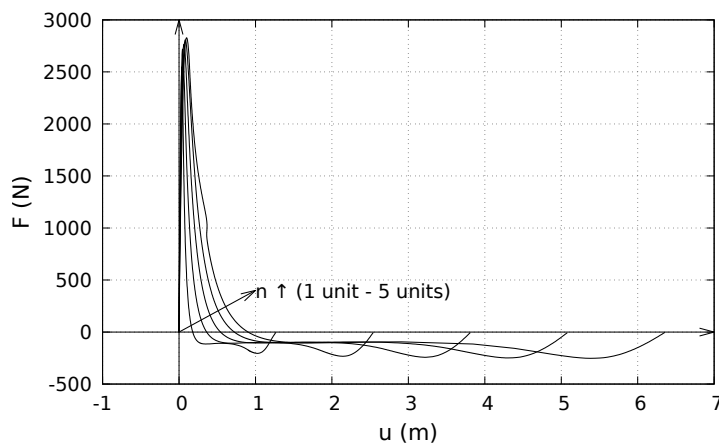
Figure 4.28: Number of modules influence on the 1D assembly.

are no connection plates and less structural elements are present, since the modules share edges with each other. Also, the structure is more compact, since the dimensions of the plates on the modular approach influences the

size of the system in the folded configuration. However, the modular approach resulting in an easier maintenance of the system as individual modules can be replaced in case of damage or general malfunction.

4.6.2
2D assembly

The deployable modules are now assembled in a 2D array forming a hanging wall (Fig. 4.29). The modules are fixed on one side and at the top, with the gravitational loads acting downwards, while pushed (or pulled) on the bottom during the folding (or deployment) process. The modular assembly approach is applied.

(a) top view

(b) folded   (c) deployed
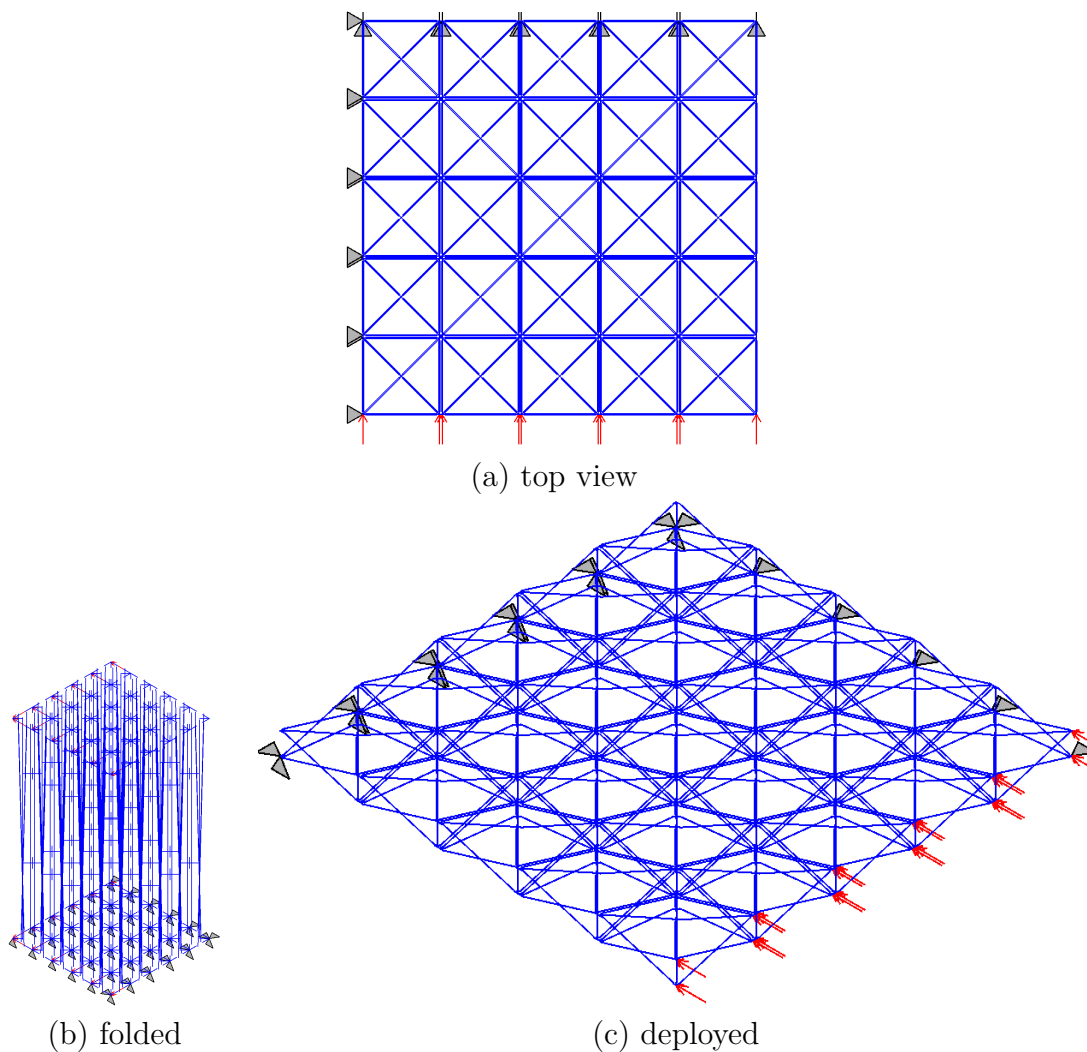
Figure 4.29: 2D assembly of the deployable modules.

Figure 4.30 shows the effect of the number of modules on the structural response. The vertical translation of the loaded hubs w is used as a measure of the efficiency of the transformation. In this case, the number of modules has a considerable influence on the peak load, as the modules interact not only with

others in the same line series but also with those in parallel. For $n = 1$ unit the peak load is 2.66 kN, while for $n = 5$ modules in each direction the peak load reaches 18.52 kN. Once more, the system is subjected to a lateral instability for $n = 5$ and the first peak load (positive) occurs approximately at the same displacement in all cases, while the second peak load (negative) position and magnitude varies as a function of the number of modules.
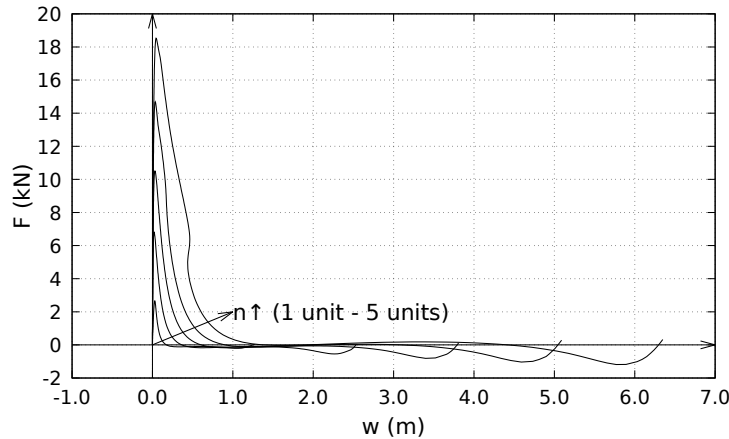
Figure 4.30: Number of modules influence on the 2D assembly.

The influence of the joints friction on the structural response is shown in Fig. 4.31, considering $n = 2$ modules in each direction. As for the single modules, the joints friction moment limit $\overline{m}_y$ is chosen to vary from 1Nm up to 5Nm with a rigid perfectly plastic behavior ($\overline{k}_3^e = 1$ kNm / rad and $\overline{k}_3^p = 1$Nm/rad). As expected, the peak load increases with the friction limit moment and all the curves with friction are above the frictionless result, as the friction moment acts against the motion of the module. The load negative part of the equilibrium path reduces with the presence of the friction moment during the folding process, as a result of the work done by friction.
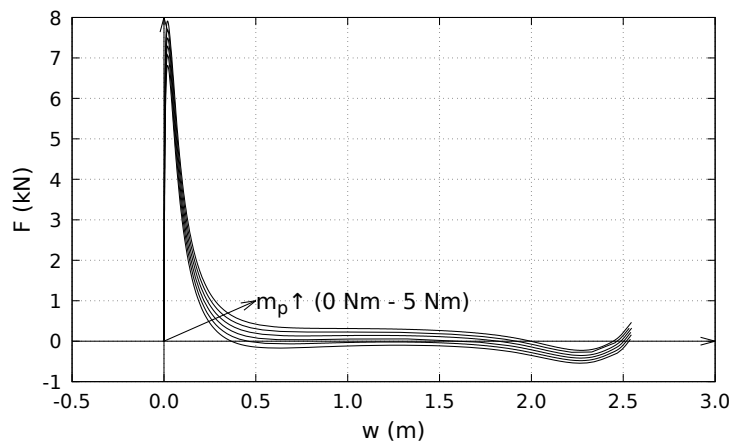
Figure 4.31: Joints friction influence on the 2D assembly.

The frictional effect could then be used on its own to stabilize the structure at any given position with a well chosen friction moment, although this would suppress the bistable nature of the structural behavior.

4.7
Conclusions

In the present chapter a spatial corotational finite element formulation framework of beams and joints was developed for the nonlinear static analysis of bistable deployable structures. The beam formulation in Appendix C considers small local deformations while retaining only the six essential deformation modes in the local reference system. The joint formulation, is considered as a special finite element, with flexibility and active contributions to the system internal force vector and stiffness matrix. As a particular case of the latter, the hinge formulation contains a deformable elastic layer and friction resistance around the current axis direction, where constitutive equations were proposed based on the material properties of its constituents. Both formulations can handle arbitrarily large displacements and rotations, and were validated with respect to benchmark examples.

The structural response of a deployable module, was studied in detail, considering a number of nonlinear effects. First, the deployment behavior, considering only the geometric nonlinearity was analyzed. A snap-through phenomenon could be captured, together with two deformation and load free configurations, characterizing the bistability of the system. The hub size and the beams and joints thicknesses were then included, showing how the eccentricities introduced cause the elements to buckle out of plane and dramatically change the nonlinear response and peak loads. The self-weight and the friction were shown to increase the required load to deploy the system. For the friction effect, as energy dissipation occurs during the deployment, the deployment and folding equilibrium paths are no longer the same. The joints stiffness was shown to have a direct effect on the peak load of the transformation.

Finally, more complex structures were modeled by the composition of several modules. The 1D line and 2D hanging wall assemblies nonlinear behavior were studied through static finite element analysis, highlighting the similarities with the module behavior in the nonlinear response.

In future work, other classes of bistable deployable structures can be studied making use of the beam and joint formulations developed here. In bistable deployable structures is common to have a snap-through behavior during the transformation, that could cause dynamic jumps, and so a dynamic

nonlinear analysis would be necessary to evaluate the response of the system for deployment safety aspects.

5
Conclusions and future work

5.1
Conclusions

- **Computational developments**

In the present work, a spatial corotational finite element formulation framework of truss (App. B), beam (App. C) and joint (Chap. 4) finite elements was developed for the nonlinear static and dynamic analysis of a large span bistable reticulated structures. The truss formulation considers finite strain measures and an elasto-plastic constitutive law. The beam formulation takes into account small local elasto-plastic deformations while retaining only the six essential deformation modes in the local reference system. When the material elasto-plastic constitutive behavior is considered, the beam cross section is discretized into fibers. The joint finite element formulation is tailored to bistable deployable structures and it incorporates finite stiffness and friction, as well as finite size effects through active contributions to the system internal force vector and stiffness matrix. All proposed computational formulations can handle arbitrarily large displacements and rotations, and were validated with respect to benchmark examples.

- **Closed form expressions for the equilibrium path, natural frequencies and critical points**

Novel analytical solutions for the nonlinear behavior of pyramidal trusses were proposed and validated for the nonlinear equilibrium paths, critical loads and natural frequencies of single modules with emphasis on stability and load carrying capacity considering both elastic and elasto-plastic behavior, Eulerian buckling and the flexibility of the base nodes. Analytical expressions in terms of the geometric and material parameters were obtained to define what type of buckling occurs. The FE results were favorably compared with the analytical results, validating the closed form approach. An original closed form expression of the phase space for the unloaded elastic symmetric system was developed and investigated, where the homoclinic orbits (boundaries of the pre-buckling and post-buckling wells) were determined. When available, closed form solutions are preferred in place of numerical ones due to its reduced

computational time.

- **Non-dimensional analyses of pyramid truss modules**

A parametric analysis was carried out to study the influence of the truss height to base ratio (depth parameter) on the structural behavior and load carrying capacity of the system for each bifurcation phenomena. For shallow structures snap-through buckling to the inverted position occurred. For deep structures, however, the limit point and the truss lost stability through unstable symmetric bifurcation. The ensuing unstable secondary elliptical equilibrium path connects this critical point to its mirror inverted position. This bifurcation is associated to an asymmetric buckling mode. Again after reaching the bifurcation point the structure jumps to an inverted configuration.

- **Influence of the adopted strain measure**

The elastic and elasto-plastic structural response of the pyramidal truss with two strain measures (quadratic and logarithmic) was investigated. For deep systems, the strain in the elements are usually considerable and the adopted strain measure has a large influence on the structural response. The influence of the strain measure on the topology of the energy landscape was analyzed. The conservative Hamiltonian system displays the same behavior in the vicinity of the unloaded stable configurations but the differences increases with the displacements and velocities, due to the differences in strains when the truss bars are under increasing compression forces. The logarithmic strain measure is usually considered in the elastic and elasto-plastic constitutive law of metals and is recommended for the design of such structures, especially when dealing with deep trusses ($\alpha < 10$). The quadratic strain measure is applied in most closed form expressions for its simplicity.

- **Interactive buckling of the pyramidal truss modules**

The influence of the interaction of snap-through instability, Eulerian buckling and plastic deformations on the imperfection sensitivity and load carrying capacity of the spatial truss was investigated using finite element simulations, being an original contribution to the state of the art. The results showed that in a wide range of the shallowness parameter interactive buckling may occur, leading to further decrease of the load carrying capacity of the spatial truss and so it must be included in the design of pyramidal trusses.

- **Existence of multiple dynamic solutions**

The complex topology of the bistable truss potential energy, which is a function of the truss geometry and static preload, leads to coexisting solutions in the main resonance region, including in-well and cross-well periodic and chaotic attractors. For deep pyramidal trusses with a high height/base ratio (α) the strain measure has a considerable influence on the dynamic response

and leads to cross-well solutions for different dynamic load levels.

- **Influence of the material elasto-plastic behavior**

  The inclusion of the elasto-plastic material behavior in the static and dynamic analyses of pyramidal trusses constitutes one of the main originalities of the present work. The plastic buckling was shown to considerably reduce the load capacity of most metallic trusses compared to the elastic case. The dissipation of energy in the plastic deformations was shown to dramatically influence the dynamic response, eliminating the its chaotic behavior and leading to smaller oscillation amplitudes. When material hardening is considered the structural system exhibits a more complex response, including multiple period doubling and dynamic jumps.

- **Features and applicability of the developed joint formulation**

  A spatial corotational finite element joint formulation framework was developed for the nonlinear static analysis of a special class of bistable deployable structures. The formulation incorporates the joint finite size and contains a deformable elastic layer and friction resistance around the current axis direction. The joint can handle arbitrarily large displacements and rotations, and were validated with respect to benchmark examples.

- **Transformation analysis of bistable deployable scissor modules**

  The structural response of a deployable module was carried out were a snap-through phenomenon could be observed, together with two deformation free configurations, characterizing the bistability of the system. The eccentricities introduced by the hub size and the beams and joints thicknesses was shown to cause the elements to buckle out of plane and dramatically change the nonlinear response and peak loads. The self-weight and the friction were shown to increase the required load to deploy the system. The energy dissipation during the deployment, due to friction, causes the deployment and folding processes to follow different equilibrium paths. The joints stiffness was shown to have a direct effect on the peak load of the transformation.

- **Static nonlinear analysis of large span pyramidal and deployable structures**

  A parametric analysis of a large span curved structure composed of several pyramidal truss modules was investigated. The structure exhibited a bistable behavior except for small rise values. The upper limit point load was observed to increase with the initial curvature, number of modules and module height. More complex structures composed by the composition of several deployable modules were also investigated. The 1D line and 2D hanging wall assemblies nonlinear behavior was studied through static finite element analysis. In both cases, similar trends were found as for single module cases.

5.2
Future work

The theoretical and numerical studies carried out in this thesis clarify the influence of bistable behavior on the static and dynamic nonlinear analysis of spatial reticulated structures. Although the examples are confined to two significant geometries, the principles and concepts developed herein are applicable to other space trusses.

The following topics which can be included in future works are of importance:

- The mechanical properties of the joints connecting the beam elements (finite size, flexibility and friction) may have a considerable influence on the pyramidal truss load capacity and stability, inducing new buckling modes. The developed joint finite element should thus be included in the finite element simulations.

- The developed closed form expressions could be part of a macro finite element formulation representing the behavior of a pyramidal truss module, reducing considerably the computational cost required for the analyses of large structural models.

- As civil engineering structures are usually subjected to dynamic loads composed by a broad range of frequencies, a more realistic dynamic analysis can be performed by considering different external excitations, e.g. white noise with a variable magnitude.

- The computational results presented in this work can be further complemented with experiments in the future.

- In the dynamic nonlinear analysis, continuation algorithms should be included in the finite element software in order to obtaining the stable and unstable paths through the use of Poincaré maps. This would allow the characterizing the dynamic structural behavior between the jumps in the bifurcation diagrams. Also the stability analysis using the eigenvalues of the Floquet matrix will allow a clear definition of the bifurcation type [114].

- The joints framework can be further improved considering a mean reference system between the nodes. This allows for a better representation of the relative rotations and deformation modes since the proposed corotational system would not be attached to one node but move as a combination of the kinematics of both nodes.

- Usual guidelines on joint design in civil engineering applications could be adapted to the proposed formulation, taking into account the elastic layer flexibility.

- In bistable deployable structures is common to have a snap-through behavior during the transformation, that could cause dynamic jumps, and so a dynamic nonlinear analysis would be necessary to evaluate the response of the system for deployment safety aspects.

- The joint mechanical properties may have a considerable influence on the load carrying capacity and stability of deployable structures in the service configuration (deployed) and it should be investigated, allowing a more realistic design process.

- The investigation of more realistic large span structures, inspired from built design should be carried out.

A
Finite rotations

A.1
Rotations parametrization

Let us consider a triad $\{\mathbf{s}_1, \mathbf{s}_2, \mathbf{s}_3\}$ defined as an orthogonal unitary base of $\mathbb{R}^3$ oriented through the right hand rule. For any triad the following relations are valid:

$$\mathbf{s}_i \cdot \mathbf{s}_i^T = \mathbf{I} \tag{A-1}$$

$$\mathbf{s}_i^T \cdot \mathbf{s}_j = \delta_{ij} \tag{A-2}$$

$$\widehat{\mathbf{s}}_i = \mathbf{s}_k \cdot \mathbf{s}_j^T - \mathbf{s}_j \cdot \mathbf{s}_k^T \tag{A-3}$$

In the equations above, $\mathbf{I}$ is the 3×3 identity matrix and the sequence $\{i, j, k\}$ represents a cyclic permutation (Fig. A.1). The tensor $\widehat{\mathbf{n}} = \mathbf{n} \times$ is the skew-symmetric matrix obtained from the vector $\mathbf{n}$ by:

$$\widehat{\mathbf{n}} = \mathbf{n} \times = \begin{bmatrix} 0 & -n_3 & +n_2 \\ +n_3 & 0 & -n_1 \\ -n_2 & +n_1 & 0 \end{bmatrix} \tag{A-4}$$
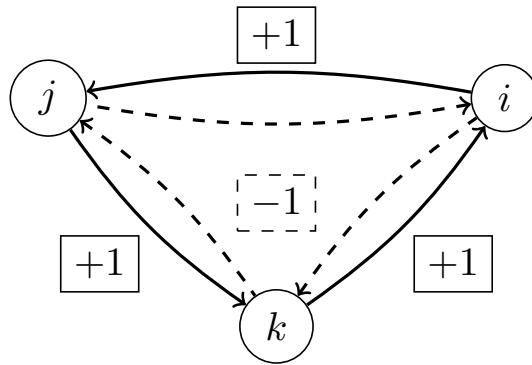
Figure A.1: Cyclic permutation.

By applying a rotation, represented by the tensor $\mathbf{R}$, to the original triad $\mathbf{s}_i$ as (Fig. A.2), a new triad $\mathbf{t}_i$ is formed:

$$\mathbf{t}_i = \mathbf{R} \cdot \mathbf{s}_i \tag{A-5}$$
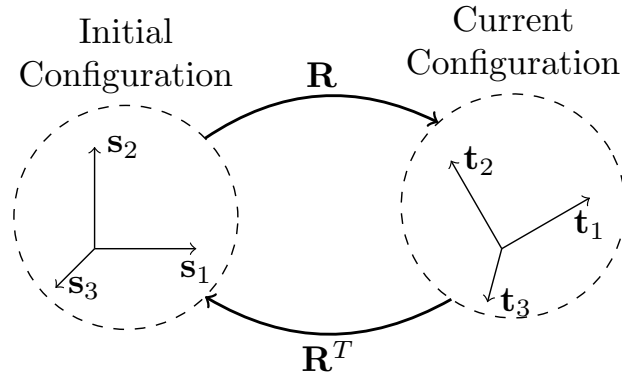
Figure A.2: Triad rotation.

As a pure rotation must preserve the length and angles between the rotated vectors, we have:

$$\mathbf{t}_i^T \cdot \mathbf{t}_j = \mathbf{s}_i^T \cdot \mathbf{R}^T \cdot \mathbf{R} \cdot \mathbf{s}_j = \mathbf{s}_i^T \cdot \mathbf{s}_j \tag{A-6}$$

Since the initial triad $\mathbf{s}_i$ is arbitrary, the equation above implies that:

$$\mathbf{R}^T \cdot \mathbf{R} = \mathbf{R} \cdot \mathbf{R}^T = \mathbf{I} \tag{A-7}$$

This means that the rotation tensor $\mathbf{R}$ is orthogonal ($\mathbf{R}^{-1} = \mathbf{R}^T$) and, pre-multiplying Eq. (A-5) by $\mathbf{R}^T$, the original triad can always be recovered as:

$$\mathbf{s}_i = \mathbf{R}^T \cdot \mathbf{t}_i \tag{A-8}$$

On the other hand, post-multiplying Eq. (A-5) by $\mathbf{s}_i^T$, and with help of Eq. (A-1), the rotation tensor $\mathbf{R}$ can be obtained as a function of the triads $\mathbf{s}_i$ and $\mathbf{t}_i$:

$$\mathbf{R} = \mathbf{t}_i \cdot \mathbf{s}_i^T \tag{A-9}$$

From the orthogonality condition in Eq. (A-7), the rotation tensor $\mathbf{R}$ only has three independent components, and hence, can be parameterized in a number of ways [115]. Given a rotation angle θ and unit direction $\mathbf{n}$, the rotation tensor $\mathbf{R}$ may be written as a function of the pseudo-vector $\boldsymbol{\theta} = \theta\mathbf{n}$ through the well know Rodrigue's formula [116]:

$$\mathbf{R} = \exp(\widehat{\boldsymbol{\theta}}) \tag{A-10}$$

$$\mathbf{R} = \cos(\theta)\mathbf{I} + \sin(\theta)\widehat{\mathbf{n}} + [1 - \cos(\theta)]\,\mathbf{n} \cdot \mathbf{n}^T \tag{A-11}$$

The term pseudo-vector is used here because $\boldsymbol{\theta}$ does not respect the additive rule of vectors. In fact, if two consecutive rotations $(\mathbf{R}_1, \mathbf{R}_2)$ are applied in a triad, the resultant rotation $\mathbf{R}_{12}$ is, in general, not the addition of the rotations $(\mathbf{R}_{12} \neq \mathbf{R}_2 + \mathbf{R}_1)$, but $\mathbf{R}_{12} = \mathbf{R}_2 \cdot \mathbf{R}_1$. Also, in general, the order of the rotations matter, that is: $\mathbf{R}_{12} = \mathbf{R}_2 \cdot \mathbf{R}_1 \neq \mathbf{R}_1 \cdot \mathbf{R}_2 = \mathbf{R}_{21}$. Planar rotations $(\mathbf{n}_1 = \mathbf{n}_2)$ are an exception where the additive and commutative vector properties are valid.

Taking the skew-symmetric part and the trace of the rotation tensor $\mathbf{R}$ in Eqs. (A-9) and (A-11), the rotation direction $\mathbf{n}$ and angle θ can be obtained as:

$$\mathbf{n} = \frac{\mathbf{s}_i \times \mathbf{t}_i}{2 \sin(\theta)} \tag{A-12}$$

$$\theta = \arccos\left(\frac{\mathbf{t}_i^T \cdot \mathbf{s}_i - 1}{2}\right) \tag{A-13}$$

From the above equations, the rotation components $\theta_i = \boldsymbol{\theta}^T \cdot \mathbf{s}_i = \boldsymbol{\theta}^T \cdot \mathbf{t}_i$ are:

$$\theta_i = \frac{\theta}{2 \sin(\theta)} \left(\mathbf{t}_j^T \cdot \mathbf{s}_k - \mathbf{t}_k^T \cdot \mathbf{s}_j\right) \tag{A-14}$$

A.2
Rotations variation

The virtual variation of the rotation tensor $\delta\mathbf{R}$, with respect to the current configuration, is important in the derivation of the finite element equations and can be obtained from the orthogonality condition in Eq. (A-7) as:

$$\delta\mathbf{R} \cdot \mathbf{R}^T + \mathbf{R} \cdot \delta\mathbf{R}^T = \mathbf{0} \tag{A-15}$$

$$\delta\mathbf{R} \cdot \mathbf{R}^T = -\left(\delta\mathbf{R} \cdot \mathbf{R}^T\right)^T \tag{A-16}$$

In the above equations, and through the manuscript, $\delta(\cdot)$ and $\Delta(\cdot)$ represents a virtual variation and an infinitesimal increment of a given quantity with respect to the current configuration, respectively. The above equation shows that the tensor $\delta\mathbf{R} \cdot \mathbf{R}^T$ is skew-symmetric and so, there is a variation spin $\delta\boldsymbol{\omega}$ such that:

$$\delta\mathbf{R} = \delta\widehat{\boldsymbol{\omega}} \cdot \mathbf{R} \tag{A-17}$$

Considering a fixed original triad $\mathbf{s}_i$, Eqs. (A-5) and (A-17) gives the

variation of the new triad $\delta\mathbf{t}_i$ as:

$$\delta\mathbf{t}_i = \delta\boldsymbol{\omega} \times \mathbf{t}_i \tag{A-18}$$

Also, the variation of the orthogonality condition expressed in Eq. (A-2) gives:

$$\delta\mathbf{t}_i^T \cdot \mathbf{t}_j + \delta\mathbf{t}_j^T \cdot \mathbf{t}_i = 0 \tag{A-19}$$

On the other hand, given the new triad variations $\delta\mathbf{t}_i$, the variation spin $\delta\boldsymbol{\omega}$ can be obtained combining the triad rules in Eqs. (A-2) - (A-3) with the variations in Eqs. (A-18) - (A-19) as:

$$\delta\boldsymbol{\omega} = \frac{1}{2}\left(\mathbf{t}_i \times \delta\mathbf{t}_i\right) \tag{A-20}$$

It's important to notice the difference between the virtual variation spin $\delta\boldsymbol{\omega}$ and the rotation pseudo-vector $\delta\boldsymbol{\theta}$. It's possible to show [116] that $\delta\boldsymbol{\omega} = \mathbf{H} \cdot \delta\boldsymbol{\theta}$, where:

$$\mathbf{H} = \mathbf{I} + \frac{1 - \cos(\theta)}{\theta}\widehat{\mathbf{n}} + \frac{\theta - \sin(\theta)}{\theta}\widehat{\mathbf{n}}^2 \tag{A-21}$$

For small rotations ($\theta \approx 0$) however, we have $\cos(\theta) \approx 1$, $\sin(\theta) \approx \theta$ and, hence, $\mathbf{H} \approx \mathbf{I}$. Analogously to the virtual variations, there is an infinitesimal increment spin $\Delta\boldsymbol{\omega}$ such that, the correspondent increments of the rotation tensor $\Delta\mathbf{R}$ and of the new triad $\Delta\mathbf{t}_i$, with respect to the current configuration, are given as:

$$\Delta\mathbf{R} = \Delta\widehat{\boldsymbol{\omega}} \cdot \mathbf{R} \tag{A-22}$$

$$\Delta\mathbf{t}_i = \Delta\boldsymbol{\omega} \times \mathbf{t}_i \tag{A-23}$$

It's convenient to work with the full tensor $\mathbf{R}$, instead of the rotation pseudo-vector $\boldsymbol{\theta}$ [117]. In fact, a crucial issue of this parametrization is that, from Eq. (A-21):

$$\det(\mathbf{H}) = 2\left[\frac{1 - \cos(\theta)}{\theta}\right] \tag{A-24}$$

Hence, for $\theta = 2\pi p$, with $p \in \mathbb{N}$, $\mathbf{H}$ becomes singular [6]. This means that, in a step $n+1$, given a finite increment spin $\Delta\boldsymbol{\omega}_{n+1}$ one would be unable to compute the finite increment pseudo-vector $\Delta\boldsymbol{\theta}_{n+1}$. In practice, we don't precisely obtain a singular correlation matrix $\mathbf{H}_n$, but for θ_n near this critical

values, $\mathbf{H}_n$ becomes ill conditioned, reducing the convergence rate or causing the solution algorithm to fail in founding an equilibrium point [118]. Yet, to preserve its orthogonality, the increment of the rotation tensor $\mathbf{R}_{n+1}$ is done using the finite version of Eq. (A-22):

$$\mathbf{R}_{n+1} = \exp(\Delta\widehat{\boldsymbol{\omega}}_{n+1}) \cdot \mathbf{R}_n \tag{A-25}$$

B
Corotational truss finite element

A tri-dimensional corotational truss finite element, allowing the analysis of spatial truss structures under arbitrarily large displacements and rotations, is developed. The spatial corotational truss element (see Fig. B.1) consist of a straight bar subjected to an axial force and connecting two nodes denoted by (i, j), respectively. Considering the initial $(\mathbf{X}_i, \mathbf{X}_j)$ and current $(\mathbf{x}_i, \mathbf{x}_j)$ configuration vectors defining the nodal positions, the initial and current element lengths are given, respectively, by $L = \|\mathbf{X}_j - \mathbf{X}_i\|$ and $l = \|\mathbf{x}_j - \mathbf{x}_i\|$.
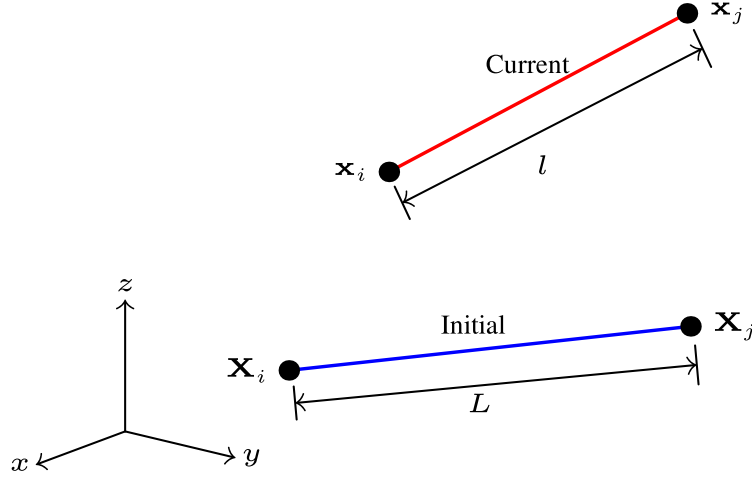
Figure B.1: Spatial truss element.

B.1
Corotational framework

In the initial configuration, the orientation of the bar is described by the axial direction $\mathbf{s}_1 = (\mathbf{X}_j - \mathbf{X}_i)/L$ and the cross section directions $\mathbf{s}_2$ and $\mathbf{s}_3$. The position of a material point $\mathbf{x}_0$ is given by:

$$\mathbf{X} = \mathbf{X}_i + \xi_a \mathbf{s}_a \qquad a = 1, 2, 3 \qquad \text{(B-1)}$$

$$\mathbf{X} = \left(1 - \frac{\xi_1}{L}\right) \mathbf{X}_i + \left(\frac{\xi_1}{L}\right) \mathbf{X}_j + \xi_\alpha \mathbf{s}_\alpha \qquad \alpha = 1, 2 \qquad \text{(B-2)}$$

The parameter ξ_1 varies along the element initial length and the parameters ξ_2 and ξ_3 map the cross section domain Ω with initial area A. In the

current configuration, the bar element is subjected to a uniform stretch along the principal directions λ_k. The orientation of the bar is described by the axial direction $\mathbf{t}_1 = (\mathbf{x}_j - \mathbf{x}_i)/l$ and the cross section directions $\mathbf{t}_2$ and $\mathbf{t}_3$. The position of a material point $\mathbf{x}$ is given by:

$$\mathbf{x} = \mathbf{x}_i + \lambda_k \xi_a \mathbf{t}_a \qquad\qquad a = 1, 2, 3 \qquad \text{(B-3)}$$

$$\mathbf{x} = \left(1 - \frac{\xi_1}{L}\right)\mathbf{x}_i + \left(\frac{\xi_1}{L}\right)\mathbf{x}_j + \lambda_r \xi_\alpha \mathbf{t}_\alpha \qquad\qquad \alpha = 1, 2 \qquad \text{(B-4)}$$

The axial stretch can be obtained as $\lambda_1 = l/L$ and, considering a homogeneous and isotropic material, the cross section has a uniform transversal stretch λ_r. These correspond to the principal stretches of the bar under axial load. Considering $\mathbf{d}^T = \left\{\mathbf{x}_i^T \quad \mathbf{x}_j^T\right\}$ and the material specific mass ρ, the element kinetic energy T is given by:

$$T = \int_0^L \int_\Omega \rho \dot{\mathbf{x}}_n^T \cdot \dot{\mathbf{x}}_n d\xi_1 d\xi_2 d\xi_3 = \dot{\mathbf{d}}^T \cdot \mathbf{M} \cdot \dot{\mathbf{d}} \qquad \text{(B-5)}$$

Ignoring the cross section rotational inertia, the mass matrix $\mathbf{M}$ can be obtained as:

$$\mathbf{M} = \frac{\rho AL}{3}\begin{bmatrix} \mathbf{I} & \mathbf{0} \\ \mathbf{0} & \mathbf{I} \end{bmatrix} + \frac{\rho AL}{6}\begin{bmatrix} \mathbf{0} & \mathbf{I} \\ \mathbf{I} & \mathbf{0} \end{bmatrix} \qquad \text{(B-6)}$$

where $\mathbf{I}$ and $\mathbf{0}$ are the identity and zero 3×3 matrices, respectively.

The strain field is constant over the element and is a function of the axial stretch $\varepsilon = \varepsilon(\lambda_1)$ for an adopted strain measure. The energetically conjugated stress is obtained for a given strain ε and plastic strain history ε_p through the material constitutive law $\sigma = \sigma(\varepsilon, \varepsilon_p)$. In the current configuration, the virtual work, δU, can be written as:

$$\delta U = \int_0^L \int_\Omega \sigma \delta \varepsilon d\xi_1 d\xi_2 d\xi_3 = \mathbf{f}^T \cdot \delta \mathbf{d} \qquad \text{(B-7)}$$

where the variation of the strain $\delta \varepsilon$ is given by:

$$\delta \varepsilon = \frac{1}{L}\frac{\partial \varepsilon}{\partial \lambda_1}\delta l = \frac{1}{L}\frac{\partial \varepsilon}{\partial \lambda_1}\mathbf{t}_1^T \cdot (\delta \mathbf{x}_j - \delta \mathbf{x}_i) \qquad \text{(B-8)}$$

The element internal forces vectors vector $\mathbf{f}$ is then given by:

$$\mathbf{f} = \overline{f}\begin{Bmatrix} -\mathbf{t}_1 \\ +\mathbf{t}_1 \end{Bmatrix} \qquad \text{(B-9)}$$

where the axial force in the bar $\overline{f}$ is defined as:

$$\overline{f} = \sigma A \frac{\partial \varepsilon}{\partial \lambda_1} \tag{B-10}$$

Taking the increment of the internal forces vectors vector $\mathbf{f}$ with respect to the nodal positions $\mathbf{d}$, the element stiffness matrix $\mathbf{K}$ can be obtained as:

$$\mathbf{K} = \frac{\partial \mathbf{f}}{\partial \mathbf{d}} = \overline{k} \begin{bmatrix} +\mathbf{T}_1 & -\mathbf{T}_1 \\ -\mathbf{T}_1 & +\mathbf{T}_1 \end{bmatrix} + \frac{\overline{f}}{l_n} \begin{bmatrix} +\mathbf{P}_1 & -\mathbf{P}_1 \\ -\mathbf{P}_1 & +\mathbf{P}_1 \end{bmatrix} \tag{B-11}$$

where $\mathbf{T}_1 = \mathbf{t}_1 \cdot \mathbf{t}_1^T$, $\mathbf{P}_1 = \mathbf{I} - \mathbf{t}_1 \cdot \mathbf{t}_1^T$ are projection matrices and $\overline{k}$ is the element local stiffness given by:

$$\overline{k} = \frac{\partial \overline{f}}{\partial l} = \left[\frac{\partial \sigma}{\partial \varepsilon} \left(\frac{\partial \varepsilon}{\partial \lambda_1} \right)^2 + \sigma \frac{\partial^2 \varepsilon}{\partial \lambda_1^2} \right] \frac{A}{L} \tag{B-12}$$

The first term in Eq. (B-11), represents the element stiffness matrix, related to the increment of deformations in the bar, while the second term represents the geometric stiffness matrix, due to the large displacements and rotations and the forces acting on the element.

B.2
Strain measures and material law

There is a large variety of strain measures in literature for finite strains [119]. The finite strain theory deals with deformations in which the undeformed and deformed configurations of the continuum are significantly different, as in the case of elastomers and plastically-deforming materials. An admissible generic strain measure $\varepsilon(\lambda_1)$ should respect the following constraints [120]:

$$\varepsilon(1) = 0 \tag{B-13}$$

$$\frac{\partial \varepsilon}{\partial \lambda_1} > 0 \tag{B-14}$$

$$\lim_{\lambda_1 \to 0} \varepsilon = -\infty \tag{B-15}$$

$$\lim_{\lambda_1 \to +\infty} \varepsilon = +\infty \tag{B-16}$$

Here, the bar element response is studied considering the quadratic, ε_q, and logarithmic, ε_l, strain measures. They are energetically conjugated through the virtual work δU with the second Piola-Kirchhoff stress and the Kirchhoff stress, respectively. For the quadratic strain measure (QSM) ε_q the required expressions for the computation of the element axial force (Eq. B-10) and stiffness (Eq. B-12) are:

$$\varepsilon_q = \frac{\lambda_1^2 - 1}{2} \quad \frac{\partial \varepsilon_q}{\partial \lambda_1} = \lambda_1 \quad \frac{\partial^2 \varepsilon_q}{\partial \lambda_1^2} = 1 \tag{B-17}$$

while for the logarithmic strain measure (LSM) ε_l the analogous expressions are:

$$\varepsilon_l = \ln(\lambda_1) \quad \frac{\partial \varepsilon_l}{\partial \lambda_1} = \frac{1}{\lambda_1} \quad \frac{\partial^2 \varepsilon_l}{\partial \lambda_1^2} = -\frac{1}{\lambda_1^2} \tag{B-18}$$

The two strain measures are compared in Fig. (B.2). The elasto-plastic behavior of the material is characterized by a hardening (or softening) constitutive law (Fig. B.3). The plastic strain ε_p and hardening parameter ψ in the current step, for a given set of material properties, namely the elastic modulus E, the yield stress $\sigma_y(\psi)$ and the plastic modulus $K(\psi)$, can be computed by a return mapping algorithm [110]. The stress σ and the element stiffness matrix $\partial\sigma/\partial\varepsilon$ are given respectively by:

$$\sigma = E(\varepsilon - \varepsilon_p) \tag{B-19}$$

$$\frac{\partial \sigma}{\partial \varepsilon} = \begin{cases} E & \dot{\psi} = 0 \\ \frac{EK}{E+K} & \dot{\psi} > 0 \end{cases} \tag{B-20}$$
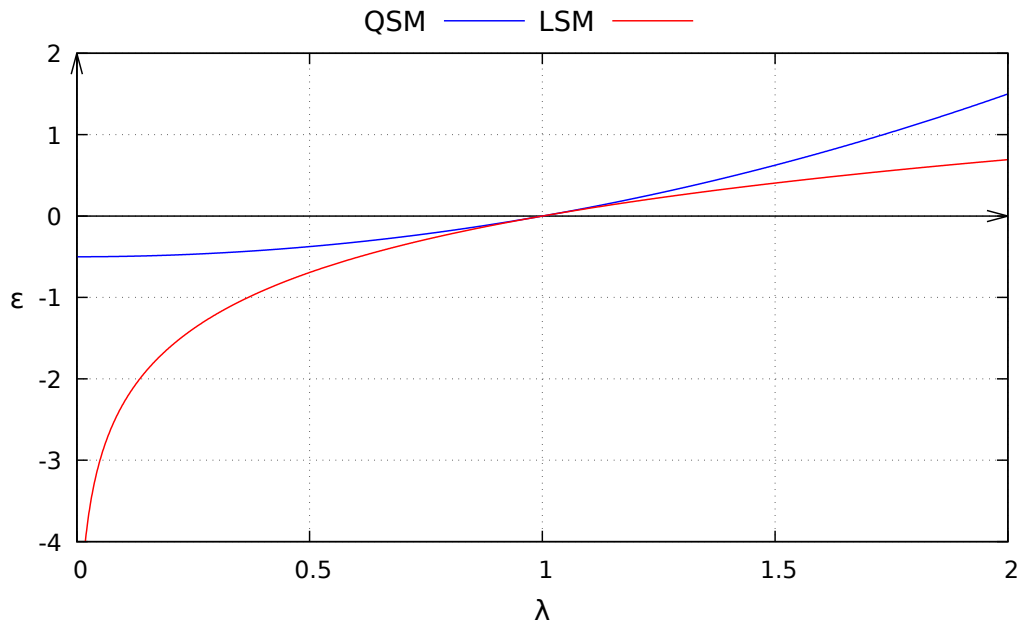
Figure B.2: Quadratic and logarithmic strain measures.

When large elasto-plastic deformations are taken into account, it's usual to consider a multiplicative decomposition of the strain gradient [67]. However this approach is equivalent to an additive decomposition of the strain into elastic and plastic parts provided that only axial deformations are present and the logarithmic strain measure is considered.

The adopted constitutive law is frequently used to relate the logarithmic strain measure with the Kirchhoff stress for steels and other metals. The
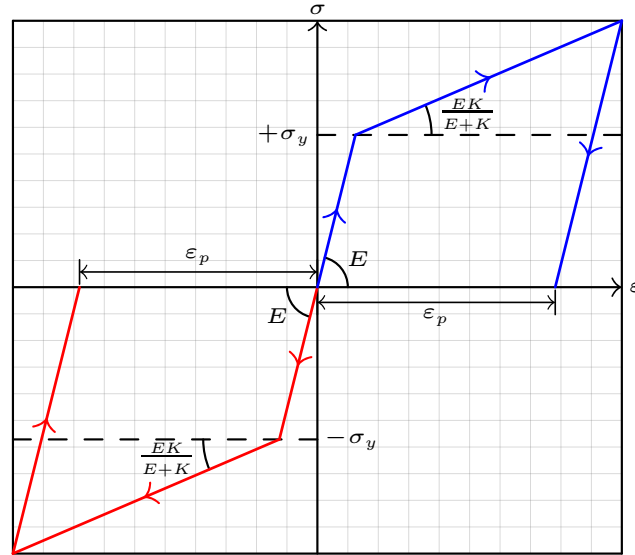
Figure B.3: Elasto-plastic constitutive law.

logarithmic strain measure complies with all the conditions in Eqs. (B-13) to (B-16), while the quadratic one does not satisfy Eq. (B-15). Therefore, although the quadratic strain measure provides a simpler model and allows the derivation of some analytical results, the logarithmic strain measure is more suitable for a realistic modeling of the elasto-plastic pyramidal truss under large deformations, as expected in some bistable systems exhibiting snap-through buckling and dynamic jumps between coexisting attractors. The influence of the strain measure is particularly important in systems liable to buckling where the constraint described by Eq. (B-15) plays an important role, as will be shown thereafter.

B.3
Benchmarks

To test the developed finite element software, the present corotational formulation is used in the analysis of the double pendulum model shown in Fig. B.4 . In this example, the elements are subjected to large displacements and rotations, which induce high geometric and inertial nonlinearities. The lengths are $l_1 = l_2 = 1$m, the bar is made of a material with $E = 200$GPa and circular cross section with diameter $d = 1$cm. The nodal masses are $m_1 = m_2 = 1$kg, and the gravitational accelerations is $g = 9.81$m/s^2. The double pendulum equations of motion, considering rigid bars, are given by [121]:

$$m_t l_1 \ddot{\theta}_1 + m_2 l_2 \left[\cos(\theta_r) \ddot{\theta}_2 - \sin(\theta_r) \dot{\theta}_2^2 \right] + m_t f_1 = 0 \tag{B-21}$$

$$m_2 l_2 \ddot{\theta}_2 + m_2 l_1 \left[\cos(\theta_r) \ddot{\theta}_1 + \sin(\theta_r) \dot{\theta}_1^2 \right] + m_2 f_2 = 0 \tag{B-22}$$
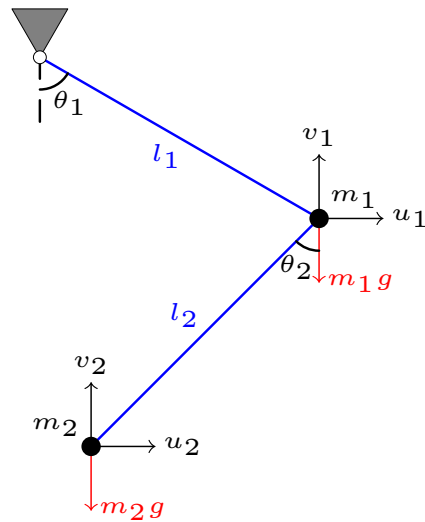
Figure B.4: Discrete elastic double pendulum.

In Eqs. (B-21) and (B-22), $m_t = m_1 + m_2$, $\theta_r = \theta_2 - \theta_1$ and $f_i = g \sin(\theta_i)$. The initial conditions are $\theta_1 = \pi/2$, $\theta_2 = \pi$ and $\dot{\theta}_1 = \dot{\theta}_2 = 0$. In Fig. B.5, the horizontal (u_i) and vertical (v_i) displacement components obtained with the FE formulation are favorably compared with the response obtained by the numerical integration of Eqs. (B-21) and (B-22). The nonlinear Newmark method [116] is used for the time integration of the equations of motion in both cases.
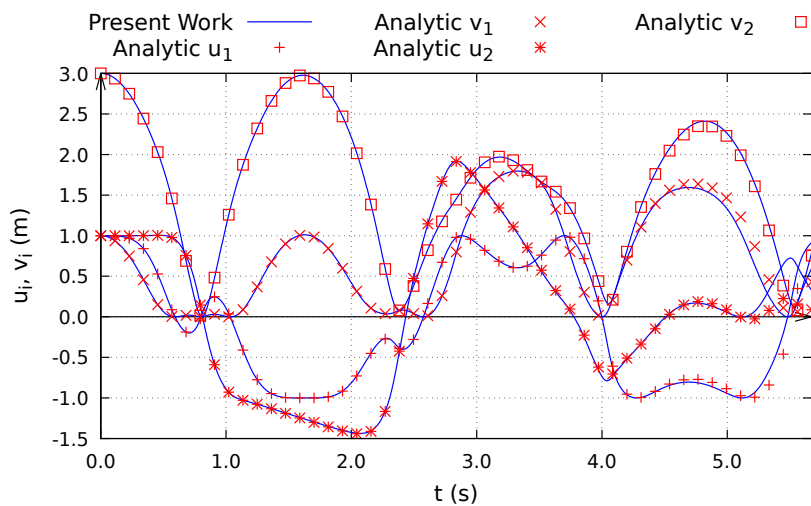
Figure B.5: Time response of the double pendulum.

C
Corotational fiber beam finite element

Figure C.1 shows the motion of a beam in the $\mathbb{R}^3$ space. The triad $\mathbf{e}_a$ is the canonical base of $\mathbb{R}^3$ and represents the global coordinates system, where the contribution of all finite elements is added in order to obtain the equilibrium equations. In its initial configuration, the beam element is assumed to be straight and free of deformations, with nodal positions $\mathbf{X}_i$ and $\mathbf{X}_j$. The beam initial longitudinal axis is $\mathbf{s}_1$ and the cross section principal directions are $\mathbf{s}_2$ and $\mathbf{s}_3$. With the motion, the beam nodes translates to the positions $\mathbf{x}_i$ and $\mathbf{x}_j$. Each node α is subjected to a rotation $\mathbf{R}_\alpha$, and its nodal triad becomes $\mathbf{r}_a^\alpha$. A local system is then adopted with its origin at $\mathbf{x}_i$ and orientation given by a triad $\mathbf{t}_a$, defined later. The beam current l and initial L lengths are given by:

$$l = \|\mathbf{x}_j - \mathbf{x}_i\| \tag{C-1}$$

$$L = \|\mathbf{X}_j - \mathbf{X}_i\| \tag{C-2}$$
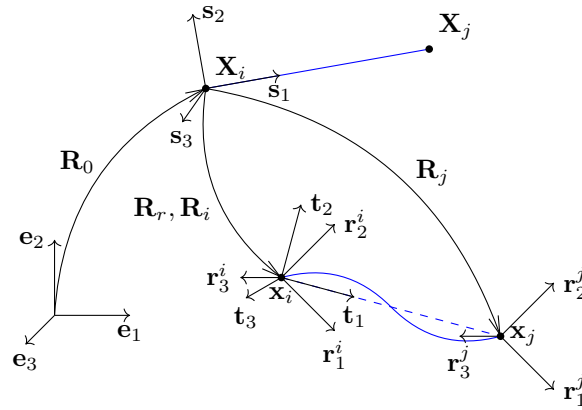
Figure C.1: Corotational beam motion.

C.1
Corotational framework

The initial beam axis is defined as $\mathbf{s}_1 = (\mathbf{X}_j - \mathbf{X}_i)/L$. The cross section principal direction $\mathbf{s}_3$ is a given parameter, from which the other principal direction is obtained as $\mathbf{s}_2 = \mathbf{s}_3 \times \mathbf{s}_1$. The rotation tensor $\mathbf{R}_0$, that rotates the

global triad $\mathbf{e}_a$ to $\mathbf{s}_a$, and the nodal rotation tensor $\mathbf{R}_\alpha$ are given by:

$$\mathbf{R}_0 = \mathbf{s}_a \cdot \mathbf{e}_a^T \tag{C-3}$$

$$\mathbf{R}_\alpha = \mathbf{r}_a^\alpha \cdot \mathbf{s}_a^T \tag{C-4}$$

The local system rotation tensor $\mathbf{R}_r$, that rotates the global triad $\mathbf{e}_a$ to the local system triad $\mathbf{t}_a$ is given by:

$$\mathbf{R}_r = \mathbf{t}_a \cdot \mathbf{e}_a^T \tag{C-5}$$

The relative nodal rotation tensor $\widetilde{\mathbf{R}}_\alpha$, measured in the global system, rotates the local triad $\mathbf{t}_a$ to the nodal triad $\mathbf{r}_a^\alpha$ is given by:

$$\widetilde{\mathbf{R}}_\alpha = \mathbf{r}_a^\alpha \cdot \mathbf{t}_a^T \tag{C-6}$$

Combining Eqs. (C-3) to (C-6), the two rotation tensors are related by:

$$\widetilde{\mathbf{R}}_\alpha \cdot \mathbf{R}_r = \mathbf{R}_\alpha \cdot \mathbf{R}_0 \tag{C-7}$$

The relative nodal rotation tensor $\overline{\mathbf{R}}_\alpha$, measured in the local system, is obtained by rotating the tensor $\widetilde{\mathbf{R}}_\alpha$ to this system through the following operations:

$$\overline{\mathbf{R}}_\alpha = \mathbf{R}_r^T \cdot \widetilde{\mathbf{R}}_\alpha \cdot \mathbf{R}_r = \mathbf{R}_r^T \cdot \mathbf{R}_\alpha \cdot \mathbf{R}_0 \tag{C-8}$$

$$\overline{\mathbf{R}}_\alpha = \left(\mathbf{t}_a^T \cdot \mathbf{r}_b^\alpha \right) \mathbf{e}_a \cdot \mathbf{e}_b^T \tag{C-9}$$

The local triad can be defined in a number of different ways. It is usual to set the local triad direction $\mathbf{t}_1$ equal to the current beam orientation, i.e.:

$$\mathbf{t}_1 = (\mathbf{x}_j - \mathbf{x}_i)/l \tag{C-10}$$

Making the assumption of small strains for the beams, the local rotations are also small and the nodal triad vectors $\mathbf{r}_3^i$ and $\mathbf{r}_3^j$ are never aligned with $\mathbf{t}_1$ (being approximately orthogonal). This allows defining the local triad direction $\mathbf{t}_2$ as [6]:

$$\mathbf{t}_2 = \frac{\left(\mathbf{r}_3^i + \mathbf{r}_3^j \right) \times \mathbf{t}_1}{\| \left(\mathbf{r}_3^i + \mathbf{r}_3^j \right) \times \mathbf{t}_1 \|} \tag{C-11}$$

The third triad direction is obtained as $\mathbf{t}_3 = \mathbf{t}_1 \times \mathbf{t}_2$ (see Eq. (A-3)). The position of a material point $\mathbf{x}$ with respect to the local system $\overline{\mathbf{x}}$ is then given

by:

$$\bar{\mathbf{x}} = \mathbf{R}_r^T \cdot (\mathbf{x} - \mathbf{x}_i) \tag{C-12}$$

Thus, $\bar{\mathbf{x}}_i = \mathbf{0}$ and $\bar{\mathbf{x}}_j = l\mathbf{e}_1$, and in the initial configuration, $\overline{\mathbf{X}}_i = \mathbf{0}$ and $\overline{\mathbf{X}}_j = L\mathbf{e}_1$. The local displacements are defined as $\bar{\mathbf{u}} = \bar{\mathbf{x}} - \bar{\mathbf{x}}_0$, with the only non null nodal displacement being the beam stretch $\bar{u}_x^j$:

$$\bar{u}_x^j = l - L \tag{C-13}$$

The local nodal rotation angle $\bar{\theta}_\alpha$, associated to the tensor $\overline{\mathbf{R}}_\alpha$ is obtained as (see Eq. A-13):

$$\bar{\theta}_\alpha = \arccos\left[\frac{1}{2}\left(\mathbf{t}_a^T \cdot \mathbf{r}_a^\alpha - 1\right)\right] \tag{C-14}$$

Finally, the local nodal rotation components are given by (see Eq. A-14):

$$\bar{\theta}_a^\alpha = \frac{\bar{\theta}_\alpha}{2\sin(\bar{\theta}_\alpha)}\left(\mathbf{t}_c^T \cdot \mathbf{r}_b^\alpha - \mathbf{t}_b^T \cdot \mathbf{r}_c^\alpha\right) \tag{C-15}$$

Since the triads $\mathbf{t}_a$ and $\mathbf{r}_a^i$ are not identical, the rotation $\bar{\theta}_x^i$ is, in general, not null and, hence, the twist angle of the beam is given by $\bar{\theta}_x^j - \bar{\theta}_x^i$. The set of local deformations $\bar{\mathbf{d}}$ is then:

$$\bar{\mathbf{d}} = \left\{\bar{u}_x^j \quad \bar{\theta}_z^i \quad \bar{\theta}_z^j \quad \bar{\theta}_x^j - \bar{\theta}_x^i \quad \bar{\theta}_y^i \quad \bar{\theta}_y^j\right\}^T \tag{C-16}$$

C.2
Constitutive relations

The beam local internal forces vectors vector $\bar{\mathbf{f}}$ and stiffness matrix $\overline{\mathbf{K}}$ considering the material elasto-plastic behavior is obtained using the plastic zone method [122], in which the cross section is discretized in fibers where the inelastic response is computed along the element length. In the present formulation, a linear strain measure is used with respect to the local deformations $\bar{\mathbf{d}}$. Taking into account different higher order terms in the strain measure could result in a different bucking response for some structural systems.

The beam cross section has an area A and principal moments of inertia in the directions $\bar{y}$ and $\bar{z}$ in the local frame I_y and I_z in the principal directions $\bar{y}$ and $\bar{z}$, respectively. The torsional moment of inertia is $I_x = I_y + I_z - I_w$, where I_w is the moment of inertia reduction related to the cross section warping. In

the particular case of a linear elastic isotropic material, with shear modulus G and elastic modulus E, the local internal forces vectors vector is simply $\overline{\mathbf{f}} = \overline{\mathbf{K}} \cdot \overline{\mathbf{d}}$, with the local stiffness matrix $\overline{\mathbf{K}}$ given by:

$$\overline{\mathbf{K}} = \begin{bmatrix} \frac{EA}{L} & 0 & 0 & 0 & 0 & 0 \\ 0 & \frac{4EI_z}{L} & \frac{2EI_z}{L} & 0 & 0 & 0 \\ 0 & \frac{2EI_z}{L} & \frac{4EI_z}{L} & 0 & 0 & 0 \\ 0 & 0 & 0 & \frac{GI_x}{L} & 0 & 0 \\ 0 & 0 & 0 & 0 & \frac{4EI_y}{L} & \frac{2EI_y}{L} \\ 0 & 0 & 0 & 0 & \frac{2EI_y}{L} & \frac{4EI_y}{L} \end{bmatrix} \tag{C-17}$$

In all applications considered in the present work, the beams are slender and so the Bernoulli theory (which neglects the shear deformations) is used.

C.3
Internal forces vector

As small deformations are considered, $\overline{\mathbf{H}}_\alpha \approx \mathbf{I}$ (Eq. A-21) and $\delta\overline{\boldsymbol{\omega}}_\alpha = \delta\overline{\boldsymbol{\theta}}_\alpha$. Therefore, the variation local deformations vector $\delta\overline{\mathbf{d}}$ takes the form:

$$\delta\overline{\mathbf{d}} = \left\{ \delta\overline{u}_x^j \quad \delta\overline{\omega}_z^i \quad \delta\overline{\omega}_z^j \quad \delta\overline{\omega}_x^j - \delta\overline{\omega}_x^i \quad \delta\overline{\omega}_y^i \quad \delta\overline{\omega}_y^j \right\}^T \tag{C-18}$$

The variation of the deformation vector $\delta\mathbf{d}$ in the global configuration is given by:

$$\delta\mathbf{d} = \left\{ \delta\mathbf{x}_i^T \quad \delta\boldsymbol{\omega}_i^T \quad \delta\mathbf{x}_j^T \quad \delta\boldsymbol{\omega}_j^T \right\}^T \tag{C-19}$$

The global $\mathbf{f}$ and local $\overline{\mathbf{f}}$ internal forces vectors, energetically conjugated to the variations $\delta\mathbf{d}$ and $\delta\overline{\mathbf{d}}$, are, respectively:

$$\mathbf{f} = \left\{ \mathbf{n}_i^T \quad \mathbf{m}_i^T \quad \mathbf{n}_j^T \quad \mathbf{m}_j^T \right\}^T \tag{C-20}$$

$$\overline{\mathbf{f}} = \left\{ \overline{n}_x^j \quad \overline{m}_z^i \quad \overline{m}_z^j \quad \overline{m}_x^j \quad \overline{m}_y^i \quad \overline{m}_y^j \right\}^T \tag{C-21}$$

As the local deformations $\overline{\mathbf{d}}$ are functions of the global displacements $\mathbf{d}$, it is possible to relate their variations through a system transformation $\mathbf{T}$:

$$\delta\overline{\mathbf{d}} = \mathbf{T} \cdot \delta\mathbf{d} \tag{C-22}$$

The virtual work δU can be written as:

$$\delta U = \delta\overline{\mathbf{d}}^T \cdot \overline{\mathbf{f}} = \delta\mathbf{d}^T \cdot \mathbf{f} \tag{C-23}$$

As the global variations $\delta\mathbf{d}$ are arbitrary, the relation between the local $\bar{\mathbf{f}}$ and global $\mathbf{f}$ internal forces vectors, based on the above equations, is given by:

$$\mathbf{f} = \mathbf{T}^T \cdot \bar{\mathbf{f}} \tag{C-24}$$

The variation of the axial stretch $\delta\bar{u}_x^j$ in Eq. (C-1) is:

$$\delta\bar{u}_x^j = \delta l = \mathbf{t}_1^T \cdot (\delta\mathbf{u}_j - \delta\mathbf{u}_i) \tag{C-25}$$

The variation of the spin vector $\delta\bar{\boldsymbol{\omega}}_\alpha$ can be obtained from Eq. (C-8) as [6]:

$$\delta\widehat{\bar{\boldsymbol{\omega}}}_\alpha = \delta\bar{\mathbf{R}}_\alpha \cdot \bar{\mathbf{R}}_\alpha^T \tag{C-26}$$

$$\delta\widehat{\bar{\boldsymbol{\omega}}}_\alpha = \mathbf{R}_r^T \cdot (\delta\widehat{\boldsymbol{\omega}}_\alpha - \delta\widehat{\boldsymbol{\omega}}_r) \cdot \mathbf{R}_\alpha \cdot \mathbf{R}_0 \cdot \bar{\mathbf{R}}^T \tag{C-27}$$

$$\delta\widehat{\bar{\boldsymbol{\omega}}}_\alpha = \mathbf{R}_r^T \cdot (\delta\widehat{\boldsymbol{\omega}}_\alpha - \delta\widehat{\boldsymbol{\omega}}_r) \cdot \mathbf{R}_r \tag{C-28}$$

$$\delta\bar{\boldsymbol{\omega}}_\alpha = \mathbf{R}_r^T \cdot (\delta\boldsymbol{\omega}_\alpha - \delta\boldsymbol{\omega}_r) \tag{C-29}$$

From Eq. (C-10), the variation of local triad $\mathbf{t}_i$ is given by:

$$\delta\mathbf{t}_1 = \frac{1}{l}\left(\mathbf{t}_2 \cdot \mathbf{t}_2^T + \mathbf{t}_3 \cdot \mathbf{t}_3^T\right) \cdot (\delta\mathbf{x}_j - \delta\mathbf{x}_i) \tag{C-30}$$

$$\delta\mathbf{t}_2 = -\frac{1}{l}\mathbf{t}_1 \cdot \mathbf{t}_2^T \cdot (\delta\mathbf{x}_j - \delta\mathbf{x}_i) + \delta\phi\mathbf{t}_3 \tag{C-31}$$

$$\delta\mathbf{t}_3 = -\frac{1}{l}\mathbf{t}_1 \cdot \mathbf{t}_3^T \cdot (\delta\mathbf{x}_j - \delta\mathbf{x}_i) - \delta\phi\mathbf{t}_2 \tag{C-32}$$

In the above equations the variation $\delta\phi$ depends on the choice of the local system two other directions. It can be expressed in a general form as:

$$\delta\phi = \mathbf{t}_3^T \cdot \delta\mathbf{t}_2 = -\mathbf{t}_2^T \cdot \delta\mathbf{t}_3 \tag{C-33}$$

$$\delta\phi = \frac{1}{l}\mathbf{a}_r^T \cdot (\delta\mathbf{x}_j - \delta\mathbf{x}_i) + \mathbf{b}_a^T \cdot \delta\boldsymbol{\omega}_a + \mathbf{b}_b^T \cdot \delta\boldsymbol{\omega}_b \tag{C-34}$$

From Eq. (C-11), the transformation vectors $\mathbf{b}_i$, $\mathbf{b}_j$ and $\mathbf{a}_r$ results in:

$$\mathbf{b}_i = \frac{\mathbf{t}_2 \times \mathbf{r}_3^i}{\|\mathbf{t}_3^T \cdot \left(\mathbf{r}_3^i + \mathbf{r}_3^j\right)\|} \tag{C-35}$$

$$\mathbf{b}_j = \frac{\mathbf{t}_2 \times \mathbf{r}_3^j}{\|\mathbf{t}_3^T \cdot \left(\mathbf{r}_3^i + \mathbf{r}_3^j\right)\|} \tag{C-36}$$

$$\mathbf{a}_r = \frac{\mathbf{t}_1^T \cdot \left(\mathbf{r}_3^i + \mathbf{r}_3^j\right)}{\|\mathbf{t}_3^T \cdot \left(\mathbf{r}_3^i + \mathbf{r}_3^j\right)\|}\mathbf{t}_2 \tag{C-37}$$

From Eq. (A-20) and Eqs. (C-30) to (C-32), the variation of the local system spin vector $\delta\boldsymbol{\omega}_r$ is then given by:

$$\delta\boldsymbol{\omega}_r = \frac{1}{l}\mathbf{t}_1 \times (\delta\mathbf{x}_j - \delta\mathbf{x}_i) + \delta\phi\mathbf{t}_1 \tag{C-38}$$

Finally, combining Eqs. (C-25), (C-29) and (C-38), the system transformation matrix $\mathbf{T}$ can be written as:

$$\mathbf{T} = \begin{bmatrix} -\mathbf{t}_1 & \frac{1}{l}\mathbf{t}_2 & \frac{1}{l}\mathbf{t}_2 & \mathbf{0} & -\frac{1}{l}\mathbf{t}_3 & -\frac{1}{l}\mathbf{t}_3 \\ \mathbf{0} & \mathbf{t}_3 & \mathbf{0} & -\mathbf{t}_1 & \mathbf{t}_2 & \mathbf{0} \\ \mathbf{t}_1 & -\frac{1}{l}\mathbf{t}_2 & -\frac{1}{l}\mathbf{t}_2 & \mathbf{0} & \frac{1}{l}\mathbf{t}_3 & \frac{1}{l}\mathbf{t}_3 \\ \mathbf{0} & \mathbf{0} & \mathbf{t}_3 & \mathbf{t}_1 & \mathbf{0} & \mathbf{t}_2 \end{bmatrix}^T \tag{C-39}$$

C.4
Tangent stiffness

The beam tangent stiffness matrix $\mathbf{K}$ is then obtained by taking the increment of the virtual work $\Delta(\delta U)$ in Eq. (C-23), i.e.:

$$\Delta(\delta U) = \delta\mathbf{d}^T \cdot \mathbf{K} \cdot \Delta\mathbf{d} = \delta\overline{\mathbf{d}}^T \cdot \Delta\overline{\mathbf{f}} + \Delta\left(\delta\overline{\mathbf{d}}\right)^T \cdot \overline{\mathbf{f}} \tag{C-40}$$

The tangent stiffness matrix can be decomposed into the element stiffness matrix $\mathbf{K}_m$ and the geometric stiffness matrix $\mathbf{K}_g$, that is, $\mathbf{K} = \mathbf{K}_m + \mathbf{K}_g$. The element stiffness matrix $\mathbf{K}_m$ is related to the increment of the local internal forces vector $\Delta\overline{\mathbf{f}}$:

$$\delta\mathbf{d}^T \cdot \mathbf{K}_m \cdot \Delta\mathbf{d} = \delta\mathbf{d}^T \cdot \mathbf{T}^T \cdot \overline{\mathbf{K}} \cdot \Delta\overline{\mathbf{d}} = \delta\mathbf{d}^T \cdot \mathbf{T}^T \cdot \overline{\mathbf{K}} \cdot \mathbf{T} \cdot \Delta\mathbf{d} \tag{C-41}$$

Hence, the element stiffness matrix $\mathbf{K}_m$ acts as a transformation of the local stiffness matrix $\overline{\mathbf{K}} = \partial\overline{\mathbf{f}}/\partial\overline{\mathbf{d}}$, i.e.:

$$\mathbf{K}_m = \mathbf{T}^T \cdot \overline{\mathbf{K}} \cdot \mathbf{T} \tag{C-42}$$

The geometric stiffness $\mathbf{K}_g$ is related to the increment of the local deformations variation $\Delta\left(\delta\overline{\mathbf{d}}\right)$. This means that one can obtain the geometric stiffness $\mathbf{K}_g$ by considering the increment of system transformation $\Delta\mathbf{T}$ (or equivalently the increment of the local triad $\Delta\mathbf{t}_i$ and current length Δl), while keeping the local forces $\overline{\mathbf{f}}$ fixed:

$$\delta\mathbf{d}^T \cdot \mathbf{K}_g \cdot \Delta\mathbf{d} = \delta\mathbf{d}^T \cdot \Delta\mathbf{T}^T \cdot \overline{\mathbf{f}} = \delta\mathbf{d}^T \cdot \left(\frac{\partial\mathbf{T}^T}{\partial\mathbf{d}} : \overline{\mathbf{f}}\right) \cdot \Delta\mathbf{d} \tag{C-43}$$

Therefore, the geometric stiffness $\mathbf{K}_g$ acts as a rigid body motion of the current local forces with respect to the global system. With the help of Eqs. (C-25), (C-30) to (C-32) and (C-39), its components can be written as:

$$\mathbf{K}_g = \frac{\partial \mathbf{T}^T}{\partial \mathbf{d}} : \bar{\mathbf{f}} = \begin{bmatrix} \mathbf{K}_{11}^g & \mathbf{K}_{12}^g & \mathbf{K}_{13}^g & \mathbf{K}_{14}^g \\ \mathbf{K}_{21}^g & \mathbf{K}_{22}^g & \mathbf{K}_{23}^g & \mathbf{K}_{24}^g \\ \mathbf{K}_{31}^g & \mathbf{K}_{32}^g & \mathbf{K}_{33}^g & \mathbf{K}_{34}^g \\ \mathbf{K}_{41}^g & \mathbf{K}_{42}^g & \mathbf{K}_{43}^g & \mathbf{K}_{44}^g \end{bmatrix} \tag{C-44}$$

$$\mathbf{K}_{22}^g = \overline{m}_y^a \mathbf{B}_3^a - \overline{m}_z^a \mathbf{B}_2^a \tag{C-45}$$

$$\mathbf{K}_{24}^g = \overline{m}_y^a \mathbf{B}_3^b - \overline{m}_z^a \mathbf{B}_2^b \tag{C-46}$$

$$\mathbf{K}_{42}^g = \overline{m}_y^b \mathbf{B}_3^a - \overline{m}_z^b \mathbf{B}_2^a \tag{C-47}$$

$$\mathbf{K}_{44}^g = \overline{m}_y^b \mathbf{B}_3^b - \overline{m}_z^b \mathbf{B}_2^b \tag{C-48}$$

$$\mathbf{K}_{12}^g = +\frac{\overline{m}_z^s}{l} \mathbf{B}_3^a + \frac{\overline{m}_y^s}{l} \mathbf{B}_2^a \tag{C-49}$$

$$\mathbf{K}_{14}^g = +\frac{\overline{m}_z^s}{l} \mathbf{B}_3^b + \frac{\overline{m}_y^s}{l} \mathbf{B}_2^b \tag{C-50}$$

$$\mathbf{K}_{32}^g = -\frac{\overline{m}_z^s}{l} \mathbf{B}_3^a - \frac{\overline{m}_y^s}{l} \mathbf{B}_2^a \tag{C-51}$$

$$\mathbf{K}_{34}^g = -\frac{\overline{m}_z^s}{l} \mathbf{B}_3^b - \frac{\overline{m}_y^s}{l} \mathbf{B}_2^b \tag{C-52}$$

$$\mathbf{K}_{21}^g = +\frac{\overline{m}_x^b}{l} \mathbf{P}_1 + \frac{\overline{m}_y^a}{l} \mathbf{H}_2 + \frac{\overline{m}_z^a}{l} \mathbf{H}_3 \tag{C-53}$$

$$\mathbf{K}_{23}^g = -\frac{\overline{m}_x^b}{l} \mathbf{P}_1 - \frac{\overline{m}_y^a}{l} \mathbf{H}_2 - \frac{\overline{m}_z^a}{l} \mathbf{H}_3 \tag{C-54}$$

$$\mathbf{K}_{41}^g = -\frac{\overline{m}_x^b}{l} \mathbf{P}_1 + \frac{\overline{m}_y^b}{l} \mathbf{H}_2 + \frac{\overline{m}_z^b}{l} \mathbf{H}_3 \tag{C-55}$$

$$\mathbf{K}_{43}^g = +\frac{\overline{m}_x^b}{l} \mathbf{P}_1 - \frac{\overline{m}_y^b}{l} \mathbf{H}_2 - \frac{\overline{m}_z^b}{l} \mathbf{H}_3 \tag{C-56}$$

$$\mathbf{K}_{11}^g = \mathbf{K}_{33}^g = +\frac{\overline{n}_x^b}{l} \mathbf{P}_1 - \frac{\overline{m}_y^s}{l^2} \mathbf{Q}_3 + \frac{\overline{m}_z^s}{l^2} \mathbf{Q}_2 \tag{C-57}$$

$$\mathbf{K}_{13}^g = \mathbf{K}_{31}^g = -\frac{\overline{n}_x^b}{l} \mathbf{P}_1 + \frac{\overline{m}_y^s}{l^2} \mathbf{Q}_3 - \frac{\overline{m}_z^s}{l^2} \mathbf{Q}_2 \tag{C-58}$$

In the above equations, $\overline{m}_{(\cdot)}^s = \overline{m}_{(\cdot)}^a + \overline{m}_{(\cdot)}^b$, and:

$$\mathbf{B}_i^\alpha = \mathbf{t}_i \cdot \mathbf{b}_\alpha^T \tag{C-59}$$

$$\mathbf{P}_1 = \mathbf{t}_2 \cdot \mathbf{t}_2^T + \mathbf{t}_3 \cdot \mathbf{t}_3^T \tag{C-60}$$

$$\mathbf{H}_2 = \mathbf{t}_1 \cdot \mathbf{t}_2^T - \mathbf{t}_3 \cdot \mathbf{a}_r^T \tag{C-61}$$

$$\mathbf{H}_3 = \mathbf{t}_1 \cdot \mathbf{t}_3^T + \mathbf{t}_2 \cdot \mathbf{a}_r^T \tag{C-62}$$

$$\mathbf{Q}_2 = \mathbf{t}_1 \cdot \mathbf{t}_2^T + \mathbf{t}_2 \cdot \mathbf{t}_1^T - \mathbf{t}_3 \cdot \mathbf{a}_r^T \tag{C-63}$$

$$\mathbf{Q}_3 = \mathbf{t}_1 \cdot \mathbf{t}_3^T + \mathbf{t}_3 \cdot \mathbf{t}_1^T + \mathbf{t}_2 \cdot \mathbf{a}_r^T \tag{C-64}$$

Given a symmetric local stiffness matrix $\overline{\mathbf{K}}$, the element stiffness matrix $\mathbf{K}_m$ preserves its symmetry. However, the geometric stiffness $\mathbf{K}_g$ is, in general, not symmetric. This is associated to the non-commutative characteristic of spatial rotations.

C.5
Benchmarks

In order to validate the developed code based on this beam formulation, the classical problem of a cantilever beam subjected to a bending moment at the free end is analyzed (Fig. C.2). The analytical solution for the axial and transversal displacements (u, v) at the free end is given by $u/L = sin(\lambda)/\lambda$ and $v/L = [1 - \cos(\lambda)]/\lambda$ [123]. The numerical solution, with twenty elements, is obtained up to $\lambda = 8\pi$, when the beam makes four revolutions around itself. The results (Fig. C.3) show a good agreement with the analytical solution up to large displacements and rotations.
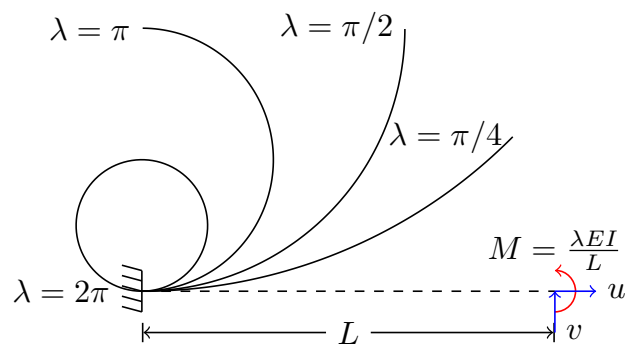
Figure C.2: Bending beam subjected to end-moment.
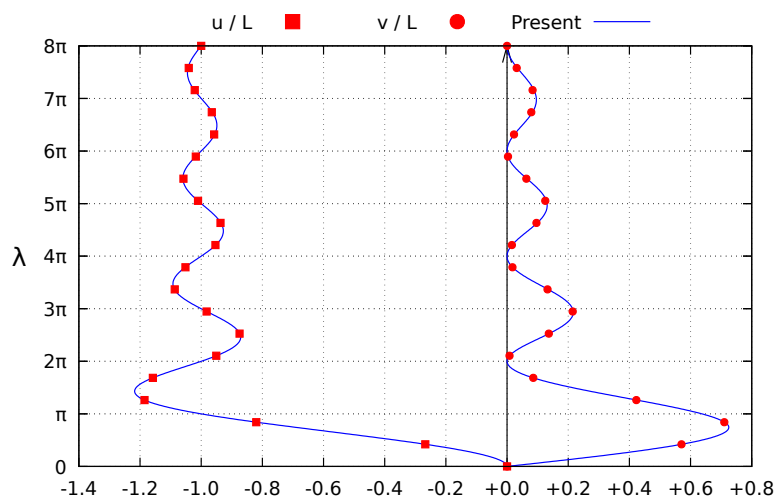
Figure C.3: Bending beam equilibrium path.

The spatial behavior of the beam element is now validated through the analysis of the right angle frame illustrated in Fig. C.4. As the beam cross sections is very thin, when the bifurcation moment $M = 626.7$ is reached, the structure follows the secondary equilibrium path, where torsional moments starts to appear. Figure C.5 shows the variation of the out of plane displacement of the tip node w with the applied moment M. The results, with five finite elements per beam, are compared with those presented in [124], showing excellent agreement.
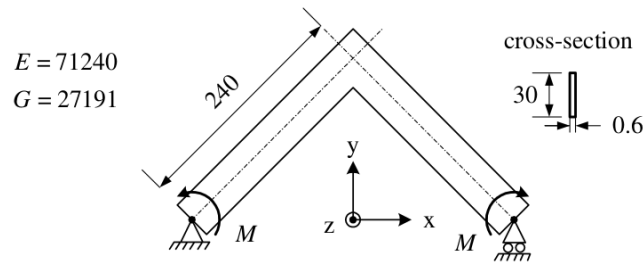
Figure C.4: Right angle frame (Source: [6]).
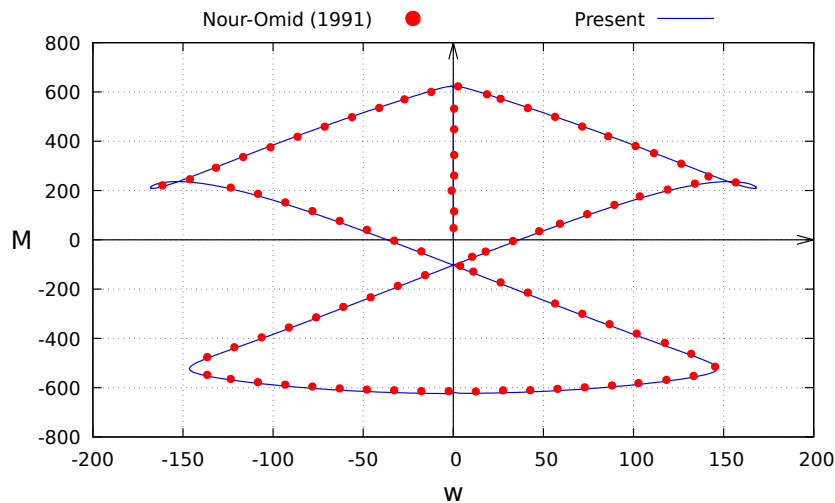
Figure C.5: Right angle frame equilibrium path.

As a third example, the torsional buckling and post-buckling behavior of a slender beam subjected to a concentrated torsion moment as illustrated in Fig. C.6 is analyzed. When the torsion moment T reaches the critical value the beam buckles, following a secondary equilibrium path, where bending moments appear. Figure. C.7, shows the highly nonlinear response of the beam. The results, with twenty beam elements, are favorably compared with those presented in [124].

$$\nu = 0.31 \qquad I_x = 2.16$$
$$E = 71.24 \qquad I_y = 0.0833$$
$$G = 27.19 \qquad I_z = 0.0833$$
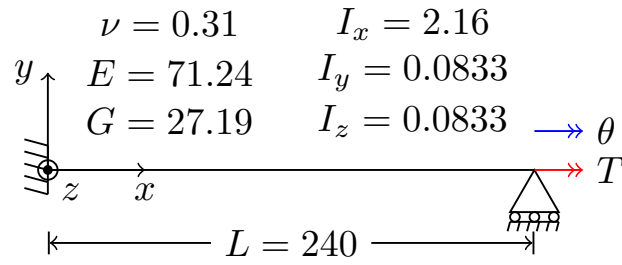
Figure C.6: Beam subjected to a torsion moment.
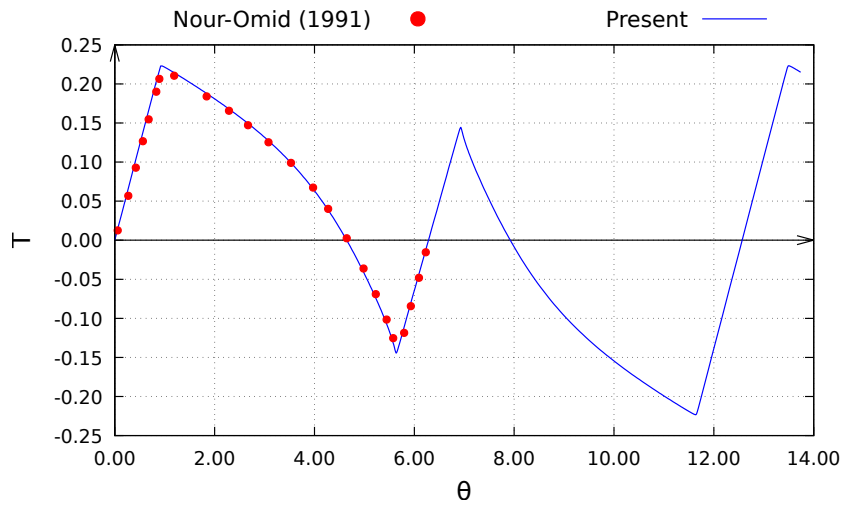
Figure C.7: Nonlinear equilibrium path of the beam under torsion.

D
Nonlinear equations solvers

This Appendix presents briefly the algorithms implemented here to solve the system of nonlinear equilibrium equations in the static analysis and the nonlinear equations of motion of the discretized structure in the dynamic analysis. The algorithms implemented to obtain the static nonlinear equilibrium paths are presented in Sec. D.1, where the Newton-Raphson algorithm is coupled with path following strategies. The methods for computation of the nonlinear dynamic response of the structural systems are discussed in Sec. D.2, where either the Newmark (Sec. D.2.1) or 4th order Runge-Kutta (Sec. D.2.2) algorithms are used. The nonlinear oscillations and bifurcations are also studied making use of Poincaré maps (Sec. D.2.3).

D.1
Static nonlinear solver

The static response of a structural system is governed by a system of nonlinear algebraic equations of the type $\mathbf{F}_i(\mathbf{x}) = \lambda \mathbf{F}_r$, where $\mathbf{x}$ is a state vector with the system degrees of freedom, $\mathbf{F}_i$ is the system internal forces vector with a nonlinear dependency on $\mathbf{x}$, $\mathbf{F}_r$ is a reference load vector and λ is a load factor. The tangent stiffness matrix on the current configuration is defined as $\mathbf{K}(\mathbf{x}) = \partial \mathbf{F}_i / \partial \mathbf{x}$.

The numerical solution this system of equations is conducted through the Newton-Raphson method coupled with a continuation strategy. The procedure is illustrated in Tab. D.1. Basically, given a known equilibrium configuration $(\mathbf{x}_n, \lambda_n)$ the aim is to determine the next configuration $(\mathbf{x}_{n+1}, \lambda_{n+1})$, using an initial load increment $\Delta\lambda_{n+1}^0$ and computing the corresponding state increment $\Delta\mathbf{x}_{n+1}^0$ in the current tangent direction. A iterative loop then starts by computing the new current configuration $(\mathbf{x}_{n+1}^k, \lambda_{n+1}^k)$ and the corresponding residual force vector $\mathbf{r}_{n+1}^k$. If the residue is sufficiently small, the current configuration is accepted and the iterative loop finishes. Otherwise, a new candidate configuration is computed making use of the current stiffness $\mathbf{K}(\mathbf{x}_{n+1}^k)$ and the adopted solution strategy.

Algorithm 1: Newton-Raphson

---

1 Predictor:

- Solution strategy $\rightarrow \Delta\lambda_{n+1}^0$
- $\Delta\mathbf{x}_{n+1}^0 = \Delta\lambda_{n+1}^0 \mathbf{K}(\mathbf{x}_n)^{-1} \cdot \mathbf{F}_r$

2 Iterative loop:

  2.1 State update:

- $\lambda_{n+1}^k = \lambda_n + \Delta\lambda_{n+1}^k$
- $\mathbf{x}_{n+1}^k = \mathbf{x}_n + \Delta\mathbf{x}_{n+1}^k$

  2.2 Residual force:

- $\mathbf{r}_{n+1}^k = \lambda_{n+1}^k \mathbf{F}_r - \mathbf{F}_i(\mathbf{x}_{n+1}^k)$
- if $\|\mathbf{r}_{n+1}^k\| < tol\|\mathbf{F}_r\|$ exit iterative loop

  2.3 Corrector:

- $\delta\mathbf{x}_{t,n+1}^k = \mathbf{K}(\mathbf{x}_{n+1}^k)^{-1} \cdot \mathbf{F}_r$
- $\delta\mathbf{x}_{r,n+1}^k = \mathbf{K}(\mathbf{x}_{n+1}^k)^{-1} \cdot \mathbf{r}_{n+1}^k$
- Solution strategy $\rightarrow \delta\lambda_{n+1}^{k+1}$
- $\delta\mathbf{x}_{n+1}^{k+1} = \delta\mathbf{x}_{r,n+1}^k + \delta\lambda_{n+1}^{k+1}\delta\mathbf{x}_{t,n+1}^k$

  2.4 Increment update:

- $\Delta\lambda_{n+1}^{k+1} = \Delta\lambda_{n+1}^k + \delta\lambda_{n+1}^{k+1}$
- $\Delta\mathbf{x}_{n+1}^{k+1} = \Delta\mathbf{x}_{n+1}^k + \delta\mathbf{x}_{n+1}^{k+1}$

Table D.1: Newton-Raphson incremental step

D.1.1
Solution strategies

The main goal of a solution strategy is to permit the solver to overcome load and displacement limit points, while making it as robust as possible. Many solution strategies have been proposed in the literature. In the present work the cylindrical arc-length [125] and the minimal norm [126] are implemented. In both methods, the load increment initial predictor $\Delta\lambda_{n+1}^0$ is computed as:

$$\Delta\lambda_{n+1}^0 = \text{sign}(\Delta\mathbf{x}_n^T \cdot \Delta\mathbf{x}_t)\frac{\|\Delta\mathbf{x}_n\|}{\|\Delta\mathbf{x}_t\|} \tag{D-1}$$

where $\Delta\mathbf{x}_t = \mathbf{K}_n^{-1} \cdot \mathbf{F}_r$.

In the cylindrical arc-length method the new configuration $(\Delta\mathbf{x}_{n+1}, \lambda_{n+1})$ is constrained to an hyper-dimensional cylinder around the know configuration $(\Delta\mathbf{x}_n, \lambda_n)$ and so, in a iterative procedure, the load sub-increment $\delta\lambda_{n+1}^{k+1}$ is

given by:

$$\delta\lambda_{n+1}^{k+1} = -\frac{b}{a} + s\sqrt{\left(\frac{b}{a}\right)^2 - \frac{c}{a}} \tag{D-2}$$

where:

$$a = \delta\mathbf{x}_{t,n+1}^k \cdot \delta\mathbf{x}_{t,n+1}^k \tag{D-3}$$

$$s = \text{sign}(\delta\mathbf{x}_{t,n+1}^k \cdot \Delta\mathbf{x}_{n+1}^k) \tag{D-4}$$

$$b = \delta\mathbf{x}_{t,n+1}^k \cdot (\delta\mathbf{x}_{r,n+1}^k + \Delta\mathbf{x}_{n+1}^k) \tag{D-5}$$

$$c = \delta\mathbf{x}_{r,n+1}^k \cdot (\delta\mathbf{x}_{r,n+1}^k + 2\Delta\mathbf{x}_{n+1}^k) \tag{D-6}$$

In the minimal norm method the load sub-increment is chosen so that the norm of the residual force vector $\mathbf{r}_{n+1}^{k+1}$ is as small as, being given by:

$$\delta\lambda_{n+1}^{k+1} = -\frac{\delta\mathbf{x}_{r,n+1}^k \cdot \delta\mathbf{x}_{t,n+1}^k}{\delta\mathbf{x}_{t,n+1}^k \cdot \delta\mathbf{x}_{t,n+1}^k} \tag{D-7}$$

In general, both methods deal well with elastic problems subjected to geometrical nonlinear behavior, such as snap-through and buckling. In elasto-plastic problems however the minimal norm method performed better than the cylindrical arc-length method in the conducted numerical simulations.

Both translational and rotational degrees of freedom are considered in the cylindrical arc-length and minimal norm methods. When finite spatial rotations are taken into account the behavior of the nonlinear system of equations becomes much more complex and convergence problems were verified frequently. Usually, this problems could be avoided via a controlled update of the load increment. For this, the number of iterations used in the last step i_n are compared to a desired number of iterations i_d and the new load increment initial predictor is computed as [116]:

$$\Delta\lambda_{n+1}^0 = \sqrt{\frac{i_d}{i_n}}\Delta\lambda_n^0 \tag{D-8}$$

In regions of the solution with a strong nonlinear behavior, a high number of iterations i_n is necessary and the new initial load increment $\Delta\lambda_{n+1}^0$ is reduced. In regions of the solution with an almost linear behavior, only a few iterations are required and the new initial load load increment $\Delta\lambda_{n+1}^0$ is increased. Other continuation methods and update strategies, suited for highly nonlinear elastic and elasto-plastic problems, are available in the literature e.g. Skatulla and Sansour [127].

D.2
Dynamic nonlinear solver

The dynamic response of a structural system is governed by a system of second order nonlinear differential equations of the type $\mathbf{M}(\mathbf{x}) \cdot \ddot{\mathbf{x}} + \mathbf{F}_i(\mathbf{x}, \dot{\mathbf{x}}) = \mathbf{F}_e(t)$, where $\mathbf{M}(\mathbf{x})$ and $\mathbf{F}_e(t)$ are the generalized mass matrix and external forces vector, respectively. The system internal forces vector $\mathbf{F}_i(\mathbf{x}, \dot{\mathbf{x}})$ may have a nonlinear dependency on the system state $\mathbf{x}$ and velocity $\dot{\mathbf{x}}$, and the system stiffness and damping are defined as $\mathbf{K}(\mathbf{x}, \dot{\mathbf{x}}) = \partial \mathbf{F}_i / \partial \mathbf{x}$ and $\mathbf{C}(\mathbf{x}, \dot{\mathbf{x}}) = \partial \mathbf{F}_i / \partial \dot{\mathbf{x}}$, respectively. As the mass matrix is always positive definite, and so invertible, the acceleration vector $\ddot{\mathbf{x}}$ can easily be determined from the equations of motion as function of the system displacements $\mathbf{x}$ and velocities $\dot{\mathbf{x}}$ in a given time step t from: $\ddot{\mathbf{x}} = \mathbf{M}(\mathbf{x})^{-1} \left[\mathbf{F}_e(t) - \mathbf{F}_i(\mathbf{x}, \dot{\mathbf{x}}) \right]$.

A variety of methods have been proposed in the literature for the numerical solution of such a system of equations. The main goal is to, given $(\mathbf{x}_n, \dot{\mathbf{x}}_n)$ in a given time step t_n, determine $(\mathbf{x}_{n+1}, \dot{\mathbf{x}}_{n+1})$ in the time step t_{n+1}. In the present work, the Newmark and 4th order Runge-Kutta methods are used. The Newmark method has a greater computational cost, since it requires the assembly of the system stiffness $\mathbf{K}$ and damping $\mathbf{C}$ matrices. Also, inversion of the resulting system matrix is generally more numerically unstable than the mass matrix $\mathbf{M}$ (which is diagonal in many applications), used in the Runge-Kutta method. However, in the Newmark method, the residual force vector $\mathbf{r}$, if is restricted to certain tolerance in each time step, the obtained numerical solution is less prone to diverge from the exact solution.

D.2.1
Newmark method

In the Newmark method, given $(\mathbf{x}_n, \dot{\mathbf{x}}_n)$, an initial candidate $(\mathbf{x}_{n+1}^0, \dot{\mathbf{x}}_{n+1}^0)$ is computed in the predictor phase by assuming a constant acceleration $(\ddot{\mathbf{x}}_{n+1}^0 = \ddot{\mathbf{x}}_n)$ over the time step Δt. A iterative loop then starts by computing the current residual force vector $\mathbf{r}_{n+1}^k$. If the residue is small enough, the current variables are accepted and the iterative loop finishes. Otherwise, the variables are interpolated in the time interval $t \in [t_n, t_{n+1}]$ making use of the parameters γ and β, usually taken as $1/2$ and $1/4$, respectively. A new candidate configuration is then computed with the system matrix $\mathbf{S}$ defined as a linear combination of the current stiffness, damping and inertia matrices. This procedure is illustrated in Tab. D.2.

Algorithm 2: Newmark

1 Predictor:

- $\ddot{\mathbf{x}}^0_{n+1} = \ddot{\mathbf{x}}_n$
- $\dot{\mathbf{x}}^0_{n+1} = \dot{\mathbf{x}}_n + \Delta t \ddot{\mathbf{x}}_n$
- $\mathbf{x}^0_{n+1} = \mathbf{x}_n + \Delta t \dot{\mathbf{x}}_n + \Delta t^2 \ddot{\mathbf{x}}_n / 2$

2 Time update:

- $t_{n+1} = t_n + \Delta t$

3 Iterative loop:

   3.1 Residual force:

- $\mathbf{r}^k_{n+1} = \mathbf{F}_e(t_{n+1}) - \mathbf{F}_i(\mathbf{x}^k_{n+1}, \dot{\mathbf{x}}^k_{n+1}) - \mathbf{M}(\mathbf{x}^k_{n+1}) \cdot \ddot{\mathbf{x}}^k_{n+1}$
- if $\|\mathbf{r}^k_{n+1}\| < tol\|\mathbf{F}_e(t_{n+1})\|$ exit iterative loop

   3.2 Corrector:

- $\mathbf{S}^k_{n+1} = \mathbf{K}(\mathbf{x}^k_{n+1}, \dot{\mathbf{x}}^k_{n+1}) + \frac{\gamma}{\beta\Delta t}\mathbf{C}(\mathbf{x}^k_{n+1}, \dot{\mathbf{x}}^k_{n+1}) + \frac{1}{\beta\Delta t^2}\mathbf{M}(\mathbf{x}^k_{n+1})$
- $\delta\mathbf{x}^k_{n+1} = \left(\mathbf{S}^k_{n+1}\right)^{-1} \cdot \mathbf{r}^k_{n+1}$

   3.3 State update:

- $\mathbf{x}^{k+1}_{n+1} = \mathbf{x}^k_{n+1} + \delta\mathbf{x}^{k+1}_{n+1}$
- $\dot{\mathbf{x}}^{k+1}_{n+1} = \dot{\mathbf{x}}^k_{n+1} + \frac{\gamma}{\beta\Delta t}\delta\mathbf{x}^{k+1}_{n+1}$
- $\ddot{\mathbf{x}}^{k+1}_{n+1} = \ddot{\mathbf{x}}^k_{n+1} + \frac{1}{\beta\Delta t^2}\delta\mathbf{x}^{k+1}_{n+1}$

Table D.2: Newmark time step

D.2.2
Runge-Kutta method

In the 4th order Runge-Kutta algorithm the finite increments $\Delta\mathbf{x}_{n+1}$ and $\Delta\dot{\mathbf{x}}_{n+1}$ are progressively computed in four points inside the interval $[t_n, t_{n+1}]$. Starting at t_n, passing through two virtual configurations at $(t_n + t_{n+1})/2$ and one at t_{n+1}, the increments are specifically weighted, computing the rate of change at each point through the system nonlinear equations of motion. When the material elasto-plastic behavior is considered in the finite element formulations, the reference configuration used in the return mapping algorithms is always taken as the real known one $(\mathbf{x}_n, \dot{\mathbf{x}}_n)$. The procedure is illustrated in Tab. D.3.

Algorithm 3: Runge-Kutta

---

1 First increment:

- $\Delta\mathbf{x}_{n+1} = \frac{\Delta t}{6}\dot{\mathbf{x}}_n$
- $\Delta\dot{\mathbf{x}}_{n+1} = \frac{\Delta t}{6}\ddot{\mathbf{x}}_n$

2 Second increment:

- $t = t_n + \frac{\Delta t}{2}$
- $\mathbf{x} = \mathbf{x}_n + \frac{\Delta t}{2}\dot{\mathbf{x}}_n$
- $\dot{\mathbf{x}} = \dot{\mathbf{x}}_n + \frac{\Delta t}{2}\ddot{\mathbf{x}}_n$
- $\ddot{\mathbf{x}} = \mathbf{M}(\mathbf{x})^{-1} \cdot [\mathbf{F}_e(t) - \mathbf{F}_i(\mathbf{x}, \dot{\mathbf{x}})]$
- $\Delta\mathbf{x}_{n+1} = \Delta\mathbf{x}_{n+1} + \frac{\Delta t}{3}\dot{\mathbf{x}}$
- $\Delta\dot{\mathbf{x}}_{n+1} = \Delta\dot{\mathbf{x}}_{n+1} + \frac{\Delta t}{3}\ddot{\mathbf{x}}$

3 Third increment:

- $\mathbf{x} = \mathbf{x}_n + \frac{\Delta t}{2}\dot{\mathbf{x}}$
- $\dot{\mathbf{x}} = \dot{\mathbf{x}}_n + \frac{\Delta t}{2}\ddot{\mathbf{x}}$

- $\ddot{\mathbf{x}} = \mathbf{M}(\mathbf{x})^{-1} \cdot [\mathbf{F}_e(t) - \mathbf{F}_i(\mathbf{x}, \dot{\mathbf{x}})]$
- $\Delta\mathbf{x}_{n+1} = \Delta\mathbf{x}_{n+1} + \frac{\Delta t}{3}\dot{\mathbf{x}}$
- $\Delta\dot{\mathbf{x}}_{n+1} = \Delta\dot{\mathbf{x}}_{n+1} + \frac{\Delta t}{3}\ddot{\mathbf{x}}$

4 Forth increment:

- $t = t_n + \Delta t$
- $\mathbf{x} = \mathbf{x}_n + \Delta t\dot{\mathbf{x}}_n$
- $\dot{\mathbf{x}} = \dot{\mathbf{x}}_n + \Delta t\ddot{\mathbf{x}}_n$
- $\ddot{\mathbf{x}} = \mathbf{M}(\mathbf{x})^{-1} \cdot [\mathbf{F}_e(t) - \mathbf{F}_i(\mathbf{x}, \dot{\mathbf{x}})]$
- $\Delta\mathbf{x}_{n+1} = \Delta\mathbf{x}_{n+1} + \frac{\Delta t}{6}\dot{\mathbf{x}}$
- $\Delta\dot{\mathbf{x}}_{n+1} = \Delta\dot{\mathbf{x}}_{n+1} + \frac{\Delta t}{6}\ddot{\mathbf{x}}$

5 Step increment:

- $\mathbf{x}_{n+1} = \mathbf{x}_n + \Delta\mathbf{x}_{n+1}$
- $\dot{\mathbf{x}}_{n+1} = \dot{\mathbf{x}}_n + \Delta\dot{\mathbf{x}}_{n+1}$

Table D.3: Runge-Kutta 4th order time step

D.2.3
Poincaré maps

In a dynamic analysis, the designer may be interested on the effect of some control parameter, such as the magnitude of the applied external load P or the exciting frequency ω, on the system response, in particular dynamic bifurcations and jumps. This can be achieved through the use of the bifurcation diagrams of the Poincaré map, which is a useful tool in nonlinear dynamics. Here, the so called brute-force method is implemented, where, for each increment or decrement of the control parameters (P or ω), the stable fixed points coordinates of the Poincaré map are obtained [92].

The method consists in computing the system time response during n_p periods of the external force, each divided in n_t time steps. Then, the first n_d periods of the time response are discarded as the transient part of the solution. The first minimum (or maximum) of the remaining data is then located and the value of the oscillation amplitude is stored for the remaining $n_p - n_d$ periods. The control parameter is then incremented and the process is repeated. The procedure is illustrated in Tab. D.4. As expected, the quality of the numerical results increases with the number of periods considered n_p and discarded n_d since the influence of the transient part of the response becomes smaller, increasing however the computational cost.

Algorithm 4: Poincaré map

---

1 Increment control parameter (P or ω)

2 Compute current time spacing: $\Delta T = 2\pi/\omega$

3 Compute time response (with $T = n_p\Delta T$ and $n_s = n_p n_t$)

4 Discard transient part (first $n_d n_t$ steps)

5 Find first limit step s_0 ($x = $ minimum)

6 Select time steps $s_0 + n_t i, i \in \mathbb{N}$

Table D.4: Poincaré bifurcation maps incremental step

Bibliography

[1] London stansted airport. `daf9627eib4jq.cloudfront.net/app/uploads/2018/07/Paul-Kalkhoven_Foster-2.jpg`, 2019. Accessed: 09/02/2019.

[2] Lattice structure. `www.virginia.edu/ms/research/wadley/images/airshockloadingfig4.JPG`, 2019. Accessed: 09/02/2019.

[3] Hoberman dome. `1.bp.blogspot.com/-7cpTnly7Xrc/Trw7cPh3gZI/AAAAAAAAAEc/trA5oQleCJI/s1600/hoberman_domepana.jpg`, 2019. Accessed: 25/02/2019.

[4] Deployable structure. `https://smg2011.files.wordpress.com/2011/02/transformable.jpg?w=300&h=225`, 2019. Accessed: 09/02/2019.

[5] Deployable space structure. `http://forth.aero.cst.nihon-u.ac.jp/e/topics/FY2016_02/0.jpg`, 2019. Accessed: 26/02/2019.

[6] J-M. Battini and C. Pacoste. Co-rotational beam elements with warping effects in instability problems. *Computer Methods in Applied Mechanics and Engineering*, 191:1755 – 1789, 2002.

[7] S. C. Pradhan. Buckling of single layer graphene sheet based on nonlocal elasticity and higher order shear deformation theory. *Physics Letters A*, 373:4182–4188, 2009.

[8] K. Shea and J. Cagan. Innovative dome design: Applying geodesic patterns with shape annealing. *Artificial Intelligence for Engineering, Design, Analysis and Manufacturing*, 11:379–394, 1997.

[9] S. S. Ligarò and P. S. Valvo. Large displacement analysis of elastic pyramidal trusses. *International Journal of Solids and Structures*, 43: 4867 – 4887, 2006.

[10] D. T. Queheillalt and H. N. G. Wadley. Pyramidal lattice truss structures with hollow trusses. *Materials Science and Engineering: A*, 397:132–137, 2005.

[11] J. Xiong, R. Ghosh, L. Ma, H. Ebrahimi, A. M. S. Hamouda, A. Vaziri, and L. Wu. Bending behavior of lightweight sandwich-walled shells with pyramidal truss cores. *Composite Structures*, 116:793–804, 2014.

[12] Y. Huang, Y. Xue, X. Wang, and F. Han. Effect of cross sectional shape of struts on the mechanical properties of aluminum based pyramidal lattice structures. *Materials Letters*, 202:55–58, 2017.

[13] Geodesic dome. `media.gettyimages.com/photos/biosphere/ environment/museum/geodesic/dome/designed/for/expo/67/by/ picture/id621709401`, 2019. Accessed: 26/02/2019.

[14] Geodesic dome (inner view). `www.tripsavvy.com/thmb/ Nr4Yj1ISxbH5XtAWGoDAQeIGpls=/960x0parc/jean/drapeau/ attractions/biosphere/montreal/geodesic/dome/yanis/ourabah/ getty/56a641113df78cf7728c2155.jpg`, 2019. Accessed: 26/02/2019.

[15] C. H. L. Castro. Nonlinear vibrations and stability of shallow pyramidal trusses. Master's thesis, Civil Engineering Department, PUC-Rio, Brazil, 2014.

[16] D. Orlando, C. H. L. de Castro, and P. B. Gonçalves. Nonlinear vibrations and instability of a bistable shallow reticulated truss. *Nonlinear Dynamics*, 2018.

[17] D. Orlando, P. B. Gonçalves, G. Rega, and S. Lenci. Influence of transient escape and added load noise on the dynamic integrity of multistable systems. *International Journal of Non-Linear Mechanics*, 109:140–154, 2019.

[18] L. Alegria Mira, A. P. Thrall, and N. De Temmerman. Deployable scissor arch for transitional shelters. *Automation in Construction*, 43:123–131, 2014.

[19] N. D. Temmerman. *Design and Analysis of Deployable Bar Structures for Mobile Architectural Applications*. PhD thesis, Vrije Universiteit Brussel, 2007.

[20] Y. Zhang, N. Li, G. Yang, and W. Ru. Dynamic analysis of the deployment for mesh reflector deployable antennas with the cable-net structure. *Acta Astronautica*, 131:182–189, 2017.

[21] L. I. W. Arnouts, T. J. Massart, N. De Temmerman, and P. Z. Berke. Computational modelling of the transformation of bistable scissor structures with geometrical imperfections. *Engineering Structures*, 177:409–420, 2018.

[22] C. J. Gantes. *A Design Methodology for Deployable Structures*. PhD thesis, Massachusetts Institute of Technology, 1991.

[23] P. B. Gonçalves, D. Orlando, F. M. Silva, S. Lenci, and G. Rega. Nonlinear dynamics, safety, and control of structures liable to interactive unstable buckling. In *In Global nonlinear dynamics for engineering design and system safety*, pages 167–228. Springer, Cham, 2019.

[24] D. L. Kozak and A. B. Liel. Reliability of steel roof structures under snow loads. *Structural Safety*, 54:46–56, 2015.

[25] F. Piroglu and K. Ozakgul. Partial collapses experienced for a steel space truss roof structure induced by ice ponds. *Engineering Failure Analysis*, 60:155–165, 2016.

[26] A. C. Altunişik, Ş. Ateş, and M. Hüsem. Lateral buckling failure of steel cantilever roof of a tribune due to snow loads. *Engineering Failure Analysis*, 72:67–78, 2017.

[27] L. Kwasniewski. Complete equilibrium paths for mises trusses. *International Journal of Non-Linear Mechanics*, 44:19 – 26, 2009.

[28] M. A. Crisfield. *Non-Linear Finite Element Analysis of Solids and Structures*, volume II. Wiley, 1997.

[29] Z. Kala and M. Kalina. Static equilibrium states of von mises trusses. *International Journal of Mechanics*, 10:294 – 298, 2016.

[30] M. Psotný and J. Ravinger. Von misses truss with imperfection. *Slovak Journal of Civil Engineering*, pages 1 – 7, 2003.

[31] M. Kalina. Stability problems of pyramidal von mises planar trusses with geometrical imperfection. *International Journal of Theoretical and Applied Mechanics*, 1:118 – 123, 2016.

[32] A. B. Halpernand and S. Adriaenssens. Nonlinear elastic in-plane buckling of shallow truss arches. *Journal of Bridge Engineering*, 20:1 – 11, 2015.

[33] R. H. Plaut. Snap-through of shallow reticulated domes under unilateral displacement control. *International Journal of Solids and Structures*, pages 1 – 11, 2017.

[34] F. Bazzucchi, A. Manuello, and A. Carpinteri. Interaction between snap-through and eulerian instability in shallow structures. *International Journal of Non–Linear Mechanics*, 88:11 – 20, 2017.

[35] F. Bazzucchi, A. Manuello, and A. Carpinteri. Instability load evaluation of shallow imperfection-sensitive structures by form and interaction parameters. *European Journal of Mechanics - A/Solids*, 66:201–211, 2017.

[36] F. Fan, Z. Cao, and S. Shen. Elasto-plastic stability of single-layer reticulated shells. *Thin-Walled Structures*, 48:827 – 836, 2010.

[37] X. Zhi, F. Fan, and S. Shen. Elasto-plastic instability of single-layer reticulated shells under dynamic actions. *Thin-Walled Structures*, 48: 837 – 845, 2010.

[38] V. Gioncu. General theory of coupled instabilities. *Thin-Walled Structures*, 19(2):81–127, 1994.

[39] J. M. T. Thompson and G. W. Hunt. *Elastic Instability Phenomena*. Wiley, 1984.

[40] J. Wu, J. Li, and S. Yan. Design of deployable bistable structures for morphing skin and its structural optimization. *Engineering Optimization*, 46:745–762, 2013.

[41] H. Yasuda and J. Yang. Reentrant origami-based metamaterials with negative poisson's ratio and bistability. *Physical Review Letters*, 114 (18), 2015.

[42] V. Tuz, S. Prosvirnin, and L. Kochetova. Optical bistability involving planar metamaterial with a broken structural symmetry. In *2010 10th International Conference on Laser and Fiber-Optical Networks Modeling*, 2010.

[43] R. L. Harne and K. W. Wang. A review of the recent research on vibration energy harvesting via bistable systems. *Smart Materials and Structures*, 22(2):023001, 2013.

[44] Z. Whitman and V. La Saponara. Bistable structures for energy absorption, i: Metallic structures. *Journal of Mechanics of Materials and Structures*, 2(2):347–358, 2007.

[45] S. Lenci and G. Rega. Control of pull-in dynamics in a nonlinear thermoelastic electrically actuated microbeam. *Journal of Micromechanics and Microengineering*, 16(2):390, 2006.

[46] E. Kebadze, S. D. Guest, and S. Pellegrino. Bistable prestressed shell structures. *International Journal of Solids and Structures*, 41(11-12): 2801–2820, 2004.

[47] M. Santer and S. Pellegrino. Compliant multistable structural elements. *International Journal of Solids and Structures*, 45(24):6190–6204, 2008.

[48] Q. Chen, Y. Haddab, and P. Lutz. Digital microrobotics based on bistable modules: Design of compliant bistable structures. In *2008 IEEE/ASME International Conference on Mechtronic and Embedded Systems and Applications*, 2008.

[49] M. Vangbo. An analytical analysis of a compressed bistable buckled beam. *Sensors and Actuators A: Physical*, 69(3):212–216, 1998.

[50] V. B. Taranenko, I. Ganne, R. J. Kuszelewicz, and C. O. Weiss. Patterns and localized structures in bistable semiconductor resonators. *Physical Review A*, 61(6), 2000.

[51] T. Xu, L. Ruzziconi, and M. I. Younis. Global investigation of the nonlinear dynamics of carbon nanotubes. *Acta Mechanica*, 228(3):1029–1043, 2017.

[52] M. R. Schultz. A concept for airfoil-like active bistable twisting structures. *Journal of Intelligent Material Systems and Structures*, 19(2): 157–169, 2008.

[53] A. Brinkmeyer, M. Santer, A. Pirrera, and P. M. Weaver. Pseudo-bistable self-actuated domes for morphing applications. *International Journal of Solids and Structures*, 49:1077 – 1087, 2012.

[54] A. Brinkmeyer, A. Pirrera, M. Santer, and P. M. Weaver. Pseudo-bistable pre-stressed morphing composite panels. *International Journal of Solids and Structures*, 50:1033 – 1043, 2013.

[55] M. E. Pontecorvo, S. Barbarino, G. J. Murray, and F. S. Gandhi. Bistable arches for morphing applications. *Journal of Intelligent Material Systems and Structures*, 24:274–286, 2012.

[56] Y. Cui and M. Santer. Highly multistable composite surfaces. *Composite Structures*, 124:44 – 54, 2015.

[57] J. Cai, X. Deng, and J. Feng. Effects of symmetric imperfections on the behavior of bistable struts. *Mathematics and Mechanics of Solids*, 22: 2240 – 2252, 2017.

[58] L-J. Feng, L-Z. Wu, and G-C. Yu. An hourglass truss lattice structure and its mechanical performances. *Materials & Design*, 99:581–591, 2016.

[59] C. J. Yungwirth, D. D. Radford, M. Aronson, and H. N. G. Wadley. Experiment assessment of the ballistic response of composite pyramidal lattice truss structures. *Composites Part B: Engineering*, 39:556–569, 2008.

[60] L. A. Danso and E. G. Karpov. Cusp singularity-based bistability criterion for geometrically nonlinear structures. *Extreme Mechanics Letters*, 13:135–140, 2017.

[61] J. Wang, A. G. Evans, K. Dharmasena, and H. N. G. Wadley. On the performance of truss panels with kagomé cores. *International Journal of Solids and Structures*, 40:6981–6988, 2003.

[62] M. V. B. Santana, P. B. Gonçalves, and R. A. M. Silveira. Static stability and load capacity of pyramidal trusses. *MATEC Web of Conferences*, 148:07005, 2018.

[63] D. Perić, D. R. J. Owen, and M. E. Honnor. A model for finite strain elasto-plasticity based on logarithmic strains: Computational issues. *Computer Methods in Applied Mechanics and Engineering*, 94(1):35–61, 1992.

[64] R. Naghdabadi, M. Yeganeh, and A. Saidi. Application of corotational rates of the logarithmic strain in constitutive modeling of hardening materials at finite deformations. *International Journal of Plasticity*, 21 (8):1546–1567, 2005.

[65] P. Neff, B. Eidel, and R. J. Martin. Geometry of logarithmic strain measures in solid mechanics. *Archive for Rational Mechanics and Analysis*, 222(2):507–572, 2016.

[66] M. Geradin and A. Cardona. *Flexible multibody dynamics.* Wiley, 2001.

[67] J. Bonet and R. D. Wood. *Nonlinear Continuum Mechanics for Finite Element Analysis.* Cambridge, 2008.

[68] R. H. Plaut and L. N. Virgin. Use of frequency data to predict buckling. *Journal of Engineering Mechanics*, 116(10):2330–2335, 1990.

[69] S. Hassiotis and G. D. Jeong. Identification of stiffness reductions using natural frequencies. *Journal of Engineering Mechanics*, 121(10):1106–1113, 1995.

[70] X. M. Jiang, H. Chen, and J. Y. R. Liew. Spread-of-plasticity analysis of three-dimensional steel frames. *Journal of Constructional Steel Research*, 58:193 – 212, 2002.

[71] A. M. A. van der Heijden, editor. *W. T. Koiter's Elastic Stability of Solids and Structures.* Cambridge University Press, 2008.

[72] S. P. Timoshenko. *Theory of elastic stability.* McGraw-Hill, 1988.

[73] 1993. ENV - 1993 - 01 - 01 - Eurocode 3. Design of Steel Structures, Commission of the European Communities, Brussels, Belgium (1993).

[74] R. D. Ziemian. *Guide to stability design criteria for metal structures.* John Wiley and Sons, 2010.

[75] J. Lindner, U. Kuhlmann, and F. Jörg. Initial bow imperfections e0 for the verification of flexural buckling according to eurocode 3 part 1-1 - additional considerations. *Steel Construction*, 11(1):30–41, 2018.

[76] Imoa materials. `www.imoa.info/molybdenum-uses/molybdenum-grade-alloy-steels-irons/maraging-steels.php`, 2018. Accessed: 04/09/2018.

[77] V. Palmov. *Vibrations of Elasto-Plastic Bodies.* Springer Berlin Heidelberg, 1998.

[78] R. Pratap, S. Mukherjee, and F. C. Moon. Limit cycles in an elasto-plastic oscillator. *Physics Letters A*, 170(5):384–392, 1992.

[79] R. Pratap, S. Mukherjee, and F. C. Moon. Dynamic behavior of a bilinear hysteretic elasto-plastic oscillator, part i: Free oscillations. *Journal of Sound and Vibration*, 172(3):321–337, 1994.

[80] R. Pratap, S. Mukherjee, and F. C. Moon. Dynamic behavior of a bilinear hysteretic elasto-plastic oscillator, part II: Oscillations under periodic impulse forcing. *Journal of Sound and Vibration*, 172(3):339–358, 1994.

[81] R. Pratap and P. Holmes. Chaos in a mapping describing elastoplastic oscillations. *Nonlinear Dynamics*, 8(1):111–139, 1995.

[82] J. Gerstmayr and H. Irschik. Vibrations of the elasto-plastic pendulum. *International Journal of Non-Linear Mechanics*, 38:111 – 122, 2003.

[83] C-S. Liu and Z-M. Huang. The steady state responses of s.d.o.f. viscous elasto-plastic oscillator under sinusoidal loadings. *Journal of Sound and Vibration*, 273(1-2):149–173, 2004.

[84] N. Challamel and G. Gilles. Stability and dynamics of a harmonically excited elastic-perfectly plastic oscillator. *Journal of Sound and Vibration*, 301(3-5):608–634, 2007.

[85] T. Kalmár-Nagy and A. Shekhawat. Nonlinear dynamics of oscillators with bilinear hysteresis and sinusoidal excitation. *Physica D: Nonlinear Phenomena*, 238(17):1768–1786, 2009.

[86] V. Karagiozov and D. Karagiozova. Chaotic phenomena in the dynamic buckling of an elastic-plastic column under an impact. *Nonlinear Dynamics*, 9(3):265–280, 1996.

[87] M. A. Savi and P. M. C. L. Pacheco. Chaotic motion of an elasto-plastic beam. *Journal of the Brazilian Society of Mechanical Sciences and Engineering*, 25(1), 2003.

[88] P. Ribeiro and G. H. M. van der Heijden. Elasto-plastic and geometrically nonlinear vibrations of beams by the p-version finite element method. *Journal of Sound and Vibration*, 325(1-2):321–337, 2009.

[89] P. Ribeiro. On the predictability of elasto-plastic and geometrically non-linear oscillations of beams under harmonic excitation. *Nonlinear Dynamics*, 67(3):1761–1778, 2012.

[90] P. L. Grognec, Q-H. Nguyen, and M. Hjiaj. Plastic bifurcation analysis of a two-layer shear-deformable beam–column with partial interaction. *International Journal of Non-Linear Mechanics*, 67:85–94, 2014.

[91] W. Lacarbonara and F. Vestroni. Nonclassical responses of oscillators with hysteresis. *Nonlinear Dynamics*, 32(3):235–258, 2003.

[92] T. S. Parker and L. O. Chua. *Practical Numerical Algorithms for Chaotic Systems*. Springer, 1989.

[93] R. J. Morante. Recommendations for revision of seismic damping values in regulatory guide 1.61, 2006.

[94] A. Kwan, Z. You, and S. Pellegrino. Active and passive cable elements in deployable/retractable masts. *Int. J. Space Struct.*, 8(1&2):29–40, 1993.

[95] A. Kwan. A parabolic pantographic deployable antenna. *Int. J. Space Struct.*, 10(4):195–203, 1995.

[96] T. Liu, S. Yan, and W. Zhang. Time–frequency analysis of nonstationary vibration signals for deployable structures by using the constant-q nonstationary gabor transform. *Mechanical Systems and Signal Processing*, 75:228–244, 2016.

[97] F. Dewalque, C. Schwartz, V. Denoël, J.-L. Croisier, B. Forthomme, and O. Brüls. Experimental and numerical investigation of the nonlineardynamics of compliant mechanisms for deployable structures. *Mech. Syst. Signal Process.*, 101:1–25, 2018.

[98] Y. Li, C. Wang, and W. Huang. Dynamics analysis of planar rigid-flexible coupling deployable solar array system with multiple revolute clearance joints. *Mechanical Systems and Signal Processing*, 117:188–209, 2019.

[99] B. Li, S-M. Wang, C-J. Zhi, X-Z. Xue, and V. Makis. Analytical and numerical study of the buckling of planar linear array deployable structures based on scissor-like element under its own weight. *Mechanical Systems and Signal Processing*, 83:474–488, 2017.

[100] T. Van Mele, N. De Temmerman, L. De Laet, and M. Mollaert. Scissor-hinged retractable membrane structures. *International Journal of Structural Engineering*, 1:374, 2010.

[101] G. E. Fenci and N. G. R. Currie. Deployable structures classification: A review. *International Journal of Space Structures*, 32(2):112–130, 2017.

[102] C. J. Gantes, J. J. Connor, R. D. Logcher, and Y. Rosenfeld. Structural analysis and design of deployable structures. *Computers and Structures*, 32:661–669, 1989.

[103] C. J. Gantes and E. Konitopoulou. Geometric design of arbitrarily curved bi-stable deployable arches with discrete joint size. *International Journal of Solids and Structures*, 41:5517–5540, 2004.

[104] C. J. Gantes, J. J. Connor, and R. D. Logcher. Simple friction model for scissor type mobile structures. *Journal of Engineering Mechanics*, 119: 456–475, 1993.

[105] M. A. Crisfield. A consistent co-rotational formulation for non linear, three-dimensional, beam-elements. *Computer methods in applied mechanics and engineering*, 81:131–150, 1990.

[106] C. Pacoste and A. Erikkson. Beam elements in instability problems. *Computer methods in applied mechanics and engineering*, 144:163–197, 1997.

[107] P. E. Nikravesh and I. S. Chung. Application of euler parameters to dynamical analysis of three-dimensional constrained mechanical systems. *Journal of mechanical design*, 104:785–791, 1982.

[108] H. Sugiyama, J. L. Escalona, and A. A. Shabana. Formulation of three-dimensional joint constraints using the absolute nodal coordinates. *Nonlinear Dynamics*, 31:167–195, 2003.

[109] G. Jelenic and M. A. Crisfield. Nonlinear 'master-slave' relationship for joints in 3-d beams with large rotations. *Computer methods in applied mechanics and engineering*, 135:211–228, 1996.

[110] J. C. Simo and T. J. R. Hughes. *Computational Inelasticity*. Springer, 1998.

[111] C. J. Gantes. Combining numerical analysis and engineering judgment to design deployable structures. *Computers and Structures*, 40:431–440, 1991.

[112] C. J. Gantes. An improved analytical model for the prediction of the nonlinear behavior of flat and curved deployable space frames. *Journal of Constructional Steel Research*, 44:129–158, 1997.

[113] C. J. Gantes, A. Giakoumakist, and P. Vousvounist. Symbolic manipulation as a tool for design deployable domes. *Computers and Structures*, 64:865–878, 1997.

[114] L. F. P. Munoz, P. B. Gonçalves, R. A. Silveira, and A. Silva. Nonlinear resonance analysis of slender portal frames under base excitation. *Shock and Vibration*, 2017.

[115] J. Argyris. An excursion into large rotations. *Computer methods in applied mechanics and engineering*, 32:85–155, 1982.

[116] S. Krenk. *Non-linear Modeling and Analysis of Solids and Structures.* Cambridge University Press, 2009.

[117] A. Ibrahimbegovic, F. Frey, and I. Kozar. Computational aspects of vector-like parametrization of three-dimensional finite rotations. *International journal for numerical methods in engineering*, 38:3653–3673, 1995.

[118] A. Ibrahimbegovic. On the choice of finite rotation parameters. *Computer methods in applied mechanics and engineering*, 149:49–71, 1997.

[119] R. Sowerby and E. Chu. Rotations, stress rates and strain measures in homogeneous deformation processes. *International Journal of Solids and Structures*, 20(11-12):1037–1048, 1984.

[120] R. W. Ogden. *Non-Linear Elastic Deformations (Dover Civil and Mechanical Engineering).* Dover Publications, 1997.

[121] V. E. Palosh. Investigation of the dynamics of a double pendulum with following and conservative forces. *Journal of Computer and Systems Sciences*, 47(3):386–396, 2008.

[122] L. H. Teh and M. J. Clarke. Plastic-zone analysis of 3d steel frames using beam elements. *Journal of Structural Engineering*, 125(11):1328–1337, 1999.

[123] P. F. Pai and A. N. Palazotto. Large-deformation analysis of flexible beams. *International Journal of Solids and Structures*, 33:1335–1353, 1996.

[124] B. N-Omid and C. C. Rankin. Finite rotation analysis and consistent linearization using projectors. *Computer methods in applied mechanics and engineering*, 93:353–384, 1991.

[125] M. A. Crisfield. *Non-Linear Finite Element Analysis of Solids and Structures*, volume I. Wiley, 1991.

[126] S. L. Chan. Geometric and material nonlinear analysis of beam-columns and frames using the minimum residual displacement method. *International Journal for Numerical Methods in Engineering*, 26:2657–2669, 1998.

[127] S. Skatulla and C. Sansour. On a path-following method for non-linear solid mechanics with applications to structural and cardiac mechanics

subject to arbitrary loading scenarios. *International Journal of Solids and Structures*, 96:181–191, 2016.